Universität Zürich[UZH]

Geographisches Institut

Spatio-Temporal Surface Temperature Dynamics and Atmospheric Controls on Murtèl Rock Glacier

GEO 511 Master's Thesis

Author: Marco Hassler, 20-723-458

Supervised by: Dr. Kathrin Naegeli, Gabriele Bramati

Faculty representative: Prof. Dr. Alexander Damm

08.07.2026

Universität Zürich[UZH]

Spatio-Temporal Surface Temperature Dynamics and Atmospheric Controls on Murtèl Rock Glacier

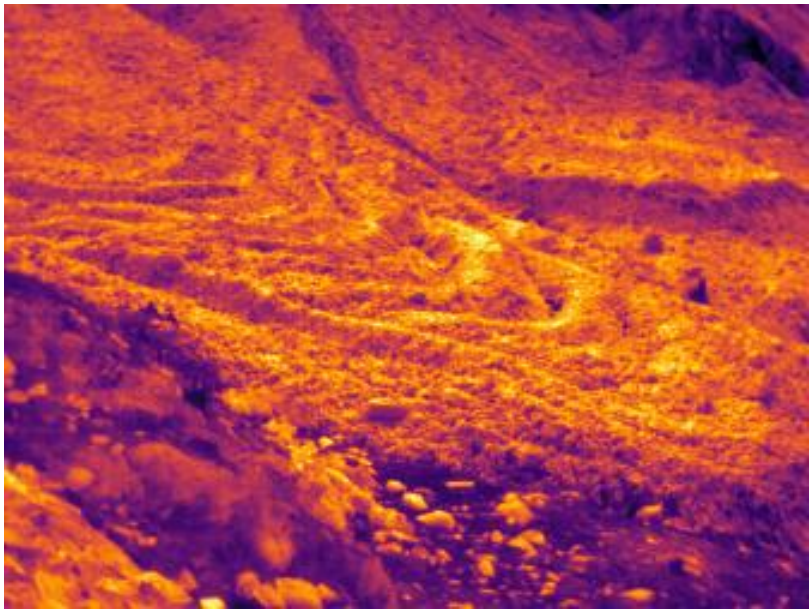

GEO 511 Master's Thesis

Author
Marco Hassler
20-723-458

Supervised by
Dr. Kathrin Naegeli
Gabriele Bramati

Faculty Representative
Prof. Dr. Alexander Damm-Reiser

Abstract

Mountain permafrost is a key component of the alpine cryosphere. Rock glaciers are part of this component and are expected to gain importance as future water reservoirs in mountain regions as they are climatically more resilient than glaciers. While their internal thermal regime has been investigated extensively, the spatial variability of their surface temperature remains poorly constrained, because conventional point-based instrumentation cannot resolve the heterogeneity introduced by ridge-and-furrow microtopography, coarse blocky debris and patchy snow.

This thesis addresses that gap by exploiting a long-term ground-based MOBOTIX M16 thermal infrared (TIR) camera installed at the Murtèl rock glacier in the Upper Engadine (Swiss Alps). An atmospheric correction was applied, and the corrected surface temperatures were validated for the period from 2021 to 2023 against borehole, ground surface temperature, radiometer and longwave-radiation-derived measurements. Two complementary grouping schemes (k-means clustering of mean diurnal temperature curves and a z-normalised anomaly persistence classification) were applied across analysis periods representing snow-free, snow-covered, transition, precipitation and day–night conditions. Multiple linear regression (MLR) and generalised additive models (GAMs) were then used to attribute surface temperature variability to seven meteorological predictors recorded at the meteorological station on top of the rock glacier.

The TIR camera reproduces the seasonal and diurnal evolution of surface temperature reliably but retains a persistent cold bias of 10 to 20 °C relative to longwave-derived station temperatures after correction. The comparison with GST loggers and borehole sensors shows a substantially smaller offset. The atmospheric correction introduces a systematic, distance-dependent shift on the order of 1.5 °C across the field of view, more pronounced in winter, spring and autumn, and weakest in summer. Both grouping schemes recover a dominantly bimodal surface temperature field, characterised by a ridge-furrow contrast within the rock glacier and a rock-glacier-versus-background contrast that reorganise systematically with snow cover, precipitation and the diurnal cycle. Across nearly all periods, air temperature is the leading statistical driver of surface temperature, with downwelling shortwave radiation acting as a competing secondary driver whose relative influence increases as that of air temperature decreases.

The study demonstrates that long-term, ground-based TIR imaging provides a cost-efficient and information-rich complement to traditional point-based permafrost monitoring, and it establishes a methodological framework for characterising both the spatial structure and the atmospheric controls of rock glacier surface temperatures.

Content

Abstract ii
Content iii
List of Figures vi
List of Tables xvi
1. Introduction 1
2. Study Site and Data 3
2.1. Study Site 3
2.2. Data 4
2.2.1. Thermal Infrared Camera 4
2.2.2. Meteorological Station 4
2.2.3. Ground Surface Temperature Measurements 5
2.2.4. Borehole Measurements 5
2.2.5. Radiometer Measurements 5
2.2.6. Digital Elevation Model (DEM) 5
3. Methods 7
3.1. Data quality control and filtering 7
3.1.1. TIR images 7
3.1.2. CSV datasets 9
3.1.2.1. Meteorological Station Data 9
3.1.2.2. Borehole and GST Measurements 11
3.2. Temperature Correction 11
3.3. Uncertainty Characterisation 15
3.4. Spatio-temporal pattern analysis 15
3.4.1. Diurnal Curve Clustering 15
3.4.2. Anomaly Persistence Classification 17
3.5. Statistical dependence analysis 17
3.5.1. Multiple linear regression 17
3.5.2. Generalized Additive Models (GAMs) 18
4. Results 19
4.1. Temperature Correction 19
4.1.1. Core Correction 19
4.1.2. Uncertainty Assessment 24
4.2. Analysis Periods 28
4.3. Spatio-temporal pattern analysis 29
4.3.1. Diurnal Curve Clustering 29

4.3.1.1. Transition Periods 30
4.3.1.2. Snow Cover vs Snow Free 31
4.3.1.3. Precipitation vs No Precipitation 32
4.3.1.4. Day vs Night 33
4.3.2. Anomaly Persistence Classification 35
4.3.2.1. Transition Periods 35
4.3.2.2. Snow Cover vs. Snow Free 36
4.3.2.3. Rain Periods vs. Dry Periods 37
4.3.2.4. Day vs. Night 37
4.4. Statistical dependence analysis 39
4.4.1. Diurnal Curve Clustering 39
4.4.1.1. Transition Periods 39
4.4.1.2. Snow vs No Snow 40
4.4.1.3. Rain Periods vs Dry Periods 41
4.4.1.4. Day vs Night 41
4.4.2. Anomaly Persistence Classification 43
4.4.2.1. Transition Periods 43
4.4.2.2. Snow vs No Snow 44
4.4.2.3. Rain Periods vs Dry Periods 45
4.4.2.4. Day vs Night 45
4.5. Generalised Additive Models 46
4.5.1. Criteria for application 46
4.5.1.1. Diurnal Curve Clustering 46
4.5.1.2. Anomaly Persistence Classification 48
4.5.2. GAM Results 48
4.5.2.1. Diurnal Curve Clustering 48
4.5.2.1.1. Transition: Snow-Covered to Snow-Free 48
4.5.2.1.2. Transition: Snow-Free to Snow-Covered 49
4.5.2.1.3. Snow-Covered, Snow-Free and Precipitation Subsets 50
4.5.2.1.4. Day / Night Periods 50
4.5.2.2. Anomaly Persistence Classification 51
4.5.2.2.1. Transition: Snow-Covered to Snow-Free 51
4.5.2.2.2. Transition: Snow-Free to Snow-Covered 52
4.5.2.2.3. Static and Precipitation Subsets 52
4.5.2.2.4. Day / Night Periods 53
5. Discussion 54

5.1. Temperature Correction 54
5.1.1. Temporal Dynamics and the Persistent Cold Bias 54
5.1.2. The Distance Dependency of the Correction 54
5.1.3. Emissivity Sensitivity 55
5.1.4. Window Transmissivity 56
5.1.5. Aluminium Plate Validation 56
5.1.6. Further limitations 57
5.2. Grouping Analysis 57
5.2.1. The Spatial Organisation of the Surface Temperature Field 57
5.2.2. Diurnal Control and the Role of Shortwave Radiation 58
5.2.3. Transition Periods, Snow Cover and Precipitation 59
5.2.4. Limitations 60
5.3. Dependency Analysis 61
5.3.1. Air temperature as the dominant driver 61
5.3.2. Model performance 62
5.3.3. The inverse relationship between air temperature and shortwave influence 62
5.3.4. The role of longwave radiation during night 63
5.3.5. Limitations 64
6. Conclusion 65
Acknowledgements 67
Bibliography 68
Appendix 73
Appendix A: Preprocessing and GitHub repository 73
Appendix B: Temperature Correction 76
Appendix C: Dependency Analysis 106
Disclosure Statement for the use of AI 184
Personal Declaration 185

List of Figures

Figure 1: Overview photograph of the Murtèl rock glacier taken on 29 September 2025, showing the characteristic ridge-and-furrow microtopography (A), large, exposed boulders (B), a section of the headwalls (C) and the surrounding topographic setting. 3
Figure 2: Overview of the study site and measurement infrastructure on the Murtèl rock glacier. The approximate field of view of the TIR camera is indicated by the shaded area. Basemap: Swisstopo. 4
Figure 3: Example of "Bad" labelled images 7
Figure 4: Example of "Good" labelled images 7
Figure 5: Entropy distributions of labelled images with resulting entropy threshold 8
Figure 6: Filtered time series of all meteorological station variables from January 2021 to September 2023. Panels show air temperature, relative humidity, downwelling and upwelling longwave radiation, downwelling and upwelling shortwave radiation, wind speed, wind direction, and snow depth. Applied filtering thresholds are summarised in Table 2. 10
Figure 7: Borehole temperature time series at multiple depths for Boreholes 1, 2, and 3. Colours indicate sensor depth (in metres). Data gaps result from permanent sensor failures; no filtering was applied. 11
Figure 8: Raw distance map (left), interpolated distance map (middle) and overlay on top of a TIR image (right) 12
Figure 9: Schematic illustration of the clustering algorithm workflow 16
Figure 10: Comparison of corrected and raw TIR-derived pixel temperatures with surface temperatures derived from upwelling longwave radiation at the meteorological station, as well as with radiometer measurements at ridge and furrow locations for 2022. Grey shaded areas indicate transition periods between snow-covered and snow-free conditions. All time series represent daily mean values. 19
Figure 11: Comparison of corrected and raw TIR-derived pixel temperatures with borehole temperatures for 2022. Grey shaded areas indicate transition periods between snow-covered and snow-free conditions. All time series represent daily mean values. 20
Figure 12: Comparison of corrected and raw TIR-derived pixel temperatures with GST logger measurements for 2022. Grey shaded areas indicate transition periods between snow-covered and snow-free conditions. All time series represent daily mean values. 21
Figure 13: Relationship between the temperature difference introduced by the atmospheric correction and the distance to the camera for 2022. Each point represents an individual pixel, coloured by point density. 22
Figure 14: Scatterplot of derived TIR temperatures (corrected and raw) vs. validation temperatures (temperature derived from longwave radiation and radiometers). This plot represents snow-free acquisitions from 2022. 22
Figure 15: Scatterplot of derived TIR temperatures (corrected and raw) vs. validation temperatures (GST measurements). This plot represents snow-free acquisitions from 2022. 23
Figure 16: Scatterplot of derived TIR temperatures (corrected and raw) vs. validation temperatures (Borehole measurements). This plot represents snow-free acquisitions from 2022. 23
Figure 17: Corrected vs Aluminium Corrected Temperatures 26
Figure 18: Temperature Difference vs Distance to Camera 27
Figure 19: Temperature Difference vs Internal Camera Temperature 27

Figure 20: Distribution of the silhouette-optimal number of clusters k across all grouping windows, pooled over analysis periods. For each window, k was evaluated in the range 2 to 7 and the value maximising the silhouette score was retained.....29
Figure 21: Representative cluster maps from the diurnal temperature curve clustering approach. Left: Start of snow-free to snow-covered transition (15.09.21); Right: Midpoint of snow-free to snow-covered transition of the year 2021 (22.10.21).....30
Figure 22: Representative cluster maps from the diurnal temperature curve clustering approach. Left: End of snow-free to snow-covered transition (10.11.22); Right: Start of snow-covered to snow-free transition (16.06.21).....31
Figure 23: Representative cluster maps from the diurnal temperature curve clustering approach. Left: Midpoint of snow-covered to snow-free transition (29.06.21); Right: End of snow-covered to snow-free transition (24.07.21).....31
Figure 24: Representative cluster maps from the diurnal temperature curve clustering approach. Left: Snow-covered (10.03.21); Right: Snow-free (21.08.21).....32
Figure 25: Representative cluster maps from the diurnal temperature curve clustering approach. Left: Snow-free dry period (16.07.22); Right: Snow-free precipitation period (01.08.22).....33
Figure 26: Representative cluster maps from the diurnal temperature curve clustering approach. Left: Snow-covered dry period (06.03.22); Right: Snow-covered precipitation period (08.02.22).....33
Figure 27: Representative cluster maps from the diurnal temperature curve clustering approach. Left: Snow-free day (02.07.22); Right: Snow-free night (02.07.22).....34
Figure 28: Representative cluster maps from the diurnal temperature curve clustering approach. Left: Snow-covered day (08.03.22); Right: Snow-covered night (08.03.22).....34
Figure 29: Representative cluster maps from the anomaly persistence classification approach. Left: begin of snow-covered to snow-free transition (17.06.21); Right: end of snow-covered to snow-free transition (22.07.21).....35
Figure 30: Representative cluster maps from the anomaly persistence classification approach. Left: halfway-point of snow-free to snow-covered transition (30.10.21); Right: end of snow-free to snow-covered transition (11.11.21).....36
Figure 31: Representative cluster maps from the anomaly persistence classification approach. Left: Snow-free period (16.08.21); Right: Snow-covered period (08.03.21).....36
Figure 32: Representative cluster maps from the anomaly persistence classification approach. Left: Snow-free precipitation period (01.08.22); Right: Snow-covered precipitation period (14.02.22).....37
Figure 33: Representative cluster maps from the anomaly persistence classification approach. Left: Snow-free day (24.06.22); Right: Snow-free night (24.06.22).....38
Figure 34: Representative cluster maps from the anomaly persistence classification approach. Left: Snow-covered day (28.02.22); Right: Snow-coved night (28.02.22).....38
Figure 35: Boxplots of the relative influence (%) of meteorological variables on camera-measured LST across different analysis periods, separated by groups resulting from the diurnal curve clustering workflow. Relative influence is computed from multiple linear regression coefficients normalized so that the sum of absolute coefficients per day equals 100 %. The coefficient of determination (R^2) of the corresponding day-wise models is shown on the secondary y-axis (right). 39

Figure 36: Boxplots of the relative influence (%) of meteorological variables on camera-measured LST across different analysis periods, separated by groups resulting from the anomaly persistence classification workflow. Relative influence is computed from multiple linear regression coefficients normalized so that the sum of absolute coefficients per day equals 100 %. The coefficient of determination (R^2) of the corresponding day-wise models is shown on the secondary y-axis (right). 43
Figure A.1: Raw (left) and filtered (right) time series of air temperature, relative humidity, downwelling longwave radiation, and upwelling longwave radiation from the meteorological station for January 2021 to September 2023. Applied filtering thresholds are summarised in Table 2. 73
Figure A.2: Raw (left) and filtered (right) time series of downwelling shortwave radiation, upwelling shortwave radiation, wind speed and wind direction from the meteorological station for January 2021 to September 2023. Applied filtering thresholds are summarised in Table 2. 74
Figure A.3: Raw (left) and filtered (right) time series of snow height from the meteorological station for January 2021 to September 2023. Applied filtering thresholds are summarised in Table 2. 75
Figure B.1: Comparison of corrected and raw TIR-derived pixel temperatures with surface temperatures derived from upwelling longwave radiation at the meteorological station, as well as with radiometer measurements at ridge and furrow locations for 2021. Grey shaded areas indicate transition periods between snow-covered and snow-free conditions. All time series represent daily mean values. 76
Figure B.2: Comparison of corrected and raw TIR-derived pixel temperatures with surface temperatures derived from upwelling longwave radiation at the meteorological station, as well as with radiometer measurements at ridge and furrow locations for 2022. Grey shaded areas indicate transition periods between snow-covered and snow-free conditions. All time series represent daily mean values. 77
Figure B.3: Comparison of corrected and raw TIR-derived pixel temperatures with surface temperatures derived from upwelling longwave radiation at the meteorological station, as well as with radiometer measurements at ridge and furrow locations for 2023. Grey shaded areas indicate transition periods between snow-covered and snow-free conditions. All time series represent daily mean values. 78
Figure B.4: Comparison of corrected and raw TIR-derived pixel temperatures with borehole temperatures for 2021. Grey shaded areas indicate transition periods between snow-covered and snow-free conditions. All time series represent daily mean values. 79
Figure B.5: Comparison of corrected and raw TIR-derived pixel temperatures with borehole temperatures for 2022. Grey shaded areas indicate transition periods between snow-covered and snow-free conditions. All time series represent daily mean values. 80
Figure B.6: Comparison of corrected and raw TIR-derived pixel temperatures with borehole temperatures for 2023. Grey shaded areas indicate transition periods between snow-covered and snow-free conditions. All time series represent daily mean values. 81
Figure B.7: Comparison of corrected and raw TIR-derived pixel temperatures with GST logger measurements for 2021. Grey shaded areas indicate transition periods between snow-covered and snow-free conditions. All time series represent daily mean values. 82
Figure B.8: Comparison of corrected and raw TIR-derived pixel temperatures with GST logger measurements for 2022. Grey shaded areas indicate transition periods between snow-covered and snow-free conditions. All time series represent daily mean values. 83

Figure B.9: Comparison of corrected and raw TIR-derived pixel temperatures with GST logger measurements for 2023. Grey shaded areas indicate transition periods between snow-covered and snow-free conditions. All time series represent daily mean values. 84
Figure B.10: Relationship between the temperature difference introduced by the atmospheric correction and the distance to the camera for spring 2022. Each point represents an individual pixel, coloured by point density. 85
Figure B.11: Relationship between the temperature difference introduced by the atmospheric correction and the distance to the camera for summer 2022. Each point represents an individual pixel, coloured by point density. 85
Figure B.12: Relationship between the temperature difference introduced by the atmospheric correction and the distance to the camera for autumn 2022. Each point represents an individual pixel, coloured by point density. 86
Figure B.13: Relationship between the temperature difference introduced by the atmospheric correction and the distance to the camera for winter 2022. Each point represents an individual pixel, coloured by point density. 86
Figure B.14: Scatterplot of derived TIR temperatures (corrected and raw) vs. validation temperatures (temperature derived from longwave radiation). This plot represents snow-free acquisitions from 2022. 87
Figure B.15: Scatterplot of derived TIR temperatures (corrected and raw) vs. validation temperatures (radiometer ridge). This plot represents snow-free acquisitions from 2022 87
Figure B.16: Scatterplot of derived TIR temperatures (corrected and raw) vs. validation temperatures (radiometer furrow). This plot represents snow-free acquisitions from 2022. 88
Figure B.17: Scatterplot of derived TIR temperatures (corrected and raw) vs. validation temperatures (GST 1). This plot represents snow-free acquisitions from 2022. 88
Figure B.18: Scatterplot of derived TIR temperatures (corrected and raw) vs. validation temperatures (GST 2). This plot represents snow-free acquisitions from 2022. 89
Figure B.19: Scatterplot of derived TIR temperatures (corrected and raw) vs. validation temperatures (GST 3). This plot represents snow-free acquisitions from 2022. 89
Figure B.20: Scatterplot of derived TIR temperatures (corrected and raw) vs. validation temperatures (GST 4). This plot represents snow-free acquisitions from 2022. 90
Figure B. 21: Scatterplot of derived TIR temperatures (corrected and raw) vs. validation temperatures (GST 5). This plot represents snow-free acquisitions from 2022. 90
Figure B.22: Scatterplot of derived TIR temperatures (corrected and raw) vs. validation temperatures (Borehole 1). This plot represents snow-free acquisitions from 2022. 91
Figure B.23: Scatterplot of derived TIR temperatures (corrected and raw) vs. validation temperatures (Borehole 2). This plot represents snow-free acquisitions from 2022. 91
Figure B.24: Scatterplot of derived TIR temperatures (corrected and raw) vs. validation temperatures (Borehole 3). This plot represents snow-free acquisitions from 2022. 92
Figure B.25: Sensitivity of corrected TIR surface temperatures to rock emissivity (ε = 0.90, 0.92, 0.94), evaluated against longwave-radiation-derived validation temperatures for the snow-free period of 2022. 92
Figure B.26: Sensitivity of corrected TIR surface temperatures to rock emissivity (ε = 0.90, 0.92, 0.94), evaluated against radiometer ridge validation temperatures for the snow-free period of 2022. 93

Figure B.27: Sensitivity of corrected TIR surface temperatures to rock emissivity (ε = 0.90, 0.92, 0.94), evaluated against radiometer furrow validation temperatures for the snow-free period of 2022. 93
Figure B.28: Sensitivity of corrected TIR surface temperatures to rock emissivity (ε = 0.90, 0.92, 0.94), evaluated against GST 1 validation temperatures for the snow-free period of 2022. 94
Figure B.29: Sensitivity of corrected TIR surface temperatures to rock emissivity (ε = 0.90, 0.92, 0.94), evaluated against GST 2 validation temperatures for the snow-free period of 2022. 94
Figure B.30: Sensitivity of corrected TIR surface temperatures to rock emissivity (ε = 0.90, 0.92, 0.94), evaluated against GST 3 validation temperatures for the snow-free period of 2022. 95
Figure B.31: Sensitivity of corrected TIR surface temperatures to rock emissivity (ε = 0.90, 0.92, 0.94), evaluated against GST 4 validation temperatures for the snow-free period of 2022. 95
Figure B.32: Sensitivity of corrected TIR surface temperatures to rock emissivity (ε = 0.90, 0.92, 0.94), evaluated against GST 5 validation temperatures for the snow-free period of 2022. 96
Figure B.33: Sensitivity of corrected TIR surface temperatures to rock emissivity (ε = 0.90, 0.92, 0.94), evaluated against borehole 1 validation temperatures for the snow-free period of 2022. .. 96
Figure B.34: Sensitivity of corrected TIR surface temperatures to rock emissivity (ε = 0.90, 0.92, 0.94), evaluated against borehole 2 validation temperatures for the snow-free period of 2022. .. 97
Figure B.35: Sensitivity of corrected TIR surface temperatures to rock emissivity (ε = 0.90, 0.92, 0.94), evaluated against borehole 1 validation temperatures for the snow-free period of 2022. .. 97
Figure B.36: Sensitivity of corrected TIR surface temperatures to window transmissivity (τ = 0.86, 0.90, 0.96), evaluated against longwave-radiation-derived validation temperatures for the snow-free period of 2022. 98
Figure B.37: Sensitivity of corrected TIR surface temperatures to window transmissivity (τ = 0.86, 0.90, 0.96), evaluated against radiometer ridge validation temperatures for the snow-free period of 2022. 98
Figure B.38: Sensitivity of corrected TIR surface temperatures to window transmissivity (τ = 0.86, 0.90, 0.96), evaluated against radiometer furrow validation temperatures for the snow-free period of 2022. 99
Figure B.39: Sensitivity of corrected TIR surface temperatures to window transmissivity (τ = 0.86, 0.90, 0.96), evaluated against GST 1 validation temperatures for the snow-free period of 2022. 99
Figure B.40: Sensitivity of corrected TIR surface temperatures to window transmissivity (τ = 0.86, 0.90, 0.96), evaluated against GST 2 validation temperatures for the snow-free period of 2022. 100
Figure B.41: Sensitivity of corrected TIR surface temperatures to window transmissivity (τ = 0.86, 0.90, 0.96), evaluated against GST 3 validation temperatures for the snow-free period of 2022. 100
Figure B.42: Sensitivity of corrected TIR surface temperatures to window transmissivity (τ = 0.86, 0.90, 0.96), evaluated against GST 4 validation temperatures for the snow-free period of 2022. 101
Figure B.43: Sensitivity of corrected TIR surface temperatures to window transmissivity (τ = 0.86, 0.90, 0.96), evaluated against GST 5 validation temperatures for the snow-free period of 2022. 101

Figure B.44: Sensitivity of corrected TIR surface temperatures to window transmissivity (τ = 0.86, 0.90, 0.96), evaluated against borehole 1 validation temperatures for the snow-free period of 2022. 102
Figure B.45: Sensitivity of corrected TIR surface temperatures to window transmissivity (τ = 0.86, 0.90, 0.96), evaluated against borehole 2 validation temperatures for the snow-free period of 2022. 102
Figure B.46: Sensitivity of corrected TIR surface temperatures to window transmissivity (τ = 0.86, 0.90, 0.96), evaluated against borehole 3 validation temperatures for the snow-free period of 2022. 103
Figure B.47: Comparison of corrected, raw and aluminium-corrected TIR-derived pixel temperatures with surface temperatures derived from upwelling longwave radiation at the meteorological station, as well as with radiometer measurements at ridge and furrow locations for 2022. Grey shaded areas indicate transition periods between snow-covered and snow-free conditions. All time series represent daily mean values. 104
Figure B.48: Comparison of corrected, raw and aluminium-corrected TIR-derived pixel temperatures with borehole temperatures for 2023. Grey shaded areas indicate transition periods between snow-covered and snow-free conditions. All time series represent daily mean values. ... 105
Figure B.49: Comparison of corrected, raw and aluminium-corrected TIR-derived pixel temperatures with GST logger measurements for 2023. Grey shaded areas indicate transition periods between snow-covered and snow-free conditions. All time series represent daily mean values. 106
Figure C.1: Relative influence plots of seven predictor variables used in the multiple linear regression models of the diurnal curve clustering approach with corresponding R^2 and residual values and the temporal evolution of the predictor variables. Grey shaded areas indicate days which were flagged for too low R^2 or residual values. Left: Snow-Covered to Snow-Free transition 2021; right: Snow-Covered to Snow-Free transition 2022 107
Figure C.2: Relative influence plots of seven predictor variables used in the multiple linear regression models of the diurnal curve clustering approach with corresponding R^2 and residual values and the temporal evolution of the predictor variables. Grey shaded areas indicate days which were flagged for too low R^2 or residual values. Left: Snow-Covered to Snow-Free transition 2023; right: Snow-Free to Snow-Covered transition 2021 108
Figure C.3: Relative influence plots of seven predictor variables used in the multiple linear regression models of the diurnal curve clustering approach with corresponding R^2 and residual values and the temporal evolution of the predictor variables. Grey shaded areas indicate days which were flagged for too low R^2 or residual values. Left: Snow-Free to Snow-Covered transition 2022, right: Snow-Free period 2021 109
Figure C.4: Relative influence plots of seven predictor variables used in the multiple linear regression models of the diurnal curve clustering approach with corresponding R^2 and residual values and the temporal evolution of the predictor variables. Grey shaded areas indicate days which were flagged for too low R^2 or residual values. Left: Snow-Free period 2022; right: Snow-Covered period 110
Figure C.5: Relative influence plots of seven predictor variables used in the multiple linear regression models of the diurnal curve clustering approach with corresponding R^2 and residual values and the temporal evolution of the predictor variables. Grey shaded areas indicate days which

were flagged for too low R^2 or residual values. Left: Snow- Free Precipitation period; right: Snow-Covered Precipitation period 111
Figure C.6: Relative influence plots of seven predictor variables used in the multiple linear regression models of the diurnal curve clustering approach with corresponding R^2 and residual values and the temporal evolution of the predictor variables. Grey shaded areas indicate days which were flagged for too low R^2 or residual values. Left: Snow-Free No Precipitation period; right: Snow-Covered Precipitation period 112
Figure C.7: Relative influence plots of seven predictor variables used in the multiple linear regression models of the diurnal curve clustering approach with corresponding R^2 and residual values and the temporal evolution of the predictor variables. Grey shaded areas indicate days which were flagged for too low R^2 or residual values. Left: Snow-Free Day period; right: Snow-Free Night period 113
Figure C.8: Relative influence plots of seven predictor variables used in the multiple linear regression models of the diurnal curve clustering approach with corresponding R^2 and residual values and the temporal evolution of the predictor variables. Grey shaded areas indicate days which were flagged for too low R^2 or residual values. Left: Snow-Covered Day period; right: Snow-Covered Night period 114
Figure C.9: Relative influence plots of seven predictor variables used in the multiple linear regression models of the anomaly persistence classification approach with corresponding R^2 and residual values and the temporal evolution of the predictor variables. Grey shaded areas indicate days which were flagged for too low R^2 or residual values. Left: Snow-Covered to Snow-Free transition 2021; right: Snow-Covered to Snow-Free transition 2022 115
Figure C.10: Relative influence plots of seven predictor variables used in the multiple linear regression models of the anomaly persistence classification approach with corresponding R^2 and residual values and the temporal evolution of the predictor variables. Grey shaded areas indicate days which were flagged for too low R^2 or residual values. Left: Snow-Covered to Snow-Free transition 2023; right: Snow-Free to Snow-Covered transition 2021 116
Figure C.11: Relative influence plots of seven predictor variables used in the multiple linear regression models of the anomaly persistence classification approach with corresponding R^2 and residual values and the temporal evolution of the predictor variables. Grey shaded areas indicate days which were flagged for too low R^2 or residual values. Left: Snow-Free to Snow-Covered transition 2022; right: Snow-Free period 2021 117
Figure C.12: Relative influence plots of seven predictor variables used in the multiple linear regression models of the anomaly persistence classification approach with corresponding R^2 and residual values and the temporal evolution of the predictor variables. Grey shaded areas indicate days which were flagged for too low R^2 or residual values. Left: Snow-Free period 2022; right: Snow-Covered period 2022 118
Figure C.13: Relative influence plots of seven predictor variables used in the multiple linear regression models of the anomaly persistence classification approach with corresponding R^2 and residual values and the temporal evolution of the predictor variables. Grey shaded areas indicate days which were flagged for too low R^2 or residual values. Left: Snow-Free Precipitation period, right: Snow-Covered Precipitation period 119
Figure C.14: Relative influence plots of seven predictor variables used in the multiple linear regression models of the anomaly persistence classification approach with corresponding R^2 and residual values and the temporal evolution of the predictor variables. Grey shaded

areas indicate days which were flagged for too low R^2 or residual values. Left: Snow-Free No Precipitation period, right: Snow-Covered No Precipitation period 120
Figure C.15: Relative influence plots of seven predictor variables used in the multiple linear regression models of the anomaly persistence classification approach with corresponding R^2 and residual values and the temporal evolution of the predictor variables. Grey shaded areas indicate days which were flagged for too low R^2 or residual values. Left: Snow-Free Day period, right: Snow-Free Night period 121
Figure C.16: Relative influence plots of seven predictor variables used in the multiple linear regression models of the anomaly persistence classification approach with corresponding R^2 and residual values and the temporal evolution of the predictor variables. Grey shaded areas indicate days which were flagged for too low R^2 or residual values. Left: Snow-Covered Day period, right: Snow-Covered Night period 122
Figure C.17: GAM results of the diurnal curve clustering approach of days 7, 8 and 9 of the 2021 snow-covered to snow-free transition period..... 133
Figure C.18: GAM results of the diurnal curve clustering approach of days 17, 18 and 19 of the 2021 snow-covered to snow-free transition period..... 134
Figure C.19: GAM results of the diurnal curve clustering approach of days 26, 27 and 31 of the 2021 snow-covered to snow-free transition period..... 135
Figure C.20: GAM results of the diurnal curve clustering approach of days 32, 33 and 34 of the 2021 snow-covered to snow-free transition period..... 136
Figure C.21: GAM results of the diurnal curve clustering approach of day 35 of the 2021 snow-covered to snow-free transition period..... 137
Figure C.22: GAM results of the diurnal curve clustering approach of days 14, 15 and 16 of the 2022 snow-covered to snow-free transition period..... 138
Figure C.23: GAM results of the diurnal curve clustering approach of days 17, 18 and 19 of the 2022 snow-covered to snow-free transition period..... 139
Figure C.24: GAM results of the diurnal curve clustering approach of days 20 and 29 of the 2022 snow-covered to snow-free transition period..... 140
Figure C.25: GAM results of the diurnal curve clustering approach of days 18, 19 and 20 of the 2023 snow-covered to snow-free transition period..... 141
Figure C.26: GAM results of the diurnal curve clustering approach of days 21, 22 and 23 of the 2023 snow-covered to snow-free transition period..... 142
Figure C.27: GAM results of the diurnal curve clustering approach of days 29, 30 and 39 of the 2023 snow-covered to snow-free transition period..... 143
Figure C.28: GAM results of the diurnal curve clustering approach of days 40, 41 and 42 of the 2023 snow-covered to snow-free transition period..... 144
Figure C.29: GAM results of the diurnal curve clustering approach of day 43 of the 2023 snow-free to snow-covered transition period..... 145
Figure C.30: GAM results of the diurnal curve clustering approach of days 3, 32 and 33 of the 2021 snow-free to snow-covered transition period..... 146
Figure C.31: GAM results of the diurnal curve clustering approach of days 34, 37 and 38 of the 2021 snow-free to snow-covered transition period..... 147
Figure C.32: GAM results of the diurnal curve clustering approach of day 39 of the 2021 snow-free to snow-covered transition period..... 148

Figure C.33: GAM results of the diurnal curve clustering approach of days 7, 10 and 13 of the 2022 snow-free to snow-covered transition period. 149
Figure C.34: GAM results of the diurnal curve clustering approach of days 21, 22 and 23 of the 2021 snow-free to snow-covered transition period. 150
Figure C.35: GAM results of the diurnal curve clustering approach of days 24, 25 and 26 of the 2021 snow-free to snow-covered transition period. 151
Figure C.36: GAM results of the diurnal curve clustering approach of day 12 of the snow-covered period (left), day 6 of the snow-free precipitation period (middle) and day 18 of the snow-free precipitation period (right). Day 12 of the snow-covered period is day 14 of the snow-covered no precipitation period simultaneously. 152
Figure C.37: GAM results of the diurnal curve clustering approach of days 1, 17 and 18 of the snow-free day period. 153
Figure C.38: GAM results of the diurnal curve clustering approach of days 1 and 17 of the snow-covered day period. 154
Figure C.39: GAM results of the diurnal curve clustering approach of days 3, 4 and 5 of the snow-covered night period. 155
Figure C.40: GAM results of the diurnal curve clustering approach of days 6, 11 and 12 of the snow-covered night period. 156
Figure C.41: GAM results of the diurnal curve clustering approach of days 13, 14 and 15 of the snow-covered night period. 157
Figure C.42: GAM results of the anomaly persistence classification approach of days 7, 8 and 9 of the 2021 snow-covered to snow-free transition period. 158
Figure C.43: GAM results of the anomaly persistence classification approach of days 10, 12 and 13 of the 2021 snow-covered to snow-free transition period. 159
Figure C.44: GAM results of the anomaly persistence classification approach of days 15, 16 and 17 of the 2021 snow-covered to snow-free transition period. 160
Figure C.45: GAM results of the anomaly persistence classification approach of days 18, 19 and 20 of the 2021 snow-covered to snow-free transition period. 161
Figure C.46: GAM results of the anomaly persistence classification approach of days 22, 25 and 26 of the 2021 snow-covered to snow-free transition period. 162
Figure C.47: GAM results of the anomaly persistence classification approach of day 27 of the 2021 snow-covered to snow-free transition period. 163
Figure C.48: GAM results of the anomaly persistence classification approach of days 12, 13 and 14 of the 2022 snow-covered to snow-free transition period. 164
Figure C.49: GAM results of the anomaly persistence classification approach of days 15, 16 and 17 of the 2022 snow-covered to snow-free transition period. 165
Figure C.50: GAM results of the anomaly persistence classification approach of days 18, 19 and 20 of the 2022 snow-covered to snow-free transition period. 166
Figure C.51: GAM results of the anomaly persistence classification approach of days 21 and 29 of the 2022 snow-covered to snow-free transition period. 167
Figure C.52: GAM results of the anomaly persistence classification approach of days 18, 19 and 20 of the 2023 snow-covered to snow-free transition period. 168
Figure C.53: GAM results of the anomaly persistence classification approach of days 21, 22 and 23 of the 2023 snow-covered to snow-free transition period. 169

Figure C.54: GAM results of the anomaly persistence classification approach of days 24, 27 and 28 of the 2023 snow-covered to snow-free transition period. 170
Figure C.55: GAM results of the anomaly persistence classification approach of days 29, 30 and 31 of the 2023 snow-covered to snow-free transition period. 171
Figure C.56: GAM results of the anomaly persistence classification approach of days 32, 42 and 43 of the 2023 snow-covered to snow-free transition period. 172
Figure C.57: GAM results of the anomaly persistence classification approach of days 3, 31 and 32 of the 2021 snow-free to snow-covered transition period. 173
Figure C.58: GAM results of the anomaly persistence classification approach of days 33, 34 and 37 of the 2021 snow-free to snow-covered transition period. 174
Figure C.59: GAM results of the anomaly persistence classification approach of days 38 and 39 of the 2021 snow-free to snow-covered transition period. 175
Figure C.60: GAM results of the anomaly persistence classification approach of days 7, 10 and 13 of the 2022 snow-free to snow-covered transition period. 176
Figure C.61: GAM results of the anomaly persistence classification approach of days 21, 22 and 23 of the 2022 snow-free to snow-covered transition period. 177
Figure C.62: GAM results of the anomaly persistence classification approach of days 24, 25 and 26 of the 2022 snow-free to snow-covered transition period. 178
Figure C.63: GAM results of the anomaly persistence classification approach of day 12 of the snow-covered period (left), day 6 of the snow-free precipitation period (middle) and day 18 of the snow-covered precipitation period (right). Day 12 of the snow-covered period is day 14 of the snow-covered no precipitation period simultaneously. 179
Figure C.64: GAM results of the anomaly persistence classification approach of days 12 and 17 of the snow-covered day period. 180
Figure C.65: GAM results of the anomaly persistence classification approach of days 3, 4 and 5 of the snow-covered night period. 181
Figure C.66: GAM results of the anomaly persistence classification approach of days 6, 11 and 12 of the snow-covered night period. 182
Figure C.67: GAM results of the anomaly persistence classification approach of days 13, 14 and 15 of the snow-covered night period. 183

List of Tables

Table 1: List of data used in this thesis 6
Table 2: NaN-% after filtering thresholds have been applied 9
Table 3: R^2 values of raw and corrected TIR temperatures compared to different validation measurements 24
Table 4: R^2 values of corrected TIR temperatures (using different emissivity values) compared to different validation measurements 24
Table 5: R^2 values of corrected TIR temperatures (using different window transmissivity values) compared to different validation measurements 25
Table 6: Statistics of Aluminium-Corrected - Corrected 28
Table 7: Overview of analysis periods 29
Table 8: Overview of analysis periods with days identified for GAM-based analysis of the diurnal curve clustering approach. Days are flagged when the multiple linear regression model yielded R^2 values below 0.6 or mean residuals exceeding 2°C, indicating that surface temperature variability could not be adequately captured by linear processes. Day numbers correspond to the ordinal position within each relative period. 47
Table 9: Overview of analysis periods with days identified for GAM-based analysis of the anomaly persistence classification approach. Days are flagged when the multiple linear regression model yielded R^2 values below 0.6 or mean residuals exceeding 2°C, indicating that surface temperature variability could not be adequately captured by linear processes. Day numbers correspond to the ordinal position within each relative period. 48
Table C.1: Summary of multiple linear regression results based on groups from the diurnal curve clustering approach for transition periods. Values represent the number of observations (n), mean, standard deviation, minimum and maximum R^2 across all days within each subgroup and cluster. Driver importance is determined based on the cumulative rank of standardized regression coefficients across all days. Values in parentheses denote how often a variable was the dominant driver in this period (i.e. ranked first in influence). Cluster 1 represents the cooler temperature curve, while cluster 2 represents the warmer temperature curve. 123
Table C.2: Summary of multiple linear regression results based on groups from the diurnal curve clustering approach for snow-free and snow-covered periods. Values represent the number of observations (n), mean, standard deviation, minimum and maximum R^2 across all days within each subgroup and cluster. Driver importance is determined based on the cumulative rank of standardized regression coefficients across all days. Values in parentheses denote how often a variable was the dominant driver in this period (i.e. ranked first in influence Cluster 1 represents the cooler temperature curve, while cluster 2 represents the warmer temperature curve. 124
Table C.3: Summary of multiple linear regression results based on groups from the diurnal curve clustering approach for precipitation periods. Values represent the number of observations (n), mean, standard deviation, minimum and maximum R^2 across all days within each subgroup and cluster. Driver importance is determined based on the cumulative rank of standardized regression coefficients across all days. Values in parentheses denote how often a variable was the dominant driver in this period (i.e. ranked first in influence). Cluster 1 represents the cooler temperature curve, while cluster 2 represents the warmer temperature curve. 125

Table C.4: Summary of multiple linear regression results based on groups from the diurnal curve clustering approach for day / night comparison during snow-free periods. Values represent the number of observations (n), mean, standard deviation, minimum and maximum R^2 across all days within each subgroup and cluster. Driver importance is determined based on the cumulative rank of standardized regression coefficients across all days. Values in parentheses denote how often a variable was the dominant driver in this period (i.e. ranked first in influence). Cluster 1 represents the cooler temperature curve, while cluster 2 represents the warmer temperature curve. 126
Table C.5: Summary of multiple linear regression results based on groups from the diurnal curve clustering approach for day / night comparison during snow-free periods. Values represent the number of observations (n), mean, standard deviation, minimum and maximum R^2 across all days within each subgroup and cluster. Driver importance is determined based on the cumulative rank of standardized regression coefficients across all days. Values in parentheses denote how often a variable was the dominant driver in this period (i.e. ranked first in influence). Cluster 1 represents the cooler temperature curve, while cluster 2 represents the warmer temperature curve. 127
Table C.6: Summary of multiple linear regression results based on groups from the anomaly persistence classification approach for transition periods. Values represent the number of observations (n), mean, standard deviation, minimum and maximum R^2 across all days within each subgroup and cluster. Driver importance is determined based on the cumulative rank of standardized regression coefficients across all days. Values in parentheses denote how often a variable was the dominant driver in this period (i.e. ranked first in influence). 128
Table C.7: Summary of multiple linear regression results based on groups from the anomaly persistence classification approach for snow-free and snow-covered periods. Values represent the number of observations (n), mean, standard deviation, minimum and maximum R^2 across all days within each subgroup and cluster. Driver importance is determined based on the cumulative rank of standardized regression coefficients across all days. Values in parentheses denote how often a variable was the dominant driver in this period (i.e. ranked first in influence). 129
Table C.8: Summary of multiple linear regression results based on groups from the anomaly persistence classification approach for precipitation periods. Values represent the number of observations (n), mean, standard deviation, minimum and maximum R^2 across all days within each subgroup and cluster. Driver importance is determined based on the cumulative rank of standardized regression coefficients across all days. Values in parentheses denote how often a variable was the dominant driver in this period (i.e. ranked first in influence). 130
Table C.9: Summary of multiple linear regression results based on groups from the anomaly persistence classification approach for day / night comparison during snow-free periods. Values represent the number of observations (n), mean, standard deviation, minimum and maximum R^2 across all days within each subgroup and cluster. Driver importance is determined based on the cumulative rank of standardized regression coefficients across all days. Values in parentheses denote how often a variable was the dominant driver in this period (i.e. ranked first in influence). 131

Table C.10: Summary of multiple linear regression results based on groups from the anomaly persistence classification approach for day / night comparison during snow-covered periods. Values represent the number of observations (n), mean, standard deviation, minimum and maximum R^2 across all days within each subgroup and cluster. Driver importance is determined based on the cumulative rank of standardized regression coefficients across all days. Values in parentheses denote how often a variable was the dominant driver in this period (i.e. ranked first in influence). 132

1. Introduction

Climate change is threatening cryospheric water resources, particularly in mountainous regions. Understanding the cryospheric and hydrological components is therefore essential for effective water resource management (Chang et al., 2024). Unlike glaciers, rock glaciers are more climatically resilient and can store potentially valuable amounts of ice. This leads to an increased importance of rock glaciers as a source of summer water supply in the future (Jones et al., 2019; Lute et al., 2024). Despite their increasing potential importance in the hydrological cycle, rock glaciers have received considerably less attention than glaciers (Jones et al., 2019; Lute et al., 2024; Sorg et al., 2015). Investigating their thermal and energy exchange dynamics is crucial for assessing their future role as water resources and their sensitivity to climate change (Jones et al., 2019).

The Engadine region in the eastern Swiss Alps represents one of the major rock glacier hot spots of the European Alps and hosts numerous landforms in different activity states (Gärtner-Roer and Hoelzle, 2021). Rock glaciers in this region, particularly the Murtèl rock glacier, are among the best-studied permafrost landforms worldwide. Long-term borehole temperature measurements, geophysical investigations, deformation monitoring, radiometers and an automatic weather station provide an exceptional observation basis (Amschwand et al., 2024; Gärtner-Roer and Hoelzle, 2021). Most of this infrastructure is maintained by the Swiss Permafrost Monitoring Network (PERMOS), which has been monitoring the Murtèl rock glacier for several decades (PERMOS, 2025).

While subsurface processes and internal thermal conditions of rock glaciers have been investigated extensively, the spatial variability of their surface temperature remains poorly constrained. Surface temperature studies on glaciers are relatively well established, demonstrating the potential of thermal infrared (TIR) remote sensing to resolve spatial energy balance patterns (Aubry-Wake et al., 2015; Gök et al., 2023; Kraaijenbrink et al., 2017; Messmer and Groos, 2024; Mortimer et al., 2016; Ren et al., 2024). However, during an extensive literature review, no study could be identified that systematically analyses rock glacier surface temperature using ground-based TIR imaging, particularly not for the well-instrumented rock glaciers of the Engadine. This lack of spatially distributed surface temperature data represents a significant research gap.

Rock glaciers exhibit pronounced ridge-and-furrow microtopography, heterogeneous debris cover, variable snow persistence and strong small-scale variability in surface properties (Janke and Bolch, 2022). These characteristics likely induce substantial spatial contrasts in surface temperature and energy exchange, which cannot be captured by point measurements alone. In addition, long-term continuous measurements from a fixed ground-based thermal infrared camera allow the resolution of full diurnal cycles and short-term atmospheric responses, which would be difficult to capture with temporally discrete measurement campaigns. Compared to repeated drone-based surveys, such stationary systems are considerably more cost-efficient and enable sustained multi-year monitoring with high temporal resolution.

This thesis addresses this research gap by making use of the long-term ground-based thermal infrared imaging at the Murtèl rock glacier and by quantitatively evaluating its performance against established in-situ measurements. Specifically, the thesis provides:

- A quantitative evaluation of how accurately ground-based TIR imagery retrieves land surface temperature in complex rock glacier terrain, through comparison with borehole temperature records, radiometers, ground surface temperature (GST) measurements as well as measurements of the outgoing longwave radiation.

- A spatio-temporal characterisation of thermally distinct surface zones on the rock glacier and an analysis of how these spatial patterns reorganise across different surface and atmospheric conditions (snow cover, transition periods, precipitation and day-night cycles)
- An assessment of how different zones of the rock glacier are influenced by atmospheric variables such as air temperature, radiation, relative humidity and wind speed.

By linking spatially distributed surface temperature patterns with long-term monitoring data, this study contributes to a more comprehensive understanding of rock glacier surface-atmosphere interactions and improves the methodological basis for using thermal infrared remote sensing in alpine permafrost research.
Based on these considerations, this study aims to address following research questions:

1. How accurately can ground-based thermal infrared imaging retrieve land surface temperatures in the complex terrain of a rock glacier compared to in-situ measurements?
2. Which thermally distinct zones can be identified on the Murtèl rock glacier and how does their spatial organisation change between snow-covered and snow-free conditions, transition periods and day-night cycles?
3. Which meteorological variables dominate the statistical relationship between atmospheric forcing and spatially distributed surface temperature, and how does their relative influence vary across different surface conditions and spatial groups on the rock glacier?

2. Study Site and Data

2.1. Study Site

The study area is the Murtèl rock glacier, located in the Upper Engadine in the eastern Swiss Alps (46° 25' 47'' N; 9° 49' 15'' E). The rock glacier is situated at the north facing area of Piz Corvatsch and spans an elevation of approximately 2630 to 2710 m a.s.l., resulting in a height difference of 80 metres. The Upper Engadin is described as a weakly continental, rain-shadowed alpine valley, where high elevation and continental climate conditions support the widespread occurrence of permafrost (Amschwand et al., 2024; Gärtner-Roer and Hoelzle, 2021). Mean annual air temperature at the site is approximately -1.7 °C, and mean annual precipitation is around 900 mm (Scherler et al., 2014).

Rock glaciers are typically defined as "the visible expression of cumulative deformation by long-term creep of ice/debris mixtures under permafrost conditions" (Berthling, 2011). They are classified into three states: active, inactive, and fossil. Active rock glaciers move at rates of a few decimetres to metres per year, lack surface vegetation, and display well-defined surface features with sharp-crested, cascading front slopes indicative of ongoing deformation (Barsch, 1996; Janke and Bolch, 2022). Inactive rock glaciers still contain ice but are no longer moving, while fossil rock glaciers are ice-free and typically vegetated (Barsch, 1996). Based on these definitions, the Murtèl rock glacier is classified as an active rock glacier with a creeping rate of ~10 cm / yr that has shown an acceleration in the past decade (Swiss Permafrost Monitoring Network, 2022).

The Murtèl rock glacier is approximately 400 m long and 200 m wide. It is bordered by steep rock faces and is directly connected to a talus slope. The surface gently dips towards the north-northwest with a mean slope of 10 - 12° and can be dissected into pronounced furrow and ridge microtopographies (see Figure 1). The furrows are typically 3-5 m deep and alternate with the ridges that exhibit steep to near-vertical slopes, particularly in the lower part of the rock glacier. Snow cover is generally thicker and more persistent in furrows than on ridges, which has a great influence on the thermal surface regime in this area (Amschwand et al., 2024; Bernhard et al., 1998; Keller, 1993).

The debris mantle consists of coarse blocks with characteristic clast sizes ranging from decimetres to several metres, while fine material is largely absent at the surface and increases with depth. The thickness of this mantle varies spatially, being thinner in furrows (approximately 1 - 2 m) and thicker beneath the rest of the rock glacier (up to 3 - 5 m). Due to the high permeability of this blocky surface layer, rain and meltwater rapidly infiltrate, resulting in generally dry surface conditions (Amschwand et al., 2024).

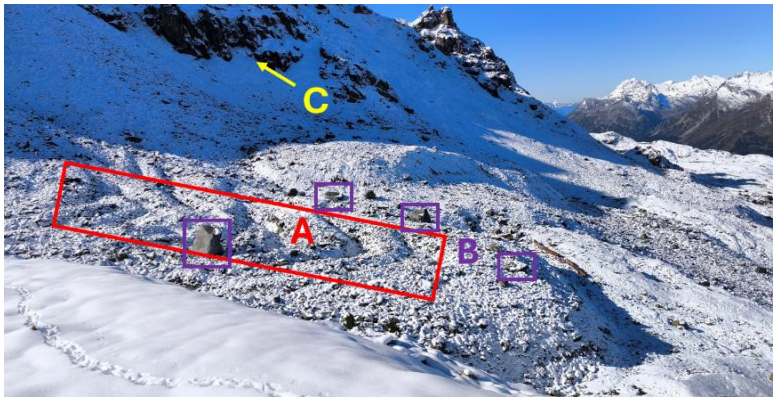

Figure 1: Overview photograph of the Murtèl rock glacier taken on 29 September 2025, showing the characteristic ridge-and-furrow microtopography (A), large, exposed boulders (B), a section of the headwalls (C) and the surrounding topographic setting

2.2. Data

The analyses presented in this thesis draw on multiple data sources with different spatial and temporal characteristics, summarised in Table 1. These include thermal infrared imagery, meteorological station records, ground surface temperature loggers, borehole temperature profiles, thermal infrared radiometer measurements, and a digital elevation model. The locations of all in-situ measurement points are shown in Figure 2. The following subsections describe each data source in detail.

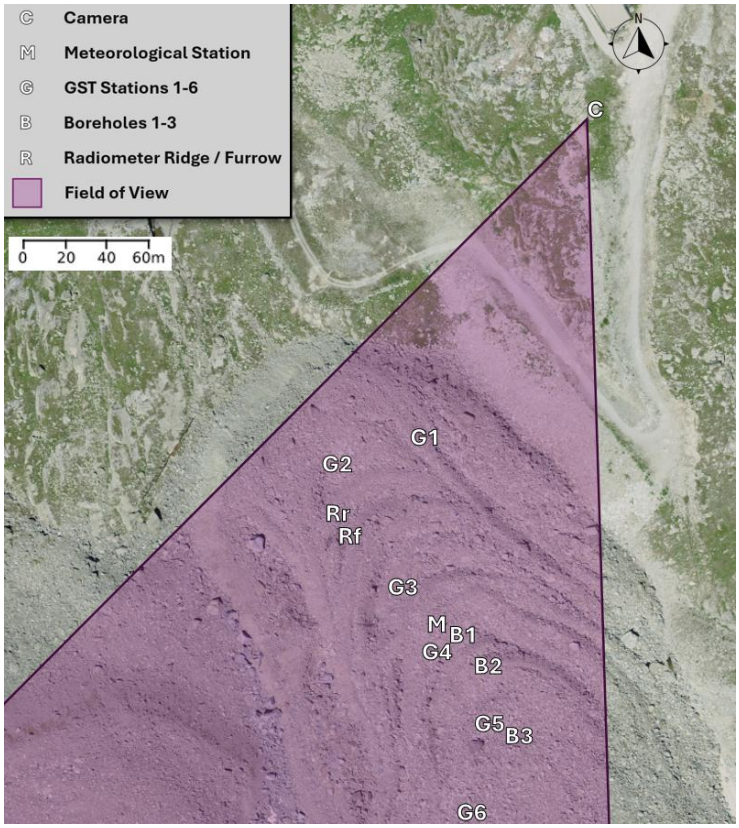

Figure 2: Overview of the study site and measurement infrastructure on the Murtèl rock glacier. The approximate field of view of the TIR camera is indicated by the shaded area. Basemap: Swisstopo

2.2.1. Thermal Infrared Camera

The key data used for this thesis were obtained using a MOBOTIX M16 B Thermal-TR camera, which captured thermal infrared (TIR) and natural colour (RGB) images of the study site simultaneously since 2020. The sensor operates in the 7.5 - 13.5 µm thermal infrared band and the resulting TIR images have a resolution of 336 x 252 pixels. The measurement interval varies between 1 minute to 2 hours over the analysis period.

The MOBOTIX M16 B Thermal-TR-camera was installed by Amschwand et al. (2024) and made available to the author through personal communication. At the time of writing, these images are not publicly available.

2.2.2. Meteorological Station

Meteorological measurements from a station located on top of the rock glacier were used to obtain the air temperature, surface temperature, relative humidity, incoming and outgoing longwave and shortwave radiation, snow height, wind speed and wind direction. The meteorological station has been operating since 1997 with a measurement interval of 10 minutes, and the raw data contains no data gaps for the period analysed in this study. These meteorological measurements are part of the

Swiss Permafrost Monitoring Network and are not publicly available at the time of writing (PERMOS, 2025).
Additionally, precipitation data from the MeteoSwiss station at Corvatsch (station code COR, elevation 3315 m a.s.l.) were used to distinguish dry from precipitation periods during the study period. This station is operated by MeteoSwiss and the data are available through their data portal (MeteoSchweiz, 2026).

2.2.3. Ground Surface Temperature Measurements

Ground surface temperature (GST) measurements from six different sensor locations on the rock glacier were used to support the evaluation of the thermal data and the atmospheric temperature correction. These GST measurements have an acquisition interval of one day (at 0:00) and are part of the Swiss Permafrost Monitoring Network and are publicly available through the PERMOS data repository (PERMOS, 2025).

2.2.4. Borehole Measurements

Borehole temperature time series of three different boreholes were used to provide additional information on subsurface thermal conditions to support the interpretation of the surface temperature measurements. These borehole measurements have an acquisition interval of one day (at 00:00) and are also part of the Swiss Permafrost Monitoring Network and are publicly available through the PERMOS data repository (PERMOS, 2025).

2.2.5. Radiometer Measurements

Thermal infrared radiometer measurements from a furrow and a ridge position on top of the rock glacier were also used to verify the atmospheric temperature correction applied to the camera data. These radiometers recorded at 10-minute intervals, operating from 28 July to 16 October 2022, and from 28 July to 22 August 2023, respectively. These datasets were made available to the author for this analysis and are not publicly available at the time of writing (Naegeli et al., 2026).

2.2.6. Digital Elevation Model (DEM)

A digital elevation model of the study site was used to derive the distances between the camera location and the different camera pixels. The DEM has a resolution of 0.5 m, is based on the LV95 coordinate system and is publicly available through the Federal Office of Topography swisstopo (Swisstopo, 2024).

Table 1: List of data used in this thesis

Data Source	Period	Measurement Interval	Variables
MOBOTIX M 16 B Thermal-TR camera (Amschwand et al., 2024)	2020 – 2024	Different measurement intervals ranging from 1 min to 2 h	TIR and RGB images
Meteorological Station Murtèl (PERMOS, 2025)	1997 – 08.2023	10 min	• Air temp. [°C] • Surface temp. [°C] • Relative humidity [%] • Longwave radiation up/down/net [W/m^2] • Shortwave radiation up/down/net [W/m^2] • Snow height [cm] • Windspeed and direction
Meteorological Station Corvatsch (MeteoSchweiz, 2026)	2020 – 2026	10 min	• Precipitation [mm]
Ground Surface Temperature (GST) Station 1 (PERMOS, 2025)	09.2008 – 11.2008, 08.2009 – 12.2009, 09.2010 – 12.2010, 09.2011 – 09.2016, 09. 2018 – 08.2023	Daily	• Temperature [°C]
GST Station 2 (PERMOS, 2025)	09.2003 – 11.2023	Daily	• Temperature [°C]
GST Station 3 (PERMOS, 2025)	09.2018 – 2026	Daily	• Temperature [°C]
GST Station 4 (PERMOS, 2025)	09.2018 – 08.2023	Daily	• Temperature [°C]
GST Station 5 (PERMOS, 2025)	09.2018 – 2026	Daily	• Temperature [°C]
GST Station 6 (PERMOS, 2025)	09.2018 – 02.2023	Daily	• Temperature [°C]
Borehole 1 (PERMOS, 2025)	01.2016 – 2026	Daily	• Temperature [°C] at depths 0.25m, 0.5m, 0.75m, 1m, 1.5m, 2m, 2.5m, 3m, 3.5m, 4m, 4.5m, 5m, 6m, 8m, 10m
Borehole 2 (PERMOS, 2025)	01.1988 – 09.2023	Daily	• Temperature [°C] at depths 0.55m, 1.55m, 2.55m, 3.55m, 4.55m, 5.55m, 6.55m, 7.55m, 8.55m, 9.55m
Borehole 3 (PERMOS, 2025)	11.2000 – 05.2022	Daily	• Temperature [°C] at depths 0.5m, 1m, 1.5m, 2m, 2.5m, 3m, 3.5m, 4m, 5m, 7.5m, 10m
TIR Radiometer (Furrow) (Naegeli et al., 2026)	28.07.22 – 16.10.22	10 min	• Temperature [°C]
TIR Radiometer (Ridge) (Naegeli et al., 2026)	28.07.22 – 22.08.23	10 min	• Temperature [°C]
DEM (Swisstopo, 2024)	-	-	• Height above sea level [m]

3. Methods

All data processing, analysis, and visualization were conducted in Python 3.13. The workflows were implemented using a range of open-source Python packages. Numerical computations and data handling were performed with NumPy 2.4.3 (Harris et al., 2020) and Pandas 3.0.1 (The pandas development team, 2026), while visualization tasks were carried out using Matplotlib 3.10.8 (Hunter, 2007). Statistical analyses and regression modelling relied on Statsmodels 0.14.6 (Seabold and Perktold, 2010), scikit-learn 1.8.0 (Pedregosa et al., 2011), and PyGAM 0.12.0 (Servén and Brummitt, 2018). Spatial data processing and coordinate transformations were performed using PyProj 3.7.2 (Whitaker et al., 2019) and SciPy 1.16.3 (Virtanen et al., 2020), whereas three-dimensional geometric analyses were conducted with Trimesh 4.12.2 (Dawson-Haggerty et al., 2019). Image processing and file handling were supported by OpenCV 4.13.0 (Bradski, 2000) and ImageIO 2.37.3 (Klein et al., 2026). Additional functionality was provided through modules included in the Python Standard Library, such as os, glob, datetime, math, csv, and related utilities.

3.1. Data quality control and filtering

3.1.1. TIR images

The quality control and filtering of the TIR images in this study are based on a Shannon entropy threshold, following the idea proposed by Hurmer et al. (2025). Image entropy provides a scalar measure of the spatial information content and is particularly sensitive to image degradation caused by fog, snowfall, precipitation, or condensation on the camera window. Such conditions strongly reduce thermal contrast and spatial variability, resulting in low-entropy images that are unsuitable for quantitative surface temperature analysis.

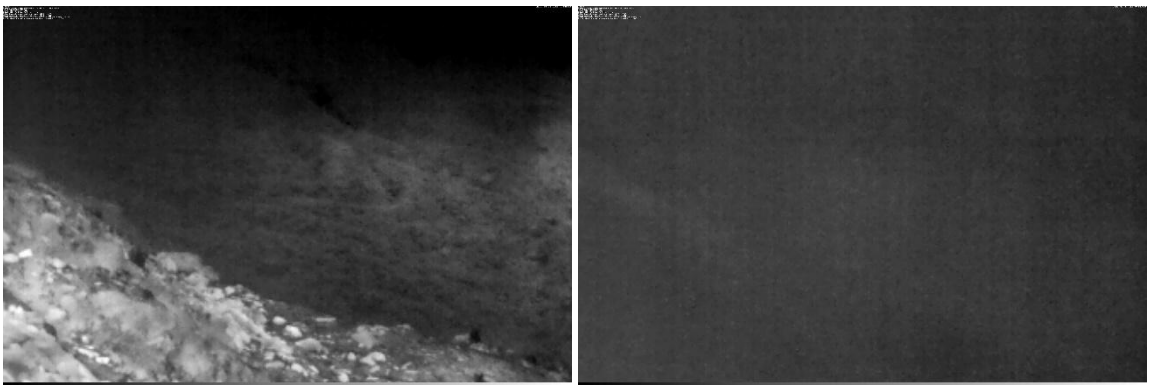

Figure 3: Example of "Bad" labelled images

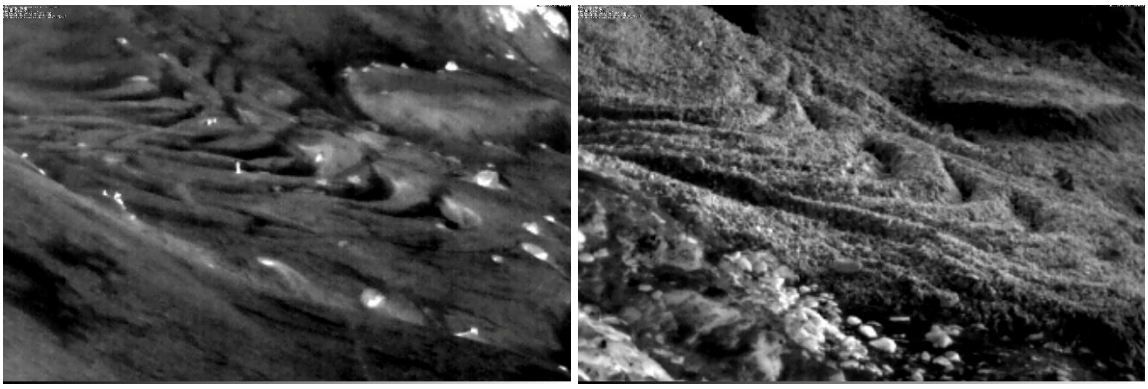

Figure 4: Example of "Good" labelled images

As the entropy threshold reported by Hurmer et al. (2025) (6.693) was derived from a subset of manually selected images rather than from the full distribution of image conditions, it cannot be directly transferred to this study. Therefore, another entropy threshold was derived, which captures the whole dataset.

For this purpose, 1000 images randomly sampled between 2021 and 2023 were manually classified into "Bad" (Figure 3) and "Good" (Figure 4) quality based on visual inspection. For each image, the Shannon entropy of the corresponding temperature map was computed from the distribution of pixel values. The Shannon entropy H was calculated as

$$H = -\sum_{i}^{N} p_i \log_2(p_i), \tag{1}$$

where p_i is the probability of pixels values falling into the i-th histogram bin and N is the number of bins used (Hurmer et al., 2025). The probabilities were obtained from the normalized histogram of all pixel values in the temperature map. Low entropy values indicate spatially uniform or low-contrast scenes, while high entropy values correspond to images with good spatial structures.

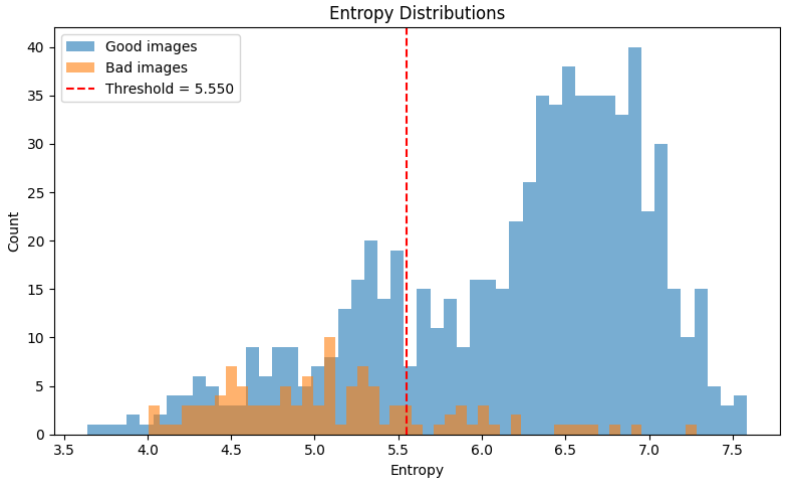

Figure 5: Entropy distributions of labelled images with resulting entropy threshold

To determine a threshold separating "Good" and "Bad" quality images, a receiver operating characteristic (ROC)-based approach was applied (Baker and Kramer, 2007; Schisterman et al., 2005). For a given entropy threshold t, images were classified as "Good" if $H \geq t$ and as bad if $H < t$. From this classification, the true positive rate (TPR) and false positive rate (FPR) were computed as

$$TPR(t) = \frac{TP(t)}{TP(t) + FN(t)}, \qquad FPR(t) = \frac{FP(t)}{FP(t) + TN(t)}, \tag{2}$$

where TP, FN, FP and TN denote the numbers of true positives, false negatives, false positives and true negatives, respectively (Baker and Kramer, 2007). The optimal entropy threshold was selected by maximizing the Youden Index

$$J(t) = TPR(t) - FPR(t) = Sensitivity(t) + Specificity(t) - 1, \quad (3)$$

which yields to a threshold that maximizes the separation between "Good" and "Bad" quality images under equal misclassification costs (Schisterman et al., 2005). The entropy distribution and selected entropy threshold of this study is visible in Figure 5.

3.1.2. CSV datasets

All CSV-based datasets were screened for unreasonable values using descriptive statistics (minimum, maximum, mean, median, standard deviation) and visual inspection of time series. Where applicable, physically plausible thresholds were defined for each variable, and values outside these thresholds were set to NaN.

3.1.2.1. Meteorological Station Data

The meteorological station dataset includes air temperature, relative humidity, wind speed and direction, downwelling and upwelling longwave and shortwave radiation, and snow height. Filtering thresholds were defined individually for each variable based on physical plausibility and visual inspection of the time series (Table 2). Air temperature was filtered to remove a single anomalous value in April 2021 and to exclude data after September 2023, when the sensor appears to have ceased functioning. Relative humidity was constrained to the range 0–100%. Wind speed and wind direction required no filtering, as no unreasonable values were detected. For downwelling and upwelling longwave radiation, a minimum threshold of 50 W/m^2 was applied to exclude implausible values recorded after September 2023. Downwelling shortwave radiation contained implausible negative values during nighttime, which account for the elevated NaN percentage visible in Table 2. As these negative values are evenly distributed across the dataset, their removal does not introduce a temporal bias. Snow height was filtered to remove two unrealistically high values (~70 m) in the first half of 2021. Figure 6 shows the filtered time series for all meteorological variables over the full study period, and Figure A.1 to Figure A.3 show the corresponding raw versus filtered comparisons.

Table 2: NaN-% after filtering thresholds have been applied

Variable	Chosen Threshold	NaN-%
Air Temperature	-25; 40	3.31
Relative Humidity	0; 100	3.98
LW Radiation Downward	50; 600	3.31
LW Radiation Upward	50; 600	3.31
SW Radiation Downward	0; 1400	41.64
SW Radiation Upward	0; 1400	2.83
Wind Speed	0; 60	0
Wind Direction	0; 360	0
Snow Height	0.01; 500	3.65

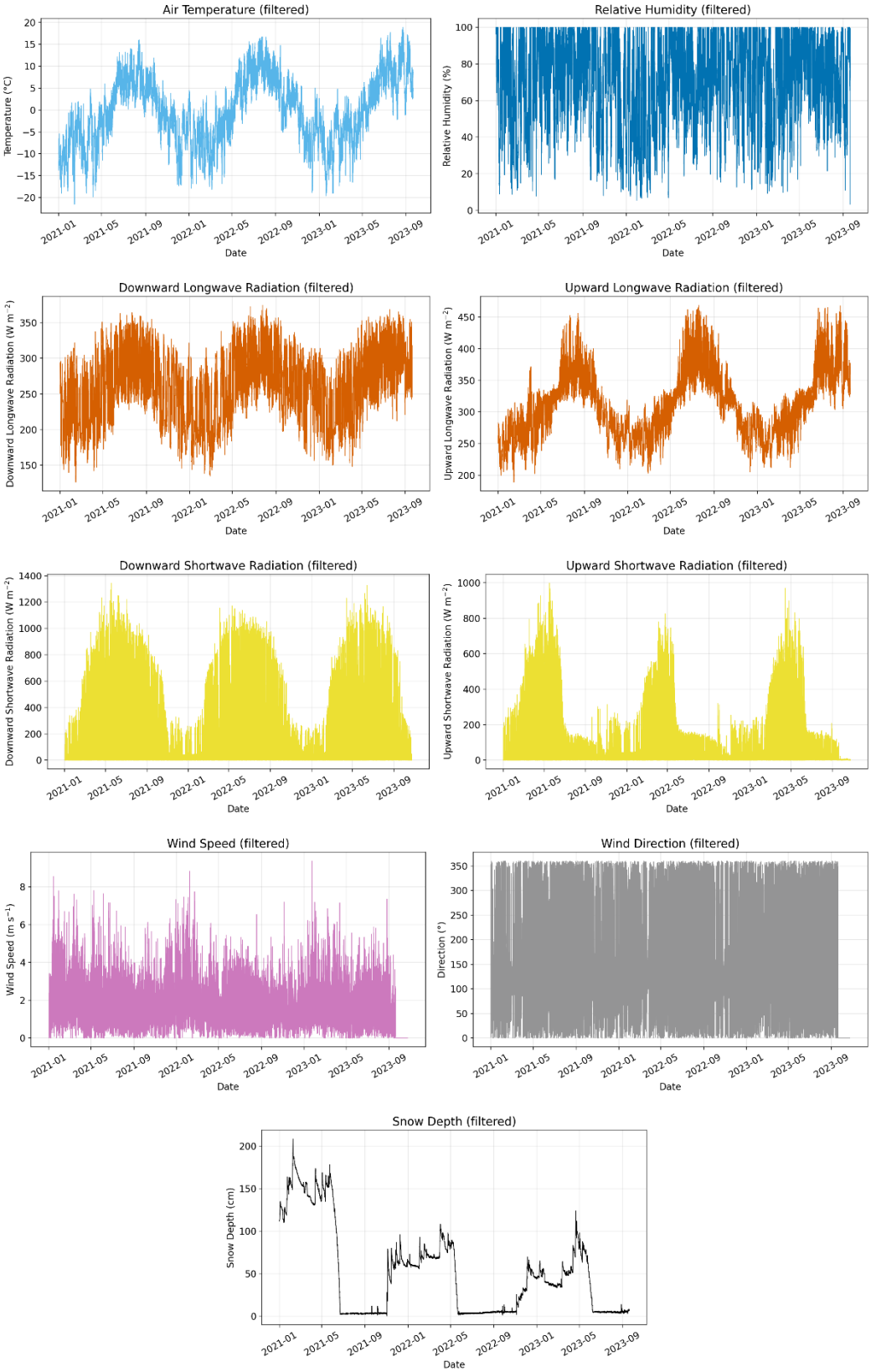

Figure 6: Filtered time series of all meteorological station variables from January 2021 to September 2023. Panels show air temperature, relative humidity, downwelling and upwelling longwave radiation, downwelling and upwelling shortwave radiation, wind speed, wind direction, and snow depth. Applied filtering thresholds are summarised in Table 2

3.1.2.2. Borehole and GST Measurements

The borehole temperature time series show occasional data gaps and abrupt stops at individual depths. These gaps are mainly explained by permanent failure of individual sensors. As the rest of the data showed no clear unreasonable values or patterns, no filtering was applied. Missing values were kept as NaN and appear as gaps in the time series (as shown in Figure 7). The GST measurements showed no clear data gaps or unreasonable values in the period between 2021 and 2023, therefore, no filtering has been applied.

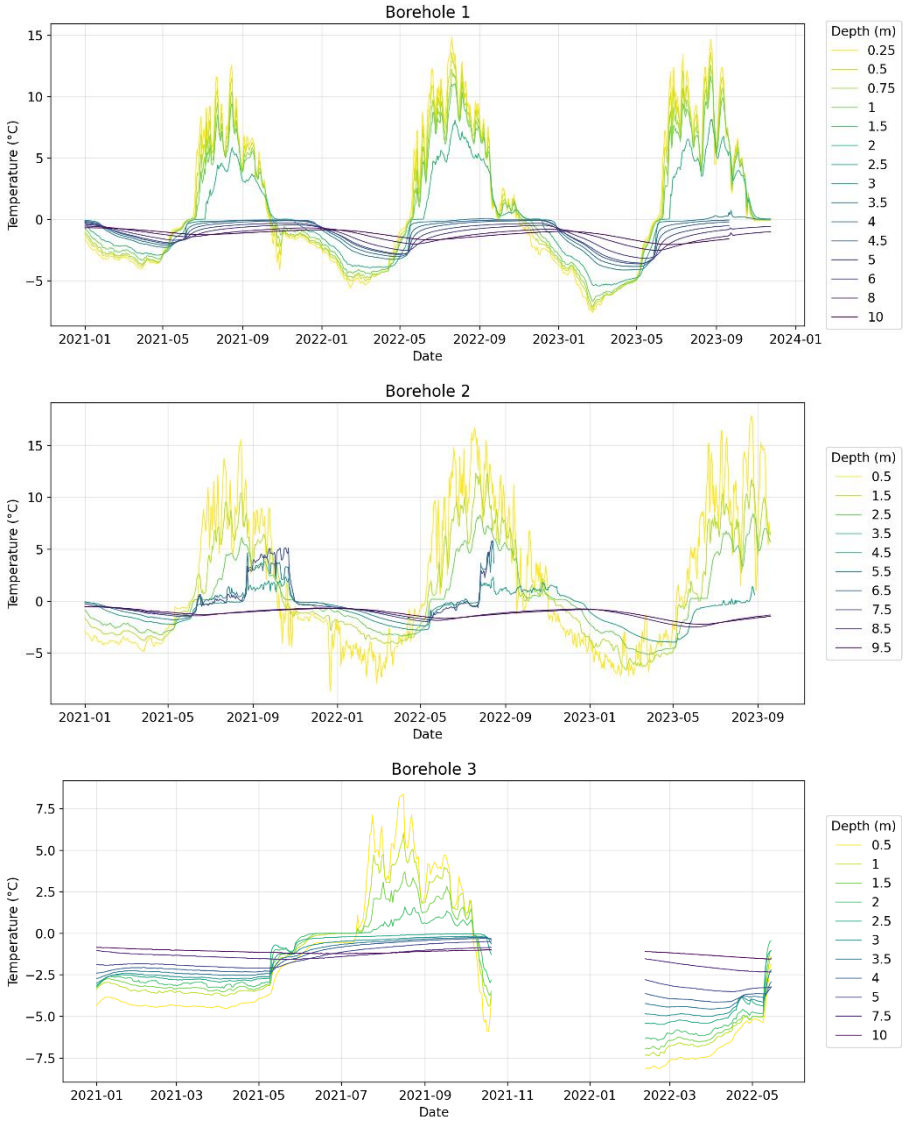

Figure 7: Borehole temperature time series at multiple depths for Boreholes 1, 2, and 3. Colours indicate sensor depth (in metres). Data gaps result from permanent sensor failures; no filtering was applied

3.2. Temperature Correction

To enable accurate analysis of thermal infrared camera data, it's a common approach to correct the measurements for atmospheric effects. As the radiation from the target object traverses through the atmosphere before reaching the sensor, the recorded signal is modified by atmospheric processes such as atmospheric transmittance and the atmospheric path radiance (Kavak and Özsaraç, 2015). The overall correction process applied in this study follows the approach of Aubrecht et al. (2016), adapted for the alpine terrain of the study site.

Accurate atmospheric correction requires knowledge of the optical path between the camera and the target object. Because the MOBOTIX camera observes a complex three-dimensional terrain, a single representative distance is insufficient. Instead, a per-pixel distance map was acquired to support pixel-wise correction of the TIR data. This distance map was generated using the camera position (coordinates and elevation in m a.s.l.), the position of the centremost image pixel (coordinates and elevation), a DEM of the area and some camera parameters such as camera field of view and image resolution. Based on these inputs, a ray-tracing approach was applied in which a viewing ray was projected from the camera into the terrain for each pixel, and the distance to the first intersection with the DEM surface was calculated. The resulting distance map contained a large number of implausible small distance values (Figure 8, left). All of these pixels with a distance value of less than 100 metres were therefore flagged as invalid and then filled using a nearest-neighbour interpolation based on the Euclidean distance to the closest valid pixel (Figure 8, middle).
In the end, the derived distances were manually evaluated using distance measurements from the Swiss national geospatial platform (map.geo.admin.ch). Some small deviations between measured and modelled distances remain, but the overall performance of the modelled distance map is considered sufficient for the purpose of this study.

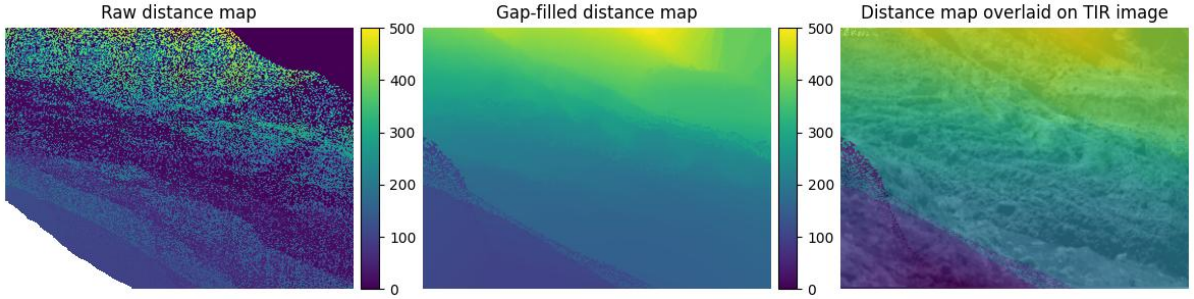

Figure 8: Raw distance map (left), interpolated distance map (middle) and overlay on top of a TIR image (right)

The temperature correction was based on a combination of the correcTIR approach (Diehl et al., 2026) and the radiative transfer formulation implemented in the raw2temp function of the Thermimage R package (Tattersall, 2023). Specifically, atmospheric transmissivity was calculated following the implementation in correcTIR, using air temperature, relative humidity, elevation above sea level and object distance as input variables. This transmissivity term was then used within the raw2temp-based correction framework to account for emissivity, reflected radiation, atmospheric attenuation, and path radiance in the retrieval of corrected surface temperatures.
At first, the output values (in °C) from the MOBOTIX camera were converted to radiance by integrating Planck's law (Vollmer and Möllmann, 2010) over the camera's spectral response band:

$$B(\lambda, T) = \int_{\lambda_1}^{\lambda_2} \frac{2hc^2}{\lambda^5} * \frac{1}{e^{\frac{hc}{\lambda kT}} - 1} d\lambda, \tag{4}$$

where k is the Boltzmann constant, h is the Planck constant, c is the speed of light, T is the temperature in Kelvin measured for each pixel and λ_1 = 7.5 µm and λ_2 = 13.5 µm are the lower and upper bounds of the MOBOTIX spectral range (MOBOTIX AG, 2018). The resulting quantity is therefore the band-integrated longwave infrared radiance rather than a monochromatic radiance (Vollmer and Möllmann, 2018). Accordingly, Planck's law was evaluated at N = 400 evenly spaced wavelength points across this interval and numerically integrated using the trapezoidal rule to obtain band-inte-

grated radiance for each pixel (Chapra and Canale, 2015). Then, the atmospheric transmissivity was estimated following the approach of Diehl et al. (2026).
For the atmospheric transmissivity, the vapor density needs to be calculated. The vapor density is dependent on the air temperature, the relative humidity and the atmospheric pressure at the study site. The air temperature and the relative humidity are measured at the meteorological station on top of the Murtèl rock glacier and the atmospheric pressure is calculated using the simplified barometric formula (Diehl et al., 2026):

$$\mathrm{P} = \mathrm{P}_0 * \left(1 - \frac{L * h}{T_0}\right)^{\frac{g * M_a}{R} * L} \tag{5}$$

where P_0 is the atmospheric pressure at sea level (101'325 Pa), L is the temperature gradient (0.0065 K/m), h is the height at which the pressure is calculated (2700 m), T_0 is the sea-level standard temperature (288.15 K), g is the gravitational acceleration (9.80665 m/s^2), M_a is the molar mass of air (0.0289644 kg/mol) and R is the universal gas constant (8.31447 J/molK) (Diehl et al., 2026).
Using the derived pressure, the measured air temperature and relative humidity, the vapor density is calculated based on this formula (Diehl et al., 2026):

$$\rho_v = \frac{\left(\frac{RH}{100}\right) * \left(\frac{\mathrm{P}}{101325}\right) * a * e^{\frac{b * T_{air}}{c + T_{air}}} * M_w}{R * (T_{air} + 273.15)}, \tag{6}$$

where RH is the relative humidity measured at the meteorological station, T_{air} is the measured air temperature at the meteorological station, M_w is the molar mass of water (18.015 g/mol), R is the universal gas constant and a, b and c are constants for Tetens equation (a = 610.94 Pa, b = 17.625, c = 243.04 °C) (Diehl et al., 2026).
Using the derived vapor density, it's now possible to calculate the atmospheric transmissivity using following formula (Diehl et al., 2026):

$$\tau = X * e^{-\sqrt{d} * \alpha_1 + \beta_1 * \sqrt{\rho_v}} + (1 - X) * e^{-\sqrt{d} * \alpha_2 + \beta_2 * \sqrt{\rho_v}}, \tag{7}$$

where X, α_1, α_2, β_1 and β_2 are LOWTRAN constants (1.89999997, 0.00656899996101856, 0.0126200001686811, -0.000227600010111928 and -0.00667000003159046 respectively), d is the distance of each pixel to the camera and ρ_v is the derived vapor density (Diehl et al., 2026). Aubrecht et al. (2016) demonstrated that:

$$\Phi_{tot} = \tau\varepsilon\Phi_{obj} + \tau\left(1 - \varepsilon_{obj}\right)\varepsilon_{refl}\Phi_{refl} + (1 - \tau)\Phi_{air}), \tag{8}$$

where Φ_{tot} is the total received radiation by the camera sensor, Φ_{obj} is the radiation emitted from the target pixel, Φ_{refl} is the reflected background radiance incident on the surface and reflected to the sensor and Φ_{air} is the thermal emission of the atmosphere along the optical path between the surface and the camera.

The MOBOTIX camera is equipped with a protective infrared-transparent window that the radiation must pass before reaching the detector. This window is not perfectly transparent in the thermal infrared; part of the incoming radiance is absorbed and re-emitted by the window material itself. To account for this effect, a window transmission term (IRT = infrared transmission) is introduced in the radiative transfer model. A fraction IRT of the incoming atmospheric-corrected radiance reaches the sensor, while the remaining fraction *(1 - IRT)* is replaced by thermal emission from the window at its own temperature.
This leads to the modified radiance balance in Eq. (9), where the physically meaningful scene radiance is multiplied by IRT and an additional term proportional to Φ_{wind} is added.

$$\Phi_{tot} = IRT\left[\tau\varepsilon\Phi_{obj} + \tau\left(1-\varepsilon_{obj}\right)\varepsilon_{refl}\Phi_{refl} + (1-\tau)\Phi_{air}\right] + (1-IRT)\Phi_{wind} \qquad (9)$$

This results in:

$$\Phi_{obj} = \frac{1}{\tau\varepsilon_{obj}}\left(\frac{\Phi_{tot}}{IRT} - \tau\left(1-\varepsilon_{obj}\right)\varepsilon_{refl}\Phi_{refl} - (1-\tau)\Phi_{air} - \frac{1-IRT}{IRT}\Phi_{wind}\right) \qquad (10)$$

Similar to the study of Aubrecht et al. (2016), ε_{refl} is assumed to be equal to 1. The surface type at the study site changes seasonally between snow-covered and snow-free conditions, which makes the use of a single constant emissivity inappropriate. To account for this, emissivity was made time dependent using the snow height measured at the meteorological station. Because the thermal infrared images could not be reliably co-registered with the RGB imagery, a pixel-wise discrimination between snow and bare rock was not possible. Consequently, a single emissivity value was applied to all pixels within each image, but this value was allowed to vary over time.
Days with a mean snow height of at least 10 cm were classified as snow-covered and assigned an emissivity of 0.98 (Hori et al., 2013), while snow-free conditions were assigned an emissivity of 0.92 (Mineo and Pappalardo, 2021). To avoid unrealistically abrupt transitions caused by short-lived snow events or measurement noise, a persistence filter was applied, requiring that a change in snow state be maintained for at least three consecutive days before it was accepted as a valid switch. Each valid transition between snow and no-snow conditions then triggered a symmetric 11-day transition period (5 days before and 5 days after the switching date), during which emissivity was gradually adjusted in equal daily steps between the two end-member values. This produces smooth and physically plausible seasonal emissivity trajectories while still preserving the timing of real snow cover changes observed at the meteorological station.
While Φ_{tot} in Eq. (9) represents the total radiance received by the sensor (measured radiance), Φ_{refl}, Φ_{air} and Φ_{wind} are calculated based on the apparent reflected background, air and camera window temperature respectively using Planck's law (Eq.5).
Since no independent measurements of reflected background temperature were available, the background temperature was assumed to be equal to the temperature derived from the downwelling longwave radiation measured at the meteorological station. The camera-window temperature was set to the air temperature measured at the meteorological station.

3.3. Uncertainty Characterisation

Uncertainty in the retrieved land surface temperatures was assessed by combining instrument specifications with sensitivity analyses and comparative validation approaches.

First, the baseline measurement uncertainty was defined using the manufacturer specified accuracy of the MOBOTIX M16 Thermal-TR camera, which is ±10 °C (MOBOTIX AG, 2018). This value is treated as a reference for evaluating the magnitude of additional uncertainty sources introduced during the correction workflow.

To account for uncertainties in surface properties, a sensitivity analysis of emissivity was performed. Since the exact emissivity of rock glacier surface may vary from the literature, three representative values for stone surfaces were tested (0.90, 0.92 and 0.94). The full correction workflow was applied independently for each emissivity scenario and resulting temperature differences were quantified to assess the sensitivity of the final temperatures to emissivity assumptions.

Similarly, uncertainty related to the camera window transmission was also evaluated. As the transmissivity of the window is not precisely known, three plausible values (0.96, 0.90 and 0.86) were tested based on ranges suggested by Adams (personal communication). The impact of these values on corrected temperatures was analysed by repeating the atmospheric correction for each transmissivity scenario.

Another relevant source of uncertainty is the omission of background (reflected) radiation. The sky emissivity which was set to 1 is not conceptually correct. This value is only correct if there aren't any structures in the field of view which may create some background radiation like large buildings, or in this case: mountains and headwalls. Due to time constraints, sky emissivity was simplified and assumed to be equal to 1 like in a case with no interfering structures (Diehl et al., 2026).

To further characterise uncertainty associated with the estimation of reflected apparent temperature, an independent correction approach was implemented using an aluminium reference plate installed at the study site. The plate was deployed during two distinct periods (28.07.22 - 08.08.22, 31.05.23 - 27.08.23) and is assumed to approximate a high-emissivity surface, thereby providing a more direct estimate of the apparent reflected temperature compared to values derived from longwave downward radiation measured at the meteorological station.

A comparative analysis was conducted between the standard atmospheric correction applied in this study using meteorological data and the aluminium plate-based correction. Results were then compared with the internal camera temperature extracted from the image metadata.

Together, these steps provide a structured assessment of uncertainty, including instrumental accuracy, sensitivity to emissivity and window transmissivity assumptions and variability in reflected temperature estimation.

3.4. Spatio-temporal pattern analysis

3.4.1. Diurnal Curve Clustering

To identify thermally distinct zones on the Murtèl rock glacier, a spatio-temporal clustering approach was applied to the corrected TIR image time series. The analysis focuses on temporal evolution of temperature at the pixel scale, allowing regions with similar diurnal behaviour to be grouped together.

To avoid interference from areas not belonging to the rock glacier environment, the foreground part of the images was masked out prior to clustering. This ensures that only pixels representing the rock glacier surface and its background contribute to the clustering results.

The analysis was performed for each target day using a rolling five-day window (day X-4 to day X, data driven method). It was applied to the analysis periods defined in Section 4.2.

The clustering algorithm followed the approach of Liu et al. (2018) by doing these steps:

1. For each pixel (x, y), the raw temperature values across a single day are extracted from the corrected TIR images (Figure 9, A).
2. Using all images within the 5-day rolling window, the acquisition times are rounded to half-hour intervals, images falling within the same half-hour slot are averaged, and the resulting values are interpolated onto a regular 24-hour grid to produce a mean diurnal temperature curve for that pixel (Figure 9, B).
3. This procedure is repeated for every valid pixel in the image, resulting in a spatial field of mean daily temperature curves (Figure 9, C).
4. The resulting mean daily temperature curves are then grouped together using k-means clustering (Figure 9, D).

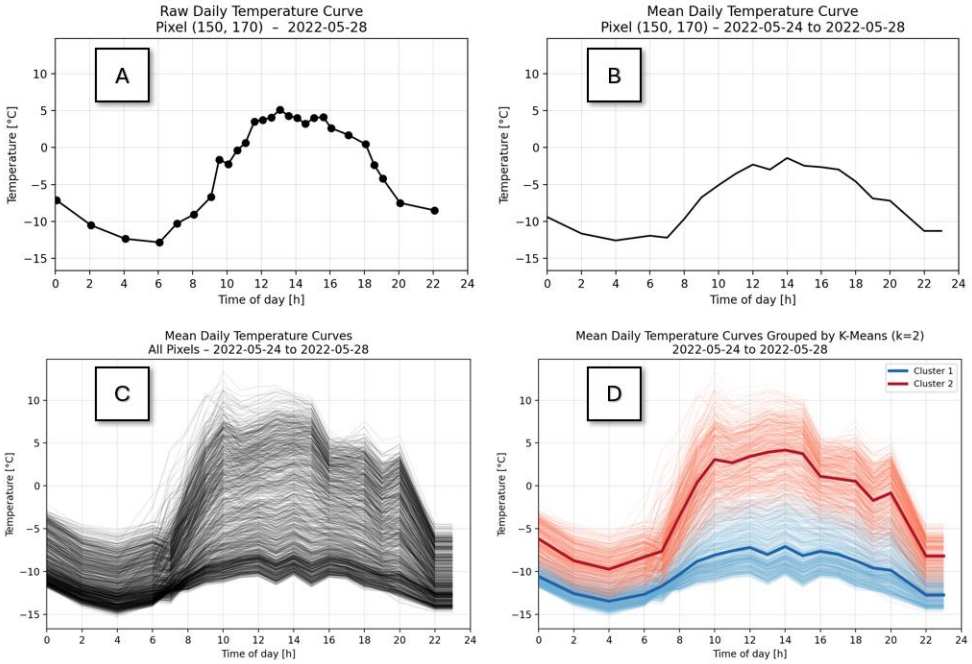

Figure 9: Schematic illustration of the clustering algorithm workflow

In this study, k-means is used to identify thermally coherent surface zones based on their diurnal temperature behaviour, rather than on instantaneous temperature values alone. Within the framework described above, k-means clusters the set of TIR pixels into a predefined number of clusters *k* by iteratively assigning each pixel to the nearest cluster centroid and updating the centroids until the within-cluster sum of squared distances is minimised (Jain, 2010). Each cluster is characterised by a centroid, which represents the mean diurnal temperature curve of all pixels assigned to that cluster. Pixels within the same cluster should therefore experience similar timing, amplitude and overall shape in their behaviour.

The amount of clusters *K* was restricted to a range from two to seven clusters. Rather than assuming a single optimal clustering solution, multiple values of *K* were evaluated for each aggregation period. Cluster quality was assessed using the silhouette score, which quantifies how well individual pixels are separated from neighbouring clusters (Shahapure and Nicholas, 2020). The value of *K* with the best silhouette score was then chosen for further analysis.

Importantly, clustering results are interpreted as exploratory descriptors of dominant thermal patterns, not as effective surface classifications.

3.4.2. Anomaly Persistence Classification

While the above explained clustering workflow reveals similar thermal patterns, it does not quantify how persistently some areas deviate from the overall thermal state. To address this, a complementary analysis based on z-normalisation was applied to the corrected TIR image sequence.

For each TIR image, the temperature field was standardised by subtracting the image-wide mean temperature and dividing by the corresponding standard deviation. This results in a z-score for each pixel, expressing how strongly the pixel deviates from the spatial mean temperature at the time of acquisition. Positive z-values indicate pixels that are warmer than the corresponding image average and negative z-values indicate colder pixels.

This analysis removes influences such as seasonal patterns and meteorological influences. As a result, this analysis emphasises relative spatial anomalies that persist over a chosen period.

Based on the z-normalised images, one metric was computed at the pixel scale for the same five-day rolling window time frame as described in Section 3.4.1. This metric was the percentage of acquisitions in which a pixel exhibited a positive anomaly ($z > 0$). A metric regarding the negative anomaly ($z < 0$) was not calculated, as it would result in the opposite (as the percentage of $z = 0$ values is expected to be negligible).

Pixels were then classified into three groups based on fixed thresholds of this metric: *persistently warm* (positive anomaly in ≥ 75% of acquisitions), *persistently cold* (positive anomaly in ≤ 25% of acquisitions), and *intermediate* (between 25% and 75%). These thresholds define the groups by the temporal persistence of relative warmth or coldness, not by the proportion of pixels – the number of pixels in each group varies depending on the surface conditions in a given window.

3.5. Statistical dependence analysis

3.5.1. Multiple linear regression

To investigate which environmental variables influence the measured surface temperature and how this influence varies over time, multiple linear regression models were applied. The predictor variables included air temperature, relative humidity, downwelling shortwave radiation, downwelling longwave radiation, wind speed and wind direction, which was decomposed into north-south and east-west components. Prior to the regression analysis, all variables were z-normalised to ensure comparability and to allow direct interpretation of regression coefficients in terms of relative influence (Yin et al., 2019).

The analysis was conducted for a set of predefined temporal windows (analysis periods, see section 4.2), which were further subdivided into the five-day rolling window subperiods described earlier. For each five-day subperiod, separate multiple linear regression models were fitted. This approach allowed capturing temporal variability in the relationships between measured surface temperature and the predictor variables.

To account for spatial heterogeneity, the regression analysis was performed separately for different pixel groups. These groups were derived from two independent approaches: (1) diurnal curve clustering (Section 3.4.1) and (2) anomaly persistence classification (Section 3.4.2). For each group withing each subperiod, a separate regression model was fitted using the mean temperature of the corresponding pixel group as the response variable.

Following the regression, the resulting coefficients for each predictor variable were aggregated per group and subperiod. To enable comparison between variables and groups, the coefficients were normalised by dividing each coefficient by the sum of all coefficients within the respective model. This yielded relative contribution values, representing the proportional influence of each environ-

mental variable on surface temperature. These relative contributions were subsequently used to compare dominant drivers across time periods and spatial groups.

3.5.2. Generalized Additive Models (GAMs)

To complement the multiple linear regression analysis and to account for potential non-linear relationships, generalized additive models were applied for each group within each subperiod. The GAMs were based on the same predefined analysis periods, subperiod structure, and z-normalised predictor variables as used in the linear regression approach. These included air temperature, relative humidity, downwelling shortwave and longwave radiation, wind speed and the decomposed wind direction components (north-south, east-west).

In contrast to multiple linear regression, which assumes a strictly linear relationship between predictors and the response variable, GAMs allow for flexible, non-linear relationships by fitting smooth functions to each predictor (Gomez-Rubio, 2018; Tranmer et al., 2020). Instead of estimating a single coefficient per variable, GAMs model the response variable as the sum of smooth functions of each predictor. These smooth functions are typically constructed using spline-based approaches, which enable the model to adapt to complex patterns in the data without requiring an explicit functional form (Gomez-Rubio, 2018).

For each pixel group and subperiod, a separate GAM was fitted using the mean surface temperature of the respective group as the response variable.

The flexibility of GAMs allows capturing threshold effects, saturation behaviour and non-linear sensitivities that cannot be represented by linear models. For example, the influence of shortwave radiation may increase rapidly above a certain threshold.

To interpret the results, partial dependence plots (PDPs) were generated for each predictor variable, showing the isolated effect of that variable on surface temperature while holding all other variables constant.

By combining GAMs with linear regression framework, both linear and non-linear dependencies could be systematically evaluated, providing a more comprehensive understanding of the environmental controls on surface temperature across difference temporal periods and spatial groups.

4. Results

4.1. Temperature Correction

4.1.1. Core Correction

The validation of the corrected TIR temperature was made using independent measurements from boreholes, GST loggers, radiometers and the temperature derived from the longwave outgoing radiation measured at the meteorological station. Figure 10 to Figure 12 show representative examples for 2022, while the complete set of year-wise validation plots for 2021 - 2023 is provided in Appendix (Figure B.1 - Figure B.9).

Across all validation datasets, both the raw and corrected TIR time series reproduced the expected seasonal evolution with low temperature during winter, increasing temperature in summer and decreasing again in autumn. The corrected temperatures generally remained close to the raw values but showed shifts towards colder temperatures during snow covered periods and no systematic shift in snow free periods.

For the meteorological station comparison, the corrected TIR temperatures followed the temporal

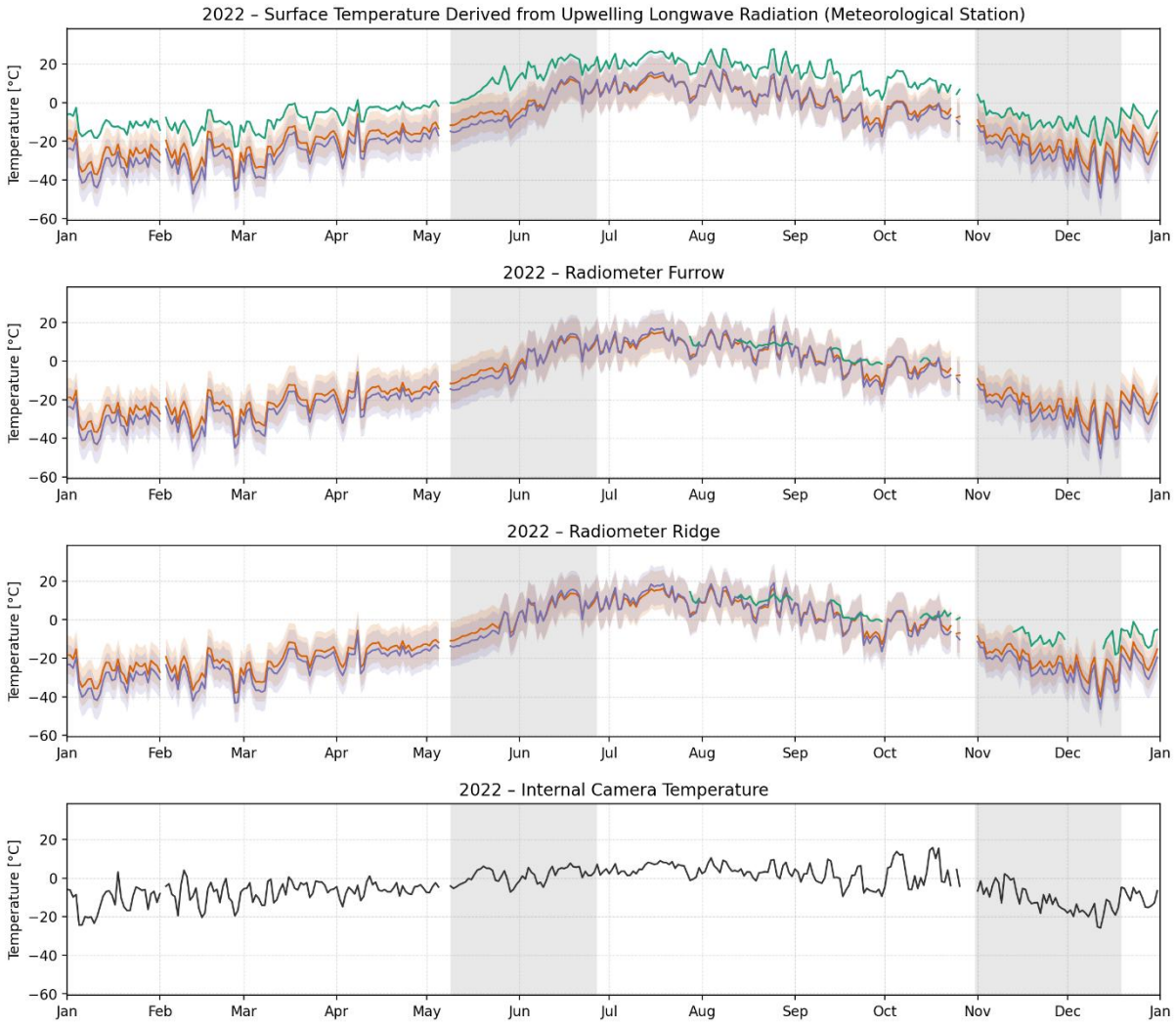

Figure 10: Comparison of corrected and raw TIR-derived pixel temperatures with surface temperatures derived from upwelling longwave radiation at the meteorological station, as well as with radiometer measurements at ridge and furrow locations for 2022. Grey shaded areas indicate transition periods between snow-covered and snow-free conditions. All time series represent daily mean values

evolution of the longwave-radiation-derived temperatures well. The validation signal generally showed higher temperatures with 10 - 20°C difference to the corrected TIR temperature. Similar behaviour is visible for the radiometer comparisons, where both furrow and ridge radiometers showed similar temporal variability with a smaller amplitude in fluctuations than the corrected TIR temperatures.

The comparison with borehole (Figure 11, Figure B.4 - Figure B.6) and GST measurements (Figure 12, Figure B.7 - Figure B.9) showed a consistent seasonal agreement during snow-free periods. Under snow-covered conditions, the GST loggers were buried beneath the snowpack and therefore exhibited a different temperature evolution compared to the TIR temperatures which are measured on the snow surface. The borehole temperatures likewise displayed a distinct thermal behaviour during these periods. In contrast, during snow-free conditions, the GST loggers showed a thermal response similar to the corrected TIR temperatures, although the TIR-derived temperatures exhibited a larger amplitude of short-term fluctuations. A similar pattern was observed in the borehole temperature timeseries.

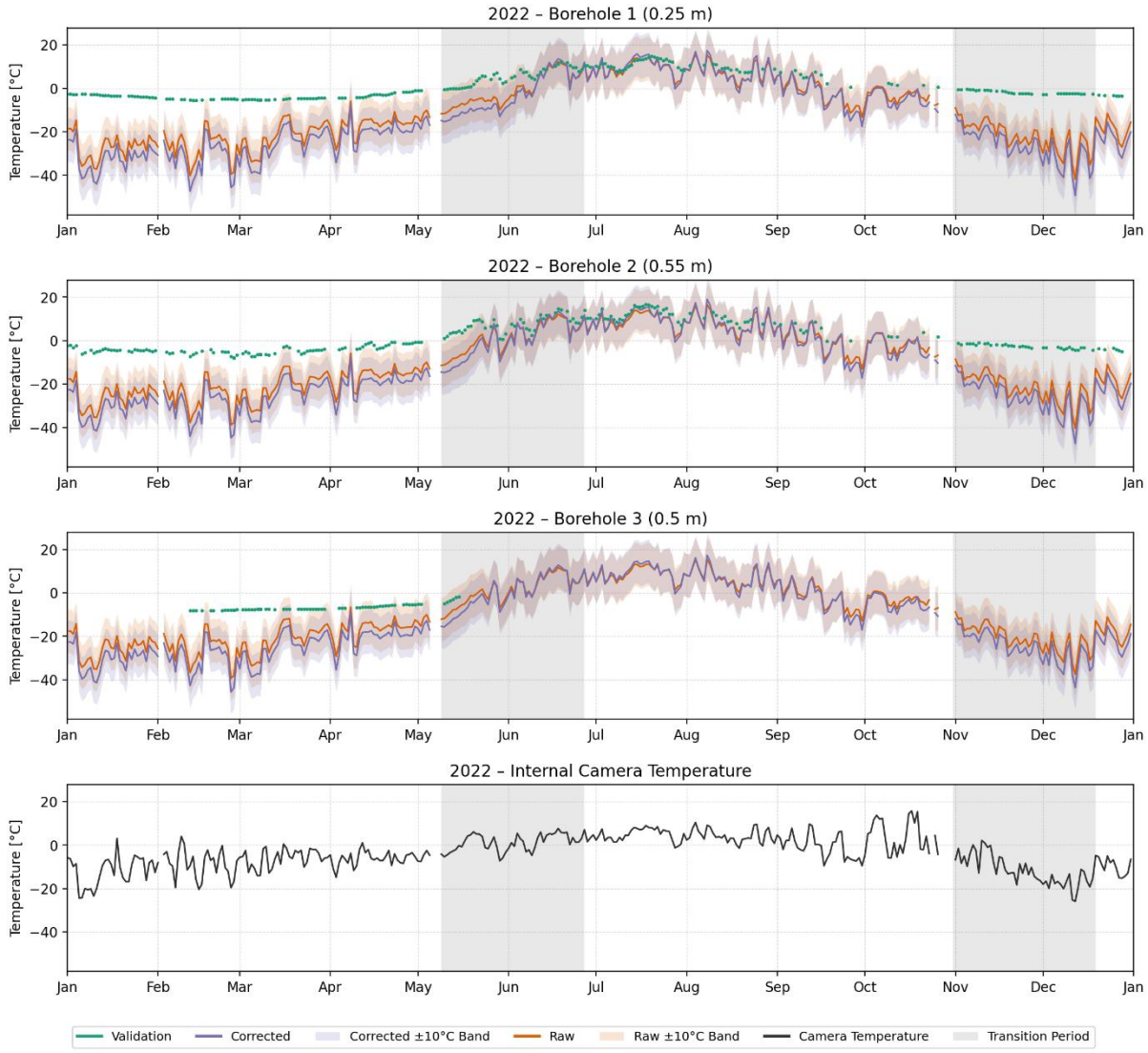

Figure 11: Comparison of corrected and raw TIR-derived pixel temperatures with borehole temperatures for 2022. Grey shaded areas indicate transition periods between snow-covered and snow-free conditions. All time series represent daily mean values

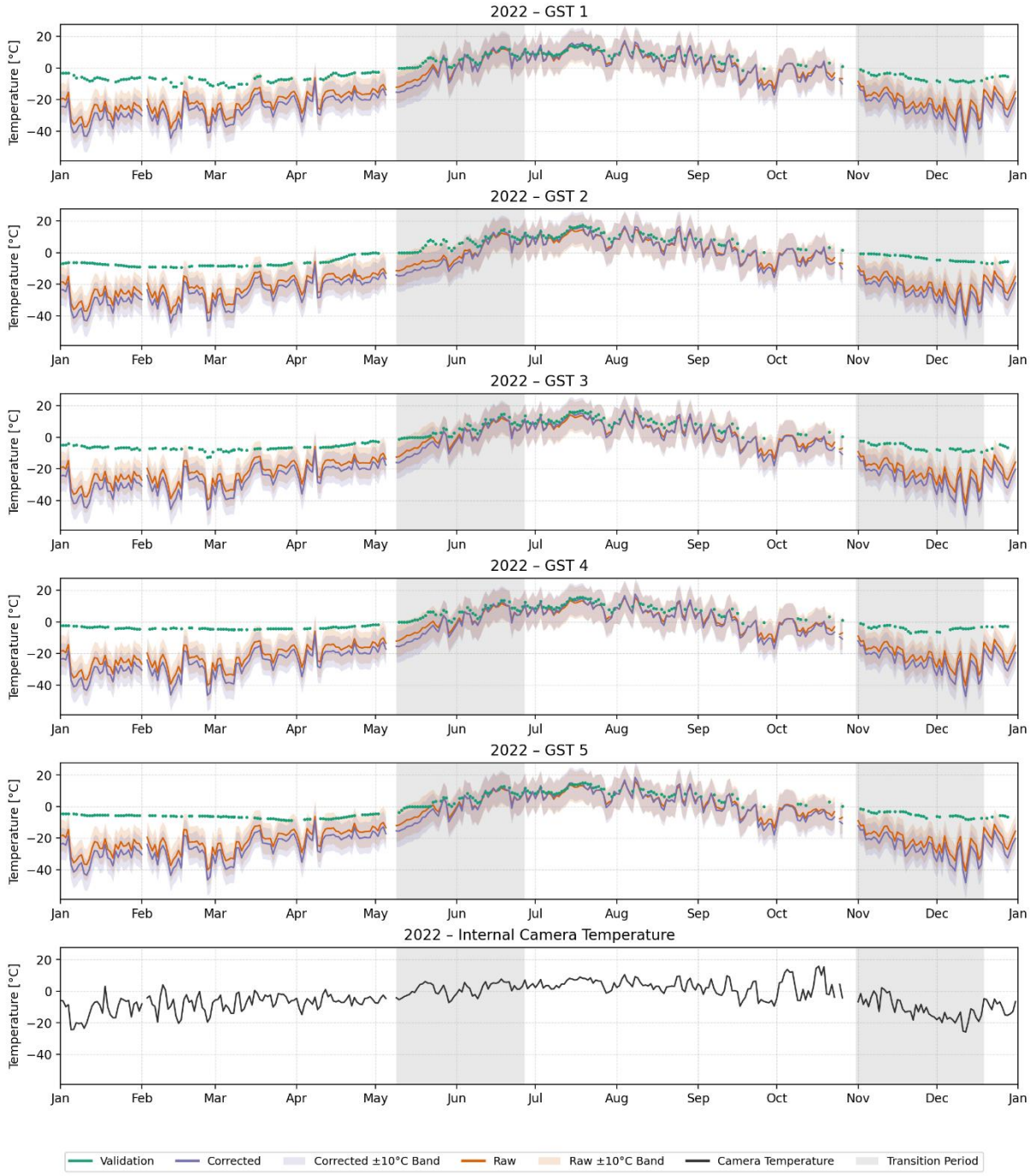

Figure 12: Comparison of corrected and raw TIR-derived pixel temperatures with GST logger measurements for 2022. Grey shaded areas indicate transition periods between snow-covered and snow-free conditions. All time series represent daily mean values

In addition to the temporal validation, the effect of the atmospheric correction as a function of distance to the camera was analysed by subtracting the raw from the corrected images and comparing the result with the distance of each pixel to the camera. In the ΔT-distance plot (Figure 13) a systematic shift can be observed, reflecting the influence of the atmospheric correction. From pixels located close to the camera to those at the farthest distances, this shift amounts to approximately 1.5 °C over the full year 2022. This relationship is consistent with the increasing atmospheric path length of the radiance.

A seasonal analysis of the ΔT-distance relationship (Figure B.10 - Figure B.13) shows that this distance-dependent effect persists throughout the year, but with varying magnitude. In spring, autumn

and winter, a clear negative shift with increasing distance is visible. In contrast, during summer, the ΔT values are closer to 0 °C and exhibit a weaker distance dependency, suggesting reduced atmospheric effects under warmer conditions. Despite these seasonal differences, the overall pattern remains consistent, with more distant pixels systematically showing larger corrections than those closer to the camera.

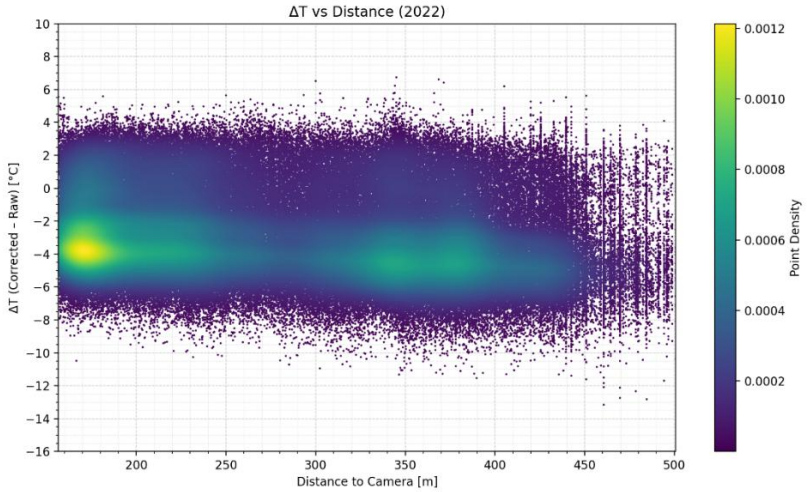

Figure 13: Relationship between the temperature difference introduced by the atmospheric correction and the distance to the camera for 2022. Each point represents an individual pixel, coloured by point density

Figure 14 to Figure 16 show the comparison between TIR-derived temperatures and validation measurements, and Table 3 summarises the corresponding R^2 values for raw and corrected temperatures across all validation sources. Figure B.14 to Figure B.24 in Appendix show the same type of plots separately for each individual validation metric including the regression line. The comparison with the longwave derived temperatures shows a slight improvement in R^2, while the regression line remains visually similar to the raw fit. In contrast, the radiometer comparisons show that the correction introduces a stronger temperature dependency: deviations increase at lower temperatures and decrease at higher temperatures. In these cases, the raw data exhibits higher R^2 values than the corrected data, indicating that the correction does not improve the statistical agreement with radiometer measurements.

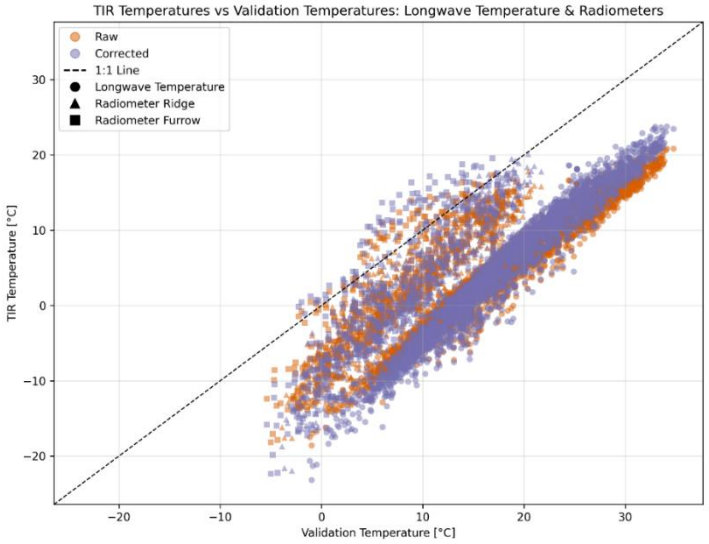

Figure 14: Scatterplot of derived TIR temperatures (corrected and raw) vs. validation temperatures (temperature derived from longwave radiation and radiometers). This plot represents snow-free acquisitions from 2022

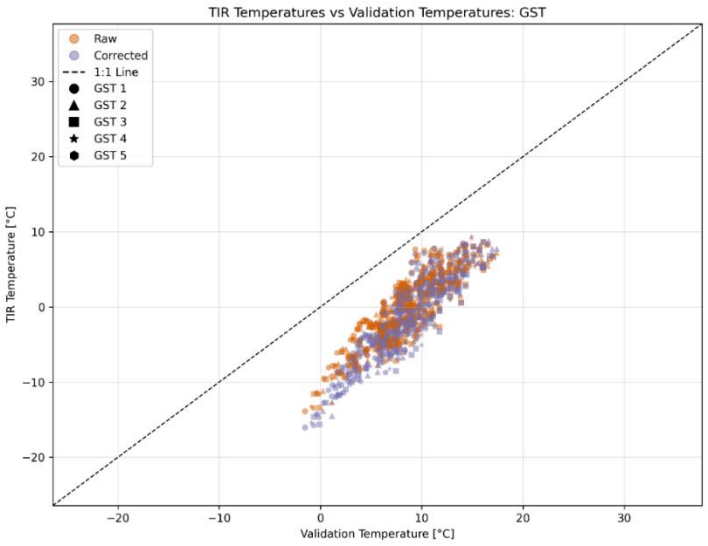

Figure 15: Scatterplot of derived TIR temperatures (corrected and raw) vs. validation temperatures (GST measurements). This plot represents snow-free acquisitions from 2022

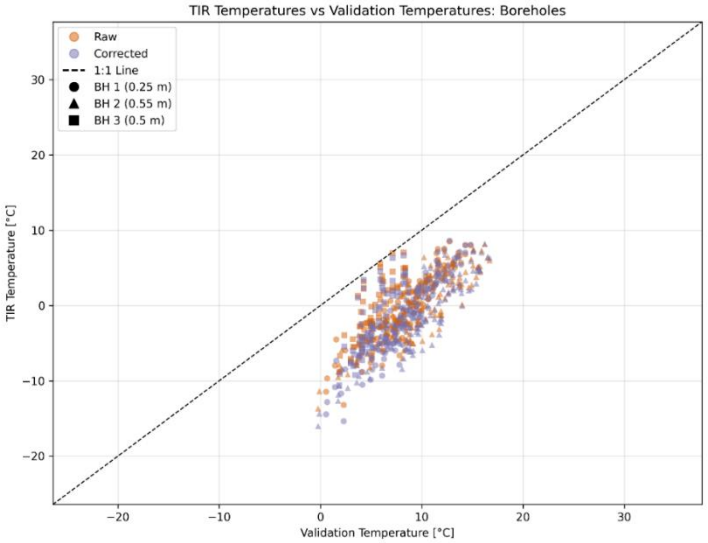

Figure 16: Scatterplot of derived TIR temperatures (corrected and raw) vs. validation temperatures (Borehole measurements). This plot represents snow-free acquisitions from 2022

For the GST sensors, the correction consistently increases the R^2 values across all loggers. However, the visual behaviour of the regression changes. For all GST stations, the corrected fit does not improve the alignment with the 1:1 line; instead, deviations increase at lower temperatures, while agreement improves at higher temperatures. This indicates a temperature-dependent effect introduced by the correction.

The borehole measurements show a mixed response to the atmospheric correction (Table 3). For Borehole 1, the corrected regression line does not visually align better with the 1:1 line than the raw fit; however, the R^2 value increases with the correction. For Borehole 2, both the R^2 and the visual agreement improve after correction. The regression line follows a nearly parallel shift relative to the 1:1 line, suggesting a more linear relationship across the temperature range. In contrast, Borehole 3 shows no improvement, with both raw and corrected fits yielding similar R^2 values and no clear visual advantage.

Table 3: R^2 values of raw and corrected TIR temperatures compared to different validation measurements

Validation Measurement	Raw R^2	Corrected R^2
Longwave Temperature	0.95	**0.96**
Radiometer Ridge	**0.89**	0.85
Radiometer Furrow	**0.79**	0.75
GST 1	0.82	**0.86**
GST 2	0.79	**0.84**
GST 3	0.74	**0.80**
GST 4	0.77	**0.82**
GST 5	0.81	**0.86**
Borehole 1	0.85	**0.88**
Borehole 2	0.71	**0.77**
Borehole 3	0.68	0.68

4.1.2. Uncertainty Assessment

To assess uncertainties in the temperature correction, a sensitivity analysis was conducted for the snow-free period of 2022, focusing on the assumed surface emissivity of rocks. While a constant emissivity is required in the correction process, natural rock surfaces exhibit variability, which introduces uncertainty in the derived temperatures. Therefore, the full correction procedure was repeated using three emissivity values (0.90, 0.92, and 0.94). The resulting temperature datasets were evaluated against all validation measurements following the same framework as presented in section 4.1.1, using the coefficient of determination (R^2) as a metric to quantify agreement (Table 4). The corresponding scatter plots for each validation reference are provided separately in Appendix B (Figure B.25 - Figure B.35).

Table 4: R^2 values of corrected TIR temperatures (using different emissivity values) compared to different validation measurements

Validation Measurements	R^2 (ε = 0.90)	R^2 (ε = 0.92)	R^2 (ε = 0.94)
Longwave Temperature	0.95	**0.96**	0.95
Radiometer Ridge	0.84	**0.85**	**0.85**
Radiometer Furrow	0.73	**0.75**	**0.75**
GST 1	**0.87**	0.86	0.85
GST 2	**0.85**	0.84	0.82
GST 3	**0.81**	0.80	0.78
GST 4	**0.83**	0.82	0.80
GST 5	**0.87**	0.86	0.84
Borehole 1	**0.89**	0.88	0.87
Borehole 2	**0.78**	0.77	0.75
Borehole 3	0.67	**0.68**	0.66

Across all validation datasets, only minor differences in R^2 values are observed between the three emissivity configurations. In all cases, variations remain within a narrow range of approximately 0.01 to 0.03, indicating that the overall model performance is only weakly sensitive to the choice of emissivity. An emissivity *of* $\varepsilon = 0.92$ yields the highest R^2 values for the longwave-derived temperature, both radiometers, and Borehole 3, whereas $\varepsilon = 0.90$ produces slightly better agreement for the GST sensors and Boreholes 1 and 2.

More pronounced differences become apparent when analysing the behaviour of the regression lines. Lower emissivity values generally lead to increased deviations at lower validation temperatures, while improving the agreement at higher temperatures. However, this pattern is not consistent across all datasets. In some cases, such as borehole 1, GST 1, and both radiometers, lower emissivity values do not improve the agreement at higher temperatures but instead result in an overestimation. Conversely, higher emissivity values exhibit the opposite behaviour, with reduced deviations at lower temperatures but increased deviations at higher temperatures.

Overall, this indicates a clear temperature-dependent bias introduced by the choice of emissivity, affecting the slope and structure of the regression relationship rather than the overall goodness of fit.

An additional sensitivity analysis was performed to assess uncertainties related to atmospheric correction, focusing on the transmissivity of the camera window. This analysis too was conducted in the snow-free period of 2022. Similar to emissivity, transmissivity of the camera window is used in the correction process, although its precise value is not known. Therefore, the full correction workflow was repeated using three transmissivity values (0.86, 0.90 and 0.96), and the resulting temperature datasets were evaluated in the same framework as the previously described emissivity values. The results can be seen in Table 5 while the corresponding scatter plots for each validation reference are provided separately in Appendix B (Figure B.36 - Figure B.46).

Table 5: R^2 values of corrected TIR temperatures (using different window transmissivity values) compared to different validation measurements

Validation Measurements	R^2 ($\tau = 0.86$)	R^2 ($\tau = 0.90$)	R^2 ($\tau = 0.96$)
Longwave Temperature	0.95	**0.96**	**0.96**
Radiometer Ridge	0.84	**0.85**	**0.85**
Radiometer Furrow	0.74	**0.75**	**0.75**
GST 1	0.86	**0.86**	**0.86**
GST 2	0.83	**0.84**	**0.84**
GST 3	0.80	0.80	0.80
GST 4	0.81	**0.82**	**0.82**
GST 5	0.85	**0.86**	**0.86**
Borehole 1	0.88	0.88	0.88
Borehole 2	0.76	**0.77**	**0.77**
Borehole 3	0.66	**0.68**	**0.68**

Across all validation measurements, no differences can be observed between the transmissivity values 0.90 and 0.96 – neither in the R^2 value, nor the regression line. Indicating that in this range of window transmissivity, it has no measurable influence on the correction results.

In contrast, small but consistent differences emerge when comparing the transmissivity value of 0.86 with the higher transmissivity values. These differences remain minor in terms of overall model performance, with R^2 variations typically on the order of 0.01 and not exceeding 0.02. This suggests that, similar to emissivity, the overall goodness of fit is only weakly affected by the choice of transmissivity.

When looking at the regression lines, the differences between the window transmissivity of 0.86 and the higher transmissivities is also visible. For $\tau = 0.86$, larger deviations at lower validation temperatures occur, indicating an increased bias in colder conditions. At higher temperatures, these differences get smaller and all transmissivity values result in similar values. Overall, $\tau = 0.90$ and $\tau = 0.96$ consistently show a closer alignment with the 1:1 line across the full temperature range.

This shows that lower window transmissivity values introduce a temperature-dependent bias, particularly in colder conditions. Higher transmissivity values yield to more stable and consistent results across the observed temperature range.

In addition to the atmospheric correction used in this study, an alternative correction approach was implemented using a crinkled aluminium plate deployed at the study site. Due to its surface properties, the plate is assumed to approximate a near-blackbody radiator and thus provides an independent estimate of the apparent reflected temperature. For this purpose, the temperature measured on the aluminium plate was used as an input for the apparent reflected temperature in the correction workflow, replacing the previously used air-temperature estimate.

The aluminium plate was installed during two periods: from 28 July 2022 to 08 August 2022, and from 31 May 2023 to 27 August 2023. The resulting temperatures from the approach using the aluminium plate as the apparent reflected temperature (hereafter referred to as *aluminium-corrected temperatures*) were compared to the corrected temperatures used throughout the remainder of this study (hereafter *corrected temperatures*).

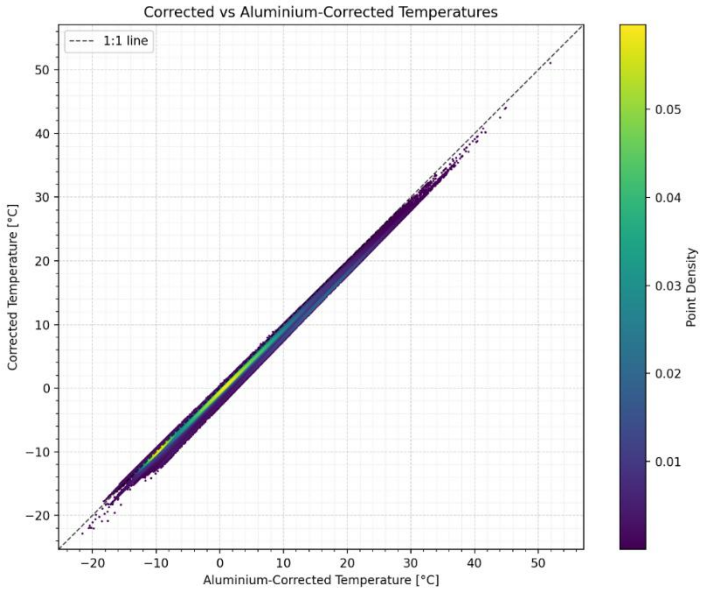

Figure 17: Corrected vs Aluminium-Corrected Temperatures

Figure 17 shows the relationship between corrected and aluminium-corrected temperatures. A near-linear relationship is observed, with most values closely aligned along the 1:1 line, indicating strong agreement between both approaches. Deviations are generally small, although slightly larger differences occur in lower temperature ranges around -10 °C.

The difference between corrected and aluminium-corrected temperatures as a function of distance to the camera is shown in Figure 18. No clear dependency on distance can be identified. The temperature differences reach a maximum of approximately 3.5 °C but are strongly concentrated around ~0.75 °C, indicating that both approaches yield very similar results across the full range of viewing distances.

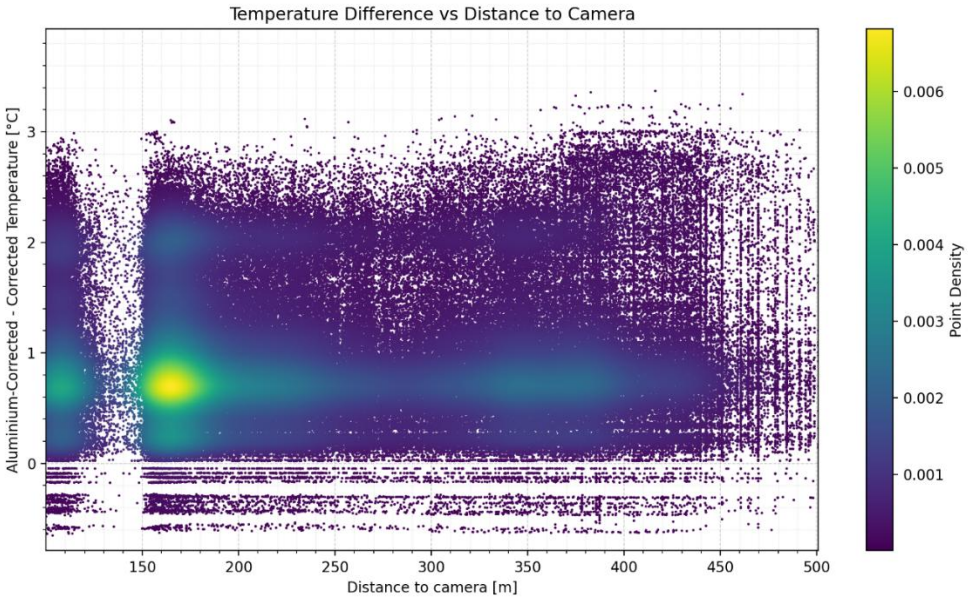

Figure 18: Temperature Difference vs Distance to Camera

Figure 19 presents the temperature difference in relation to internal camera temperature. Here, the largest deviations of up to approximately 3 °C occur at higher internal camera temperatures. However, it does not seem to be a systematic trend, suggesting that the influence of internal camera temperature on the difference between both correction approaches remains limited.

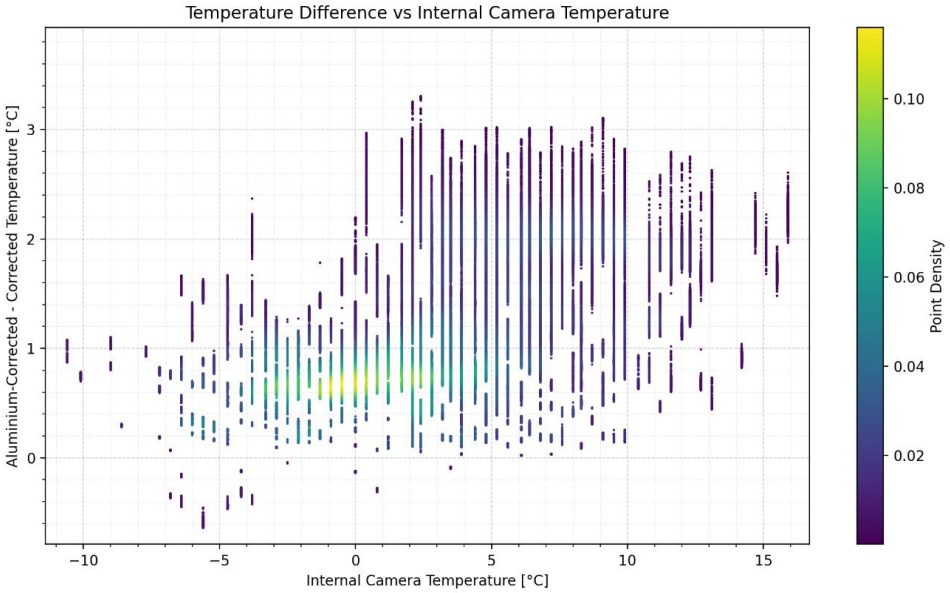

Figure 19: Temperature Difference vs Internal Camera Temperature

Furthermore, the validation plots (Figure 10 - Figure 12) presented in section 4.1.1 were also generated using aluminium-corrected temperatures (Figure B.47 - Figure B.49). These plots confirm the previously observed behaviour, showing only minor differences between aluminium-corrected and corrected temperatures across all validation datasets.
Statistical analysis of the difference between aluminium-corrected and corrected temperatures resulted in the values stated in Table 6.

Table 6: Statistics of Aluminium-Corrected - Corrected

N	**62'547'826**
Mean	0.9735 °C
Median	0.8161 °C
Standard Deviation	0.6420 °C
Min	-0.6561 °C
25th Percentile	0.5419 °C
75th Percentile	1.3249 °C
Max	3.7994 °C

4.2. Analysis Periods

The analysis periods were defined to capture key environmental transitions and conditions that are expected to influence surface temperature dynamics. Periods with transitions between snow-covered and snow-free conditions were identified based on visual interpretation of RGB images acquired simultaneously with the TIR images. In total, two periods were selected for 2021, two for 2022 and one for 2023, with the year 2023 being limited by data availability after August 2023.
For the direct comparison of snow-covered and snow-free conditions, periods were defined using incoming shortwave radiation measured at the meteorological station. Periods with high incoming shortwave radiation were selected to represent clear-sky conditions, thereby minimising atmospheric effects introduced by clouds on the surface temperature signal. These periods were subdivided into snow-covered and snow-free conditions to account for seasonal differences in the surface energy balance. Independently, periods with and without precipitation were selected based on precipitation measurements from the Corvatsch meteorological station (MeteoSchweiz, 2026), again distinguishing between snow-covered and snow-free conditions.
In addition to these period definitions, the influence of diurnal variability was assessed by separating day and night conditions within the same periods used for the snow cover analysis. Together, the snow cover, precipitation, and diurnal subsets provide complementary perspectives on the dominant controls of the surface temperature patterns observed at the study site.
These defined periods form the basis for both the pattern analysis and the statistical dependence analysis. A complete overview of all selected periods is provided in Table 7. Within each period, the analysis was performed on a daily basis using a rolling 5-day window, where each target day was evaluated together with the preceding four days. This data-driven temporal aggregation was applied consistently across all analyses and can be interpreted as a moving-window approach, allowing for robust estimation of spatial patterns and regression relationships while preserving short-term variability.

Table 7: Overview of analysis periods

Period Titles	*Period Dates*
Transition: Snow-Covered to Snow-Free	14.06.21 – 25.07.21; 09.05.22 – 26.06.22; 15.05.23 – 02.07.23
Transition: Snow-Free to Snow-Covered	13.09.21 – 14.11.21; 02.11.22 – 18.12.22
Cover Type: Snow-Free	05.08.21 – 23.08.21; 07.06.22 – 19.07.22
Cover Type: Snow-Covered	26.02.22 – 01.04.22
Precipitation: Snow-Free	23.07.22 – 08.08.22
Precipitation: Snow-Covered	29.01.22 – 23.02.22
No Precipitation: Snow-Free	05.07.22 – 22.07.22
No-Precipitation: Snow-Covered	24.02.22 – 28.03.22
Day/Night: Snow-Free	07.06.22 – 19.07.22
Day/Night: Snow-Covered	26.02.22 – 14.03.22

4.3. Spatio-temporal pattern analysis

4.3.1. Diurnal Curve Clustering

Here, the pixels were clustered based on their mean daily temperature curves within a 5-day rolling window. The curve clustering algorithm was initially designed to determine the optimal number of clusters for each period individually, selecting the number that yielded the highest silhouette score (see section 3.4.1 for a detailed explanation).

However, this approach was reconsidered, as the vast majority of periods consistently showed the highest silhouette score for a cluster number of $n = 2$, with only rare cases indicating an increase to $n = 3$ (Figure 20). To ensure consistency and comparability across all periods, the analysis was therefore restricted to a fixed cluster number of $n = 2$ in all subsequent steps.

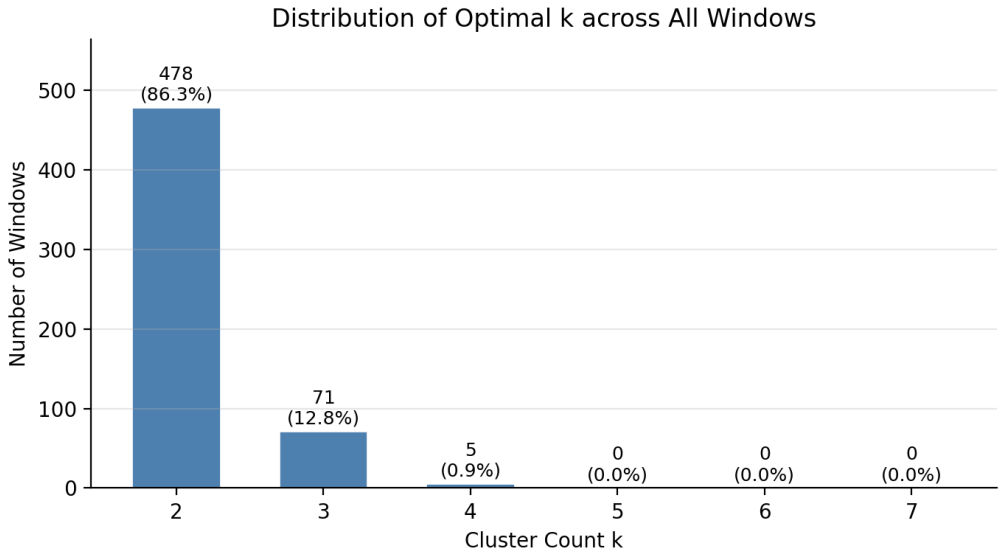

Figure 20: Distribution of the silhouette-optimal number of clusters k across all grouping windows, pooled over analysis periods. For each window, k was evaluated in the range 2 to 7 and the value maximising the silhouette score was retained.

4.3.1.1. Transition Periods

During transition periods from snow-free to snow-covered conditions, the identified clusters exhibit highly similar temperature curve shapes. The primary difference between the clusters is a temperature offset, which is relatively constant at 2 - 5 °C. In contrast, this offset is less consistent in 2021. In that year, deviations during daytime are roughly twice as large as those observed at night, reaching up to 10 °C during the day. The lower of the two temperature curves rarely exceeds the 0 °C threshold. From a spatial perspective, in both 2021 and 2022, pixels associated with the warmer temperature curve correspond almost exclusively to the block glacier surface. In contrast, pixels associated with colder temperature curves are predominantly located outside the glacier and partially within furrow structures (Figure 21, left). In 2021, the warmer areas initially appear to migrate downslope, resulting in the upper part of the glacier becoming increasingly dominated by pixels belonging to the colder cluster (Figure 21, right). In 2022, however, the warmer pixels disperse more uniformly across the glacier surface, forming an almost regular spatial pattern (Figure 22, left). Towards the end of the transition period, a similar pattern also emerges in 2021. These warmer areas can be attributed to the lateral surfaces of larger boulders that remain partially snow-free.

During transition periods from snow-covered to snow-free conditions, all analysed years (2021 - 2023) show highly consistent behaviour. Again, two distinct temperature curves can be identified: a warmer and a colder cluster. During nighttime, the temperature difference between these clusters is relatively small, typically ranging between 0 and 10 °C. During daytime, however, this difference can increase substantially, reaching up to 20 °C. A particularly pronounced feature is the stronger warming of the warmer cluster between approximately 06:00 and 10:00.

Spatially, areas associated with the colder temperature curve correspond closely to snow-covered surfaces. At the beginning of the transition, nearly the entire scene (except for the largest boulders and rock outcrops) is dominated by pixels of the colder cluster (Figure 22, right). As the transition progresses, pixels associated with the warmer temperature curve begin to emerge along ridge structures and subsequently expand across the glacier surface on a day-to-day basis (Figure 23, left). By the end of the transition period, colder areas are largely confined to remaining snow patches, primarily located outside the block glacier (Figure 23, right). The spatial evolution of these patterns is highly consistent across all analysed years.

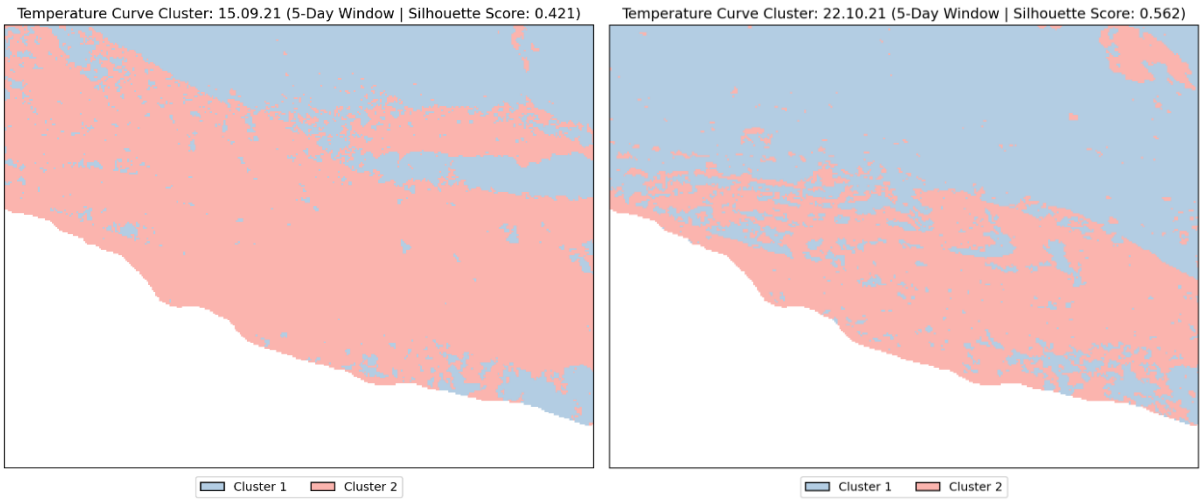

Figure 21: Representative cluster maps from the diurnal temperature curve clustering approach. Left: Start of snow-free to snow-covered transition (15.09.21); Right: Midpoint of snow-free to snow-covered transition of the year 2021 (22.10.21)

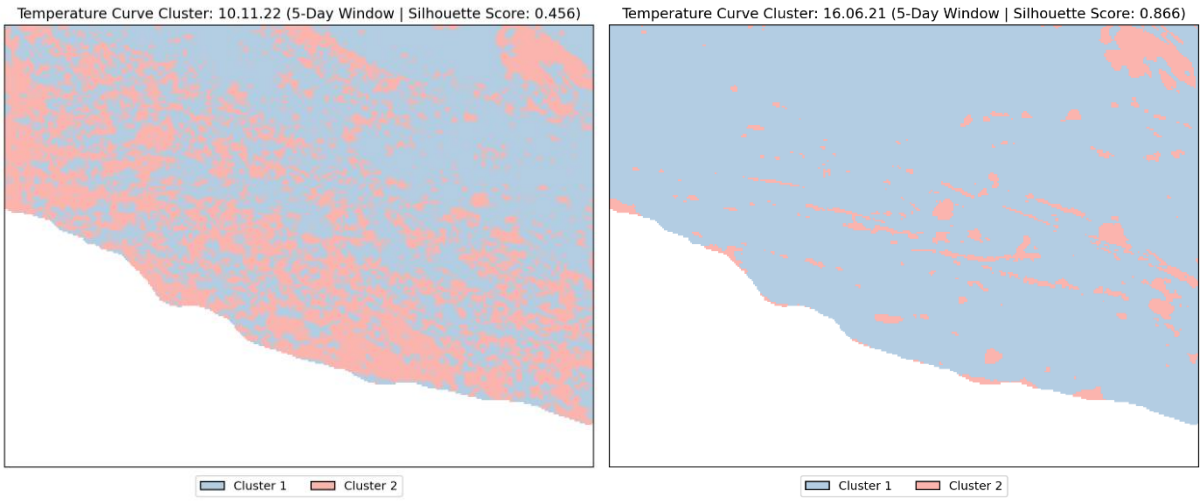

Figure 22: Representative cluster maps from the diurnal temperature curve clustering approach. Left: End of snow-free to snow-covered transition (10.11.22); Right: Start of snow-covered to snow-free transition (16.06.21)

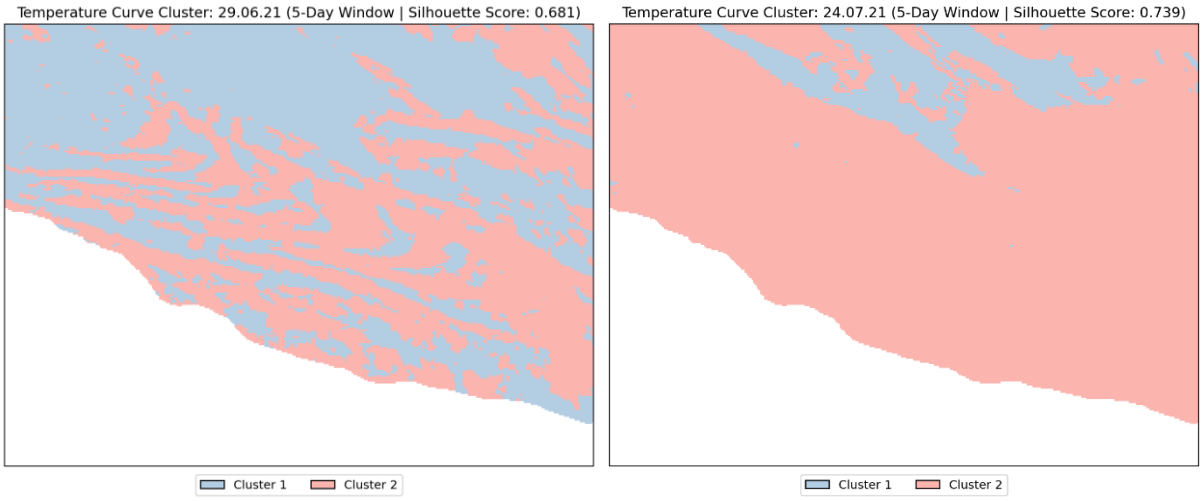

Figure 23: Representative cluster maps from the diurnal temperature curve clustering approach. Left: Midpoint of snow-covered to snow-free transition (29.06.21); Right: End of snow-covered to snow-free transition (24.07.21)

4.3.1.2. Snow Cover vs Snow Free

During snow-covered periods, the temperature curves remain very similar until approximately 08:00. After this time, the warmer temperature curve begins to increase more rapidly, leading to temporary differences of up to 10 °C between the two curves until around 16:00. Following this peak divergence, the curves converge again relatively quickly in the late afternoon and evening.

Spatially, pixels associated with the warmer temperature curve are primarily located on the block glacier, particularly along ridge structures and on larger boulders, but also more broadly distributed across the glacier surface. In contrast, the furrow structures of the block glacier and the background are consistently dominated by pixels belonging to the colder temperature curve (Figure 24, left).

In snow-free periods, distinct and more variable patterns can be observed in the temperature curves. In 2021, a relatively constant offset between the two curves is present, although this difference decreases between approximately 08:00 and 10:00 due to a faster warming of the colder curve. Subsequently, the temperature difference increases again, reaching maximum values of up to 10 °C.

In 2022, the behaviour differs between two phases. During the first ~20 days, the two curves remain well separated at all times. Nighttime differences are relatively constant at around 10 °C, while a

pronounced increase in the warmer curve between approximately 07:00 and 10:00 leads to maximum differences of up to 20 °C. Toward the end of the day, these differences gradually decrease again to around 10 °C.
During the subsequent ~30 days, the two curves are much closer to each other. In some cases, the colder temperature curve warms earlier in the morning (between approximately 05:00 and 10:00), temporarily exceeding the warmer curve before the latter becomes dominant again after around 10:00. In this phase, maximum temperature differences are generally limited to approximately 5 °C.
From a spatial perspective, in 2021, pixels associated with the warmer temperature curve are concentrated on the block glacier and partially in the background area of the scene, while pixels of the colder temperature curve are primarily located in the background and occasionally within the furrow structures of the glacier (Figure 24, right). In 2022, a similar spatial pattern is observed, with no clear distinction between the early and late phases of the period, despite the differences evident in the temporal temperature curves.

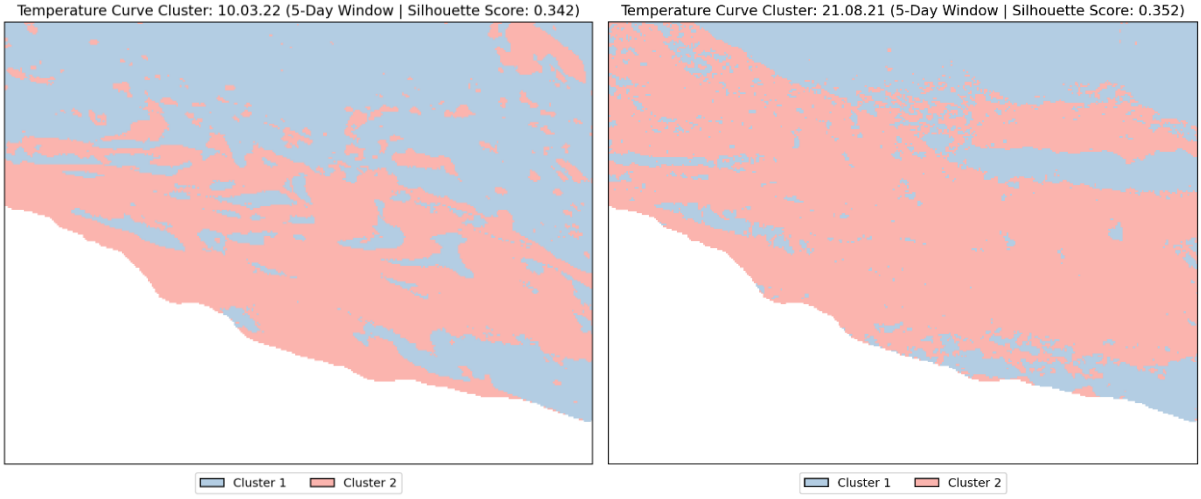

Figure 24: Representative cluster maps from the diurnal temperature curve clustering approach. Left: Snow-covered (10.03.21); Right: Snow-free (21.08.21)

4.3.1.3. Precipitation vs No Precipitation

A distinction is made between precipitation and dry periods under both snow-free and snow-covered conditions. The analysis first focuses on snow-free periods.
During snow-free conditions, the temperature curves show only minor differences between precipitation and dry periods. In both cases, the warmer temperature curve remains consistently about 5 °C higher than the colder one. An exception occurs during the morning warming phase: between approximately 06:00 and 10:00, the colder temperature curve may exhibit an earlier increase, temporarily exceeding the warmer curve. After this phase, the warmer curve regains dominance.
From a spatial perspective, no substantial differences can be observed between precipitation and dry periods either. Pixels associated with the warmer temperature curve cover nearly the entire block glacier, with only a few colder pixels occurring in furrow structures. Conversely, pixels of the colder temperature curve dominate the background areas. This spatial pattern remains consistent regardless of whether precipitation occurs (Figure 25; left: dry period, right: precipitation period).
During snow-covered conditions, the temperature curves also show only minor differences between precipitation and dry periods. The most notable distinction is that during dry periods, the diurnal temperature range is generally larger, with day–night differences of approximately 5 - 7 °C. In con-

trast, during precipitation periods, almost no clear difference between day and night temperatures can be observed.
In contrast to the temporal patterns, more pronounced differences emerge in the spatial distribution. During dry periods, the spatial pattern resembles the typical configuration: pixels of the warmer temperature curve cover a large portion of the block glacier, while colder pixels are primarily found in furrow structures, the background, and higher-elevation areas of the glacier (Figure 26, left).
During precipitation periods, however, pixels associated with the warmer temperature curve are largely confined to larger boulders and rock outcrops, as well as small sections of ridge structures. The majority of the study area is dominated by pixels belonging to the colder temperature curve (Figure 26, right).

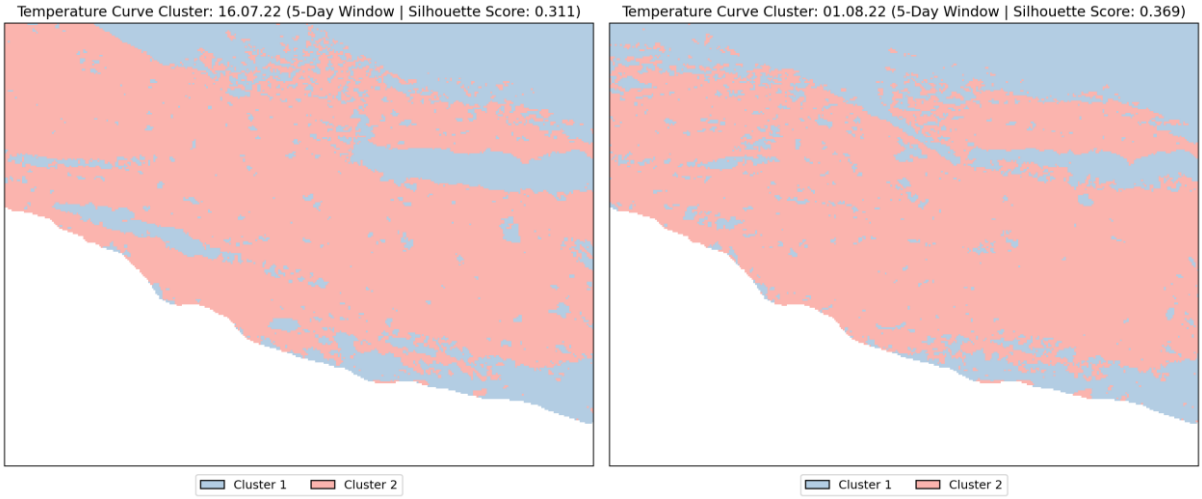

Figure 25: Representative cluster maps from the diurnal temperature curve clustering approach. Left: Snow-free dry period (16.07.22); Right: Snow-free precipitation period (01.08.22)

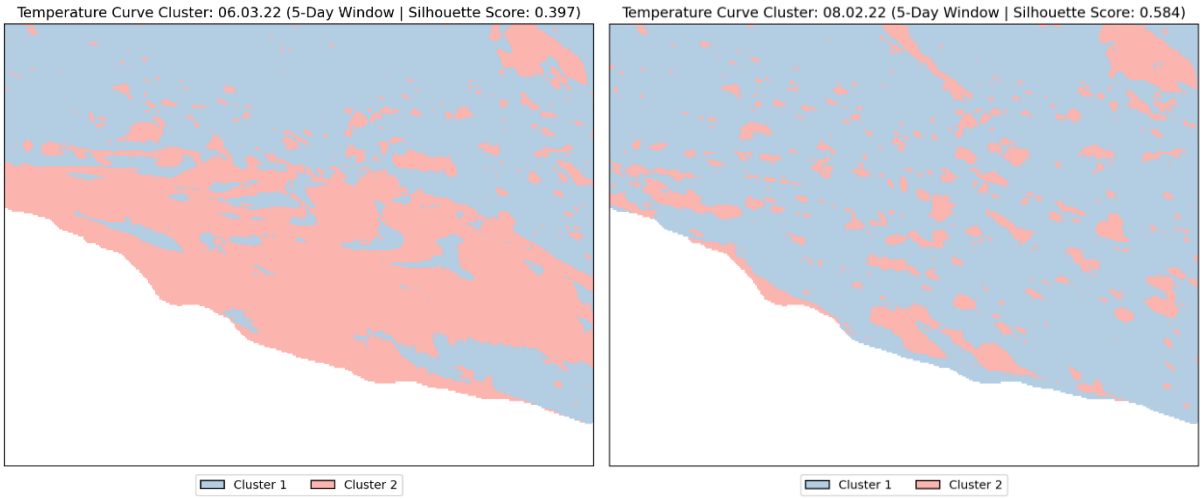

Figure 26: Representative cluster maps from the diurnal temperature curve clustering approach. Left: Snow-covered dry period (06.03.22); Right: Snow-covered precipitation period (08.02.22)

4.3.1.4. Day vs Night

In the distinction between day and night, a further differentiation is made between snow-free and snow-covered periods. The analysis again begins with snow-free conditions.
During snow-free periods, the temperature curves exhibit greater variability during the day than at night. At night, the temperature difference between the two curves remains relatively constant. In

contrast, daytime conditions are characterized by the previously described warming and cooling phases, leading to a higher variability in the distance between the curves.
Despite these temporal differences, no substantial changes are observed in the spatial grouping. Pixels associated with the warmer temperature curve consistently concentrate on the block glacier, both during the day (Figure 27, left) and at night (Figure 27, right), while pixels of the colder temperature curve are predominantly located in the background.
During snow-covered periods, the temperature curves show a similar temporal pattern to that observed under snow-free conditions, with relatively stable differences at night and increased variability during the day.
However, more pronounced differences are evident in the spatial distribution. During daytime, pixels of the warmer temperature curve are primarily located along ridge structures and their adjacent areas on the glacier. In contrast, pixels of the colder temperature curve are concentrated in furrow structures and in the surrounding background (Figure 28, left).
At night, the spatial pattern shifts: pixels associated with the warmer temperature curve are mainly confined to larger boulders and only occasionally extend across broader areas of the glacier surface ((Figure 28, right). The remaining areas are predominantly occupied by pixels belonging to the colder temperature curve.

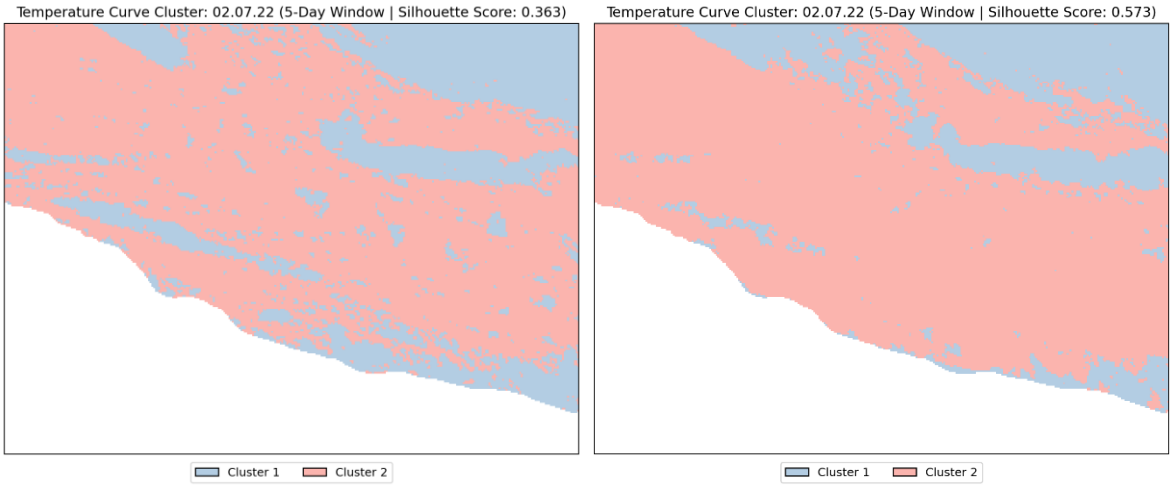

Figure 27: Representative cluster maps from the diurnal temperature curve clustering approach. Left: Snow-free day (02.07.22); Right: Snow-free night (02.07.22)

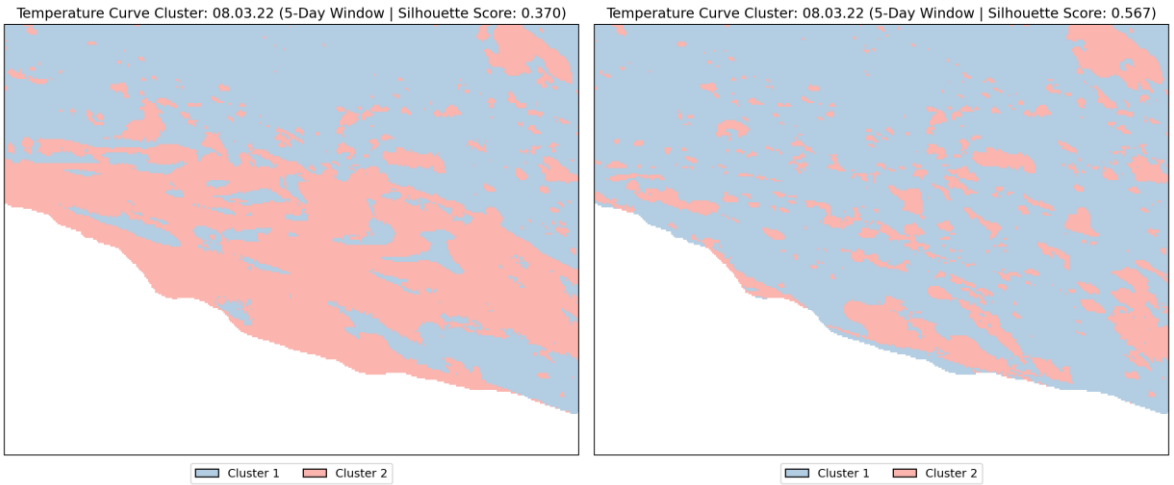

Figure 28: Representative cluster maps from the diurnal temperature curve clustering approach. Left: Snow-covered day (08.03.22); Right: Snow-covered night (08.03.22)

4.3.2. Anomaly Persistence Classification

In this approach, each pixel of every acquisition was first z-normalised. Then, for each target day, the number of occurrences in which a pixel was higher than the image mean was calculated over the rolling five-day period from day X-4 to day X. As a result, each pixel was assigned a count value representing how often it was warmer than the mean image temperature within this time window. These count values were subsequently used to divide the image into three classes: persistently warm, intermediate and persistently cold pixels. The detailed procedure is described in Section 3.4.2.

4.3.2.1. Transition Periods

In the transition period from snow-covered to snow-free conditions, the spatial patterns remain largely consistent across the years 2021, 2022 and 2023. At the beginning of this transition period, cold areas are concentrated on the rock glacier, while warm areas are mainly associated with larger boulders, ridge crests and the steep slopes in the background (Figure 29, left). As the transition progresses, the cold areas shift towards the background, and the warm areas expand along the ridges. By the end of the transition period, cold areas are no longer present within the furrows, these areas are dominated by the intermediate group. Overall, cold areas nearly disappear from the glacier surface by the end of this transition and are almost exclusively in the background (Figure 29, right).
In the transition period from snow-free to snow-covered conditions, two periods are analysed (2021 and 2022). At the beginning of this transition period, the spatial pattern resembles the final stage of the previous transition (Figure 29, right). Particularly in 2021, a clear differentiation between cold, intermediate and warm areas emerges: Over time, the warm areas shift towards lower elevation, while cold areas migrate towards higher elevations (Figure 30, left). Following this differentiation, another change occurs: warm areas become increasingly associated with larger boulders, whereas cold areas expand back onto the glacier surface (Figure 30, right).

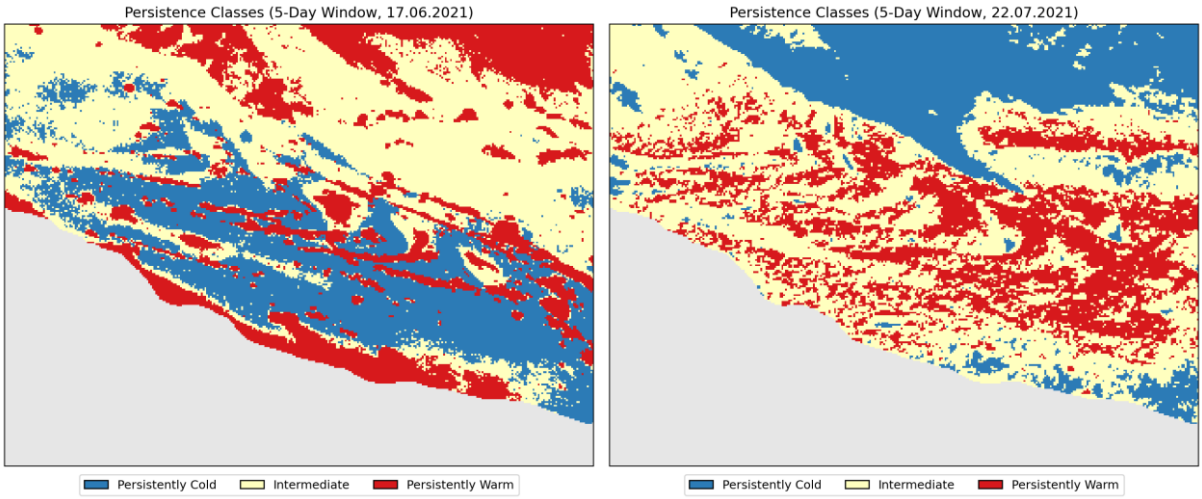

Figure 29: Representative cluster maps from the anomaly persistence classification approach. Left: begin of snow-covered to snow-free transition (17.06.21); Right: end of snow-covered to snow-free transition (22.07.21)

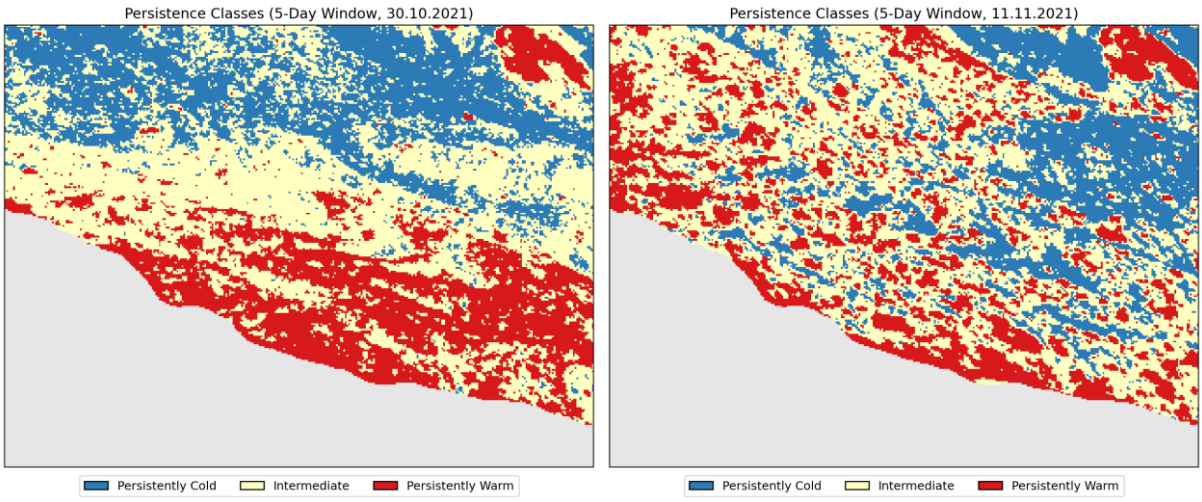

Figure 30: Representative cluster maps from the anomaly persistence classification approach. Left: halfway-point of snow-free to snow-covered transition (30.10.21); Right: end of snow-free to snow-covered transition (11.11.21)

4.3.2.2. Snow Cover vs. Snow Free

In the snow-free periods, the spatial patterns are broadly consistent with those described for the late stage of the snow-covered-to-snow-free transition. Cold areas are primarily concentrated in regions that do not belong to the rock glacier, while warm areas are mainly associated with the ridges and the frontal part of the rock glacier. Intermediate areas are distributed between these zones (Figure 31, left).

In contrast, the snow-covered periods are characterised by much coarser and more homogeneous spatial patterns. Whereas in snow-free conditions individual rocks can still be distinguished at the margins on a pixel level, the snow-covered periods appear as more continuous surfaces. During these periods, the warm areas alternate between being concentrated along the ridges and the foreground – similar to snow-free conditions – and shifting towards larger boulders and rocks. At the same time, the cold areas extent from the background towards the furrows on the rock glacier (Figure 31, right).

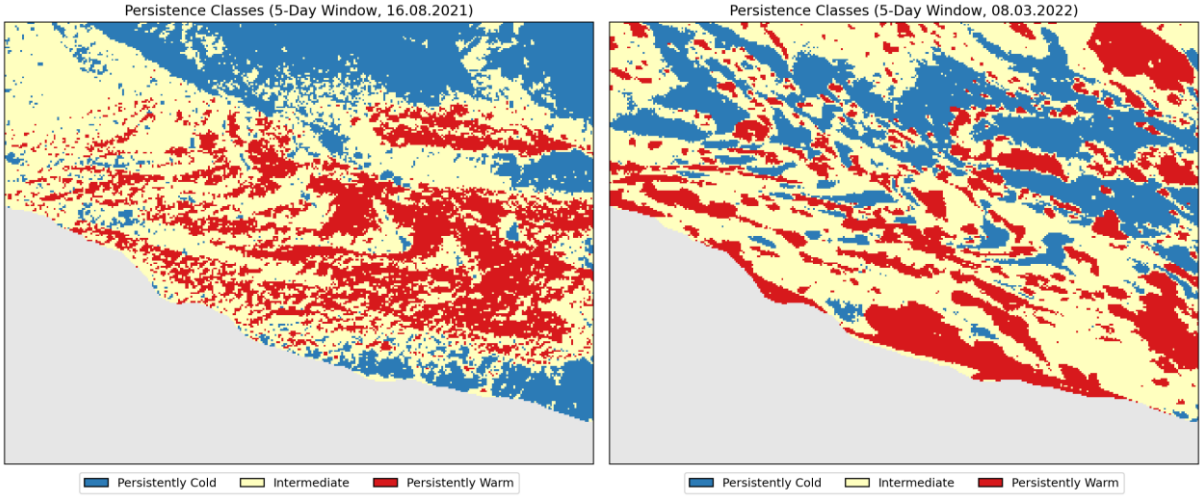

Figure 31: Representative cluster maps from the anomaly persistence classification approach. Left: Snow-free period (16.08.21); Right: Snow-covered period (08.03.21)

4.3.2.3. Rain Periods vs. Dry Periods

In the rain and dry periods, a further distinction is made between periods with and without snow cover. The spatial patterns of dry periods, both under snow-cover and snow-free conditions, have already been described in the previous section.

For rain periods under snow-free conditions, the spatial groups do not differ substantially from those observed during dry conditions. Warm pixels remain predominantly distributed along the ridges, while cold areas are still largely confined to regions outside the rock glacier (Figure 32, left).

In contrast, during precipitation periods under snow-covered conditions, the spatial patterns appear more fragmented, particularly at the beginning of the period. Warm areas are mostly discontinuous and are associated with the ridges. Cold areas, on the other hand, tend to form more continuous patterns in the furrows. In the background, larger continuous zones of cold areas can be observed (Figure 32, right).

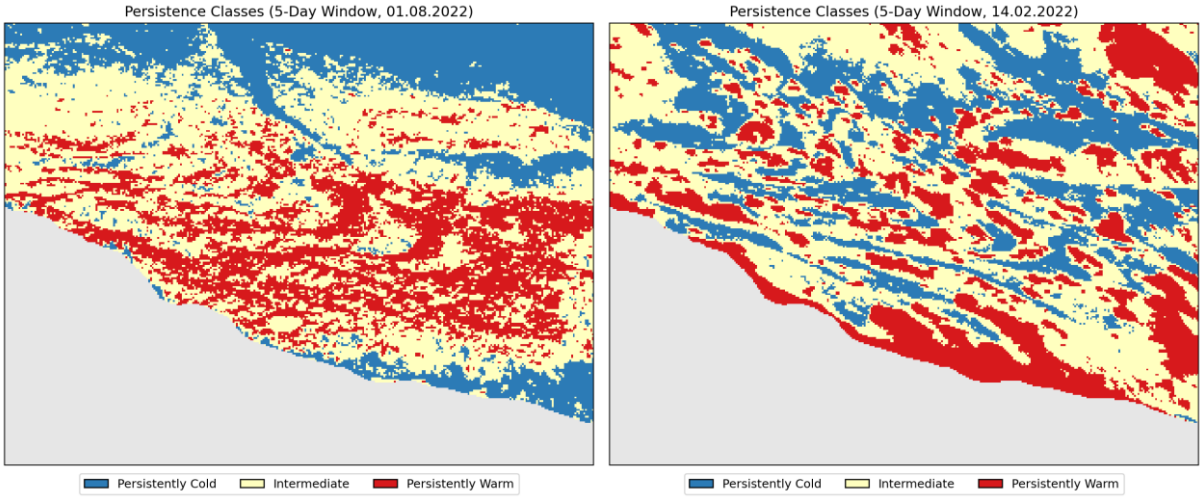

Figure 32: Representative cluster maps from the anomaly persistence classification approach. Left: Snow-free precipitation period (01.08.22); Right: Snow-covered precipitation period (14.02.22)

4.3.2.4. Day vs. Night

In the day vs. night periods, a further distinction is made between snow-free and snow-covered conditions. For each period, only days with no or low cloud cover are considered.

For the snow-free conditions during the day, the spatial patterns follow the expected distribution: warm areas are concentrated along the ridges and at a steep section in the background, while cold areas are mainly located outside the rock glacier. In addition, some colder spots are present in the furrows of the rock glacier (Figure 33, left). At night, the pattern changes substantially. Warm areas cover most of the rock glacier surface, no longer being restricted to the ridges and are found almost everywhere across the rock glacier. In contrast, cold areas are primarily confined to the background (Figure 33, right).

Under snow-covered conditions during the day, warm areas are again distributed along the ridges, particularly in the lower part of the rock glacier. Cold areas are concentrated at higher elevations, both on the rock glacier itself and in the background (Figure 34, left).

During snow-covered conditions at night, warm areas appear as scattered across the rock glacier and the surrounding terrain. The warm patches likely correspond to larger boulders or areas with reduced snow cover, where the underlying surface influences the observed temperatures more strongly (Figure 34, right).

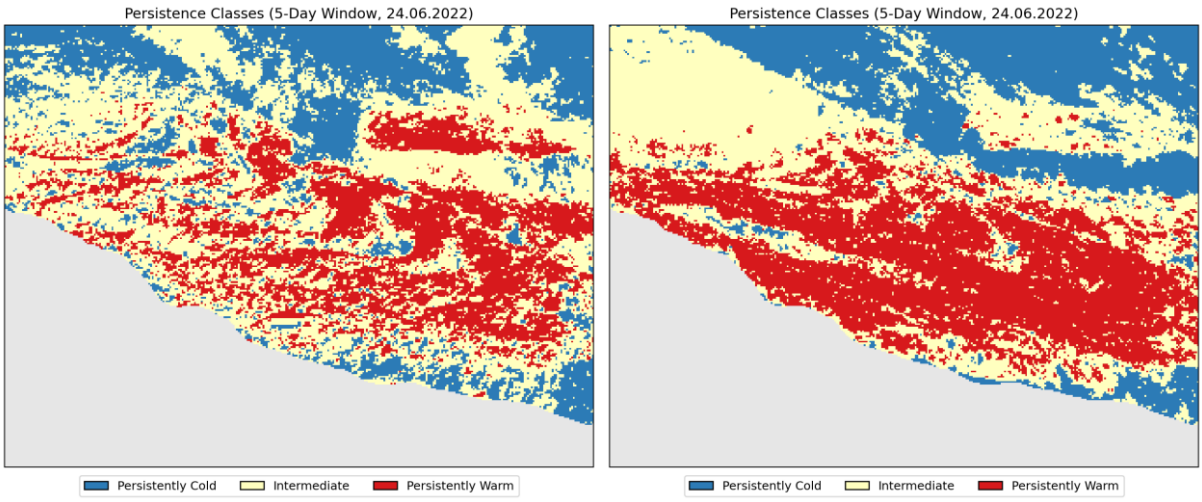

Figure 33: Representative cluster maps from the anomaly persistence classification approach. Left: Snow-free day (24.06.22); Right: Snow-free night (24.06.22)

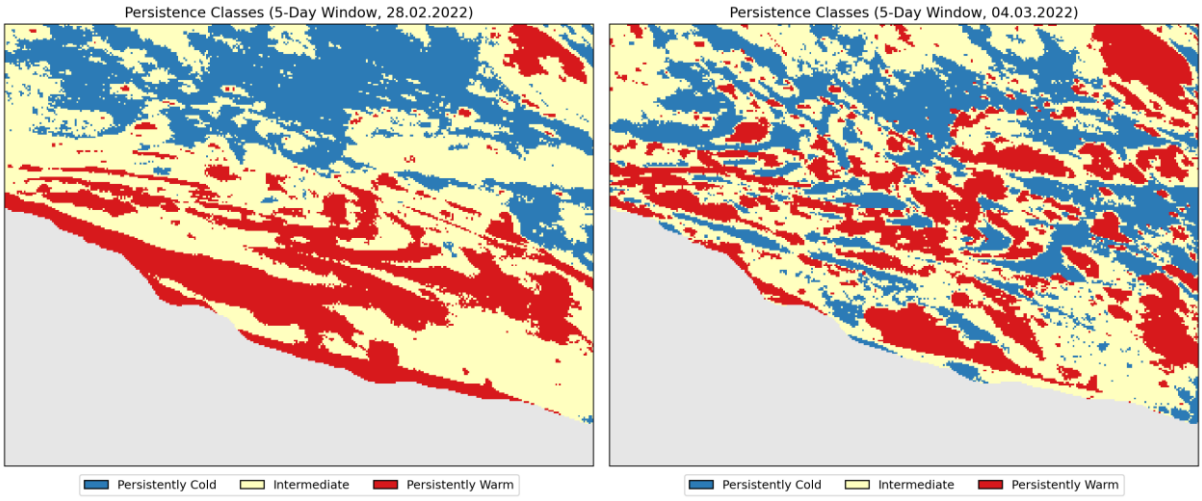

Figure 34: Representative cluster maps from the anomaly persistence classification approach. Left: Snow-covered day (28.02.22); Right: Snow-coved night (28.02.22)

4.4. Statistical dependence analysis

4.4.1. Diurnal Curve Clustering

In the following analysis, the colder temperature curve is referred to as Cluster 1, while the warmer temperature curve is referred to as Cluster 2. All values expressed in percentages are the 25th - 75th percentiles of all the data in this analysis period to minimise the effect of outliers. Every value of each variable is listed in the tables of Appendix C (Table C.1 - Table C.5). An overview of the relative influence of meteorological variables across all analysis periods and both clusters is provided in Figure 35.



Figure 35: Boxplots of the relative influence (%) of meteorological variables on camera-measured LST across different analysis periods, separated by groups resulting from the diurnal curve clustering workflow. Relative influence is computed from multiple linear regression coefficients normalised so that the sum of absolute coefficients per day equals 100 %. The coefficient of determination (R^2) of the corresponding day-wise models is shown on the secondary y-axis (right).

4.4.1.1. Transition Periods

During transition periods from snow-free to snow-covered conditions (see Figure C.1, Figure C.2, Table C.1), no substantial differences are observed between the two clusters. In both 2021 and 2022, air temperature represents the dominant driver, with typical relative influence values between 34 % and 51 %. The second most important driver alternates between relative humidity and downwelling

shortwave radiation, each contributing around 10 - 24 %. The remaining variables rarely exceed 20 % and show relatively high variability.
A notable exception occurs in 2022 (Figure C.3, left), where a pronounced peak in downwelling longwave radiation reaches approximately 50 %. During this event, the influence of air temperature decreases to around 20 %, while relative humidity drops below 10 %. In contrast, downwelling shortwave radiation remains stable.
The R^2 values in both years (2021 and 2022) show considerable variability, ranging from nearly 1 down to approximately 0.35. The lowest R^2 value coincides with the peak in downwelling longwave radiation. Apart from this event, no clear systematic relationship between individual variables and model performance can be identified.
In contrast, clear differences between the two clusters are evident during transition periods from snow-covered to snow-free conditions (Figure C.2, Figure C.3, Table C.1). Cluster 1 is associated with snow-covered surfaces, whereas Cluster 2 represents bare ground or larger boulders.
In Cluster 1, an alternating pattern between air temperature (20 - 41 %) and downwelling shortwave radiation (22 - 34 %) as the dominant driver is observed consistently across all three years (2021 - 2023). Downwelling shortwave radiation maintains a relatively stable and high influence, while air temperature exhibits strong declines – often dropping below 10 % – during periods when shortwave radiation becomes dominant. Relative humidity and downwelling longwave radiation represent the next most important variables, although all variables aside from air temperature and shortwave radiation show high variability and generally remain below 20 %.
The R^2 values in Cluster 1 range from nearly 1 to approximately 0.4 and appear to be closely linked to the influence of air temperature. Periods with a reduced contribution of air temperature are associated with lower R^2 values.
In Cluster 2, considerably lower variability is observed. Air temperature is clearly the dominant driver throughout, with more stable contributions between 34 % and 49 %. Downwelling shortwave radiation consistently represents the second most important variable, with values between 26 % and 35 %. All remaining variables are of minor importance and typically remain below 20 %.
Downwelling longwave radiation shows temporal patterns similar to shortwave radiation but at a lower magnitude. Relative humidity exhibits moderate peaks (approximately 20 - 40 %) in each year, which are associated with some increases or decreases in the influence of air temperature.
The R^2 values in Cluster 2 are substantially more stable (standard deviation of 0.066) than in Cluster 1 (standard deviation of 0.139), ranging between 0.992 and 0.603, reflecting the more consistent dominance of air temperature in this cluster.

4.4.1.2. Snow vs No Snow

During snow-covered periods (Figure C.4, Table C.2), clear differences between the clusters can be observed. Spatially, Cluster 1 corresponds to furrow structures and the surrounding background, whereas Cluster 2 represents ridge structures, adjacent glacier surfaces, and larger boulders.
In Cluster 1, air temperature is the dominant driver, with relative influence values ranging between 28 % and 48 %, followed by downwelling shortwave radiation (20 - 24 %). The next most important variables are downwelling longwave radiation and relative humidity, which alternate in importance and reach values of up to 20 %.
In Cluster 2, air temperature and downwelling shortwave radiation alternate as the dominant driver, both typically ranging between 21 % and 41 %. Relative humidity represents the third most important variable, with contributions of up to approximately 20 %.

In both clusters, a notable outlier event is observed, during which downwelling longwave radiation increases to 35 - 45 % over a period of four days, temporarily becoming the dominant driver. This event does not have a noticeable impact on model performance. The R^2 values are generally similar in both clusters, although Cluster 1 exhibits a larger variability (0.776 - 0.962 with standard deviation of 0.045) compared to Cluster 2 (0.67 - 0.942 with standard deviation of 0.08).
During snow-free periods (Figure C.3, Figure C.4, Table C.2), only minor differences between the clusters are observed. In both clusters, air temperature is the dominant driver (32 - 43 % in Cluster 1; 42 - 54 % in Cluster 2), followed by downwelling shortwave radiation (26 - 41 %; 27 - 33 %). All other variables typically remain below 11 %.
A slight difference can be identified in the behaviour of downwelling shortwave radiation: in Cluster 1, downwelling shortwave radiation becomes the dominant driver in approximately half of the days within the 2022 analysis period, whereas in Cluster 2 this occurs only in 2 out of 43 days.
The R^2 values are more stable in Cluster 2, typically ranging between 0.965 and 0.855 (standard deviation of 0.025). In Cluster 1, R^2 values are also high but exhibit a wider range, between 0.941 and 0.68 (standard deviation of 0.059).

4.4.1.3. Rain Periods vs Dry Periods

A distinction is again made between snow-covered and snow-free conditions. The behaviour during dry periods has already been described in the previous section; the following focuses on precipitation periods.
During precipitation periods under snow-free conditions (Figure C.5, Table C.3), air temperature remains the dominant driver, with relative influence values between (34 - 47 %; 40 - 53 %). In Cluster 1, downwelling shortwave radiation is consistently the second most important variable, with contributions between 20 % and 28 %. In Cluster 2, a short period of approximately six days can be identified during which downwelling shortwave radiation (17 - 23 %) is temporarily surpassed by either downwelling longwave radiation or relative humidity. Outside of this interval, both clusters show very similar behaviour.
The R^2 values are nearly identical in both clusters, typically ranging between 0.853 and 0.962.
Under snow-covered conditions (Figure C.5, Table C.3), both clusters exhibit very similar patterns. Air temperature is the dominant driver, with contributions between 42 % and 55 %. The second most important variables are downwelling shortwave radiation and relative humidity, both showing similar influence levels of around 20 %. All remaining variables are relatively stable and rarely exceed 10 %. The R^2 values show a comparatively large variability during this period, ranging from approximately 0.605 up to 0.954. This variability appears to be linked to the influence of air temperature: periods with a stronger contribution of air temperature generally correspond to higher R^2 values.

4.4.1.4. Day vs Night

During daytime under snow-free conditions (Figure C.7, Table C.4), slight differences between the clusters are evident. In Cluster 2 (associated with the block glacier surface), air temperature consistently dominates, with contributions between 41 % and 53 %, remaining clearly above downwelling shortwave radiation (21 - 30 %). In Cluster 1 (associated with the background), air temperature is generally lower (28 - 45 %) and is more frequently matched or exceeded by downwelling shortwave radiation (21 - 34 %).
All other variables remain below 20 % in both clusters, although downwelling longwave radiation shows a comparatively stronger influence in Cluster 1 than in Cluster 2. Differences are also reflected in model performance: Cluster 2 exhibits stable R^2 values between 0.847 and 0.949, whereas

Cluster 1 shows a larger variability (0.519 - 0.847), partly associated with decreases in air temperature influence and simultaneous peaks in downwelling shortwave and longwave radiation.
At night (Figure C.7, Table C.4), no substantial differences between the clusters are observed. Air temperature remains the dominant driver (Cluster1; 36 - 54 %; Cluster 2: 43 - 58 %). The second most important variable shifts over time: during the first ~20 days, downwelling longwave radiation dominates, while in the subsequent ~20 days, downwelling shortwave radiation becomes more influential. Both variables typically range between 5 % and 20 %. The remaining variables show moderate variability between 2 % and 12 %. R^2 values are similar in both clusters, ranging between 0.731 and 0.953.
During daytime under snow-covered conditions (Figure C.8, Table C.5), clearer differences between the clusters emerge. Cluster 1 corresponds to ridge structures and adjacent areas, while Cluster 2 represents furrows and the background. In Cluster 1, air temperature is the dominant driver (33 - 41 %), followed by downwelling shortwave radiation (20 - 23 %) and relative humidity (15 - 22 %). All other variables typically remain below 10 %, and overall variability is low.
In Cluster 2, air temperature remains the primary driver (31 - 37 %), but downwelling shortwave radiation exhibits a very similar level of influence (28 - 33 %), indicating a more balanced contribution between the two variables. Relative humidity ranks third (14 - 22 %), while all remaining variables rarely exceed 10 %. The R^2 values are similar in both clusters, generally ranging between 0.753 and 0.924.
At night (Figure C.8, Table C.5), no clear differences between the clusters are observed. Downwelling longwave radiation represents the dominant driver for approximately two-thirds of the time (19 - 40 %; 15 - 38 %), while air temperature dominates during the remaining third (16 - 40 %; 19 - 39 %). When downwelling longwave radiation is dominant, no consistent secondary driver can be identified. In contrast, when air temperature is the primary driver, downwelling longwave radiation typically ranks second. The remaining variables show considerable variability but generally remain below 15 %.
The R^2 values are similar for both clusters and strongly depend on the dominant driver. Periods dominated by downwelling longwave radiation are associated with lower R^2 values (around 0.5), whereas periods dominated by air temperature show substantially higher model performance, with R^2 values around 0.9.

4.4.2. Anomaly Persistence Classification

All values expressed as percentages in the following chapters are representing the 25th to 75th percentile of each variable in each period. All values can be seen in the tables shown in Appendix C Table C.6 – Table C.10. An overview of the relative influence of meteorological variables across all analysis periods and all three groups is provided in Figure 36.

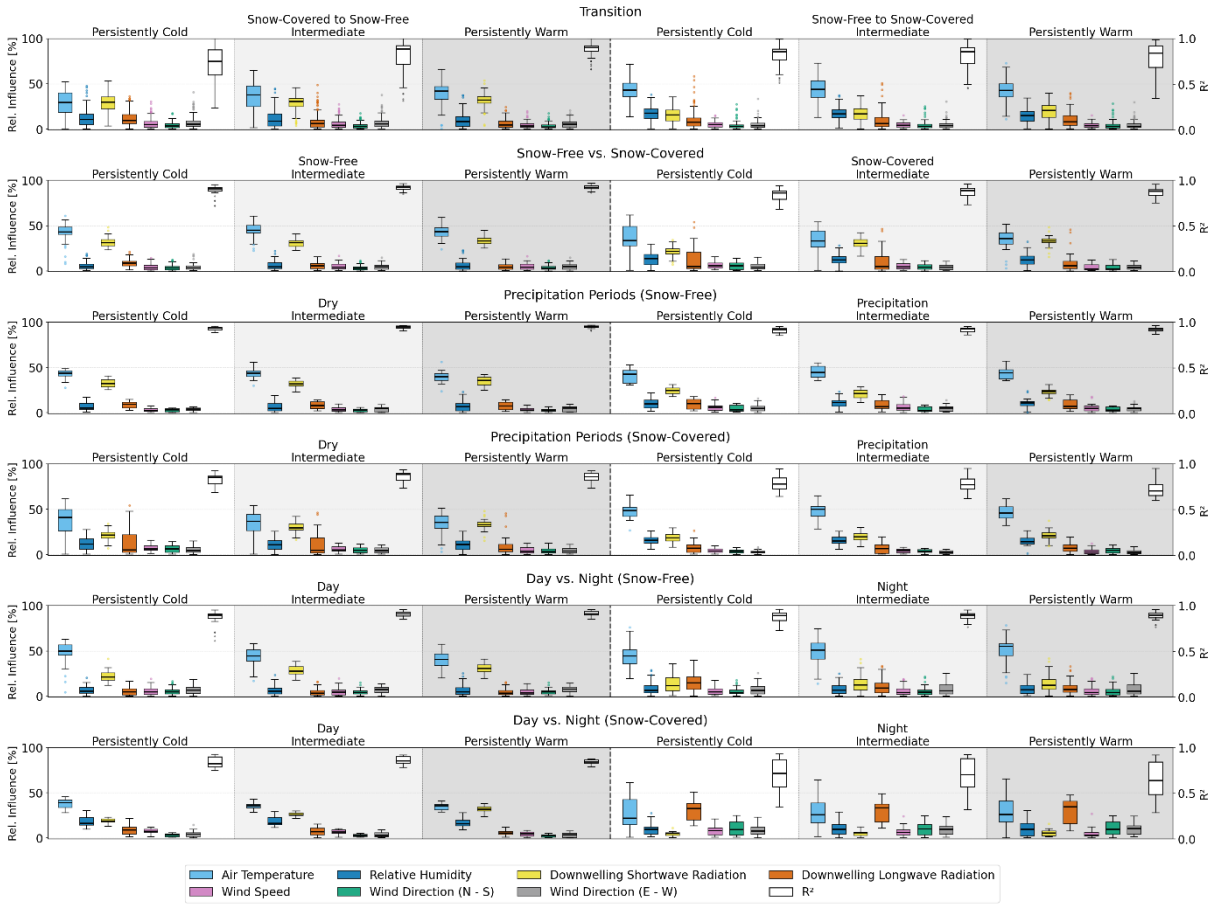

Figure 36: Boxplots of the relative influence (%) of meteorological variables on camera-measured LST across different analysis periods, separated by groups resulting from the anomaly persistence classification workflow. Relative influence is computed from multiple linear regression coefficients normalised so that the sum of absolute coefficients per day equals 100 %. The coefficient of determination (R^2) of the corresponding day-wise models is shown on the secondary y-axis (right).

4.4.2.1. Transition Periods

During transition periods from snow-free to snow-covered conditions (Figure C.10, Figure C.11, Table C.6), the results of the multiple linear regression show no substantial differences between the analysed periods. In general, air temperature represents the dominant driver, with typical relative influence values ranging between 36 % and 53 %. The second most important predictor alternates between relative humidity and downwelling shortwave radiation, with contributions of 9 % and 25 %. Both periods are characterised by generally high R^2 values (mean of 0.8), indicating a good model performance. An exception occurs on days with pronounced peaks in downwelling longwave radiation, during which R^2 drops markedly to values with a minimum of 0.344. Wind-related variables show negligible influence throughout, with the exception of a single event in 2022, where both wind direction components contributed approximately 30% and 20%, respectively, without a corresponding decrease in R^2. No meaningful differences are observed between the individual groups.

During transition periods from snow-covered to snow-free conditions (Figure C.9, Figure C.10, Table C.6), a gradual increase in the influence of downwelling shortwave radiation can be observed over time, accompanied by a more pronounced increase in the importance of air temperature. In the persistently cold pixels, downwelling shortwave radiation and air temperature alternate as the dominant driver. However, air temperature progressively gains importance and becomes the primary controlling factor in the persistently warm pixels.
Across all three years (2021 - 2023), a distinct peak in downwelling longwave radiation occurs after a short initial phase (approximately 7 days in 2021 and 2022, and around 15 days in 2023). This peak coincides with a drop in air temperature and an increase in downwelling shortwave radiation. Apart from this event, downwelling longwave radiation shows no high influence. Following the drop in air temperature, its influence steadily increases again, eventually becoming the dominant driver toward the end of the transition period.
A further notable pattern is the continuous decline in the importance of relative humidity over time (e.g., from approximately 45 % at the beginning of 2021 to below 10 % at the end of the period). The R^2 values show a clear dependence on the dominance of air temperature: whenever air temperature is not the primary predictor, R^2 decreases substantially, in extreme cases down to 0.243. The persistently warm pixels consistently exhibit the highest R^2 values across all three years (mean R^2 of 0.875 compared to 0.809 and 0.722), which coincides with the stronger influence of air temperature in this group.

4.4.2.2. Snow vs No Snow

Snow-free periods (Figure C.11, Figure C.12, Table C.7) are characterised by a strong dominance of air temperature, which typically accounts for approximately 39 - 53 % of the relative influence. The second most important driver is downwelling shortwave radiation, contributing 26 - 36 %. While shortwave radiation remains relatively stable over time, air temperature exhibits more pronounced variability. All other variables generally show low contributions, rarely exceeding 20 %. An exception occurs during a short anomalous phase in the 2022 analysis period, where relative humidity reaches a noticeable peak of approximately 20 %. This coincides with a substantial drop in the influence of air temperature (from about 60 % five days earlier to roughly 30 %). As this anomaly persists for approximately five days, it is likely related to the applied rolling window. There are no clear differences between the three groups.
The R^2 values remain consistently high throughout snow-free periods, typically around 0.9, indicating strong model performance. The persistently cold pixels show the largest standard deviation of 0.047 compared to 0.027 and 0.023.
The snow-covered period (Figure C.12, Table C.7) exhibits a generally similar structure, but with greater variability across all variables. In contrast to snow-free conditions (where no clear differences between the groups are observed) a systematic pattern emerges under snow-covered conditions. Specifically, the influence of downwelling shortwave radiation increases from the persistently cold (19 - 24 %) to the persistently warm pixels (31 - 35 %). In the persistently cold pixels, downwelling shortwave radiation is clearly the second most important driver after air temperature. In the persistently warm pixels, however, it becomes nearly equal in importance to air temperature (in all three groups 26 - 49 % relative influence) over the course of the period. Toward the end of the period, a pronounced peak in downwelling longwave radiation is observed, which coincides with a strong reduction in the influence of air temperature to values below 10 %. Despite this, no corresponding effect on model performance is detected.

The R^2 values during snow-covered periods are generally slightly lower than in snow-free conditions, with R^2 means of around 0.86. Occasional short-term drops to around 0.7 occur, after which the model performance gradually recovers over several days. These fluctuations do not appear to be directly linked to specific peaks or declines in individual predictor variables.

4.4.2.3. Rain Periods vs Dry Periods

The general characteristics of snow-free and snow-covered conditions have already been described in the previous section. Under snow-free conditions, air temperature is the primary driver and downwelling shortwave radiation the second most important, while all other variables show comparatively low contributions. However, this pattern becomes less distinct during precipitation periods.
In snow-free periods with precipitation (Figure C.13, Table C.8), air temperature remains the dominant driver across all three groups, with relative influence values ranging between (33 - 53 %). In the persistently cold pixels, downwelling shortwave radiation consistently represents the second most important variable with a relative influence of 20 - 27 %. In contrast, within the intermediate and persistently warm pixels, the second most influential factor still downwelling shortwave radiation, but its alternating in importance with relative humidity, and occasionally downwelling longwave radiation. The remaining variables exhibit moderate variability but generally remain below 10 %. The R^2 values remain consistently high, above 0.852, with only minor fluctuations.
Under snow-covered conditions, the patterns differ depending on whether precipitation occurs. As previously described, during dry periods, air temperature is the dominant driver, while the influence of downwelling shortwave radiation increases systematically from the persistently cold to the persistently warm pixels, where it becomes nearly as important as air temperature.
During precipitation periods (Figure C.13, Table C.8), air temperature clearly dominates, with relative influence values between 41 % and 54 %. The second most important variables are downwelling shortwave radiation followed by relative humidity, both contributing at similar levels of approximately 20%. All other variables remain of minor importance, although downwelling longwave radiation occasionally exhibits higher contributions, reaching up to about 11 %.
In contrast to snow-free conditions, the model performance during snow-covered precipitation periods is lower, with R^2 values ranging between 0.619 and 0.953 across all three groups.

4.4.2.4. Day vs Night

During daytime under snow-free conditions (Figure C.15, Table C.9), the typical pattern is observed. Air temperature represents the dominant driver across all three groups, generally accounting for 39 - 57 % of the relative influence. Downwelling shortwave radiation consistently acts as the second most important driver, with a slightly stronger influence in the persistently warm (26 - 34 %) compared to the persistently cold pixels (17 - 25 %). All other variables show negligible contributions. The R^2 values remain consistently high, with means around 0.9 across all three groups.
At night (Figure C.15, Table C.9), air temperature remains the dominant driver; however, its influence shows larger variability, with minimum and maximum values of relative influence ranging between approximately 20 % and 75 %. As secondary drivers, both downwelling longwave and shortwave radiation can be identified. During the first ~20 days, downwelling longwave radiation dominates as the second driver, while in the subsequent period, downwelling shortwave radiation becomes more influential. Despite these shifts, the R^2 values remain relatively stable, between 0.713 and 0.954.
During daytime under snow-covered conditions (Figure C.16, Table C.10), all variables exhibit relatively stable behaviour. Air temperature again emerges as the primary driver, with an influence between 31 % and 42 %. Downwelling shortwave radiation is the second most important variable, in-

creasing systematically from 18 - 21 % in the persistently cold, to 24 - 27 % in the intermediate, and up to 31 - 35 % in the persistently warm pixels. Relative humidity represents a consistent third driver, with contributions of around 13 - 23 %. The R^2 values remain stable and above 0.748.
At night (Figure C.16, Table C.10), the pattern becomes more variable. During the first six days and the last four days of the analysed period, downwelling longwave radiation represents the dominant driver (19 - 40 % in the whole period). In the intermediate period (approximately six days), air temperature becomes the primary influencing factor (15 - 42 % in the whole period). The remaining variables show no consistent ranking and exhibit irregular behaviour, although downwelling shortwave radiation generally remains low (3 - 8 %).
The R^2 values reflect this variability. During periods dominated by downwelling longwave radiation, R^2 values drop significantly, reaching values as low as 0.286. In contrast, when air temperature is the dominant driver, model performance improves markedly, with R^2 values increasing to 0.928. This highlights the strong dependence of model performance on the influence of air temperature.

4.5. Generalised Additive Models

4.5.1. Criteria for application

For days within the individual analysis periods in which the multiple linear regression model yielded particularly R^2 values below 0.6 or mean residuals larger than 2 °C, it can be assumed that surface temperature variability cannot be adequately described by linear processes alone. To capture the underlying non-linear behaviour, the analysis was therefore extended to the generalised additive models (GAMs) described in section 3.5.2. Unlike the multiple linear regression, GAMs are capable of modelling non-linear relationships between predictors and the response variable, making them better suited for periods in which the linear assumption breaks down (Wood, 2006).

4.5.1.1. Diurnal Curve Clustering

As shown in Table 8, the majority of days requiring GAM-based analysis are concentrated in the transition periods and in the snow-covered nighttime subset. The transition periods produced the highest numbers of flagged days, both in terms of R^2 and residuals, reflecting the complex and non-linear energy balance dynamics that accompany changes in surface cover. Similarly, the snow-covered nighttime period exhibited notable model deficiencies, particularly during nighttime hours when longwave radiation takes the place as the first driver. In contrast, snow-free periods in general were consistently well captured by the multiple linear regression models, with no days flagged by the R^2 criterion and only isolated days exceeding the residual threshold. This suggests that under snow-free conditions, the relationship between atmospheric drivers and surface temperature at the Murtèl rock glacier is predominantly linear and well constrained by the selected predictor variables.

Table 8: Overview of analysis periods with days identified for GAM-based analysis of the diurnal curve clustering approach. Days are flagged when the multiple linear regression model yielded R^2 values below 0.6 or mean residuals exceeding 2 °C, indicating that surface temperature variability could not be adequately captured by linear processes. Day numbers correspond to the ordinal position within each relative period.

Period Titles	*Period Dates*	*Number of Days in Period*	*Days with $R^2 < 0.6$*	*Days with |residual| > 2 °C*
Transition: Snow-Covered to Snow-Free	14.06.21 – 25.07.21; 09.05.22 – 26.06.22; 15.05.23 – 02.07.23	42 49 49	7-9; 17-19; 26; 27; 31-35 14-19 18-23; 29; 30; 39-41	8; 9 20; 29 41-43
Transition: Snow-Free to Snow-Covered	13.09.21 – 14.11.21; 02.11.22 – 18.12.22	63 49	32-34; 37-39 7; 10; 13; 22-26	3 21
Cover Type: Snow-Free	05.08.21 – 23.08.21; 07.06.22 – 19.07.22	19 43	- -	- -
Cover Type: Snow-Covered	26.02.22 – 01.04.22	35	-	12
Precipitation: Snow-Free	23.07.22 – 08.08.22	17	-	6
Precipitation: Snow-Covered	29.01.22 – 23.02.22	26	-	18
Dry: Snow-Free	05.07.22 – 22.07.22	18	-	-
Dry: Snow-Covered	24.02.22 – 28.03.22	33	-	14
Day/Night: Snow-Free	07.06.22 – 19.07.22	43	Day: 1; 17; 18 Night: -	Day: 17 Night: -
Day/Night: Snow-Covered	26.02.22 – 14.03.22	17	Day: - Night: 4; 5; 11-15	Day: 12; 17 Night: 3; 6; 12

4.5.1.2.Anomaly Persistence Classification

Table 9 shows the distribution of days requiring GAM-based analysis for the anomaly persistence classification workflow. Similar to the diurnal curve clustering workflow, the days are concentrated in the transition periods and in the snow-covered nighttime subset.

Table 9: Overview of analysis periods with days identified for GAM-based analysis of the anomaly persistence classification approach. Days are flagged when the multiple linear regression model yielded R^2 values below 0.6 or mean residuals exceeding 2 °C, indicating that surface temperature variability could not be adequately captured by linear processes. Day numbers correspond to the ordinal position within each relative period.

Period Titles	*Period Dates*	*Number of Days in Period*	*Days with $R^2 < 0.6$*	*Days with |residual| > 2 °C*
Transition: Snow-Covered to Snow-Free	14.06.21 – 25.07.21; 09.05.22 – 26.06.22; 15.05.23 – 02.07.23	42 49 49	7-10; 12; 13; 15-20; 25-27 12-21 18-24; 27-32	8; 9; 22 20; 29 27; 28; 42; 43
Transition: Snow-Free to Snow-Covered	13.09.21 – 14.11.21; 02.11.22 – 18.12.22	63 49	31-34; 37-39 7; 10; 13; 22-26	3 13; 21
Cover Type: Snow-Free	05.08.21 – 23.08.21; 07.06.22 – 19.07.22	19 43	- -	- -
Cover Type: Snow-Covered	26.02.22 – 01.04.22	35	-	12
Precipitation: Snow-Free	23.07.22 – 08.08.22	17	-	6
Precipitation: Snow-Covered	29.01.22 – 23.02.22	26	-	18
Dry: Snow-Free	05.07.22 – 22.07.22	18	-	-
Dry: Snow-Covered	24.02.22 – 28.03.22	33	-	14
Day/Night: Snow-Free	07.06.22 – 19.07.22	43	-	-
Day/Night: Snow-Covered	26.02.22 – 14.03.22	17	Day: - Night: 3-5; 11-15	Day: 12; 17 Night: 3; 4; 6; 12

4.5.2. GAM Results

4.5.2.1. Diurnal Curve Clustering

To assess the extent to which surface temperature variability on flagged days could be attributed to non-linear rather than linearly unresolvable processes, GAMs were fitted to each identified day and the resulting R^2 values were compared against those of the multiple linear regression. The R^2 difference between GAM and multiple linear regression serves as the primary diagnostic: a large gain indicates genuine non-linearity captured by the flexible spline terms, while a minimal gain suggests that low predictability rather than non-linearity is responsible for the failure of the multiple linear regression.

4.5.2.1.1. Transition: Snow-Covered to Snow-Free

In the transition from snow-covered to snow-free conditions in the year 2021, the comparison revealed a consistent pattern across the majority of flagged days. In most cases, flagging was triggered by Cluster 1 failing the $R^2 < 0.6$ threshold in the multiple linear regression, yet the GAM showed virtually no improvement over the linear model for this cluster. On days 7 to 9 (Figure C.17), GAM R^2 values

of 0.618, 0.479 and 0.506 barely exceeded the corresponding multiple regression values of 0.593, 0.460 and 0.482. The PDPs confirmed this: effects for Cluster 1 remained close to zero with smooth, near-linear trajectories across all predictor variables. The same pattern held for days 17 to 19 (Figure C.18) (GAM: 0.698 / 0.676 / 0.778; MLR: 0.594 / 0.520 / 0.600) and days 26 and 27 (Figure C.19) (GAM: 0.538 / 0.671; MLR: 0.448 / 0.544). This systematic absence of GAM improvement indicates that the multiple linear regression failure for Cluster 1 during this period does not reflect non-linear behaviour but rather a generally low explanatory power of the predictor set. Days 31 to 35 (Figure C.19 - Figure C.21) (n = 118 - 151) were all flagged for too low R^2 values for Cluster 1. Days 31 to 33 showed no non-linear behaviour in the PDPs and the R^2 values showed only moderate improvements for Cluster 1 on day 31 (GAM 0.759 / MLR 0.574) and almost no gains for the other days (day 32: GAM 0.630 / MLR 0.556; day 33: GAM 0.574 / MLR 0.515). On day 34, a tendency towards non-linearity in Cluster 2 is visible, but the GAM R^2 values don't change much for both clusters (Cluster 1: GAM 0.466 / MLR 0.515; Cluster 2: GAM 0.771/ MLR 0.751). Day 35 showed clear non-linearity for Cluster 1 and linear behaviour for Cluster 2. In this case, the non-linearity can also be seen in the R^2 comparison, where a strong gain for Cluster 1 is visible and almost no change for Cluster 2 (Cluster 1: GAM 0.982 / MLR 0.550; Cluster 2: GAM 0.754/ MLR 0.749).

In the transition from snow-covered to snow-free conditions in the year 2022, days 14 to 19 (Figure C.22, Figure C.23) were flagged because of the low R^2 values of Cluster 1. During days 14 to 16, the GAM again showed only a small gain over the MLR (e.g. day 14: GAM 0.641 / MLR 0.539). On days 17 - 19, a remarkable change occurred: Cluster 1 improved substantially from MLR values of 0.523, 0.578 and 0.552 to GAM values of 0.982, 0.968 and 0.981 respectively. Cluster 2 also improved substantially over these three days (e.g. day 17: GAM 0.995/ MLR 0.827), confirming that non-linearity affected both clusters simultaneously. The PDPs for these days showed curved but well-constrained effects, particularly for air temperature and downwelling shortwave radiation. Day 20 (Figure C.24) was flagged because of slightly too high residuals for Cluster 2. While Cluster 1 did not gain much on this day (GAM 0.706 / MLR 0.619), Cluster 2 achieved a larger gain (GAM 0.991 / MLR 0.810). Day 29 (Figure C.24), which also had slightly too high residuals for both clusters, resulted in an improvement for Cluster 1 from 0.619 to 0.639 while Cluster 2 improved from 0.894 to 0.993.

The 2023 transition from snow-covered to snow-free conditions (Figure C.25 - Figure C.29) produced GAM R^2 values of 1.000 for both clusters across almost all flagged days, yet with sample sizes of only 36 – 79 and MLR R^2 values for Cluster 1 as low as 0.306 (Day 20, n = 55) and 0.330 (Day 22, n = 64), these results are interpreted as overfitting artefacts.

4.5.2.1.2. Transition: Snow-Free to Snow-Covered

In the transition from snow-free to snow-covered conditions in the year 2021, day 3 (Figure C.30) (n = 106), flagged for slightly elevated residuals for both clusters, showed moderate GAM gains for both clusters (Cluster 1: GAM 0.993 / MLR 0.851; Cluster 2: GAM 0.996 / MLR 0.892) with PDP effects remaining near zero across all predictors and wider accuracy bands than the R^2-flagged days. On days 32 to 34 (Figure C.30, Figure C.31), Cluster 2 failed the $R^2 < 0.6$ threshold in the regression (MLR R^2: 0.585 / 0.597 / 0.590), while Cluster 1 remained above it but with moderate values (0.685 / 0.685 / 0.662). The GAM improved both clusters moderately (e.g., Day 32, n = 105: Cluster 1 GAM 0.872 / MLR 0.685; Cluster 2 GAM 0.756 / MLR 0.585), with narrow PDP bands and non-linear structure concentrated in air temperature and downwelling longwave radiation. On days 37 to 39 (Figure C.31, Figure C.32), both clusters fell below or near the $R^2 < 0.6$ threshold and the GAM produced large improvements for both, reaching GAM $R^2 \geq 0.990$ across all three days. Given the sample sizes on

those days (n = 103, 88, 68), these results may reflect genuine non-linearity, though overfitting cannot be excluded and they should therefore be interpreted with the same caution as before.
For the 2022 transition, days 7, 10, and 13 (Figure C.33) (n = 63 - 83) showed large GAM improvements for both clusters, with both failing the $R^2 < 0.6$ threshold in the regression. However, given the oscillatory PDP structures, broad accuracy bands, and sample sizes of 63 - 83 producing gains exceeding +0.4, these results are at risk of overfitting and cannot be interpreted as reliable evidence of genuine non-linearity. Days 21 to 26 (Figure C.34, Figure C.35) (n = 58 - 71) produced GAM $R^2 \approx 1.000$ against regression values as low as 0.364 and are likewise treated as overfitting artefacts.

4.5.2.1.3. Snow-Covered, Snow-Free and Precipitation Subsets

For the snow-covered period (26.02.22 - 01.04.22) and dry snow-covered period (24.02.22 - 28.03.22), which identified the same day (09.03.22, n = 279 (Figure C.36)) because of slightly too high residuals, showed moderate GAM improvements (Cluster 1: GAM 0.889 / MLR 0.706; Cluster 2: GAM 0.941 / MLR 0.804). The large sample size lends confidence to these gains, and the non-linear air temperature structure in the PDPs is a reliable finding. The snow-covered, precipitation day 18 (Figure C.36) (n = 73) showed substantial gains for both clusters but is assumed to be an overfitting artifact. The snow-free precipitation day 6 (Figure C.36) (n = 106), which was flagged for slightly too high residuals, showed modest GAM improvement (Cluster 1: GAM 0.996 / MLR 0.879; Cluster 2: GAM 0.997 / MLR 0.899), confirming that the relationship on this day was already well captured by the linear model.

4.5.2.1.4. Day / Night Periods

In the snow-free day subset, days 1, 17, and 18 (Figure C.37) showed different results for the two clusters. Cluster 1 increased by more than +0.4 in all three cases (day 1: GAM 0.998 / MLR 0.572, n = 86; day 17: GAM 0.976 / MLR 0.519, n = 89; day 18: GAM 0.997 / MLR 0.568, n = 80), while Cluster 2 showed more modest but consistent gains of roughly +0.1 to +0.12. Given the small sample sizes (n = 80 - 89) and the near-perfect GAM R^2 values for Cluster 1, these results carry a high overfitting risk and are treated accordingly. Day 17, which was additionally flagged for residuals, showed the largest PDP variability of the three days.
For the snow-covered day subset, day 17 (Figure C.38) (n = 152) showed moderate gains for both clusters (Cluster 1: GAM 0.916 / MLR 0.784; Cluster 2: GAM 0.929 / MLR 0.804), with near-linear PDP behaviour and narrow accuracy bands. Day 1 (Figure C.38) (n = 76) reached GAM $R^2 = 1.000$ for both clusters from regression values of 0.854 and 0.841; while the gain is real, the perfect GAM score at n = 76 warrants caution and the non-linear tendency in the PDPs may partly reflect overfitting.
The snow-covered night subset provided the most statistically robust GAM results in the entire analysis, combining large sample sizes (n = 72 - 205) with large and consistent improvements. Days 3 to 6 (Figure C.39, Figure C.40) showed gains of 0.28-0.36 per cluster (e.g., Day 4: Cluster 1 GAM 0.960 / MLR 0.581; Cluster 2 GAM 0.950 / MLR 0.451, n = 149). Days 11 to 15 (Figure C.40, Figure C.41) showed large absolute improvements: day 14 (n = 205) achieved gains of +0.529 and 0.545 for clusters 1 and 2 respectively (GAM 0.844 / 0.847; MLR 0.315 / 0.302), yet with final GAM R^2 values remaining below 0.85, indicating that substantial unexplained variance persisted even after accounting for non-linearity. This distinguishes these days clearly from the overfitting cases and confirms that the night snow-covered surface temperature regime contains genuine non-linear complexity only partially resolved by the predictor set. Days flagged for residuals (Days 6 and 12) showed the most pronounced non-linear PDP structures within this subset.

4.5.2.2. Anomaly Persistence Classification

4.5.2.2.1. Transition: Snow-Covered to Snow-Free

In the transition from snow-covered to snow-free conditions in 2021, the comparison revealed a pattern closely paralleling the diurnal curve clustering approach. Flagging was triggered almost exclusively by the persistently cold group failing the $R^2 > 0.6$ threshold, while the intermediate group was additionally affected on days 7 to 10 (Figure C.42, Figure C.43). Despite this, the GAM showed virtually no improvement over the regression for the flagged groups. On days 7 to10 (n = 161 - 166), the persistently cold and intermediate group reached GAM R^2 values only marginally above their regression counterparts (e.g., Day 8: cold GAM 0.490 / MLR 0.472; intermediate GAM 0.414 / MLR 0.379), while the persistently warm group (flagged only for slightly elevated residuals on days 8 and 9) remained consistently well-explained by both models (e.g., Day 9: GAM 0.674 / MLR 0.642). The PDPs confirmed the absence of non-linearity: the persistently warm group showed clear and well-constrained effects across predictors, while the persistently cold and intermediate groups effects remained near zero with narrow accuracy bands throughout. The same pattern held across all remaining flagged days in this year. Days 12, 13 and days 15 to 20 (Figure C.43 – Figure C.45) (n = 154 - 167) were flagged exclusively because of the persistently cold group failing the R^2 threshold. GAM gains for this group showed small improvements (e.g., Day 17: cold GAM 0.593 / MLR 0.467; Day 20: cold group GAM 0.699 / MLR 0.586), with PDP effects close to zero and very narrow accuracy bands. Day 22 (Figure C.46), flagged for slightly elevated residuals of the persistently warm group, showed no non-linear behaviour and narrow accuracy bands across all groups (cold GAM 0.693 / MLR 0.645; warm GAM 0.871 / MLR 0.855). Days 25 to 27 (Figure C.46, Figure C.47) followed the same pattern as days 12 and 13, with the persistently cold group consistently showing near-zero PDP effects and minimal GAM improvement. As in the diurnal curve clustering approach, this systematic absence of GAM improvement indicates that the regression failure for the coldest pixels reflects genuinely low explanatory power of the predictor set rather than non-linear behaviour.

In the 2022 transition, days 12 to 21 (Figure C.48 - Figure C.51) were flagged due to the low R^2 of the persistently cold group, with days 12 to 16 additionally affected in the intermediate group. During days 12 to 16 (n = 130 - 150), the pattern matched that of the 2021 transition: near-zero PDP effects and minimal GAM gains for the persistently cold and intermediate groups (e.g., Day 14: cold GAM 0.577 / MLR 0.473; intermediate GAM 0.632 / MLR 0.532). On days 17 to 19, a change became apparent: a slight non-linearity was visible across all three groups in the PDPs, most clearly in air temperature, though the persistently cold and intermediate groups continued to show effects close to the zero line while the persistently warm group showed the largest effects. The GAM improvement was most pronounced for the persistently cold group (Day 17: GAM 0.975 / MLR 0.441; Day 18: GAM 0.958 / MLR 0.459; Day 19: GAM 0.970 / MLR 0.467) and intermediate group (Day 17: GAM 0.989 / MLR 0.617), while the persistently warm group already achieved high regression R^2 (Day 17: MLR 0.838). Day 20, flagged for slightly elevated residuals of the persistently warm group, showed no effects for the other two groups, while the persistently warm group exhibited similar non-linear behaviour to days 17 to 19 (GAM 0.992 / MLR 0.817). Day 21 showed no clear non-linear patterns and relatively narrow accuracy bands across all groups but a notable improvement in R^2 for the persistently cold group (GAM 0.757 / MLR 0.594). Day 29 (Figure C.51), flagged for elevated residuals of the persistently warm and intermediate group, showed the most pronounced non-linear patterns of the entire spring transition, particularly in wind direction (E - W). The GAM achieved large improve-

ments for the persistently cold (GAM 0.980 / MLR 0.632) and intermediate group (GAM 0.990 / MLR 0.865), while the persistently warm group was already well explained.
The 2023 transition from snow-covered to snow-free (Figure C.52 - Figure C.56) conditions produced GAM R^2 values at or near 1 for all three groups across all flagged days, with sample sizes of only 36 - 79. These results are interpreted as overfitting artefacts and are excluded from the analysis.

4.5.2.2.2. Transition: Snow-Free to Snow-Covered

In the 2021 transition from snow-free to snow-covered conditions, day 3 (Figure C.57) was flagged for slightly elevated residuals in all three groups and showed moderate GAM gains (cold GAM 0.993 / MLR 0.851; intermediate GAM 0.994 / MLR 0.875; warm GAM 0.997 / MLR 0.910) with a visible tendency towards non-linearity in the PDPs, most apparent in the higher ranges of downwelling longwave radiation. On days 31 to 34 (Figure C.57, Figure C.58), flagging was driven by the persistently warm group failing the R^2 threshold. The GAM improved all groups across these days (e.g., Day 32: cold GAM 0.874 / MLR 0.685; intermediate GAM 0.865 / MLR 0.668; warm GAM 0.750 / MLR 0.567), with the persistently warm group showing the clearest non-linear tendencies in the PDPs, particularly for air temperature. Days 37 and 38 (Figure C.58, Figure C.59) (n = 88 - 103) were flagged for all three groups simultaneously because of not reaching the R^2 threshold, and the GAM produced large improvements across all groups, with all three reaching GAM $R^2 \geq 0.989$. All groups showed very similar PDP curves with recognizable non-linear structures in relative humidity, downwelling longwave radiation, air temperature, and downwelling shortwave radiation. These days, however, warrants some caution given the gain of up to +0.485 for the persistently warm group on day 38 at this sample size (n = 88), which approaches the overfitting threshold applied elsewhere in this analysis. Day 39 (Figure C.59) (n = 68), flagged only for the persistently warm R^2 values, reached GAM R^2=0.999 for all groups and carries a high overfitting risk at this sample size, comparable to the excluded cases in the snow-covered to snow-free transition of the year 2023.
The entire 2022 transition from snow-free to snow-covered conditions (Figure C.60 - Figure C.62) is treated as overfitting, as all flagged days in this period have sample sizes of 58 - 83 and resulted in GAM R^2 values near 1.

4.5.2.2.3. Static and Precipitation Subsets

The snow-covered period and no-precipitation snow-covered period identified the same day (day 12 / day 14, n = 279 (Figure C.63)). Flagging was triggered by slightly elevated residuals of the persistently cold group. Moderate GAM gains were observed across all groups (cold GAM 0.894 / MLR 0.718; intermediate GAM 0.929 / MLR 0.760; warm GAM 0.930 / MLR 0.762). PDPs showed only limited non-linearity with narrow accuracy bands, confined primarily to air temperature below -12 °C, while the large sample size confirms the gains are reliable.
For the precipitation snow-free period, day 6 (Figure C.63) (n = 106) was flagged for elevated residuals across all groups. The GAM showed only modest gains, but the PDPs revealed larger non-linear patterns than in other non-transition periods, most clearly in relative humidity and in air temperature at values below 10 °C.
The precipitation snow-covered period day 18 (Figure C.63) (n = 73) is treated as an overfitting artifact. The GAM R^2 values were near 1 across all three groups and the day is therefore excluded from the analysis.

4.5.2.2.4. Day / Night Periods

In the snow-covered day subset, days 12 and 17 (Figure C.64) were flagged for slightly elevated residuals across all groups, except for the intermediate group on day 12. Day 12 showed GAM R^2 values near 1 and has a sample size of only 89, it was treated as overfitting and was excluded from the analysis. Day 17 (n = 152) showed small gains (cold GAM 0.916 / MLR 0.785; intermediate GAM 0.923 / MLR 0.793; warm GAM 0.930 / MLR 0.804) and predominantly linear PDP behaviour with narrow accuracy bands.

In the snow-covered night subset, days 3 to 5 (Figure C.65) were flagged for too low R^2 of the intermediate group and persistently warm group, with days 3 and 6 additionally flagged for elevated residuals of all groups. Days 3 to 5 (n = 149 - 151) showed substantial GAM improvements particularly for the persistently warm group (Day 4: GAM 0.953 / MLR 0.452; Day 5: GAM 0.955 / MLR 0.490), while the persistently cold pixels already achieved higher regression R^2 values. PDPs showed only slight tendencies towards non-linearity across these days, most visibly in relative humidity, with accuracy bands remaining moderate. Day 6 was (Figure C.66) removed from the analysis based on a low sample size (n = 72) and R^2 values of 0.984 or higher. Days 11 to 15 (Figure C.66, Figure C.67) (n = 144 - 205) were flagged for all three groups failing the R^2 threshold, with day 12 additionally carrying elevated residuals in all groups. Despite the large GAM improvements on these days (e.g., Day 14: cold GAM 0.853 / MLR 0.352; intermediate GAM 0.857 / MLR 0.322; warm GAM 0.854 / MLR 0.286, n = 205), all PDPs showed only slight tendencies towards non-linearity with narrow accuracy bands. The large sample sizes confirm these gains reflect genuine non-linear structure rather than overfitting. Notably, day 14 showed a markedly disproportionate influence of relative humidity and downwelling longwave radiation relative to all other predictors – an effect already present in the MLR, where these two variables ranked as the top two drivers on this day, but substantially amplified in the GAM.

5. Discussion

5.1. Temperature Correction

5.1.1. Temporal Dynamics and the Persistent Cold Bias

The raw data alone demonstrates that the thermal infrared camera is capable of accurately reproducing the temporal dynamics of surface temperature, even though a systematic shift in absolute temperature values remains even after application of the atmospheric correction.
A striking and consistent feature of the validation comparisons is the persistent cold bias of the corrected TIR temperatures relative to the longwave-radiation-derived temperatures at the meteorological station. Differences of 10 - 20 °C are observed across the study period, a magnitude that considerably exceeds the manufacturer stated accuracy of ±10 °C (MOBOTIX AG, 2018). A portion of this offset is attributable to the measurement geometry. The longwave-derived temperatures are computed from the upwelling longwave radiation integrated over the full upward hemisphere and assume that the surface behaves as a perfect blackbody.
The conversion of outgoing longwave radiation to a radiometric temperature using the Stefan-Boltzmann law implicitly assumes a broadband emissivity of unity. For a natural rock surface with an emissivity of approximately 0.92 (Mineo and Pappalardo, 2021), this assumption introduces a warm bias, as part of the detected upwelling radiation originates from reflected downwelling components rather than surface emission (Thakur et al., 2022). The direction of this artefact is consistent with what is observed: longwave-derived temperatures systematically exceed the corrected TIR values. The blackbody assumption introduces a positive bias whose magnitude depends on the actual surface emissivity (Thakur et al., 2022). The systematic direction of the offset is nonetheless physically expected and supports the interpretation that the longwave-derived temperatures overestimate the true surface temperature rather than indicating a failure of the atmospheric correction.
The radiometer comparisons at the ridge and furrow locations show a different pattern. The correction resulted in a lower R^2 value for both radiometers compared to the raw values (Table 3). This counterintuitive result suggests that the atmospheric correction introduces a temperature dependent structure into the retrieved values which does not align with the variability recorded at the radiometer locations. One plausible explanation is that the distance-based correction produces a systematic cold shift, while the radiometer signals captures the true local radiative temperature without this modification. The correction therefore changes the slope of the regression relationship in a way that worsens agreement with the radiometer, even though the underlying atmospheric physics motivates its application.

5.1.2. The Distance Dependency of the Correction

A key result of this study is the identification of a physically consistent distance dependency of the correction. The magnitude of the temperature correction increases with the distance from target to camera, confirming that atmospheric effects are relevant even at the relatively short distances present on the Murtèl rock glacier. This finding is consistent with radiative transfer theory, where atmospheric attenuation and path radiance increase with optical path length (Faye et al., 2016). The seasonal analysis further supports this interpretation, showing that the effect is more pronounced during winter, spring and autumn, while its weaker in summer.
The physical mechanism underlying this seasonal modulation can be explained in terms of two competing atmospheric quantities: the atmospheric transmissivity and the path radiance. Both quantities depend on the temperature and the humidity structure of the atmosphere between camera and

target. During summer, higher air temperatures increase saturation vapour pressure, and given the relative humidity values recorded at the meteorological station, this results in a higher absolute vapour content. Counterintuitively, this does not necessarily imply a stronger atmospheric effect on the correction. The transmissivity formula employed in this study (Equation 7, following Diehl et al., 2026) shows that the transmissivity is a function of the product of vapour density and distance; for the path lengths present at Murtèl (roughly 100 - 500 m), the resulting transmissivity remains relatively high across all seasons. The weaker distance dependency observed in summer can instead be attributed to a convergence of the path radiance toward the surface temperature: when the atmospheric temperature along the path is close to the surface temperature, the net contribution of path radiance to the received signal is small regardless of transmissivity, reducing the observable correction magnitude. This condition is most closely approached during summer, when near-surface lapse rate is shallow and the thermal contrast between surface and lower atmosphere is minimised.
In winter and spring, in contrast, the surface temperature of the snow-covered rock glacier is frequently well below -10 °C while the air column temperature, though cold, decreases more slowly with altitude than the surface does due to frequent temperature inversions. The thermal contrast between surface and atmospheric path radiance is therefore larger, and the net effect of the correction produces a more pronounced cold shift in the corrected temperatures. This is consistent with the sign and magnitude of the seasonal ΔT-distance relationship described in Section 4.1.1 and Appendix B.

5.1.3. Emissivity Sensitivity

The uncertainty related to emissivity and camera window transmissivity represents another important source of potential errors in the retrieved surface temperatures. While the R^2 metric shows only modest sensitivity to emissivity choice (variations of 0.01 to 0.03 across the tested range of 0.90 to 0.94 (Mineo and Pappalardo, 2021)), the regression line analysis reveals a more structurally significant pattern that deserves explicit attention.
A lower emissivity assumption effectively increases the magnitude of the reflected radiance term $\tau (1 - \varepsilon_{obj}) \varepsilon_{refl} \Phi_{refl}$ in Equation 9. For a fixed incoming background radiance, this leads to a larger subtraction from the total received signal during the derivation of the surface object radiance Φ_{obj} (Equation 10), thereby producing systematically cooler corrected temperatures. Conversely, a higher emissivity reduces the reflected component, shifting to slightly warmer retrieved. Because the magnitude of the reflected contribution is proportional to $(1 - \varepsilon_{obj})$, even a small change in emissivity from 0.92 to 0.90 corresponds to a 25 % increase in the reflected term (from 0.08 to 0.1), which has a disproportionate effect at lower surface temperatures where Φ_{obj} is smaller and the correction terms represent a larger fraction of the total signal.
This mechanism explains the temperature-dependent bias structure observed in the regression analyses: lower emissivity values produce greater deviations at cold temperatures while converging with higher emissivity values at warm temperatures. This is not a random error but a structured, physically predictable bias that affects the slope of the regression relationship rather than the overall goodness of fit. The practical implication for this study is that while R^2 is largely insensitive to emissivity within the tested range, the absolute temperature values and their dependence structure on validation data can shift by up to 1 - 2 °C systematically, with the effect concentrated in the winter and early spring period when surface temperatures are lowest.
An additional source of uncertainty that is not directly addressed by the sensitivity analysis originates from the spatial uniformity assumption. Because reliable pixel-wise discrimination between snow

and bare rock was not possible without co-registered RGB images, a single emissivity value was applied to all pixels within each image. During transition periods, however, the surface is characterised by a heterogeneous mixture of snow patches, partially snow-covered boulders and exposed debris. The effective image-wide emissivity during these periods is intermediate between the two end-member values, and the applied 11-day linear transition approximates the true spatial average. Nevertheless, pixels located on persistent snow patches during a snow-free period, or on exposed ridges during a snow-covered period, will be assigned an incorrect emissivity, introducing spatially structured errors that cannot be captured by the global sensitivity analysis. These errors are most significant precisely during the transition periods and this limitation should be kept in mind when interpreting the cluster behaviour and regression results during those periods.

5.1.4. Window Transmissivity

The sensitivity analysis of camera window transmissivity reveals a clear asymmetry between the lower end (0.86) and the range 0.90 - 0.96 (values suggested by Adams, personal communication), across which no measurable differences in either R^2 or regression line behaviour are detected. This result has two implications: First, it suggests that the correction is effectively insensitive to the precise value of IRT, if the camera window has a high transmissivity (above 0.9). This reduces the practical uncertainty associated with this parameter, and the use of a single representative value such as 0.90 can be considered sufficient for the purposes of this study.
Second, the divergence observed at 0.86 deserves interpretation: A lower window transmissivity implies that a larger fraction (1 – IRT) of the received signal is replaced by thermal emission from the window as its own temperature (Eq. 9). Since the window temperature is approximated here by the air temperature measured at the meteorological station, which is typically colder than camera housing during extended operation, a lower IRT amplifies the weighting of a cold window radiance term in the received signal. The retrieved object radiance must then account for this additional cold contribution, which effectively introduces a cold bias into the corrected temperatures. This represents the observed behaviour with a window transmissivity term of 0.86, where the deviations at lower validation temperatures increase. This interpretation reinforces the physical consistency of the radiative transfer framework used in this study and confirms that the systematic cold bias of the corrected temperatures relative to validation datasets at low temperatures is partly attributable to the window emission term when the transmissivity assumption is too low.

5.1.5. Aluminium Plate Validation

Since no independent measurements of reflected background temperature were available, the background temperature was assumed to equal the temperature derived from the downwelling longwave radiation measured at the meteorological station.
The apparent reflected temperature represents the effective radiometric temperature of all radiation incident on the surface from directions other than the camera viewing direction (Norman and Becker, 1995). For a surface in the open field with an unobstructed upper hemisphere, this is well approximated by the effective sky temperature, which in turn relates closely to the downwelling longwave irradiance measured at the meteorological station (Aubrecht et al., 2016). However, the Murtèl rock glacier is situated within a complex alpine terrain, surrounded by headwalls and lateral moraines. A fraction of the hemisphere above each surface pixel is therefore occupied by terrain rather than sky. The comparative analysis using the crinkled aluminium plate provides an important independent validation of the assumption that the downwelling longwave radiation is a good approximation of the reflected temperature. The strong agreement between corrected temperatures (using air tempera-

ture as a proxy for reflected apparent temperature) and aluminium-corrected temperatures indicates that the estimation of reflected apparent temperature using air temperature is reasonable and does not negatively impact the study. The mean difference of approximately 0.97 °C and the median around 0.82 °C (Table 6) represent a systematic warm offset of the aluminium-corrected temperatures relative to the standard correction.
The absence of a clear systematic distance dependency in the temperature differences between the two correction approaches (Figure 18) confirms that the reflected background term, does not produce a distance-structured bias.

5.1.6. Further limitations

Several additional limitations of the correction framework deserve explicit acknowledgement. First, the atmospheric transmissivity model is based on LOWTRAN-derived empirical constants that weren't specifically developed for this study site (Diehl et al., 2026). At the elevation of Murtèl (~2600 m a.s.l.), the near-surface aerosol loading and vapour column are substantially lower than in lowland environments (Correa et al., 2024). This could lead to an overestimation of the atmospheric attenuation at the study site, contributing to the systematic cold shift observed in the corrected temperatures.
Second, the correction workflow assumes a sky emissivity of 1. As noted in Section 3.3, this assumption is only valid in the absence of surrounding structures contributing to the incoming longwave field. At Murtèl, headwalls and lateral moraines occupy a substantial fraction of the sky hemisphere above parts of the rock glacier and emit longwave radiation at near-ambient rather than cold-sky temperatures. The effective background radiance is therefore warmer than the sky-only estimate used in the correction, meaning the reflected contribution is underestimated and the retrieved surface temperatures are slightly biased toward warmer values in terrain-exposed areas (Diehl et al., 2026).
Finally, the internal processing applied by the MOBOTIX camera prior to outputting temperature values remains unknown. It is unclear whether any onboard corrections are already embedded in the output signal, which prevents a complete reconstruction of the measurement chain from raw sensor radiance to corrected surface temperature and constitutes an irreducible source of uncertainty that cannot be addressed by the workflow applied here.

5.2. Grouping Analysis

The grouping analyses followed two complementary objectives. The k-means clustering algorithm of mean diurnal temperature curves identifies pixels whose temporal evolution is internally consistent over the analysis intervals, while the anomaly persistence classification approach instead ranks pixels by how persistently they appear warmer or colder than the image-wide mean at the time of acquisition. The two methods therefore answer different questions: diurnal curve clustering asks which pixels behave the same way over time, whereas the anomaly persistence classification asks which pixels are persistently anomalous in space. The fact that the two approaches recover broadly similar spatial structures (warm signatures along ridges and exposed boulders, cold signatures within furrows and in the rock glacier background) provides a first internal consistency check on the analysis.

5.2.1. The Spatial Organisation of the Surface Temperature Field

The silhouette analysis returned an optimal cluster number of n = 2 across the vast majority of analysis periods, with fewer than 15 % of cases pointing to n = 3 or higher. Although a fixed two-cluster solution was subsequently adopted for comparability, this is itself a substantive finding: Under the

diurnal-curve representation used here, the surface temperature field at Murtèl is dominantly bimodal rather than continuously distributed. This is consistent with the strongly bimodal microtopography of the Murtèl rock glacier, where ridges with steep to near-vertical flanks alternate with furrows that are 3 - 5 m deep and host markedly different snow-accumulation regimes (Amschwand et al., 2024).

Two superimposed spatial contrasts dominate the cluster maps. The first is a ridge-furrow contrast within the rock glacier, in which the warmer cluster aligns with ridges, larger boulders and exposed glacier surfaces and the colder cluster aligns with furrow structures. This contrast is consistently reported under snow-covered conditions and under snow-covered daytime conditions, where the warmer cluster is concentrated along ridge structures and adjacent areas and the colder cluster in furrows and the surrounding background (Sections 4.3.1.2, 4.3.1.4). The second contrast is between the rock glacier itself and the background of the scene, with the colder cluster systematically occupying the background under snow-free and dry conditions (Sections 4.3.1.2, 4.3.1.3, 4.3.1.4).

Three mechanisms plausibly contribute to the ridge-furrow contrast. First, ridges are exposed and lose snow earlier than furrows because the topographically shaded cirque hosts persistent katabatic winds that redistribute snow from windswept ridges into furrows (Amschwand et al., 2024). Second, ridges and steep slopes intercept shortwave radiation more directly than furrows, which are partially self-shaded by their own sidewalls. Third, the largest boulders retain a distinct thermal signature throughout the year and are repeatedly identified as the first locations to develop a warm signal during transitions (Sections 4.3.1.1, 4.3.2.1).

The dominant contrasts are not, however, present in every period. Three regimes systematically depart from the typical configuration. In the initial phase of the snow-covered to snow-free transition, nearly the entire scene (except for the largest boulders and rock outcrops) is dominated by pixels of the colder cluster (Section 4.3.1.1). Under snow-covered conditions with precipitation, the warmer cluster is largely confined to larger boulders, rock outcrops and small sections of ridges, with most of the study area dominated by the colder cluster (Section 4.3.1.3). On snow-covered nights, the warmer cluster is again mainly confined to larger boulders while the colder cluster dominates everywhere else (Section 4.3.1.4). These departures share a common feature: The surface is radiatively homogenised, either by complete snow cover, wet snow at or near melting, or the absence of shortwave forcing. The fact that the dominant contrasts break down together in precisely these conditions motivates the interpretation developed in the next section.

5.2.2. Diurnal Control and the Role of Shortwave Radiation

The day vs night analysis periods reveal a reproducible asymmetry in both temporal and spatial behaviour. Temporally, the clustering analysis shows greater variability during the day than at night under both snow-free and snow-covered conditions, while the nighttime offset between the two clusters remains relatively stable (Section 4.3.1.4). Spatially, the response differs sharply between snow conditions. Snow-free conditions show no big changes in the spatial grouping between day and night, with the warmer cluster on the rock glacier and the colder cluster on the background in both regimes. Under snow-covered conditions, however, the daytime configuration of warm pixels along ridge structures gives way at night to a configuration in which warm pixels are mainly confined to larger boulders and the colder cluster dominates the rest of the scene (Section 4.3.1.4). The anomaly persistence classification approach refines the picture under snow-free conditions: the daytime pattern is sharply structured, with warm areas along ridges and at a steep section in the background, whereas at night warm areas cover most of the rock glacier surface and are no longer restricted to

the ridges, and cold areas are primarily confined to the background (Section 4.3.2.4). Under snow-covered conditions, the anomaly persistence classification likewise reorganises between day and night, with daytime warm areas along the ridges in the lower rock glacier giving way at night to scattered warm patches likely corresponding to larger boulders or areas of reduced snow cover (Section 4.3.2.4).

Two key insights emerge from this comparison. First, what changes most strikingly between day and night is the spatial structure of the underlying field and not the temperature curve. Second, under snow-free conditions, the contrast that disappears at night is the within-rock-glacier ridge-furrow signal, not the rock glacier-background contrast, which persists and indeed sharpens.

This pattern is most consistent with shortwave radiation acting as the principal spatial differentiator within the rock-glacier surface. Air temperature, measured at a single point on top of the rock glacier, applies to first order to all pixels because of the well-mixed near-surface boundary layer (Amschwand et al., 2024; Stull, 2015), as developed in Section 5.3.2. Downwelling longwave radiation has a similarly homogeneous spatial structure at this scale because it is integrated over a large fraction of the sky hemisphere (Yan et al., 2020). Shortwave radiation, by contrast, is modulated locally by slope, aspect and topographic shading (Xian et al., 2024). When direct shortwave forcing is absent (at night, or under fully snow-covered or wet snow conditions where the high-albedo and high-emissivity surface erases most of the shortwave contrast) the within-rock-glacier spatial structure collapses, exactly as observed. The persistence of the rock glacier-to-background contrast at night, however, indicates that this larger-scale signal is not primarily driven by shortwave forcing. A plausible explanation is a difference in effective surface thermal inertia between the coarse-blocky rock glacier and the surrounding finer-grained terrain: the large thermal inertia of the blocky rock mass at Murtèl slows nocturnal cooling and sustains a warmer surface signature into the night (Amschwand et al., 2024).

5.2.3. Transition Periods, Snow Cover and Precipitation

The transition periods provide the most consistent and physically interpretable patterns in the grouping analysis. Transitions from snow-covered to snow-free conditions show highly consistent behaviour across all three analysed years, with a reproducible spatial sequence: at the beginning of the transition, the colder cluster dominates the entire scene except for the largest boulders and rock outcrops, then warmer pixels emerge along ridge structures and expand across the glacier surface on a day-to-day basis, and by the end of the transition the colder cluster is confined to remaining snow patches primarily outside the block glacier (Section 4.3.1.1). The anomaly persistence classification approach reproduces this sequence from a different angle: Persistently warm areas first appear at larger boulders, ridge crests and steep background slopes, and persistently cold areas migrate from the rock glacier into the background as the period progresses (Section 4.3.2.1).

This spatial progression is most plausibly a direct imprint of the snowmelt sequence. Ridges lose their snow cover first because of preferential wind erosion, thinner accumulation and more direct solar exposure (Amschwand et al., 2024). Once exposed, the underlying boulders are heated by direct shortwave radiation and warm rapidly. The TIR camera therefore observes the snow ablation pattern indirectly through its thermal signature, and the temporal sequence of cluster assignment effectively traces the spatial advance of the bare-ground fraction across the rock glacier surface.

The reverse transition from snow-free to snow-covered conditions produces a markedly weaker contrast. Spatially, in 2022 warmer pixels, which resulted from the clustering algorithm, disperse more uniformly across the glacier surface, forming an almost regular spatial pattern, and the anomaly per-

sistence classification approach shows warm areas migrating to lower elevation and cold areas to higher elevation as snowfall accumulates (Sections 4.3.1.1, 4.3.2.1). The asymmetry between the two transition periods is consistent with snowfall rapidly producing a spatially more homogeneous surface than snowmelt, during which snow persists in furrows for several days longer than on the ridges, at least for this study site.

The contrast between the two clusters in the transition periods primarily reflects a contrast between two different radiating surfaces (snow versus rock) rather than two thermal states of the same material. This distinction is essential for the physical interpretation of the corresponding regression results in Section 5.3.

The precipitation analysis is informative precisely because the contrast between dry and wet conditions depends strongly on whether snow is present. Under snow-free conditions, the dry vs wet comparison produces only minor differences in either grouping method. Spatially, the warmer cluster is covering nearly the entire rock glacier and the colder cluster is confined to furrows and the background. This pattern is present regardless of whether precipitation occurs (Sections 4.3.1.3, 4.3.2.3). This is consistent with the dry, highly permeable coarse-blocky surface of the rock glacier, in which rain rapidly infiltrates and the surface returns quickly to dry conditions after a wetting event (Amschwand et al., 2024).

Under snow-covered conditions, by contrast, the dry vs wet comparison produces a pronounced reorganisation along both axes. Dry snow-covered periods reproduce the typical ridge-aligned pattern (the warmer cluster covering a large portion of the rock glacier and the colder cluster occupying furrows, background and higher-elevation areas), while precipitation snow-covered periods confine the warmer cluster to larger boulders, rock outcrops and small sections of ridges, with the majority of the scene dominated by the colder cluster (Section 4.3.1.3). The anomaly persistence classification records the same contrast at finer resolution: dry snow-covered patterns remain organised and ridge-aligned, whereas precipitation snow-covered patterns become more fragmented, with warm areas being discontinuous and not clearly associated with the ridges and cold areas forming more continuous zones (Section 4.3.2.3). This is consistent with precipitation reorganising the radiating surface under snow cover: fresh snowfall buries the ridge-furrow micro-topography and partially covers exposed boulders, while the overcast, snowing atmosphere reduces direct shortwave forcing and the surface temperature range (Filhol and Sturm, 2019; Mandal et al., 2022). Only bare rock protruding through the fresh snow remains warm enough to populate the warmer cluster.

5.2.4. Limitations

Two limitations of the grouping analysis deserve explicit mention. First, the imposed fixed cluster number n = 2 was selected for comparability across periods but does not capture cases in which the surface organises into three or more thermally distinct regimes, as occasionally indicated by the silhouette analysis (Section 4.3.1). The anomaly persistence classification, which uses a three-class partition by construction, partially compensates for this limitation but inherits a different one: the 25th and 75th percentile thresholds are fixed and do not adapt to the underlying distribution. Second, the spatial pattern of the clusters cannot be interpreted as a surface classification in the conventional sense. The clustering operates on diurnal temperature behaviour and is therefore sensitive to combinations of surface type, exposure, snow state and topographic shading (Robledano et al., 2022), and a pixel may shift between clusters over the course of a transition period not because its physical surface has changed but because its relative thermal behaviour within the image has shifted. The clusters should accordingly be read as exploratory descriptors of dominant thermal pat-

terns, in line with the framing introduced in Section 3.4.1, rather than as fixed thermal classes of the rock glacier surface.

5.3. Dependency Analysis

To investigate how meteorological forcing translates into surface-temperature variability across the Murtèl rock glacier, multiple linear regression models were fitted between the camera-measured LST values and seven atmospheric predictors at the meteorological station on top of the rock glacier: Air temperature, relative humidity, downwelling shortwave radiation, downwelling longwave radiation, wind speed, and the north-south and east-west components of wind direction. These models were fitted in each period for daily resolutions with a moving-window of 5 days before each day. Two complementary grouping schemes were used to avoid biasing the analysis towards single classification of the surface: a k-means clustering of daily LST time series and a z-normalised ranking per acquisition that aggregates pixels into a persistently cold, intermediate and persistently warm group. For each combination of period, scheme and group, the multiple linear regression models were performed as described and the resulting regression coefficients were normalised such that the sum of their absolute values equals 100 % per day. This relative-influence formulation makes coefficients directly comparable between predictors of different physical units and across days with different absolute energy levels.

The following discussion focuses on three findings that emerged consistently across both grouping methods: (i) the near-universal dominance of air temperature as the first-order predictor of LST; (ii) a systematic substitution between air temperature and downwelling shortwave radiation, in which the relative influence of one increases as the other decreases; and (iii) a marked drop in model performance during snow-covered nights, when downwelling longwave radiation becomes the dominant driver. The implications of these findings for the interpretation of rock glacier surface-energy regimes and the limitations of the present approach are discussed in turn.

5.3.1. Air temperature as the dominant driver

Across nearly every period, both grouping methods identify air temperature as the variable with the largest relative influence on LST on the majority of days. This consistency suggests that surface temperature on the Murtèl rock glacier is, in a first-order sense, tightly coupled to the air temperature – a result with both physical and statistical roots.

Physically, the dominance of air temperature reflects the strong coupling between the atmospheric boundary layer and the rock-glacier surface through turbulent heat exchange (Amschwand et al., 2024). Hoelzle et al. (2022) report that the ground heat flux at Murtèl is reproduced from atmospheric variables with an R^2 of 0.69, with air temperature being among the leading explanatory variables. Amschwand et al. (2024) further demonstrate that the heated coarse-blocky debris surface generates a near-surface atmosphere in which approximately 90% of the net radiation is dissipated through turbulent heat fluxes during the snow-free season. This near-complete partitioning of net radiation into sensible and latent heat exchange creates a tight thermal link between the debris surface and overlying air, so that variations in air temperature are rapidly propagated to the surface.

Statistically, air temperature additionally functions as an integrative proxy for several other forcings that are not independent of it. Ohmura (2001) demonstrated that air temperature measured outside a glacier carries information about longwave irradiance, the sensible heat flux and shortwave radiation, because these quantities are mutually correlated through atmospheric processes. In particular, under clear-sky conditions a substantial fraction of downwelling longwave irradiance originates from the lowest atmospheric layer, whose temperature is closely linked to screen-level air temperature

(Sicart et al., 2008). The observed dominance of air temperature therefore reflects two complementary effects: (i) a direct turbulent coupling between air and surface and (ii) an indirect statistical absorption of variance from radiative terms that co-vary with air temperature.

5.3.2. Model performance

The relative influences and the coefficients of determination R^2 of the daily multiple linear regression models are not independent. Across all periods, R^2 is systematically higher for groups in which air temperature is the first driver and lower for groups in which another predictor takes the lead.
Air temperature represents a spatially relatively homogeneous forcing: the value recorded at the meteorological station is, to first order, applicable to all pixels because the rock-glacier surface is embedded within a turbulent atmospheric boundary layer in which potential temperature is largely homogenised by vertical mixing (Stull, 2015). When the surface response is governed by such homogeneous forcing, a single station-based predictor can explain a large share of the pixel wise variance and the R^2 is correspondingly high. When, in contrast, the surface response is governed by a forcing whose spatial structure is not captured by any of the available station predictors (for example shortwave radiation, which is modulated by local slope, aspect and shading) the model loses explanatory power. The R^2 drop is therefore not a statement about the quality of the meteorological data, but about the spatial mismatch between a point-measured predictor and a strongly heterogeneous surface response
The effect is amplified by the form of the multiple linear regression itself. It assigns variance to the predictor that best fits the cross-pixel pattern on a given day and competing predictors with different spatial structures cannot be reconciled by a linear combination if the LST field contains components that none of them can reproduce. The decrease of R^2 in shortwave-dominated groups is thus an expected consequence of attempting to reconstruct a topographically structured LST field from non-structured station inputs (Kilibarda et al., 2014; Zhang et al., 2023).
The present results carry two implications for interpretation. First, the high R^2 values observed during air temperature dominated periods should not be taken as evidence that the rock glacier surface is thermally homogeneously, but rather that the dominant driver during those periods acts homogeneous across the surface. The strong cluster contrasts visible in the relative influence boxplots make clear that the surface response is in fact spatially structured; what changes between regimes is whether that structure aligns with a predictor available at the meteorological station. Second, the lower R^2 values observed in shortwave- and longwave-dominated groups identify precisely those situations in which finer-scale, spatially distributed forcing data would be required to substantially improve the model.

5.3.3. The inverse relationship between air temperature and shortwave influence

A particularly informative pattern emerges when the relative influences of air temperature and downwelling shortwave radiation are compared across periods and groups: The two predictors behave as competing rather than additive drivers: When one increases, the other decreases by a similar magnitude. The pattern is visible in most periods and groups but is most evident in the snow-covered analysis period. There is no difference between the two grouping methods.
This inverse relationship can be interpreted in light of the integrative proxy character of air temperature established in Section 5.3.1. As long as turbulent coupling and overcast or moderately variable sky conditions prevail, much of the spatial LST variance can be explained by air temperature alone, because the shortwave signal is either spatially homogenised by clouds or absorbed indirectly into the air temperature variance (Ohmura, 2001; Sicart et al., 2008). When, however, the spatial hetero-

geneity of shortwave forcing exceeds what the well-mixed near-surface air can buffer, air temperature loses statistical primacy. Shortwave radiation then takes over as the dominant predictor, not because its physical role has changed, but because the LST field has acquired a spatial structure that air temperature, recorded at a single point, cannot solve (Wang et al., 2018; Wang et al., 2025).

5.3.4. The role of longwave radiation during night

A striking contrast emerges between snow-free and snow-covered nights. During snow-free nights, air temperature retains its first-driver position, and the model continues to perform well (R^2 mean of ~0.87-0.89 for all clusters). During snow-covered nights, the picture is more variable: aggregated over the period, downwelling longwave radiation is the most frequent first driver in 59 % of analysis days in all clusters, with air temperature relegated to second rank (29 %). Importantly, the daily time series reveals that this aggregate is the result of a regime that alternates between longwave-dominated and air-temperature-dominated days rather than a stationary longwave-dominated state: on individual days within snow-covered periods, air temperature can still account for 50 - 65 % of the relative influence and R^2 remains correspondingly high (≈ 0.85 - 0.90), whereas on adjacent days longwave radiation takes over (35 - 50 %) and R^2 collapses to 0.30 - 0.50.

This alternation can be understood as a switching between two synoptic regimes. Under clear-sky conditions, downwelling longwave irradiance is dominated by emission from the lowest kilometre of the atmosphere, whose temperature is closely tied to screen-level air temperature (Ohmura, 2001). Air temperature and longwave radiation therefore co-vary strongly: Both contain essentially the same information about the surface forcing, and the multiple linear regression model can absorb most of the variance through whichever of the two predictors fits the cross-pixel pattern better on a given day. R^2 remains high, but the attribution between air temperature and longwave radiation is statistically unstable because the two predictors are nearly collinear. Under cloudy conditions, this coupling breaks down. Cloud emission becomes the dominant source of variability in downwelling longwave irradiance and depends on cloud-base height, cloud thickness and cloud temperature rather than on the screen-level air temperature beneath the cloud (Sicart et al., 2008). Air temperature loses its function as an integrative proxy, the multiple linear regression has to fall back on direct longwave irradiance as its leading predictor, and because no variable in the model captures cloud properties a substantial fraction of the longwave variability remains spatially unresolved. R^2 therefore drops.

The asymmetry between snow-free and snow-covered nights can be explained by the contrasting thermal properties of debris and snow. The coarse-blocky debris surface at Murtèl has a high heat capacity and acts as a thermal reservoir that absorbs and stores radiative energy during the day and a subsequent release via ground heat flux and turbulent exchange, including nocturnal ventilation of the blocky layer (Amschwand et al., 2024). Consequently, the nighttime surface temperature of debris reflects an integrated history of recent atmospheric forcing, of what air temperature is the most informative single descriptor. Its dominance therefore persists into the night. Snow, in contrast, has a low heat capacity and a low thermal conductivity (Arioli et al., 2024; Sledd et al., 2024), so the snow surface decouples thermally from the substrate beneath and responds almost instantaneously to the prevailing radiative balance. Because shortwave radiation is absent at night, and the sensible heat flux is suppressed by the smoother surface and the stably stratified boundary layer that typically develops above snow (Savijärvi, 2014; Vihma et al., 2009; Westermann et al., 2009), the snow surface temperature is governed almost entirely by the net longwave exchange. The multiple linear regression therefore reflects this regime: air temperature dominated when the longwave signal is itself slaved to air temperature (clear skies) and longwave dominated when it is not (cloudy skies).

The progressive decrease of R^2 from the coldest to the warmest quartile in the anomaly persistence classification snow-covered night analysis (0.71 → 0.69 → 0.65) is consistent with this interpretation. Warmer snow-covered pixels at night typically correspond to locations where net longwave loss is reduced by limited sky view and additional longwave emission from surrounding terrain, so that the surface loses less radiative energy and cools more slowly (Webster et al., 2017). Because the station-measured downwelling longwave irradiance does not include this terrain component, the warmer pixels are precisely those for which the predictor is most incomplete, and where the model accordingly performs worst.

5.3.5. Limitations

Some limitations of the present analysis must be noted. All atmospheric predictors are derived from a single meteorological station on top of the rock glacier and therefore do not resolve the spatial heterogeneity of the forcing across the rock glacier. As discussed above, this is the principal cause of R^2 drops observed during shortwave and longwave-dominated regimes. A natural extension would be to incorporate distributed shortwave radiation derived from a topographic radiation model based on a digital elevation model and distributed longwave forcing including a sky-view-factor correction (Helbig and Löwe, 2012; Yan et al., 2016). Cloud cover, currently absent from the predictor set, would similarly help to explain the residual variance during snow-covered nights.

6. Conclusion

This thesis exploited a long-term ground-based thermal infrared imaging dataset to characterise the spatial structure and atmospheric controls of surface temperature on the Murtèl rock glacier between 2021 and 2023. By combining a physically based atmospheric correction, two complementary grouping schemes and a regression-based dependency analysis, it has provided answers to these three research questions formulated in the introduction:

4. How accurately can ground-based thermal infrared imaging retrieve land surface temperatures in the complex terrain of a rock glacier compared to in-situ measurements?
5. Which thermally distinct zones can be identified on the Murtèl rock glacier and how does their spatial organisation change between snow-covered and snow-free conditions, transition periods and day-night cycles?
6. Which meteorological variables dominate the statistical relationship between atmospheric forcing and spatially distributed surface temperature, and how does their relative influence vary across different surface conditions and spatial groups on the rock glacier?

Regarding the first question, the raw camera signal already reproduces the seasonal and diurnal evolution of surface temperature reliably across all validation datasets. The applied atmospheric correction reveals a physically consistent distance dependency on the order of 1.5 °C across the field of view, with the strongest effect in winter, spring and autumn, and the weakest in summer. The corrected temperatures retain a persistent cold offset of approximately 10 - 20 °C relative to longwave-derived station temperatures, an offset that is largely explained by the broadband-emissivity assumption and by residual uncertainties in window transmissivity, object emissivity and sky emissivity. The aluminium-plate comparison shows that the use of temperature derived from longwave incoming radiation as a proxy for reflected apparent temperature does not introduce a structurally significant bias. While the correction does not uniformly improve agreement with all validation sources, the workflow provides a physically correct way to handle the raw data and shows that even in these relatively small scales of this study site, an atmospheric correction is needed to account for atmospheric effects.

Regarding the second research question, both grouping methods recover a dominantly bimodal surface temperature field. Within the rock glacier, a contrast between warmer ridges, exposed boulders and the glacier surface on the one hand and colder furrows on the other persists across most regimes; at a larger scale, the rock glacier itself contrasts thermally with its finer-grained background. This structure reorganises systematically with surface and atmospheric conditions. Transitions from snow-covered to snow-free conditions are dominated by the spatial sequence of snowmelt, with persistently warm signatures emerging first on ridges and large boulders and persistently cold signatures migrating into the background as the period progresses. Snow-covered precipitation periods homogenise the radiating surface and largely erase the ridge-furrow contrast, whereas snow-free precipitation has little spatial effect on the highly permeable blocky surface. The contrast between the rock glacier and its background persists at night and is interpreted as a thermal inertia signature of the coarse-blocky structure.

Regarding the third research question, air temperature is the dominant statistical driver of surface temperature in nearly all periods and across both grouping methods. Its dominance reflects both a direct turbulent coupling between the boundary layer and the debris surface and an indirect statistical absorption of radiative variance through the strong cross-correlation between air temperature, downwelling longwave radiation and the sensible heat flux. Downwelling shortwave radiation acts as

a competing secondary driver: when its spatial heterogeneity exceeds what the well-mixed near-surface air can buffer, its relative influence rises and that of air temperature decreases by an approximately compensating amount. On snow-covered nights this hierarchy breaks down. The low heat capacity and conductivity of snow decouple the surface from the substrate beneath and tie its temperature directly to the net longwave exchange, so that downwelling longwave radiation becomes the leading predictor and the multiple linear regression loses explanatory power because the cloud-related component of longwave variability is not resolved by any of the available station predictors. The GAM analysis confirms that this loss is, in most cases, not the signature of non-linear processes but of missing spatially distributed forcing.

These results demonstrate that long-term, ground-based TIR imaging is a viable, comparable cheap and information-rich tool for characterising the surface energy regime of rock glaciers, complementing the point-based borehole, GST and radiometer measurements that form the backbone of conventional permafrost monitoring. The methodological framework developed here combines a distance-aware atmospheric correction, complementary clustering and persistence-based grouping schemes, and a relative-influence MLR/GAM analysis. It is portable to other instrumented permafrost sites and to other TIR camera installations in alpine terrain.

Future work could extend these results in four directions. First, the residual uncertainties in the correction would benefit from direct measurements of camera-housing temperature, object emissivity and reflected background temperature, as well as from clear insights in how the camera handles the raw data internally. Second, the explanatory power of the dependency analysis during shortwave- and longwave-dominated regimes could be substantially improved by replacing point-based station inputs with spatially distributed forcing and by including cloud cover as an explicit predictor. Third, a co-registration of TIR with RGB imagery would allow a pixel-wise discrimination between snow and bare rock and thereby a spatially explicit emissivity assignment, which is particularly relevant during transition periods. Fourth, the spatially distributed surface temperatures produced by this workflow could be coupled more directly to surface energy balance studies of rock glaciers, complementing the point-based flux measurements that currently dominate such analyses with an areal constraint on the radiative and turbulent terms. Pursuing these extensions would consolidate ground-based TIR imaging as a routine component of long-term permafrost surface-energy monitoring.

Acknowledgements

This thesis would not have been possible without the support and guidance of several people whom I wish to thank.

First and foremost, I would like to express my gratitude to my supervisors from the Remote Sensing Laboratories at the University of Zürich, Kathrin Naegeli and Gabriele Bramati, for their continuous guidance, feedback and support throughout all the stages of this work.

Special thanks go to Jennifer Adams for her help with the temperature correction. Her support during the technical phase of this project was greatly appreciated.

I also wish to thank Dominik Amschwand from the Networked Embedded Sensing group of the University of Innsbruck, who generously provided most of the data used in this thesis and shared his deep knowledge of the Murtèl rock glacier site. His introduction and advice on how to handle the data were invaluable in the beginning phase of this thesis.

Also, I am thankful to the whole TIRLab group of the Department of Geography at the University of Zürich for their ideas and inputs.

Finally, I would like to thank my friends for their continued support and the many helpful discussions during this work and for taking the time to read the thesis and provide feedback.

Bibliography

Amschwand, D., Scherler, M., Hoelzle, M., Krummenacher, B., Haberkorn, A., Kienholz, C., Gubler, H., 2024. Surface heat fluxes at coarse blocky Murtèl rock glacier (Engadine, eastern Swiss Alps). The Cryosphere 18, 2103–2139. https://doi.org/10.5194/tc-18-2103-2024

Arioli, S., Picard, G., Arnaud, L., Gascoin, S., Alonso-González, E., Poizat, M., Irvine, M., 2024. Time series of alpine snow surface radiative-temperature maps from high-precision thermal-infrared imaging. Earth Syst. Sci. Data 16, 3913–3934. https://doi.org/10.5194/essd-16-3913-2024

Aubrecht, D.M., Helliker, B.R., Goulden, M.L., Roberts, D.A., Still, C.J., Richardson, A.D., 2016. Continuous, long-term, high-frequency thermal imaging of vegetation: Uncertainties and recommended best practices. Agric. For. Meteorol. 228–229, 315–326. https://doi.org/10.1016/j.agrformet.2016.07.017

Aubry-Wake, C., Baraer, M., McKenzie, J.M., Mark, B.G., Wigmore, O., Hellström, R.Å., Lautz, L., Somers, L., 2015. Measuring glacier surface temperatures with ground-based thermal infrared imaging. Geophys. Res. Lett. 42, 8489–8497. https://doi.org/10.1002/2015GL065321

Baker, S.G., Kramer, B.S., 2007. Peirce, Youden, and Receiver Operating Characteristic Curves. Am. Stat. 61, 343–346. https://doi.org/10.1198/000313007X247643

Barsch, D., 1996. Rockglaciers and the High Mountain Environment, in: Rockglaciers, Springer Series in Physical Environment. Springer Berlin Heidelberg, Berlin, Heidelberg, pp. 231–268. https://doi.org/10.1007/978-3-642-80093-1_11

Bernhard, L., Sutter, F., Haeberli, W., Keller, F., 1998. Processes of snow/permafrost-interactions at a high-mountain site, Murtèl/Corvatsch, eastern Swiss Alps, in: Proceedings of the 7th International Conference on Permafrost, Yellowknife, Canada. Centre d'Études Nordiques, Université Laval Saint-Foy (Québec), Canada, pp. 35–41.

Berthling, I., 2011. Beyond confusion: Rock glaciers as cryo-conditioned landforms. Geomorphology 131, 98–106. https://doi.org/10.1016/j.geomorph.2011.05.002

Bradski, G., 2000. The OpenCV Library. Dr. Dobb's Journal of Software Tools.

Chang, Z., Gao, H., Yong, L., Wang, K., Chen, R., Han, C., Demberel, O., Dorjsuren, B., Hou, S., Duan, Z., 2024. Projected future changes in the cryosphere and hydrology of a mountainous catchment in the upper Heihe River, China. Hydrol. Earth Syst. Sci. 28, 3897–3917. https://doi.org/10.5194/hess-28-3897-2024

Chapra, S.C., Canale, R.P., 2015. The Trapezoidal Rule, in: Numerical Methods for Engineers. McGraw-Hill Education, New York, pp. 603–613.

Correa, L.F., Folini, D., Chtirkova, B., Wild, M., 2024. Causes for Decadal Trends in Surface Solar Radiation in the Alpine Region in the 1981–2020 Period. J. Geophys. Res. Atmospheres 129, e2023JD039998. https://doi.org/10.1029/2023JD039998

Dawson-Haggerty, M., Bacher, J., Brown-Bivins, A., Forest, C., O'Kane, J., 2019. trimesh: Load and analyze triangular meshes (Version 4.12.2).

Diehl, J.L., Javadian, M., Fell, M., Aubrecht, D.M., Richardson, A.D., 2026. correcTIR: A python package and graphical user interface for processing near-surface thermal infrared data. Agric. For. Meteorol. 381, 111099. https://doi.org/10.1016/j.agrformet.2026.111099

Faye, E., Dangles, O., Pincebourde, S., 2016. Distance makes the difference in thermography for ecological studies. J. Therm. Biol. 56, 1–9. https://doi.org/10.1016/j.jtherbio.2015.11.011

Filhol, S., Sturm, M., 2019. The smoothing of landscapes during snowfall with no wind. J. Glaciol. 65, 173–187. https://doi.org/10.1017/jog.2018.104

Gärtner-Roer, I., Hoelzle, M., 2021. Rockglaciers of the Engadine, in: Reynard, E. (Ed.), Landscapes and Landforms of Switzerland, World Geomorphological Landscapes. Springer International Publishing, Cham, pp. 235–248. https://doi.org/10.1007/978-3-030-43203-4_16

Gök, D.T., Scherler, D., Anderson, L.S., 2023. High-resolution debris-cover mapping using UAV-derived thermal imagery: limits and opportunities. The Cryosphere 17, 1165–1184. https://doi.org/10.5194/tc-17-1165-2023

Gomez-Rubio, V., 2018. Generalized Additive Models: An Introduction with *R* (2nd Edition). J. Stat. Softw. 86. https://doi.org/10.18637/jss.v086.b01
Harris, C.R., Millman, K.J., Van Der Walt, S.J., Gommers, R., Virtanen, P., Cournapeau, D., Wieser, E., Taylor, J., Berg, S., Smith, N.J., Kern, R., Picus, M., Hoyer, S., Van Kerkwijk, M.H., Brett, M., Haldane, A., Del Río, J.F., Wiebe, M., Peterson, P., Gérard-Marchant, P., Sheppard, K., Reddy, T., Weckesser, W., Abbasi, H., Gohlke, C., Oliphant, T.E., 2020. Array programming with NumPy. Nature 585, 357–362. https://doi.org/10.1038/s41586-020-2649-2
Helbig, N., Löwe, H., 2012. Shortwave radiation parameterization scheme for subgrid topography. J. Geophys. Res. Atmospheres 117, 2011JD016465. https://doi.org/10.1029/2011JD016465
Hoelzle, M., Hauck, C., Mathys, T., Noetzli, J., Pellet, C., Scherler, M., 2022. Long-term energy balance measurements at three different mountain permafrost sites in the Swiss Alps. Earth Syst. Sci. Data 14, 1531–1547. https://doi.org/10.5194/essd-14-1531-2022
Hori, M., Aoki, T., Tanikawa, T., Hachikubo, A., Sugiura, K., Kuchiki, K., Niwano, M., 2013. Modeling angular-dependent spectral emissivity of snow and ice in the thermal infrared atmospheric window. Appl. Opt. 52, 7243. https://doi.org/10.1364/AO.52.007243
Hunter, J.D., 2007. Matplotlib: A 2D Graphics Environment. Comput. Sci. Eng. 9, 90–95. https://doi.org/10.1109/MCSE.2007.55
Hurmer, N., Gallinat, M., Khan, U., Reichegger, M., 2025. Image Processing Murt`el Rock Glacier.
Jain, A.K., 2010. Data clustering: 50 years beyond K-means. Pattern Recognit. Lett. 31, 651–666. https://doi.org/10.1016/j.patrec.2009.09.011
Janke, J.R., Bolch, T., 2022. Rock Glaciers, in: Treatise on Geomorphology. Elsevier, pp. 75–118. https://doi.org/10.1016/B978-0-12-818234-5.00187-5
Jones, D.B., Harrison, S., Anderson, K., Whalley, W.B., 2019. Rock glaciers and mountain hydrology: A review. Earth-Sci. Rev. 193, 66–90. https://doi.org/10.1016/j.earscirev.2019.04.001
Kavak, Ç., Özsaraç, S., 2015. Memory efficient atmospheric effects modeling for infrared scene generators, in: Holst, G.C., Krapels, K.A. (Eds.), . Presented at the SPIE Defense + Security, Baltimore, Maryland, United States, p. 945212. https://doi.org/10.1117/12.2176852
Keller, F., 1993. Interaction between snow cover and high mountain permafrost, in: Proceedings of 6th International Conference on Permafrost, Beijing, China. South China University Technology Press, pp. 332–337.
Kilibarda, M., Hengl, T., Heuvelink, G.B.M., Gräler, B., Pebesma, E., Perčec Tadić, M., Bajat, B., 2014. Spatio-temporal interpolation of daily temperatures for global land areas at 1 km resolution. J. Geophys. Res. Atmospheres 119, 2294–2313. https://doi.org/10.1002/2013JD020803
Klein, A., Wallkötter, S., Silvester, S., Rynes, W., actions-user, Müller, P., Nunez-Iglesias, J., Harfouche, M., Pandede, Schrangl, L., Dennis, Lee, A., McCormick, M., Ladegaard, A., Rai, A., OrganicIrradiation, Smith, T.D., van Kemenade, H., Vaillant, G., jackwalker64, Nises, J., Komarčević, M., rreilink, Singleton, J., Kolar, K., scivision, Górny, M., Rosenstein, N., Hsieh, P.-C., Tempelmann, T., 2026. imageio. https://doi.org/10.5281/ZENODO.1488561
Kraaijenbrink, P.D.A., Bierkens, M.F.P., Lutz, A.F., Immerzeel, W.W., 2017. Impact of a global temperature rise of 1.5 degrees Celsius on Asia's glaciers. Nature 549, 257–260. https://doi.org/10.1038/nature23878
Liu, G., Liu, P., Yang, M., Cai, C., Xu, W., Zhang, Q., Yang, W., 2013. The significance and relationships among substitutive climatic proxies in the Holocene at the middle Loess Plateau in China. Environ. Earth Sci. 70, 2997–3004. https://doi.org/10.1007/s12665-013-2357-4
Lute, A.C., Abatzoglou, J.T., Fountain, A.G., Bartholomaus, T.C., 2024. Projected loss of rock glacier habitat in the contiguous western United States with warming. J. Glaciol. 70, e27. https://doi.org/10.1017/jog.2024.56
Mandal, A., Angchuk, T., Azam, M.F., Ramanathan, A., Wagnon, P., Soheb, M., Singh, C., 2022. An 11-year record of wintertime snow-surface energy balance and sublimation at 4863 m a.s.l. on the Chhota Shigri Glacier moraine (western Himalaya, India). The Cryosphere 16, 3775–3799. https://doi.org/10.5194/tc-16-3775-2022

Messmer, J., Groos, A.R., 2024. A low-cost and open-source approach for supraglacial debris thickness mapping using UAV-based infrared thermography. The Cryosphere 18, 719–746. https://doi.org/10.5194/tc-18-719-2024
MeteoSchweiz, 2026. Bodenmessstation: Piz Corvatsch (COV).
Mineo, S., Pappalardo, G., 2021. Rock Emissivity Measurement for Infrared Thermography Engineering Geological Applications. Appl. Sci. 11, 3773. https://doi.org/10.3390/app11093773
MOBOTIX AG, 2018. MOBOTIX M16B Thermal / M16B Thermal TR - Technical Specifications.
Mortimer, C.A., Sharp, M., Wouters, B., 2016. Glacier surface temperatures in the Canadian High Arctic, 2000–15. J. Glaciol. 62, 963–975. https://doi.org/10.1017/jog.2016.80
Naegeli, K., Adams, J.S., Bramati, G., Gärtner-Roer, I., Gröbner, J., Rietze, N., 2026. Towards Best Practices in UAV Thermal Remote Sensing in Complex Environments. https://doi.org/10.5194/egusphere-2026-787
Norman, J.M., Becker, F., 1995. Terminology in thermal infrared remote sensing of natural surfaces. Agric. For. Meteorol. 77, 153–166. https://doi.org/10.1016/0168-1923(95)02259-Z
Ohmura, A., 2001. Physical Basis for the Temperature-Based Melt-Index Method. J. Appl. Meteorol. 40, 753–761. https://doi.org/10.1175/1520-0450(2001)040%3C0753:PBFTTB%3E2.0.CO;2
Pedregosa, F., Varoquaux, G., Gramfort, A., Michel, V., Thirion, B., Grisel, O., Blondel, M., Prettenhofer, P., Weiss, R., Dubourg, V., Vanderplas, J., Passos, A., Cournapeau, D., Brucher, M., Perrot, M., Duchesnay, E., 2011. Scikit-learn: Machine Learning in Python. J. Mach. Learn. Res. 2825–2830.
PERMOS, 2025. Swiss Permafrost Monitoring Network Database (PERMOS Database). https://doi.org/10.13093/PERMOS-2025-01
Ren, S., Yao, T., Yang, W., Miles, E.S., Zhao, H., Zhu, M., Li, S., 2024. Changes in glacier surface temperature across the Third Pole from 2000 to 2021. Remote Sens. Environ. 305, 114076. https://doi.org/10.1016/j.rse.2024.114076
Robledano, A., Picard, G., Arnaud, L., Larue, F., Ollivier, I., 2022. Modelling surface temperature and radiation budget of snow-covered complex terrain. The Cryosphere 16, 559–579. https://doi.org/10.5194/tc-16-559-2022
Savijärvi, H., 2014. High-resolution simulations of the night-time stable boundary layer over snow. Q. J. R. Meteorol. Soc. 140, 1121–1128. https://doi.org/10.1002/qj.2187
Scherler, M., Schneider, S., Hoelzle, M., Hauck, C., 2014. A two-sided approach to estimate heat transfer processes within the active layer of the Murtèl–Corvatsch rock glacier. Earth Surf. Dyn. 2, 141–154. https://doi.org/10.5194/esurf-2-141-2014
Schisterman, E.F., Perkins, N.J., Liu, A., Bondell, H., 2005. Optimal Cut-point and Its Corresponding Youden Index to Discriminate Individuals Using Pooled Blood Samples: Epidemiology 16, 73–81. https://doi.org/10.1097/01.ede.0000147512.81966.ba
Seabold, S., Perktold, J., 2010. statsmodels: Econometric and statistical modeling with python., Proceedings of the 9th Python in Science Conference.
Servén, D., Brummitt, C., 2018. pyGAM: Generalized Additive Models in Python. https://doi.org/10.5281/ZENODO.1208724
Shahapure, K.R., Nicholas, C., 2020. Cluster Quality Analysis Using Silhouette Score, in: 2020 IEEE 7th International Conference on Data Science and Advanced Analytics (DSAA). Presented at the 2020 IEEE 7th International Conference on Data Science and Advanced Analytics (DSAA), IEEE, sydney, Australia, pp. 747–748. https://doi.org/10.1109/DSAA49011.2020.00096
Sicart, J.E., Hock, R., Six, D., 2008. Glacier melt, air temperature, and energy balance in different climates: The Bolivian Tropics, the French Alps, and northern Sweden. J. Geophys. Res. Atmospheres 113, 2008JD010406. https://doi.org/10.1029/2008JD010406
Sledd, A., Shupe, M.D., Solomon, A., Cox, C.J., Perovich, D., Lei, R., 2024. Snow thermal conductivity and conductive flux in the Central Arctic: Estimates from observations and implications for models. Elem Sci Anth 12, 00086. https://doi.org/10.1525/elementa.2023.00086

Sorg, A., Kääb, A., Roesch, A., Bigler, C., Stoffel, M., 2015. Contrasting responses of Central Asian rock glaciers to global warming. Sci. Rep. 5, 8228. https://doi.org/10.1038/srep08228
Stull, R., 2015. Practical Meteorology: An Algebra-based Survey of Atmospheric Science. University of British Columbia.
Swiss Permafrost Monitoring Network, 2022. Swiss Permafrost Bulletin 2022. Swiss Permafrost Monitoring Network (PERMOS). https://doi.org/10.13093/PERMOS-BULL-2023
Swisstopo, 2024. swissALTI3D - The high-resolution terrain model of Switzerland. Federal Office of Topography swisstopo. https://www.swisstopo.admin.ch/en/height-model-swissalti3d.
Tattersall, G.J., 2023. Thermal Image Analysis. Thermimage.
Thakur, G., Schymanski, S.J., Mallick, K., Trebs, I., Sulis, M., 2022. Downwelling longwave radiation and sensible heat flux observations are critical for surface temperature and emissivity estimation from flux tower data. Sci. Rep. 12, 8592. https://doi.org/10.1038/s41598-022-12304-3
The pandas development team, 2026. pandas-dev/pandas: Pandas. https://doi.org/10.5281/ZENODO.3509134
Tranmer, M., Murphy, J., Pampaka, M., 2020. Multiple Linear Regression (2nd Edition), Cathie Marsh Institute Working Paper.
Vihma, T., Johansson, M.M., Launiainen, J., 2009. Radiative and turbulent surface heat fluxes over sea ice in the western Weddell Sea in early summer. J. Geophys. Res. Oceans 114, 2008JC004995. https://doi.org/10.1029/2008JC004995
Virtanen, P., Gommers, R., Oliphant, T.E., Haberland, M., Reddy, T., Cournapeau, D., Burovski, E., Peterson, P., Weckesser, W., Bright, J., Van Der Walt, S.J., Brett, M., Wilson, J., Millman, K.J., Mayorov, N., Nelson, A.R.J., Jones, E., Kern, R., Larson, E., Carey, C.J., Polat, İ., Feng, Y., Moore, E.W., VanderPlas, J., Laxalde, D., Perktold, J., Cimrman, R., Henriksen, I., Quintero, E.A., Harris, C.R., Archibald, A.M., Ribeiro, A.H., Pedregosa, F., Van Mulbregt, P., SciPy 1.0 Contributors, Vijaykumar, A., Bardelli, A.P., Rothberg, A., Hilboll, A., Kloeckner, A., Scopatz, A., Lee, A., Rokem, A., Woods, C.N., Fulton, C., Masson, C., Häggström, C., Fitzgerald, C., Nicholson, D.A., Hagen, D.R., Pasechnik, D.V., Olivetti, E., Martin, E., Wieser, E., Silva, F., Lenders, F., Wilhelm, F., Young, G., Price, G.A., Ingold, G.-L., Allen, G.E., Lee, G.R., Audren, H., Probst, I., Dietrich, J.P., Silterra, J., Webber, J.T., Slavič, J., Nothman, J., Buchner, J., Kulick, J., Schönberger, J.L., De Miranda Cardoso, J.V., Reimer, J., Harrington, J., Rodríguez, J.L.C., Nunez-Iglesias, J., Kuczynski, J., Tritz, K., Thoma, M., Newville, M., Kümmerer, M., Bolingbroke, M., Tartre, M., Pak, M., Smith, N.J., Nowaczyk, N., Shebanov, N., Pavlyk, O., Brodtkorb, P.A., Lee, P., McGibbon, R.T., Feldbauer, R., Lewis, S., Tygier, S., Sievert, S., Vigna, S., Peterson, S., More, S., Pudlik, T., Oshima, T., Pingel, T.J., Robitaille, T.P., Spura, T., Jones, T.R., Cera, T., Leslie, T., Zito, T., Krauss, T., Upadhyay, U., Halchenko, Y.O., Vázquez-Baeza, Y., 2020. SciPy 1.0: fundamental algorithms for scientific computing in Python. Nat. Methods 17, 261–272. https://doi.org/10.1038/s41592-019-0686-2
Vollmer, M., Möllmann, K., 2018. Detectors And Detector Systems, in: Infrared Thermal Imaging: Fundamentals, Research and Applications. Wiley, pp. 107–142. https://doi.org/10.1002/9783527693306
Vollmer, M., Möllmann, K., 2010. Infrared Thermal Imaging: Fundamentals, Research and Applications, 1st ed. Wiley. https://doi.org/10.1002/9783527630868
Wang, S., Cheng, J., Liu, Q., 2025. Study on the Effect of Shortwave Radiation in Land Surface Temperature Downscaling over Rugged Terrain. Remote Sens. 17, 2436. https://doi.org/10.3390/rs17142436
Wang, T., Yan, G., Mu, X., Jiao, Z., Chen, L., Chu, Q., 2018. Toward operational shortwave radiation modeling and retrieval over rugged terrain. Remote Sens. Environ. 205, 419–433. https://doi.org/10.1016/j.rse.2017.11.006
Webster, C., Rutter, N., Jonas, T., 2017. Improving representation of canopy temperatures for modeling subcanopy incoming longwave radiation to the snow surface. J. Geophys. Res. Atmospheres 122, 9154–9172. https://doi.org/10.1002/2017JD026581

Westermann, S., Lüers, J., Langer, M., Piel, K., Boike, J., 2009. The annual surface energy budget of a high-arctic permafrost site on Svalbard, Norway. The Cryosphere 3, 245–263. https://doi.org/10.5194/tc-3-245-2009

Whitaker, J., Snow, A.D., Cochran, M., Karney, C., Ouzounoudis, G., Dearing, J., De Kloe, J., Heitor, Filipe, May, R., Itkin, M., Eubank, N., Dunphy, M., Brett, M., Da Costa, M.A., De Maeyer, J., Gohlke, C., Willoughby, C., Barker, C., Wiedemann, B.M., Couwenberg, B., 2019. pyproj. https://doi.org/10.5281/ZENODO.2592233

Wood, S.N., 2006. Generalized Additive Models, 0 ed. Chapman and Hall/CRC. https://doi.org/10.1201/9781420010404

Xian, Y., Wang, T., Leng, W., Letu, H., Shi, J., Wang, G., Yan, X., Yuan, H., 2024. Can Topographic Effects on Solar Radiation Be Ignored: Evidence From the Tibetan Plateau. Geophys. Res. Lett. 51, e2024GL108653. https://doi.org/10.1029/2024GL108653

Yan, G., Jiao, Z.-H., Wang, T., Mu, X., 2020. Modeling surface longwave radiation over high-relief terrain. Remote Sens. Environ. 237, 111556. https://doi.org/10.1016/j.rse.2019.111556

Yan, G., Wang, T., Jiao, Z., Mu, X., Zhao, J., Chen, L., 2016. Topographic radiation modeling and spatial scaling of clear-sky land surface longwave radiation over rugged terrain. Remote Sens. Environ. 172, 15–27. https://doi.org/10.1016/j.rse.2015.10.026

Yin, Z., Hadzimustafic, J., Kann, A., Wang, Y., 2019. On statistical nowcasting of road surface temperature. Meteorol. Appl. 26, 1–13. https://doi.org/10.1002/met.1729

Zhang, Z., Liang, Y., Zhang, G., Liang, C., 2023. Large-Scale Estimation of Hourly Surface Air Temperature Based on Observations from the FY-4A Geostationary Satellite. Remote Sens. 15, 1753. https://doi.org/10.3390/rs15071753

Appendix

Appendix A: Preprocessing and GitHub repository

GitHub repository: https://github.com/mhassl-UZH/Masters_Thesis_Murtel

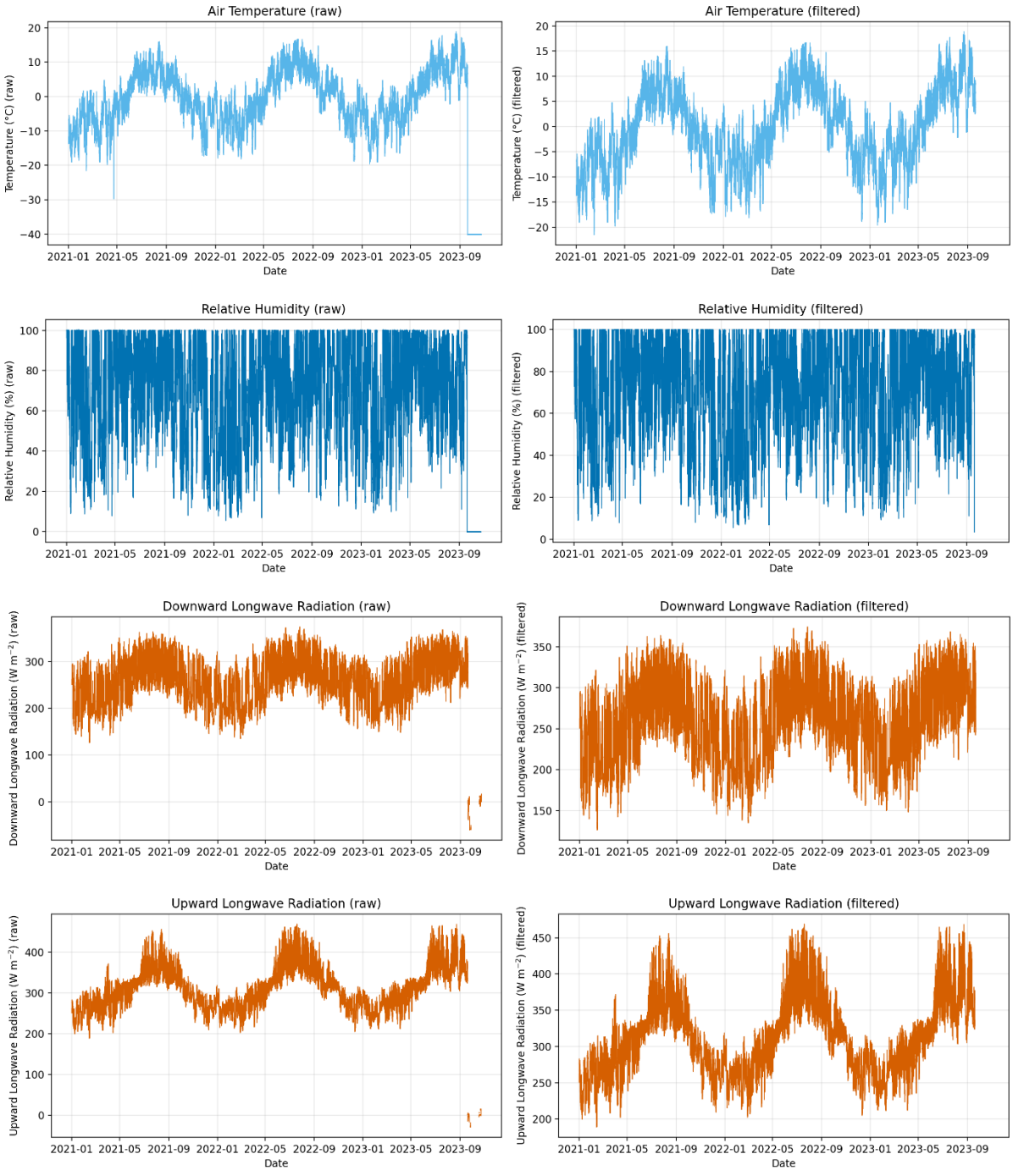

Figure A.1: Raw (left) and filtered (right) time series of air temperature, relative humidity, downwelling longwave radiation, and upwelling longwave radiation from the meteorological station for January 2021 to September 2023. Applied filtering thresholds are summarised in Table 2.

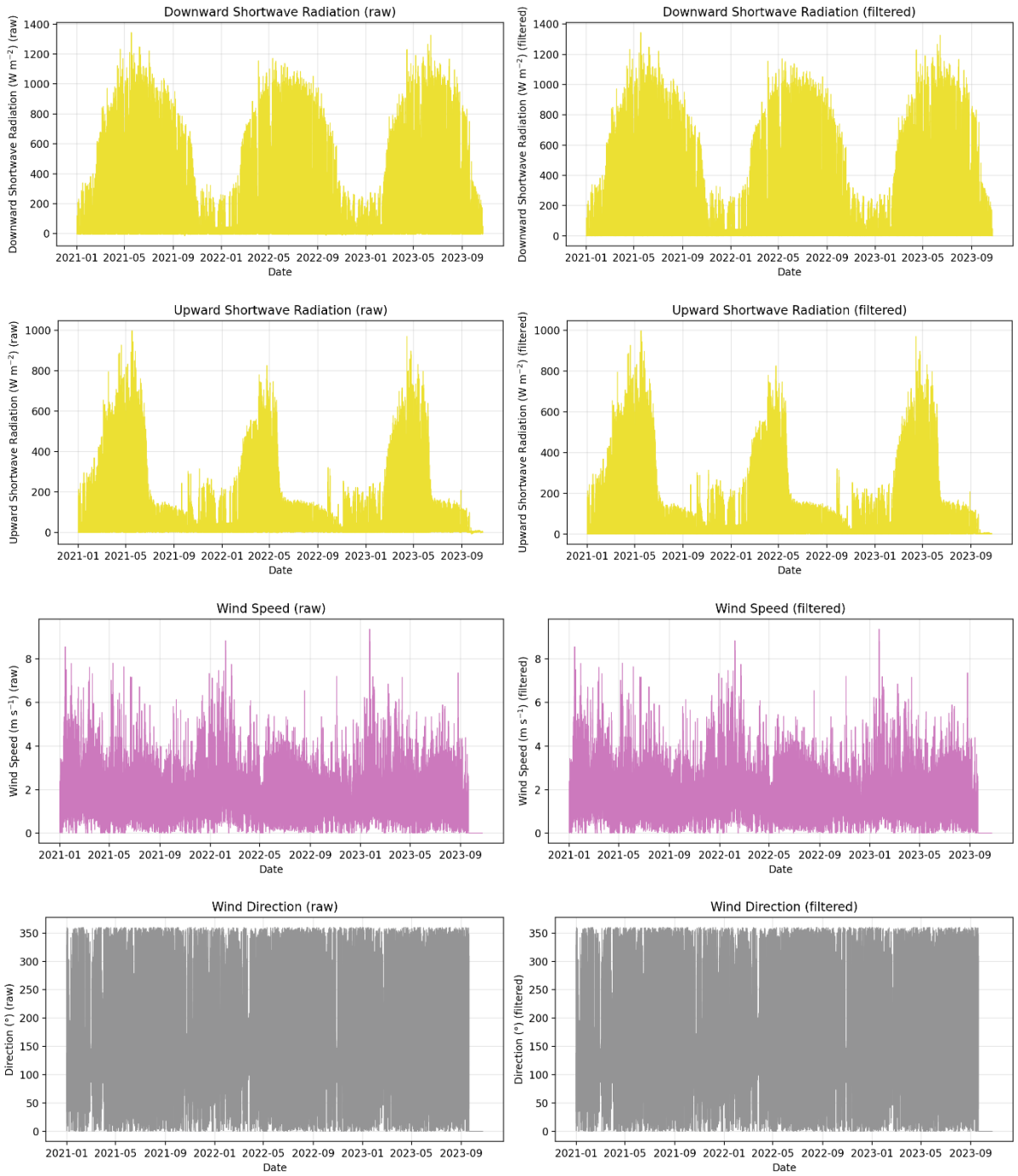

Figure A.2: Raw (left) and filtered (right) time series of downwelling shortwave radiation, upwelling shortwave radiation, wind speed and wind direction from the meteorological station for January 2021 to September 2023. Applied filtering thresholds are summarised in Table 2.

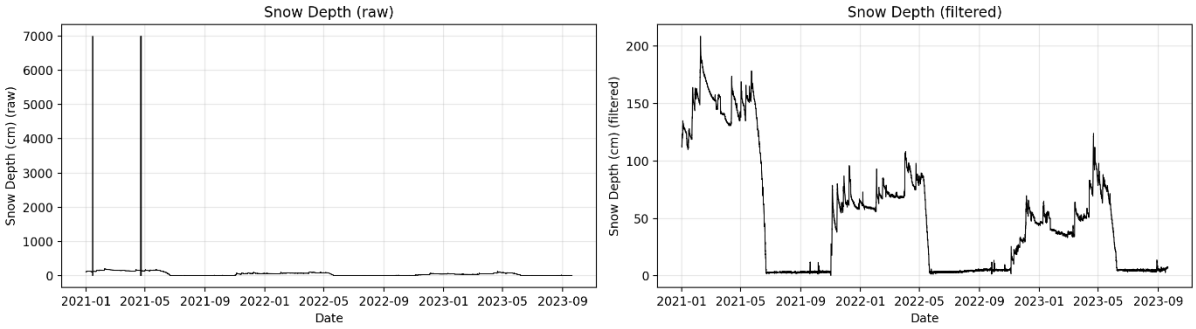

Figure A.3: Raw (left) and filtered (right) time series of snow height from the meteorological station for January 2021 to September 2023. Applied filtering thresholds are summarised in Table 2.

Appendix B: Temperature Correction

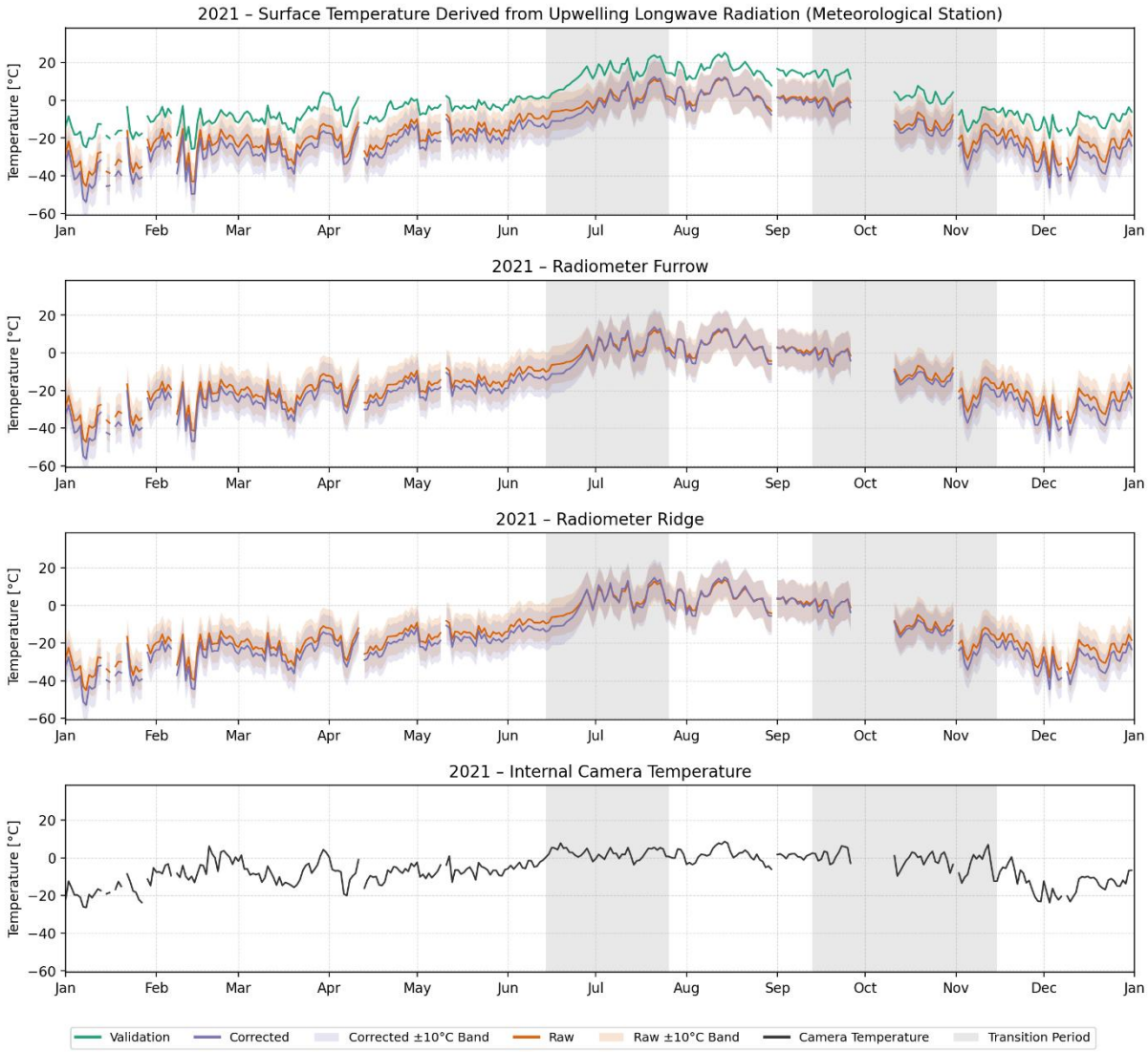

Figure B.1: Comparison of corrected and raw TIR-derived pixel temperatures with surface temperatures derived from upwelling longwave radiation at the meteorological station, as well as with radiometer measurements at ridge and furrow locations for 2021. Grey shaded areas indicate transition periods between snow-covered and snow-free conditions. All time series represent daily mean values.

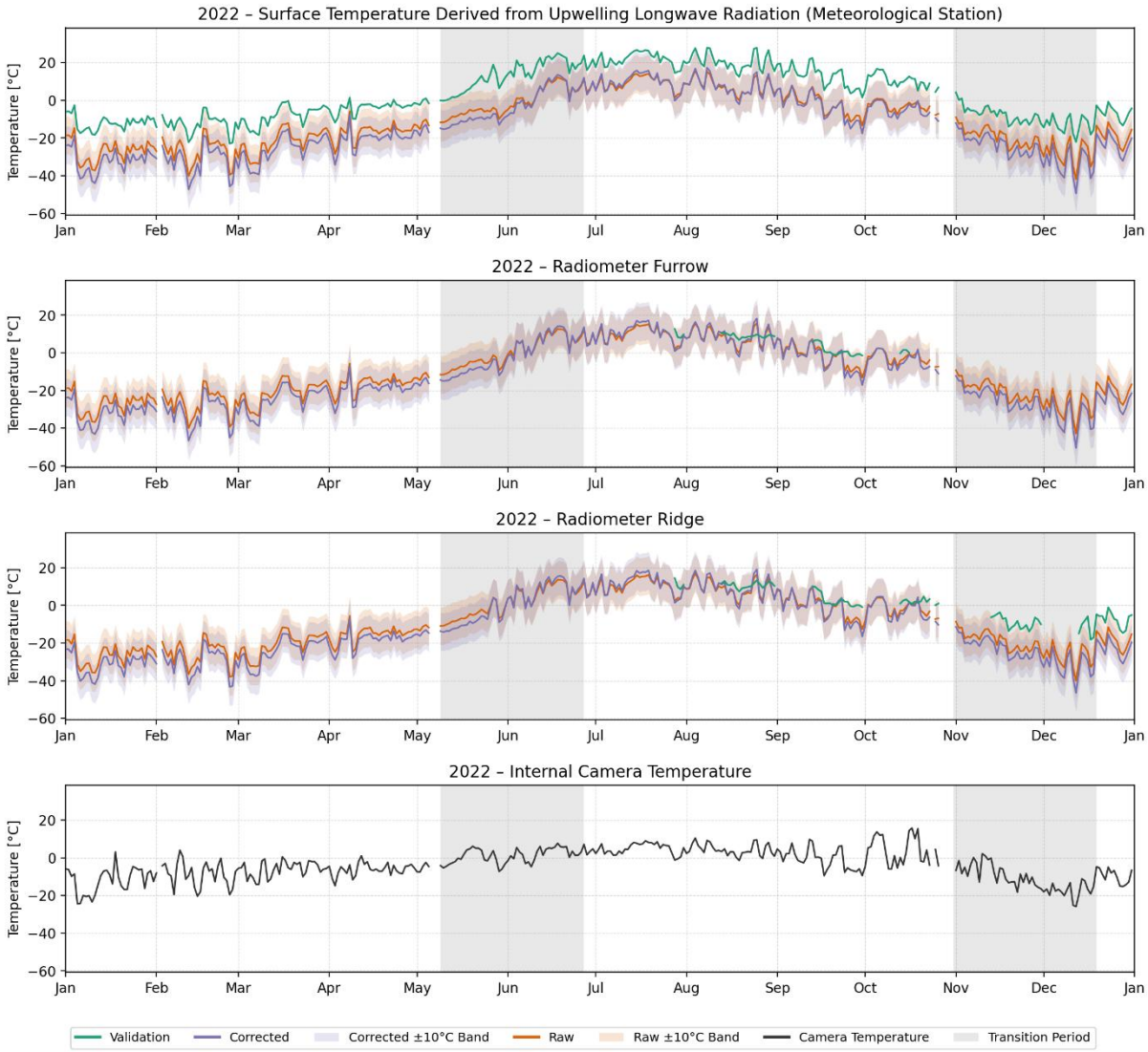

Figure B.2: Comparison of corrected and raw TIR-derived pixel temperatures with surface temperatures derived from upwelling longwave radiation at the meteorological station, as well as with radiometer measurements at ridge and furrow locations for 2022. Grey shaded areas indicate transition periods between snow-covered and snow-free conditions. All time series represent daily mean values.

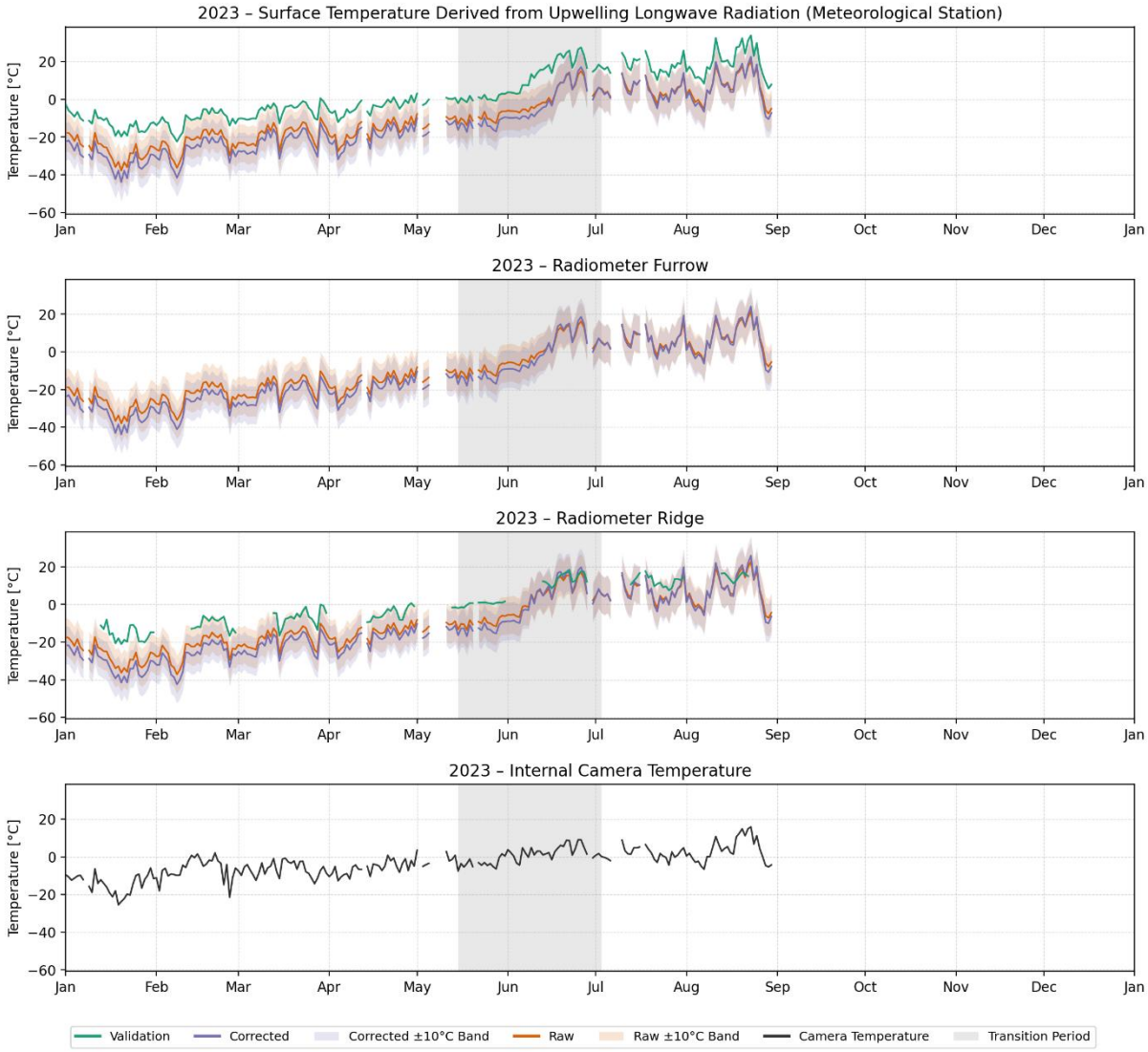

Figure B.3: Comparison of corrected and raw TIR-derived pixel temperatures with surface temperatures derived from upwelling longwave radiation at the meteorological station, as well as with radiometer measurements at ridge and furrow locations for 2023. Grey shaded areas indicate transition periods between snow-covered and snow-free conditions. All time series represent daily mean values.

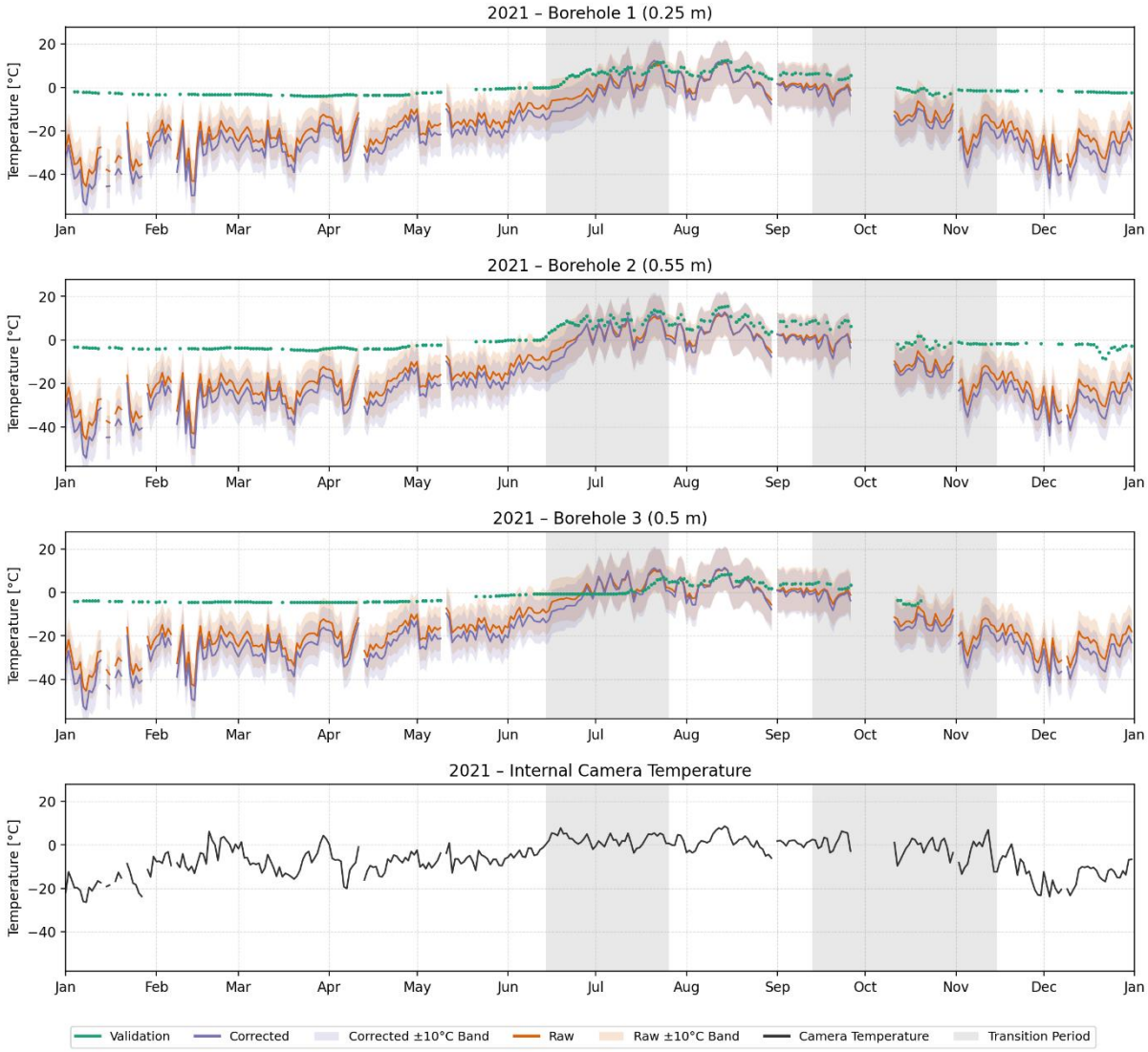

Figure B.4: Comparison of corrected and raw TIR-derived pixel temperatures with borehole temperatures for 2021. Grey shaded areas indicate transition periods between snow-covered and snow-free conditions. All time series represent daily mean values.

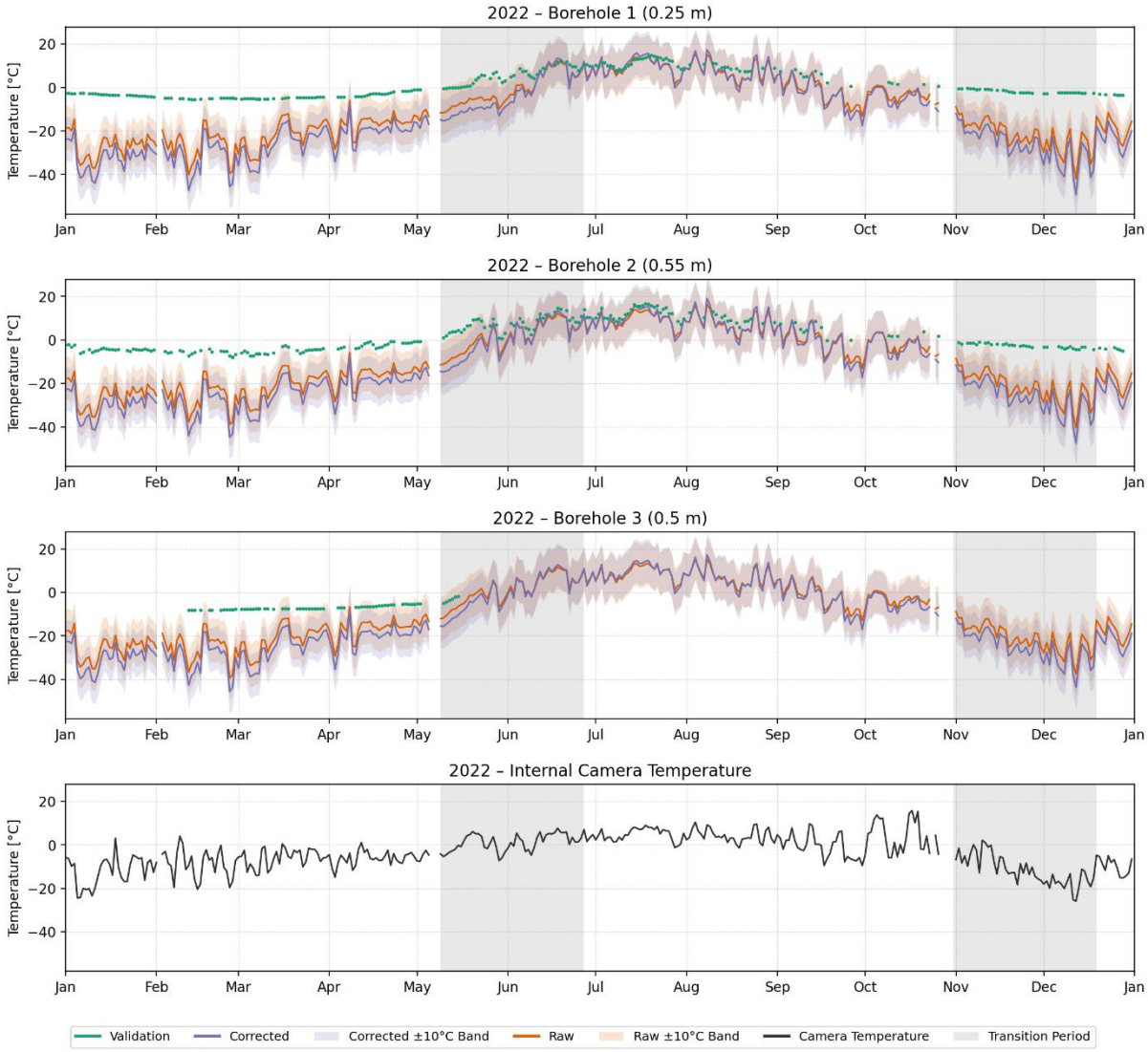

Figure B.5: Comparison of corrected and raw TIR-derived pixel temperatures with borehole temperatures for 2022. Grey shaded areas indicate transition periods between snow-covered and snow-free conditions. All time series represent daily mean values.

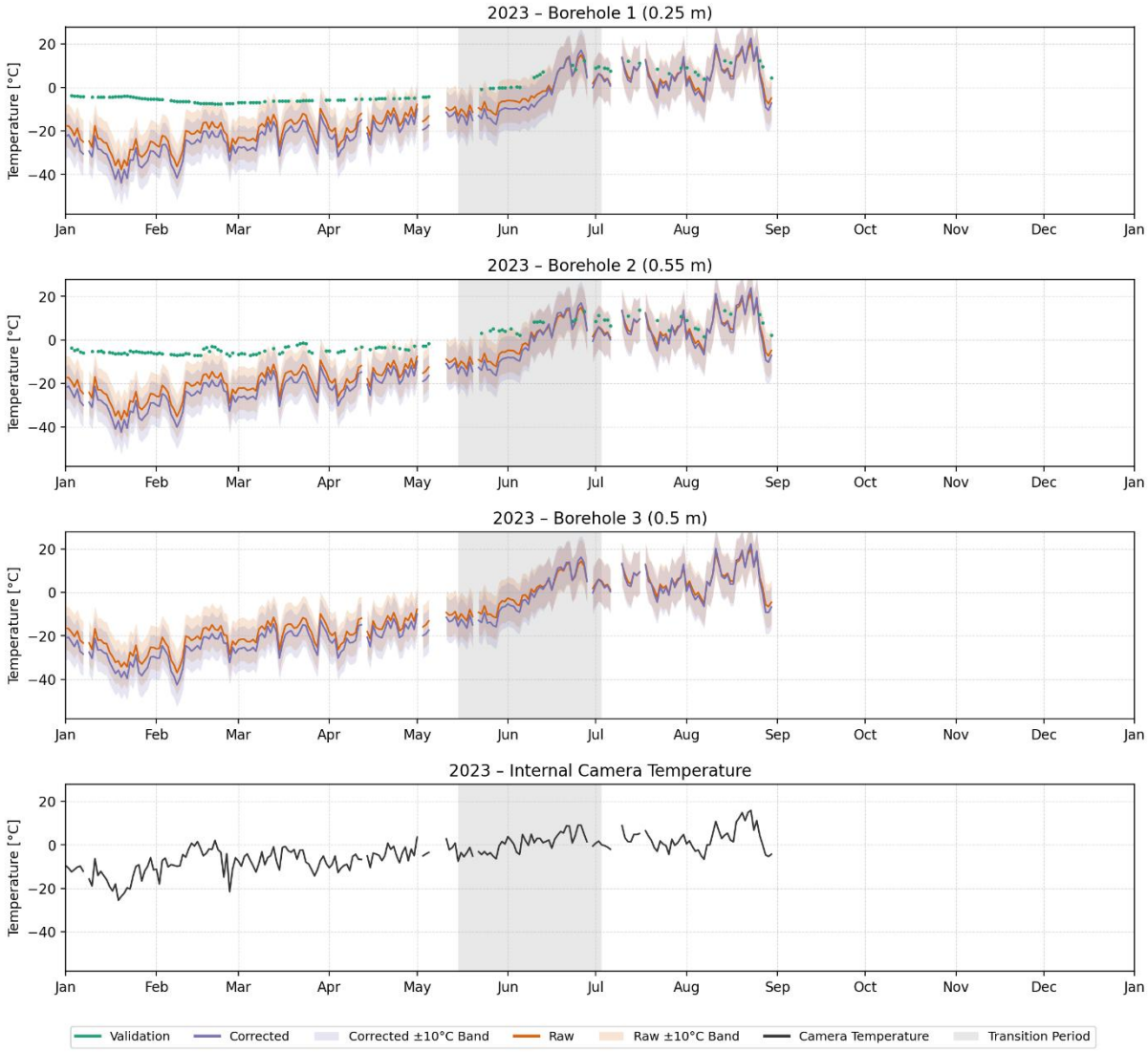

Figure B.6: Comparison of corrected and raw TIR-derived pixel temperatures with borehole temperatures for 2023. Grey shaded areas indicate transition periods between snow-covered and snow-free conditions. All time series represent daily mean values.

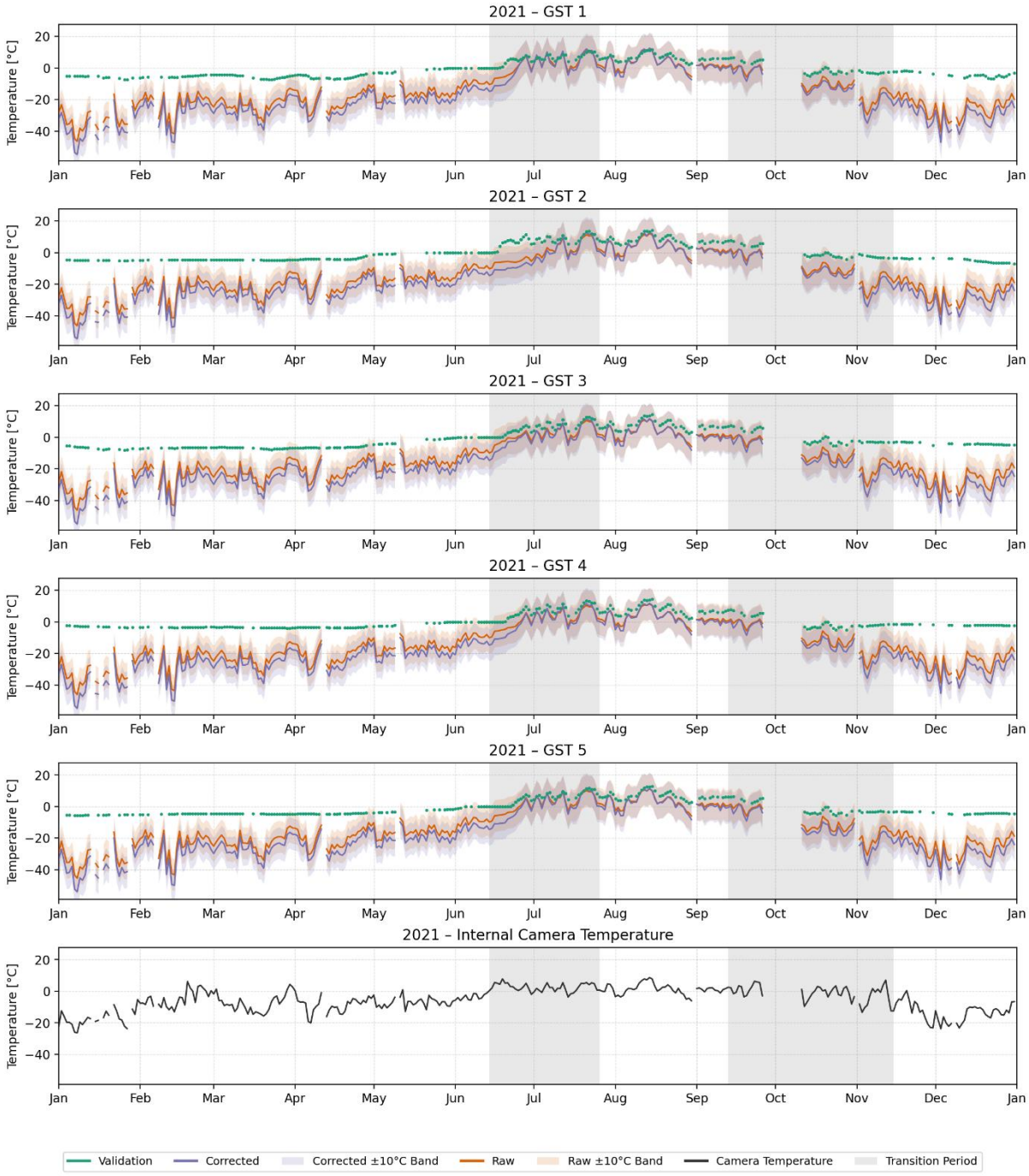

Figure B.7: Comparison of corrected and raw TIR-derived pixel temperatures with GST logger measurements for 2021. Grey shaded areas indicate transition periods between snow-covered and snow-free conditions. All time series represent daily mean values.

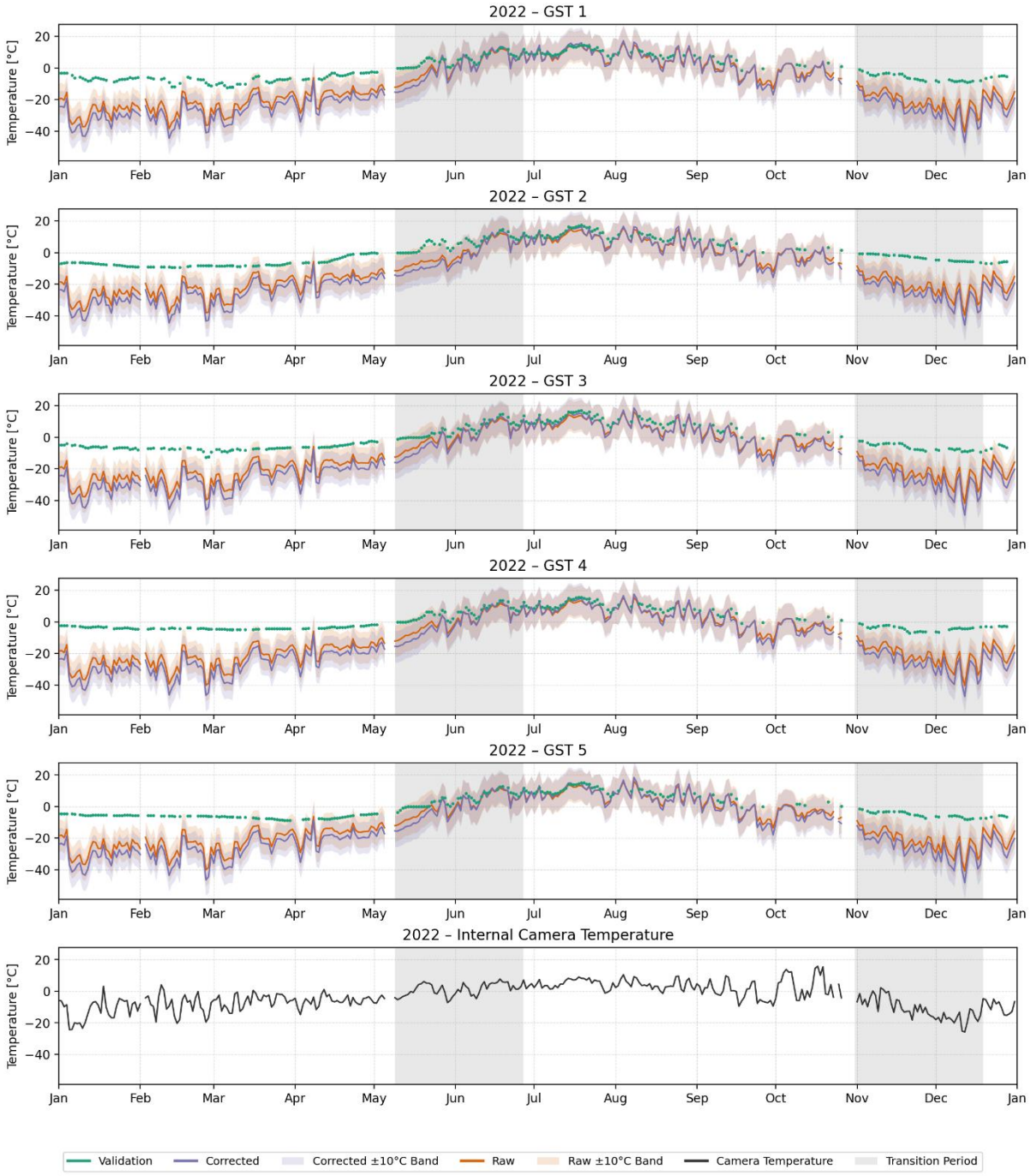

Figure B.8: Comparison of corrected and raw TIR-derived pixel temperatures with GST logger measurements for 2022. Grey shaded areas indicate transition periods between snow-covered and snow-free conditions. All time series represent daily mean values.

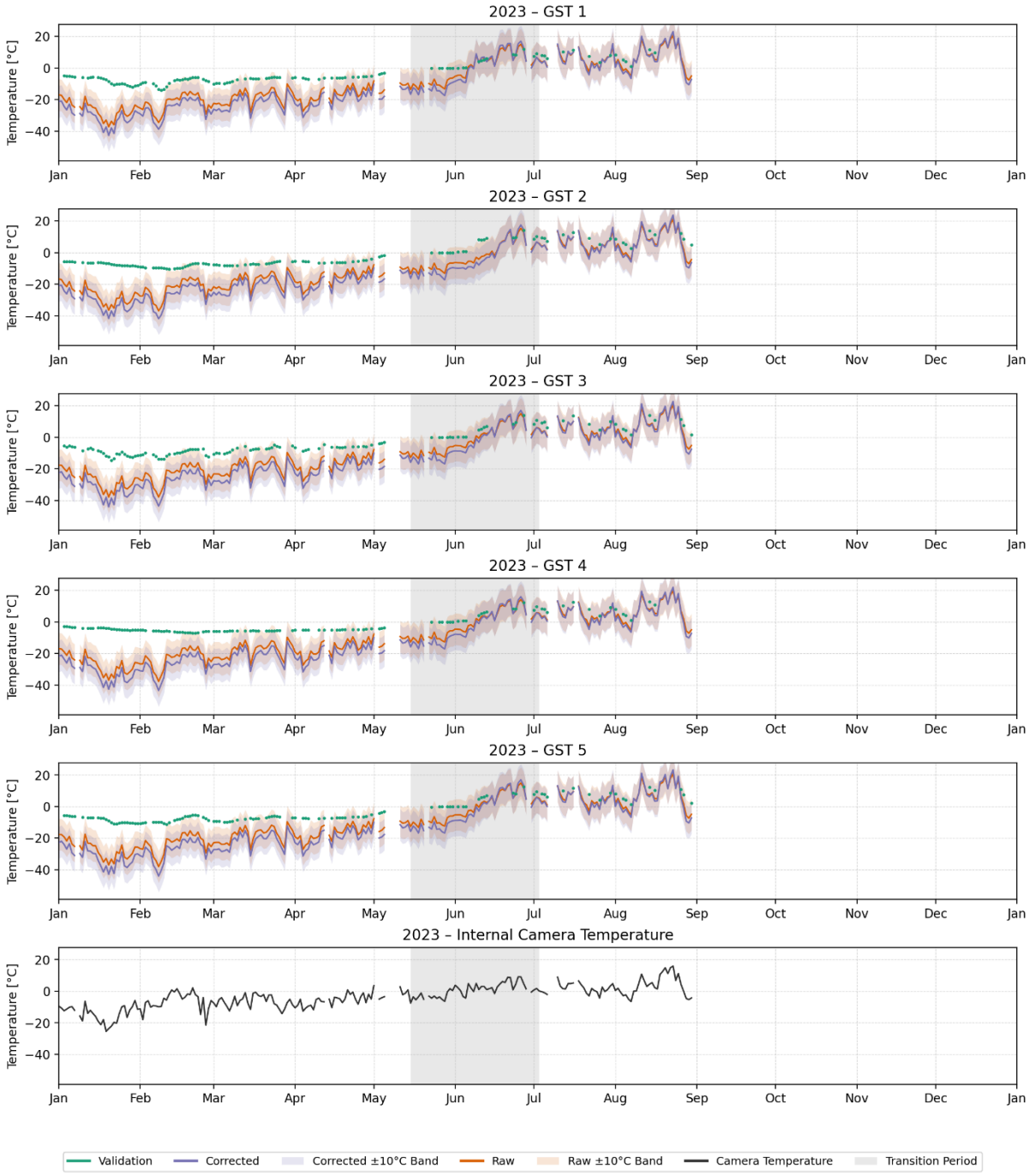

Figure B.9: Comparison of corrected and raw TIR-derived pixel temperatures with GST logger measurements for 2023. Grey shaded areas indicate transition periods between snow-covered and snow-free conditions. All time series represent daily mean values.

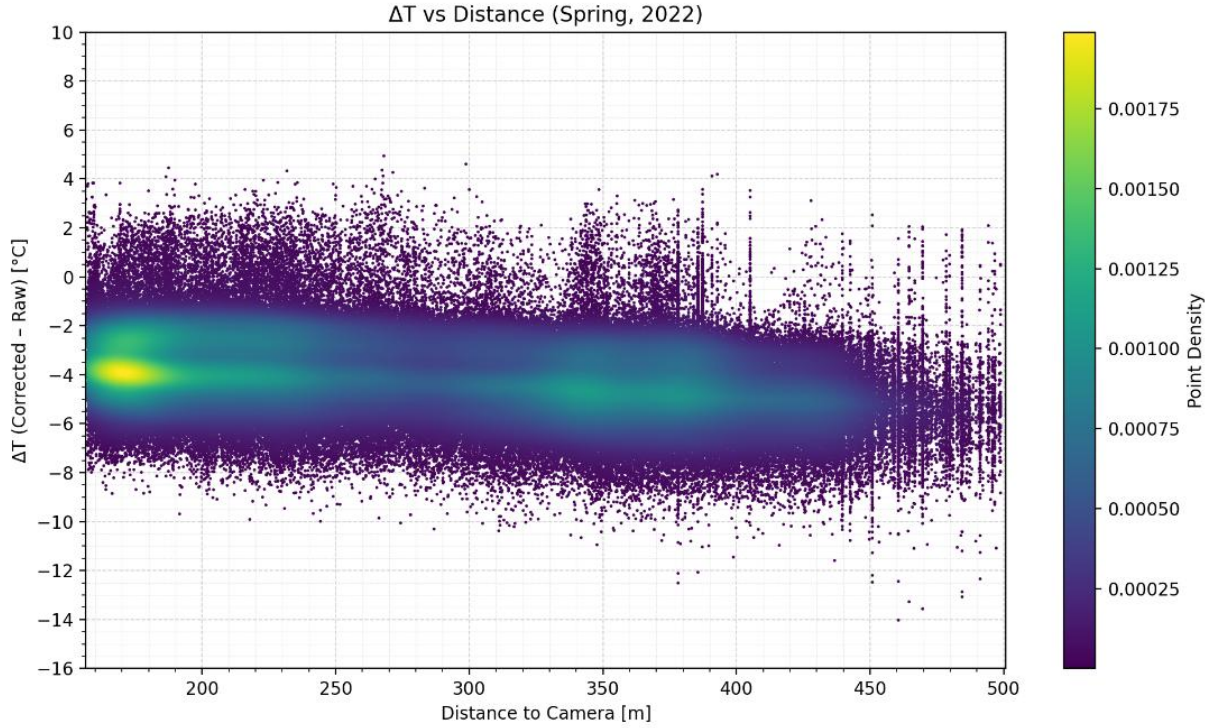

Figure B.10: Relationship between the temperature difference introduced by the atmospheric correction and the distance to the camera for spring 2022. Each point represents an individual pixel, coloured by point density.

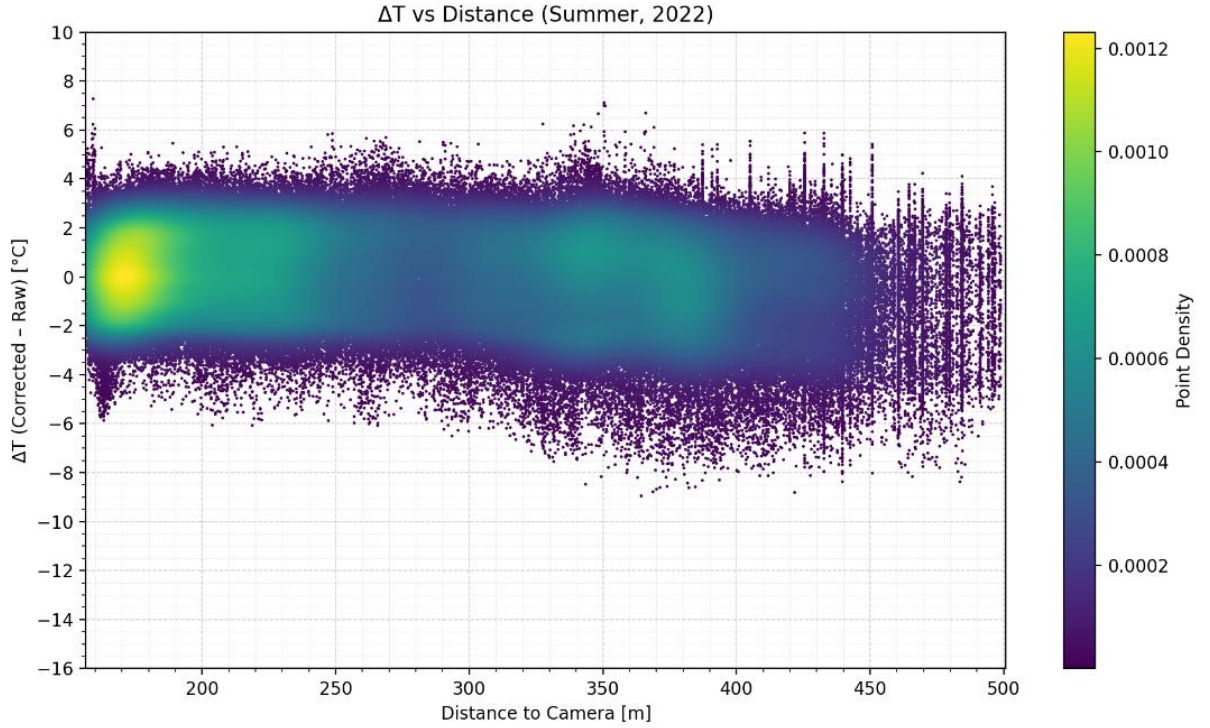

Figure B.11: Relationship between the temperature difference introduced by the atmospheric correction and the distance to the camera for summer 2022. Each point represents an individual pixel, coloured by point density.

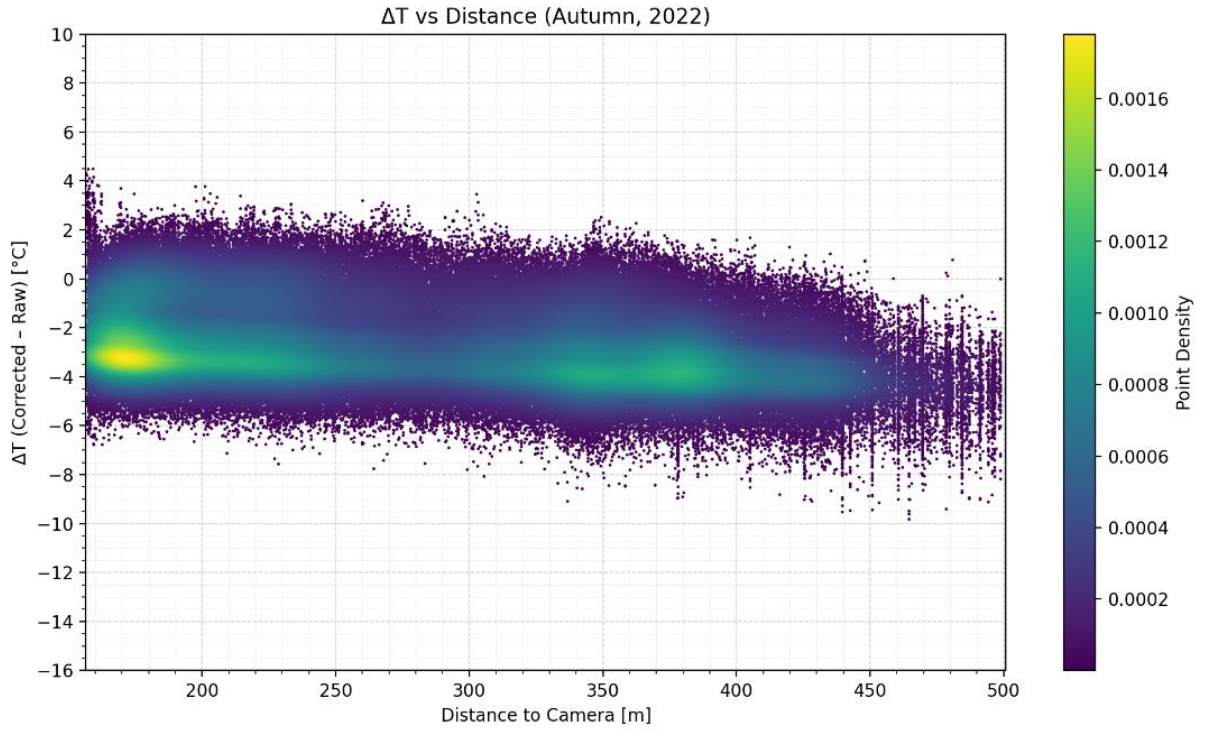

Figure B.12: Relationship between the temperature difference introduced by the atmospheric correction and the distance to the camera for autumn 2022. Each point represents an individual pixel, coloured by point density.

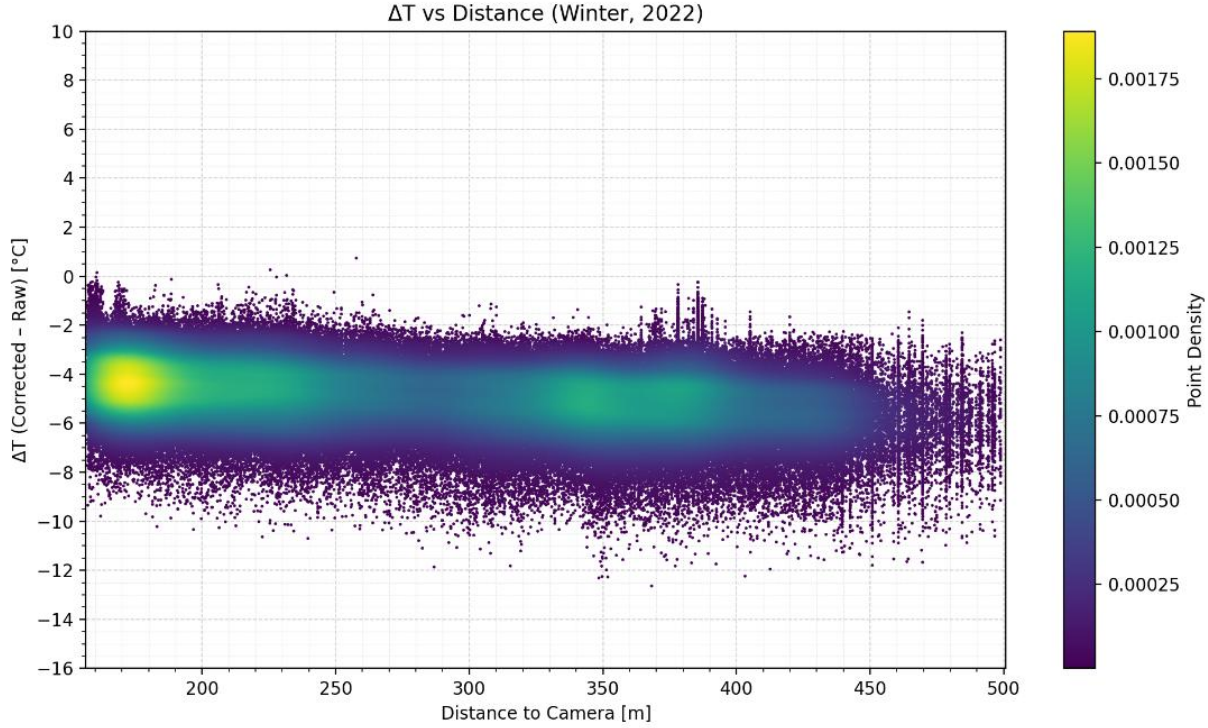

Figure B.13: Relationship between the temperature difference introduced by the atmospheric correction and the distance to the camera for winter 2022. Each point represents an individual pixel, coloured by point density.

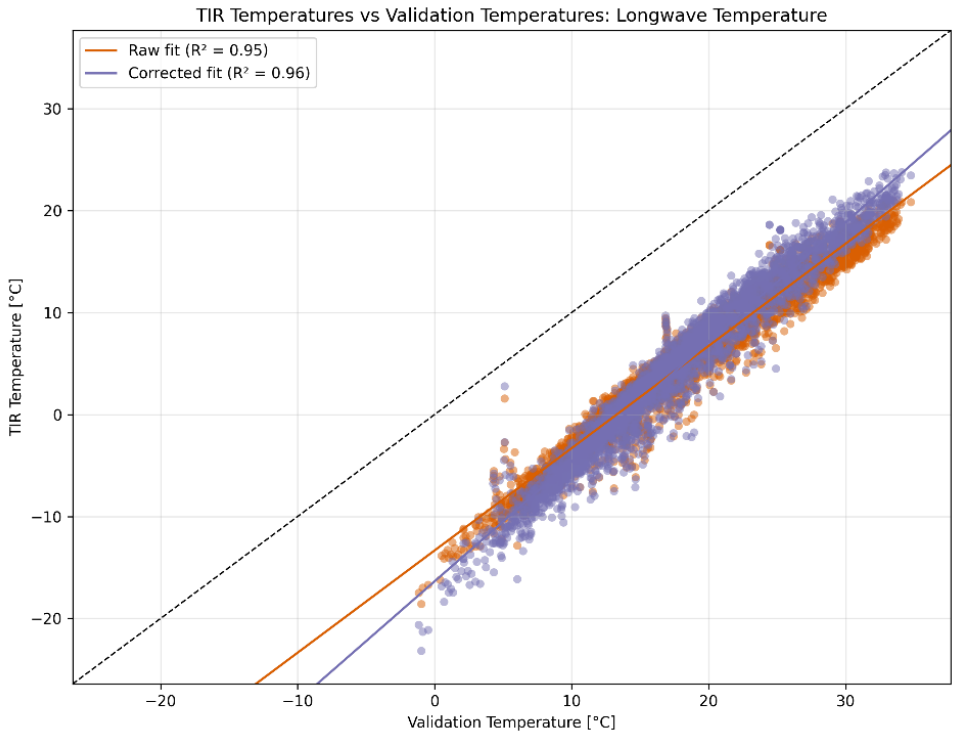

Figure B.14: Scatterplot of derived TIR temperatures (corrected and raw) vs. validation temperatures (temperature derived from longwave radiation). This plot represents snow-free acquisitions from 2022.

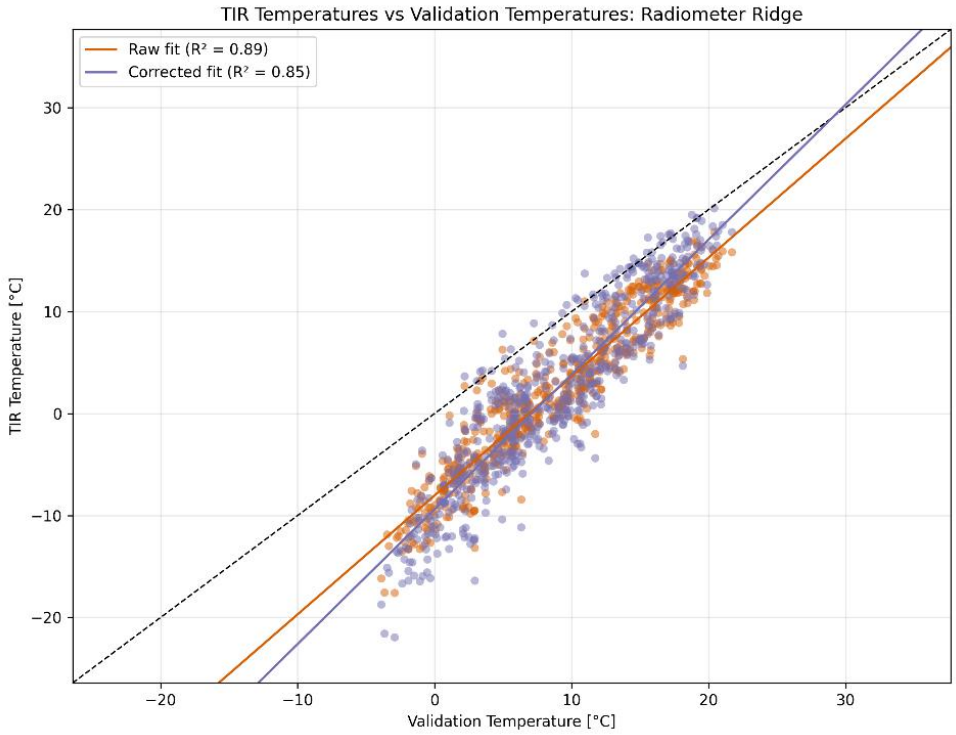

Figure B.15: Scatterplot of derived TIR temperatures (corrected and raw) vs. validation temperatures (radiometer ridge). This plot represents snow-free acquisitions from 2022

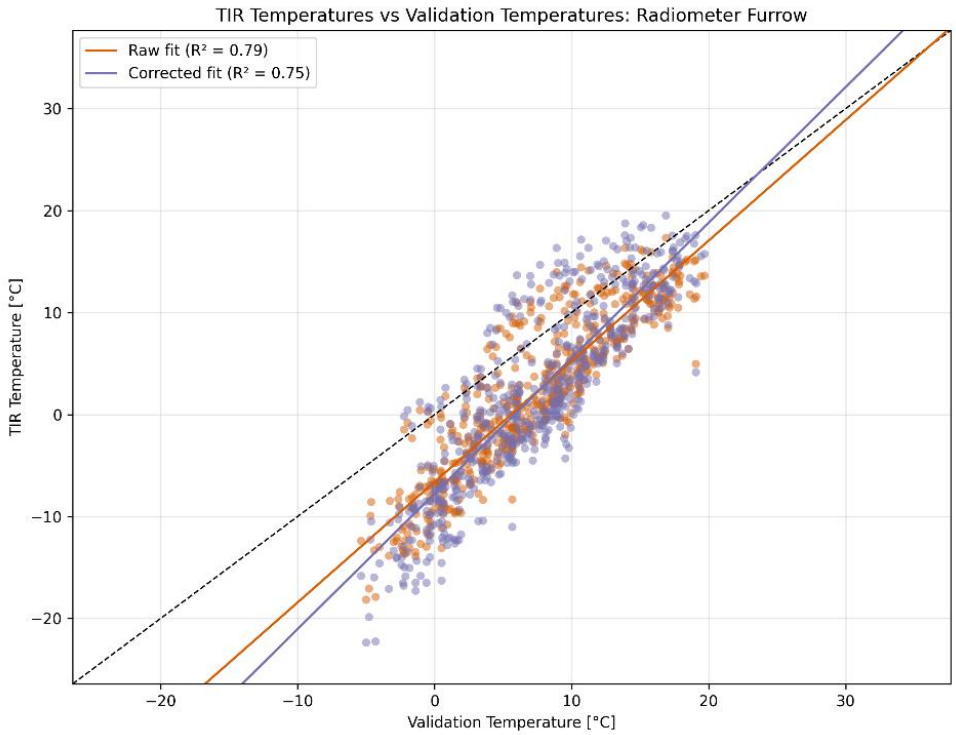

Figure B.16: Scatterplot of derived TIR temperatures (corrected and raw) vs. validation temperatures (radiometer furrow). This plot represents snow-free acquisitions from 2022.

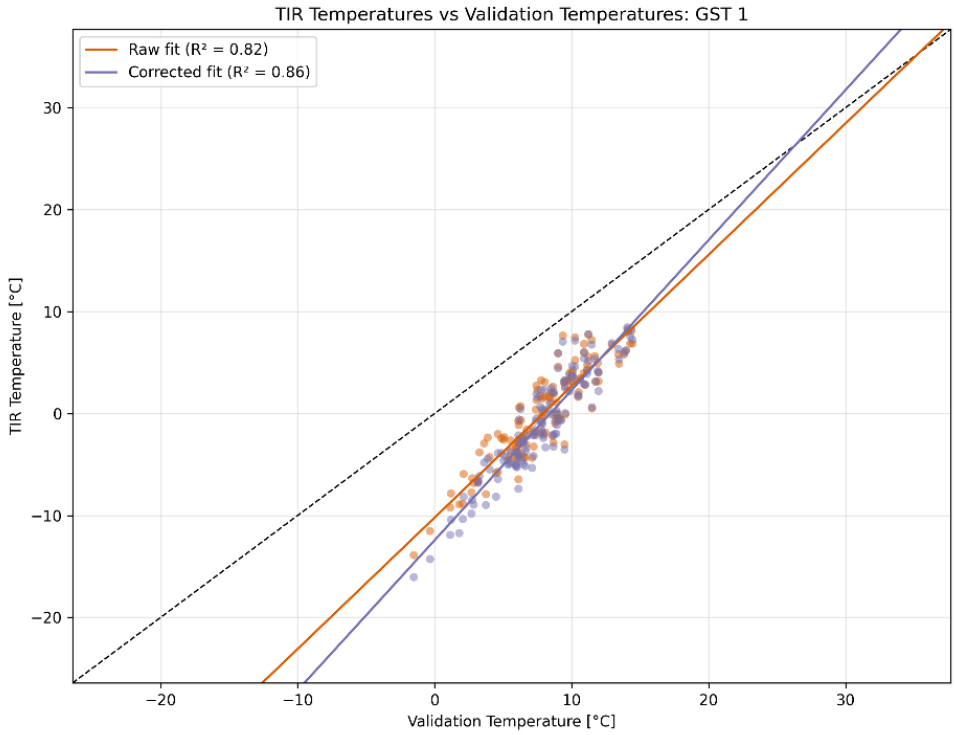

Figure B.17: Scatterplot of derived TIR temperatures (corrected and raw) vs. validation temperatures (GST 1). This plot represents snow-free acquisitions from 2022.

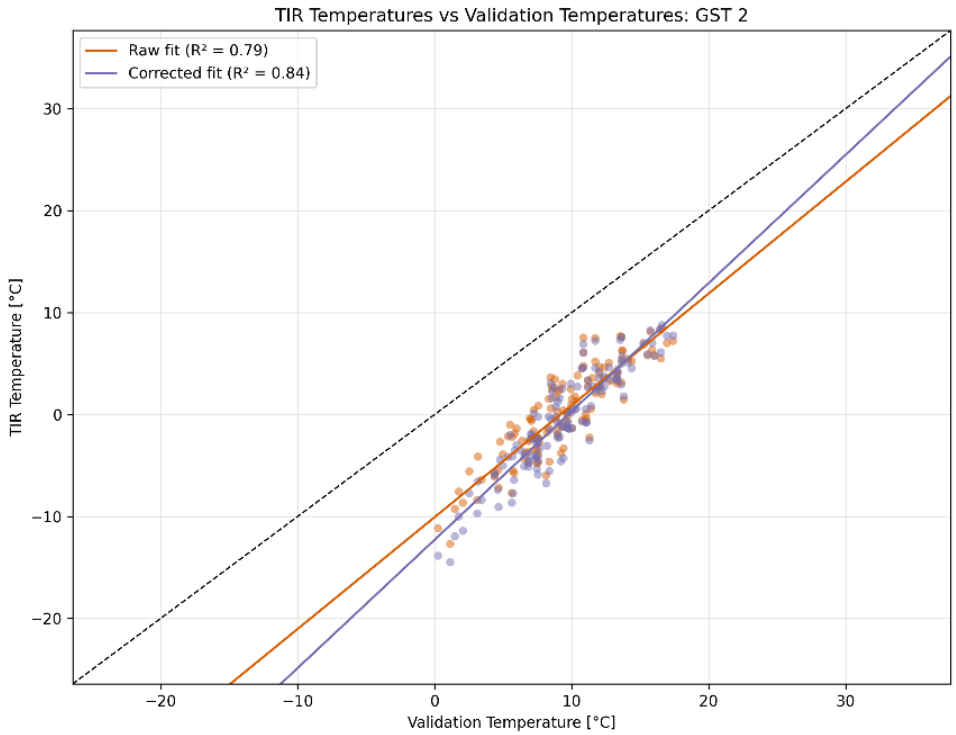

Figure B.18: Scatterplot of derived TIR temperatures (corrected and raw) vs. validation temperatures (GST 2). This plot represents snow-free acquisitions from 2022.

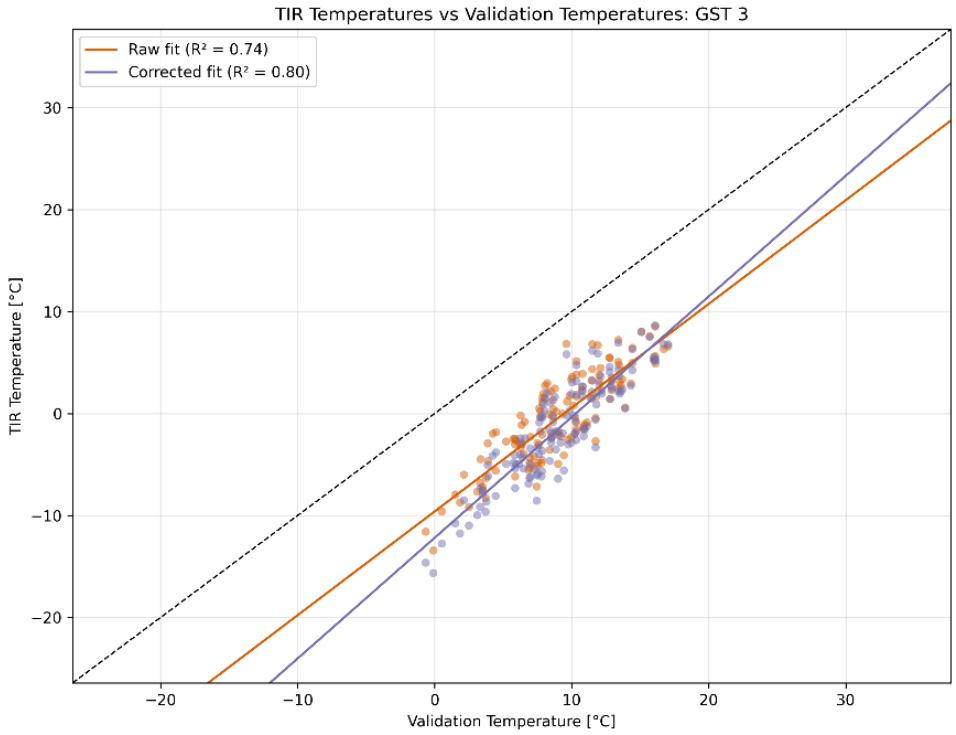

Figure B.19: Scatterplot of derived TIR temperatures (corrected and raw) vs. validation temperatures (GST 3). This plot represents snow-free acquisitions from 2022.

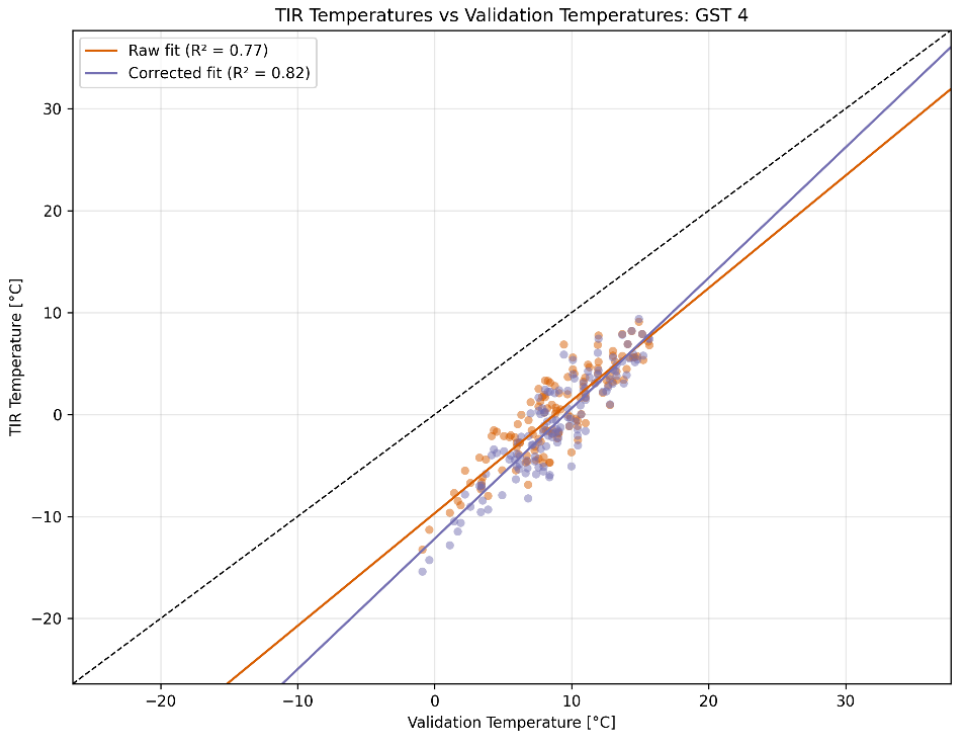

Figure B.20: Scatterplot of derived TIR temperatures (corrected and raw) vs. validation temperatures (GST 4). This plot represents snow-free acquisitions from 2022.

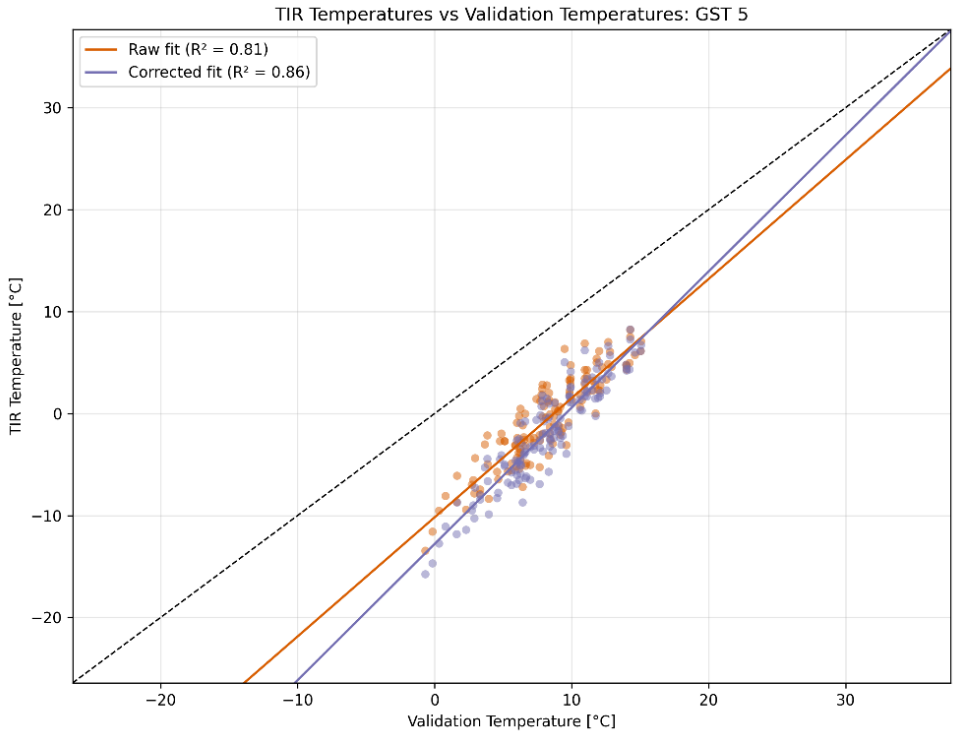

Figure B. 21: Scatterplot of derived TIR temperatures (corrected and raw) vs. validation temperatures (GST 5). This plot represents snow-free acquisitions from 2022.

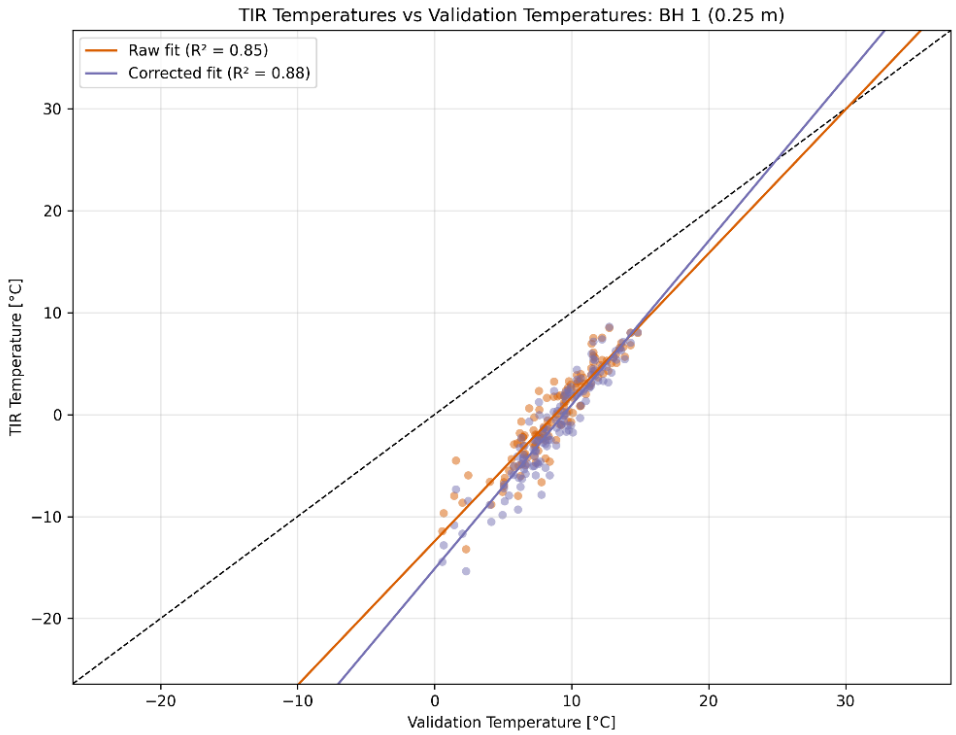

Figure B.22: Scatterplot of derived TIR temperatures (corrected and raw) vs. validation temperatures (Borehole 1). This plot represents snow-free acquisitions from 2022.

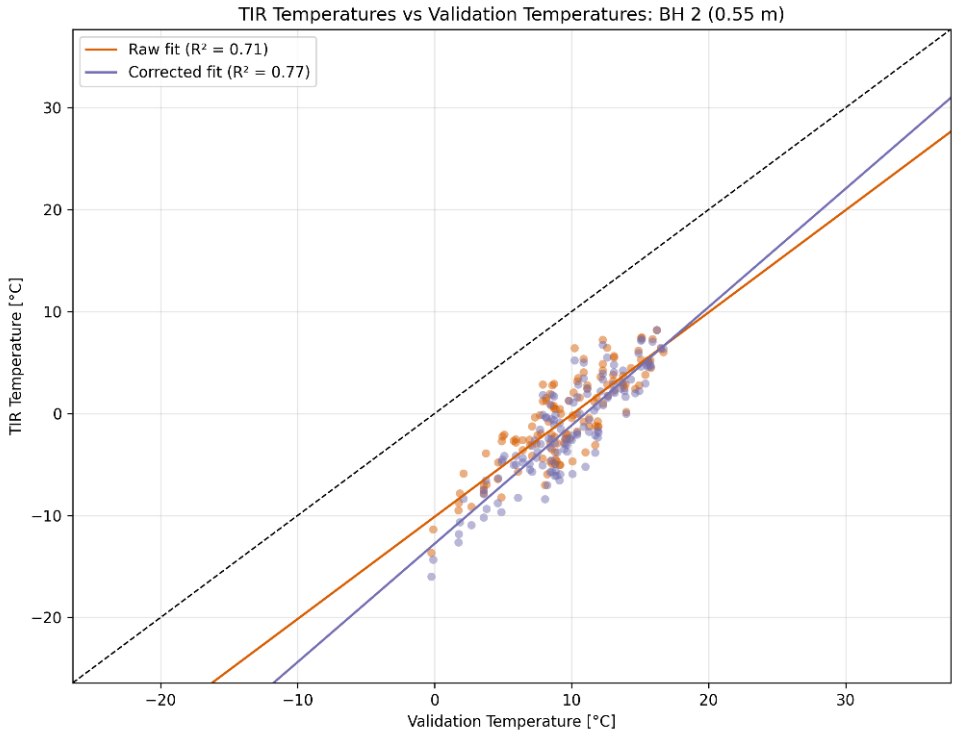

Figure B.23: Scatterplot of derived TIR temperatures (corrected and raw) vs. validation temperatures (Borehole 2). This plot represents snow-free acquisitions from 2022.

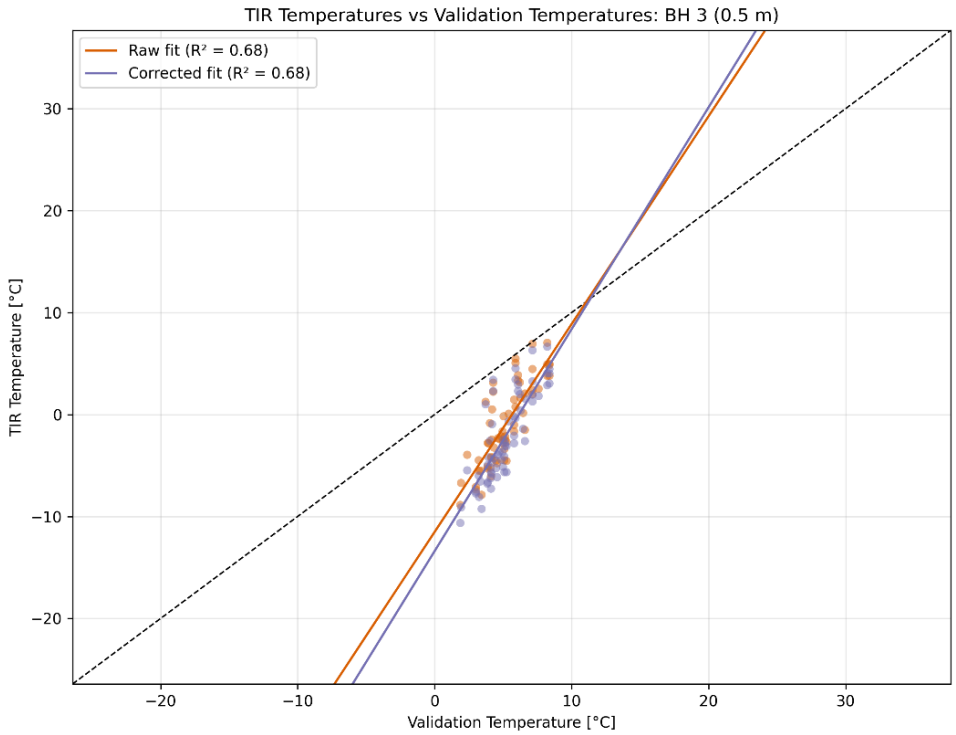

Figure B.24: Scatterplot of derived TIR temperatures (corrected and raw) vs. validation temperatures (Borehole 3). This plot represents snow-free acquisitions from 2022.

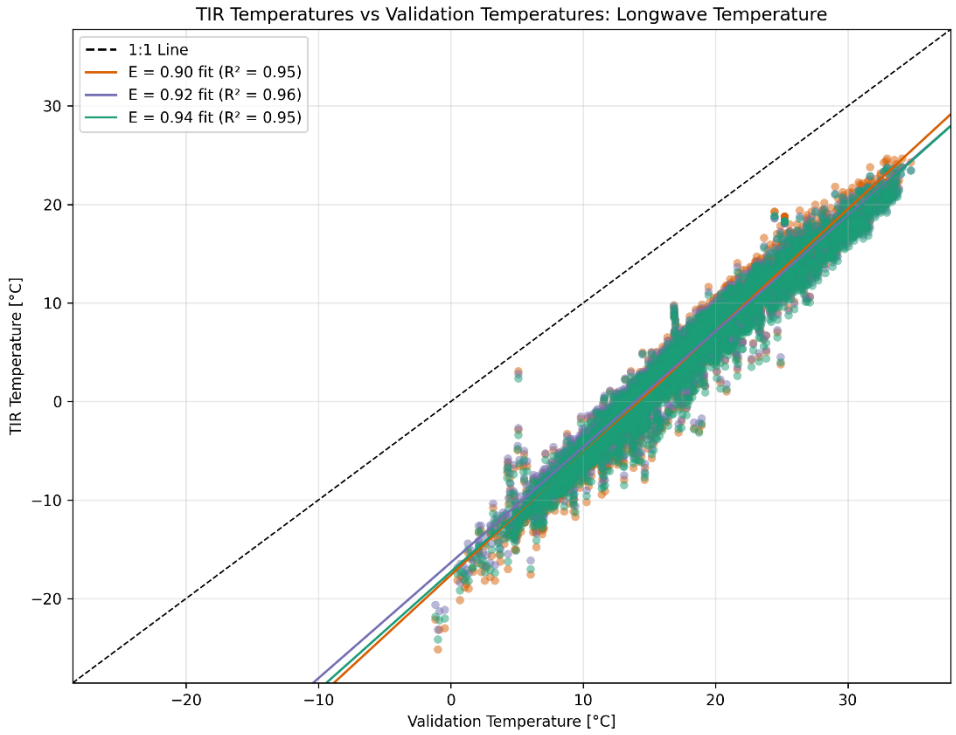

Figure B.25: Sensitivity of corrected TIR surface temperatures to rock emissivity (ε = 0.90, 0.92, 0.94), evaluated against longwave-radiation-derived validation temperatures for the snow-free period of 2022.

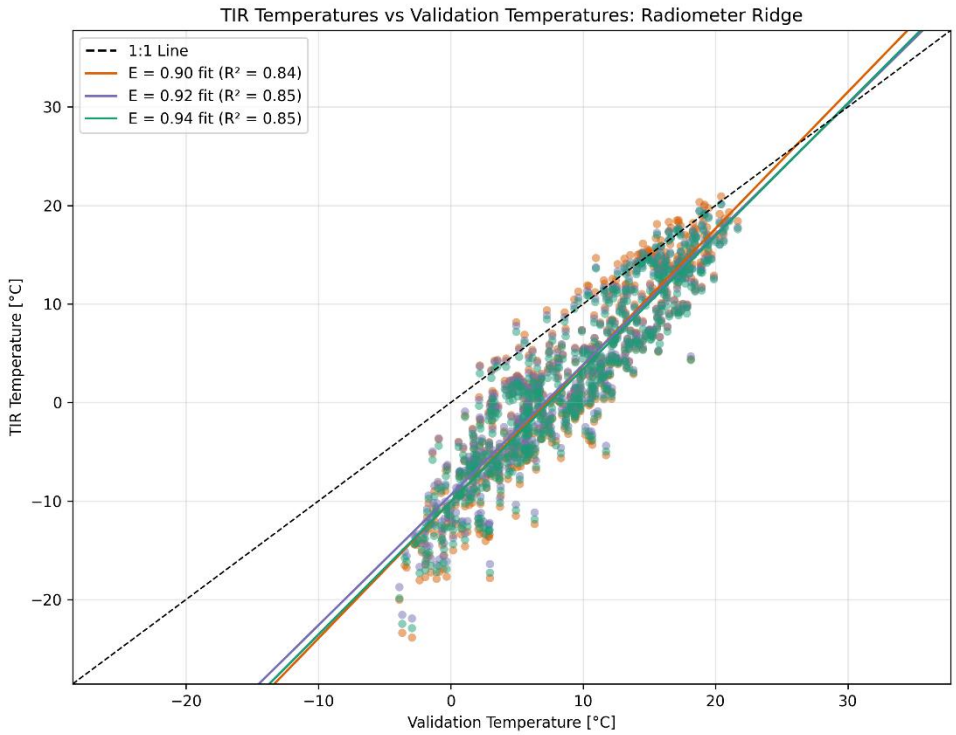

Figure B.26: Sensitivity of corrected TIR surface temperatures to rock emissivity (ε = 0.90, 0.92, 0.94), evaluated against radiometer ridge validation temperatures for the snow-free period of 2022.

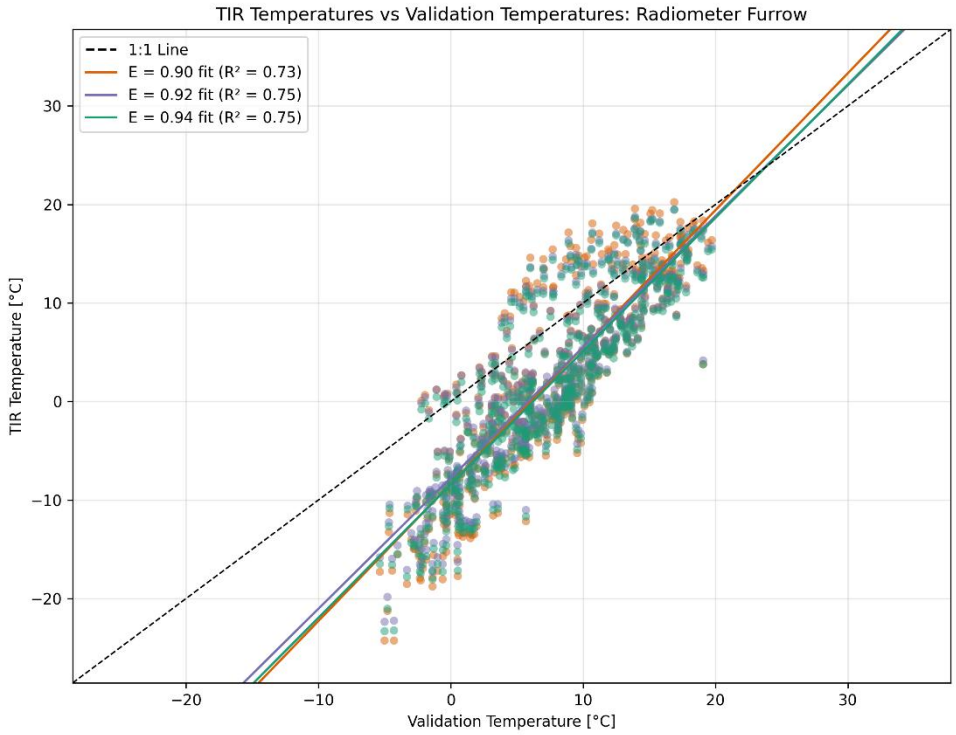

Figure B.27: Sensitivity of corrected TIR surface temperatures to rock emissivity (ε = 0.90, 0.92, 0.94), evaluated against radiometer furrow validation temperatures for the snow-free period of 2022.

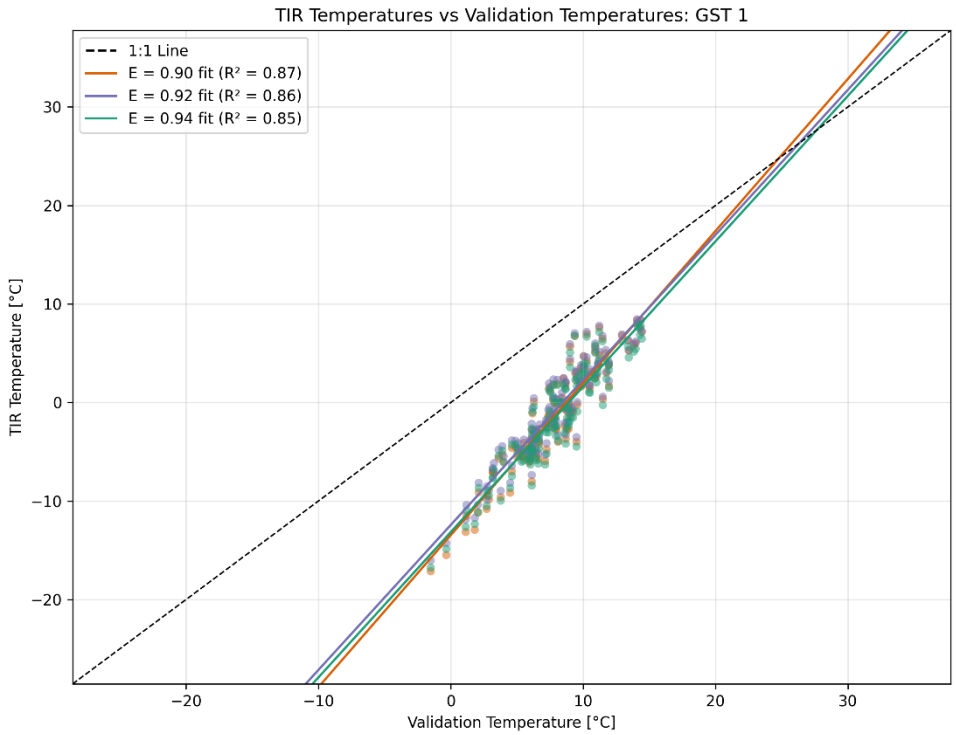

Figure B.28: Sensitivity of corrected TIR surface temperatures to rock emissivity (ε = 0.90, 0.92, 0.94), evaluated against GST 1 validation temperatures for the snow-free period of 2022.

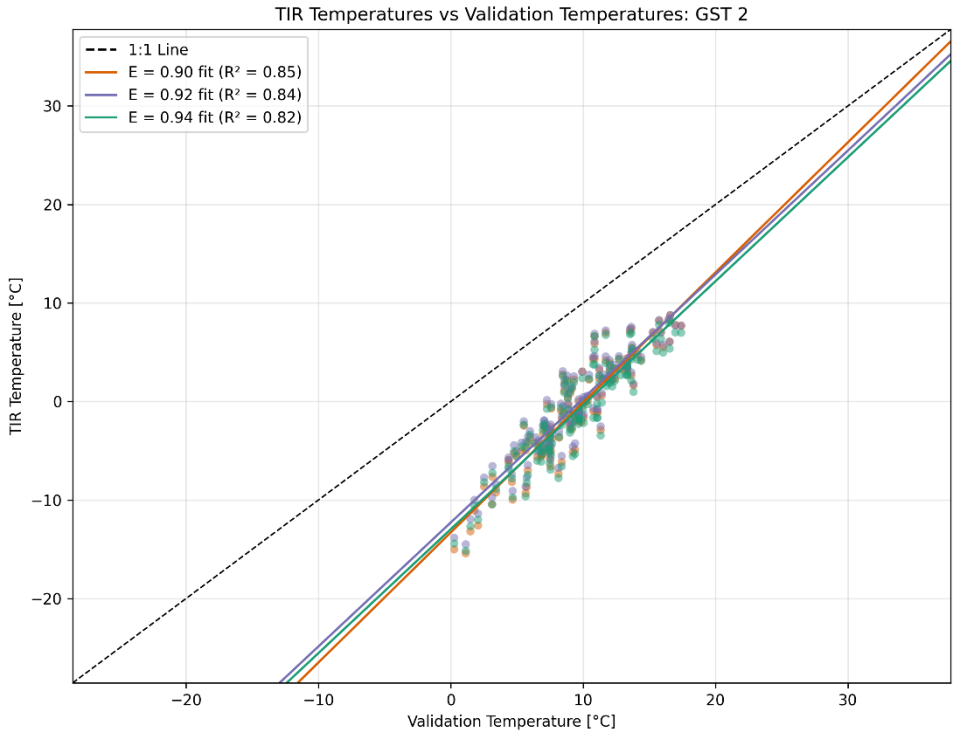

Figure B.29: Sensitivity of corrected TIR surface temperatures to rock emissivity (ε = 0.90, 0.92, 0.94), evaluated against GST 2 validation temperatures for the snow-free period of 2022.

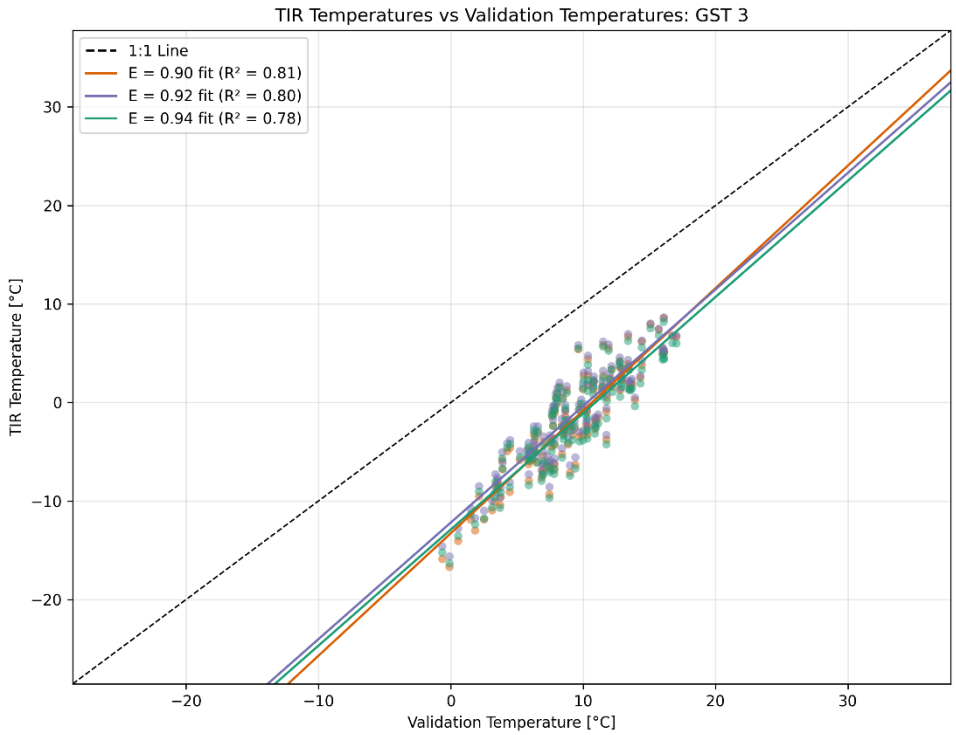

Figure B.30: Sensitivity of corrected TIR surface temperatures to rock emissivity (ε = 0.90, 0.92, 0.94), evaluated against GST 3 validation temperatures for the snow-free period of 2022.

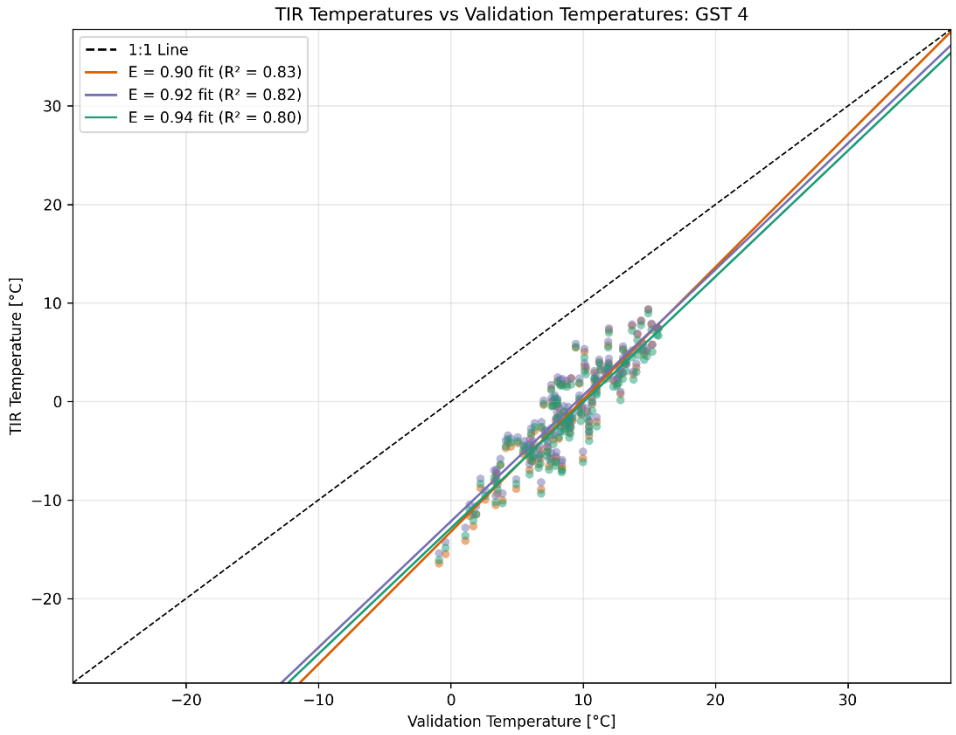

Figure B.31: Sensitivity of corrected TIR surface temperatures to rock emissivity (ε = 0.90, 0.92, 0.94), evaluated against GST 4 validation temperatures for the snow-free period of 2022.

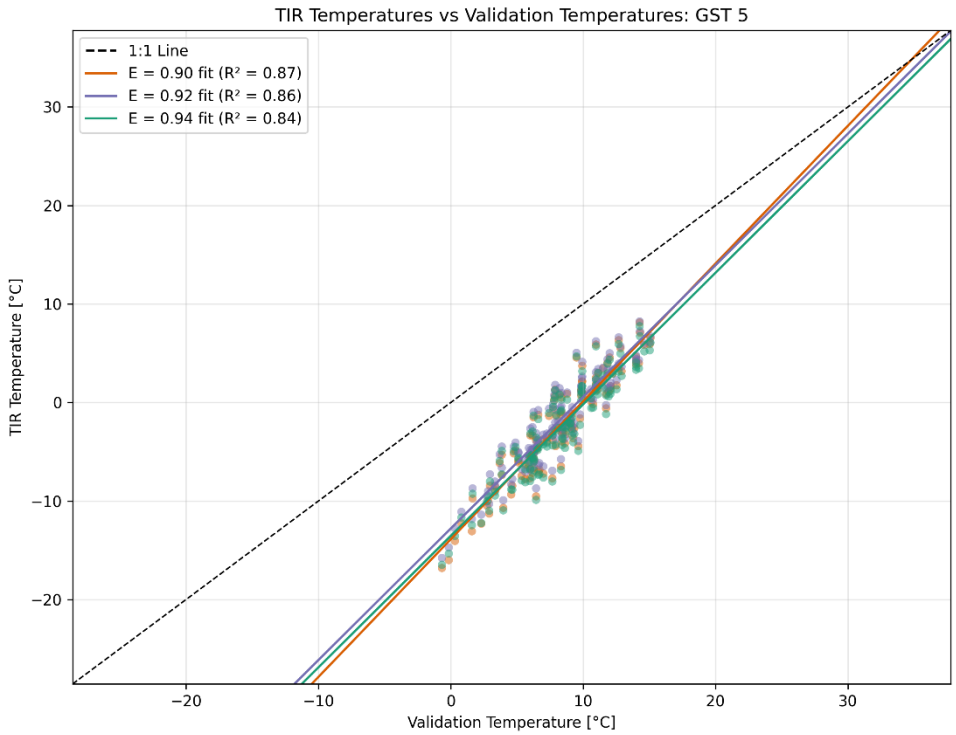

Figure B.32: Sensitivity of corrected TIR surface temperatures to rock emissivity (ε = 0.90, 0.92, 0.94), evaluated against GST 5 validation temperatures for the snow-free period of 2022.

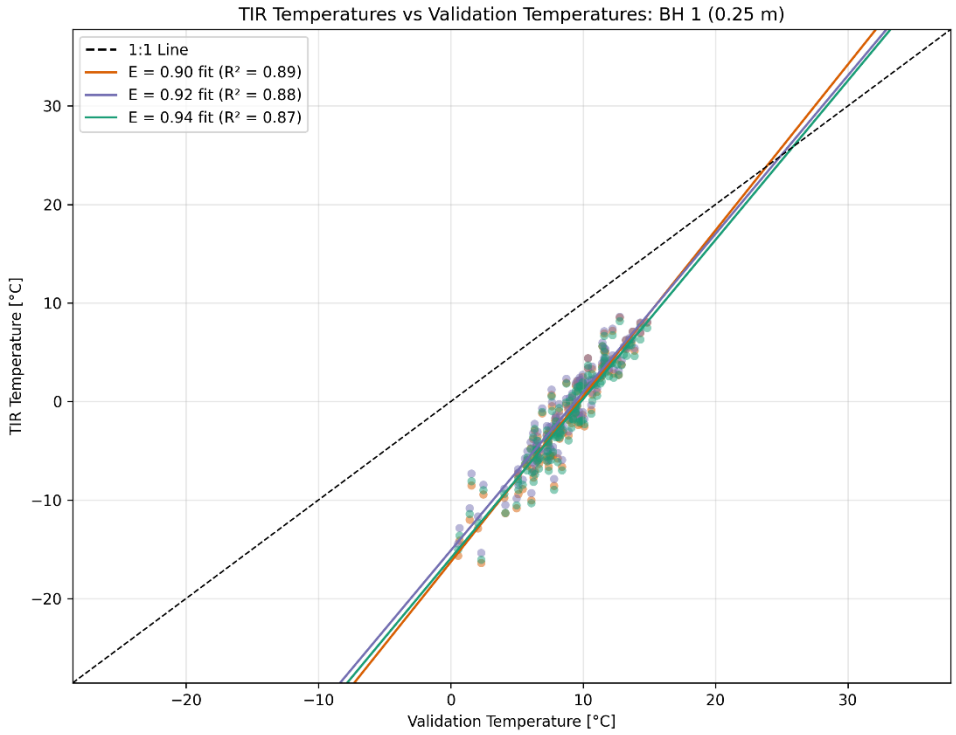

Figure B.33: Sensitivity of corrected TIR surface temperatures to rock emissivity (ε = 0.90, 0.92, 0.94), evaluated against borehole 1 validation temperatures for the snow-free period of 2022.

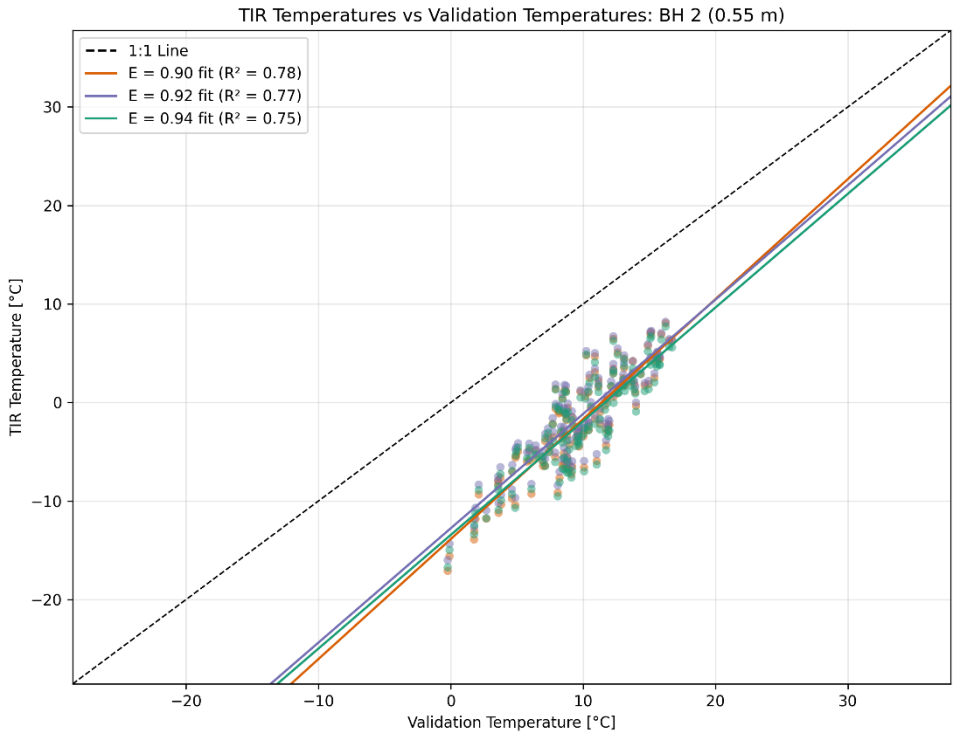

Figure B.34: Sensitivity of corrected TIR surface temperatures to rock emissivity (ε = 0.90, 0.92, 0.94), evaluated against borehole 2 validation temperatures for the snow-free period of 2022.

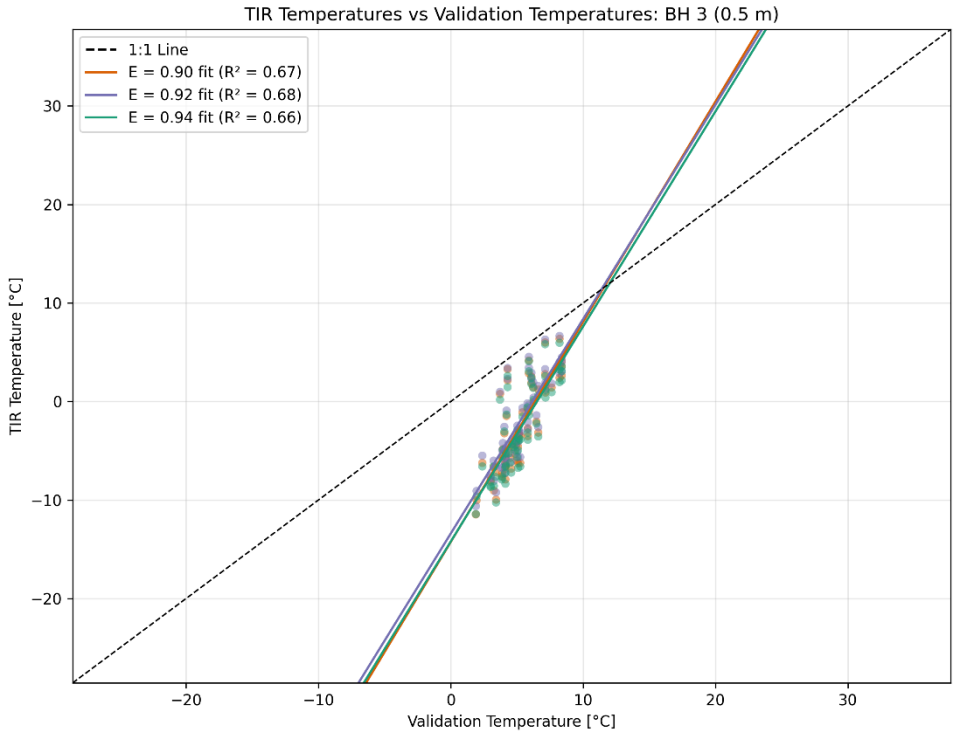

Figure B.35: Sensitivity of corrected TIR surface temperatures to rock emissivity (ε = 0.90, 0.92, 0.94), evaluated against borehole 1 validation temperatures for the snow-free period of 2022.

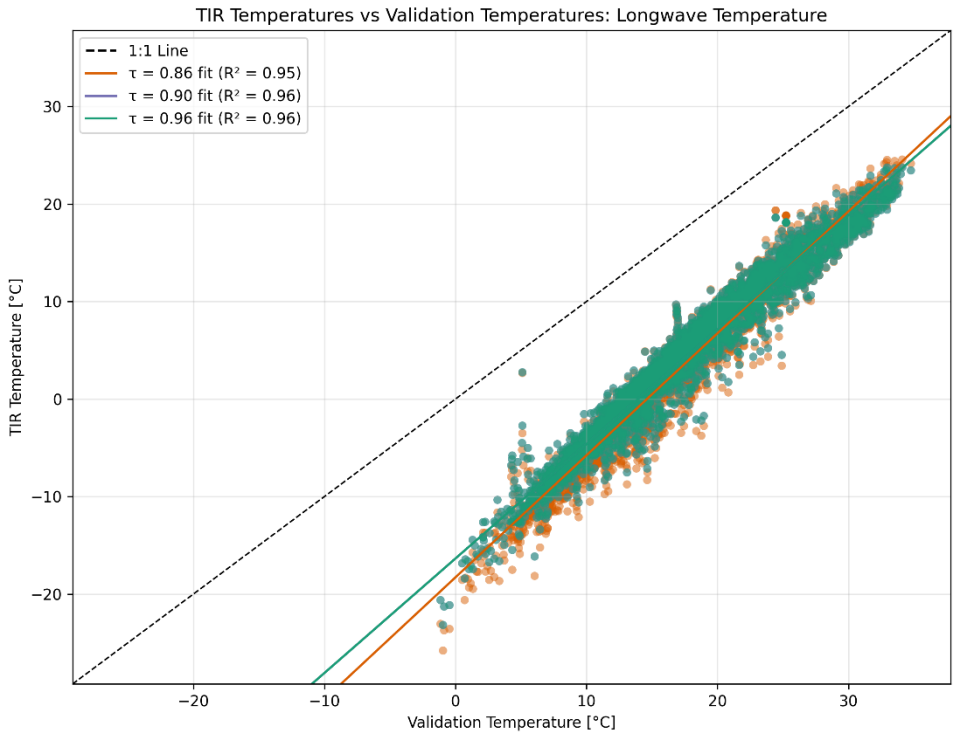

Figure B.36: Sensitivity of corrected TIR surface temperatures to window transmissivity (τ = 0.86, 0.90, 0.96), evaluated against longwave-radiation-derived validation temperatures for the snow-free period of 2022.

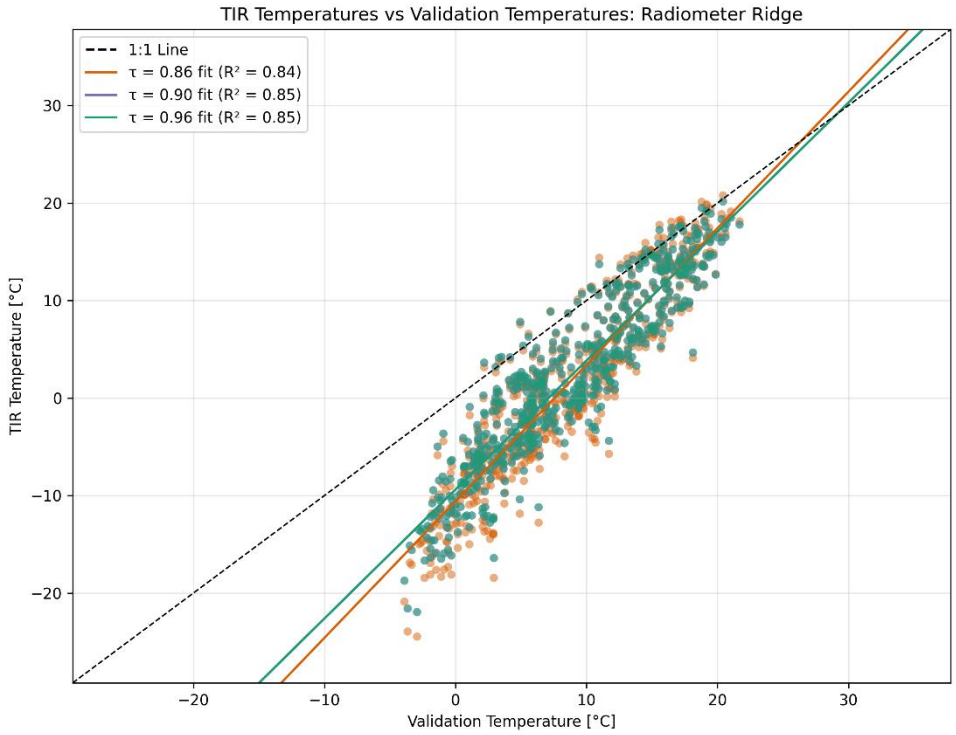

Figure B.37: Sensitivity of corrected TIR surface temperatures to window transmissivity (τ = 0.86, 0.90, 0.96), evaluated against radiometer ridge validation temperatures for the snow-free period of 2022.

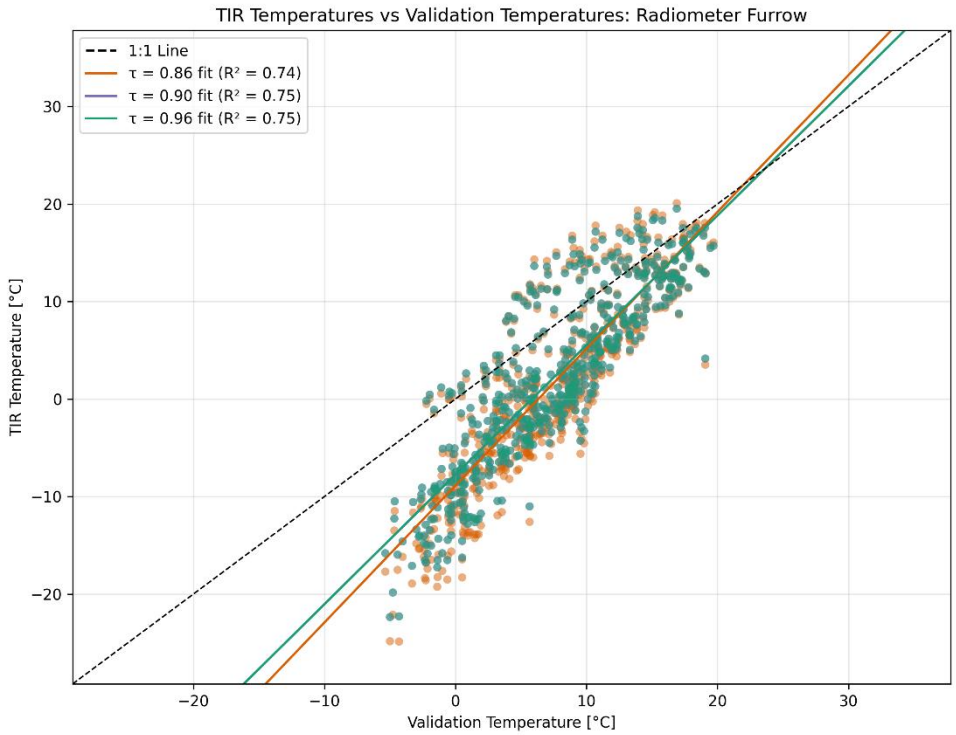

Figure B.38: Sensitivity of corrected TIR surface temperatures to window transmissivity (τ = 0.86, 0.90, 0.96), evaluated against radiometer furrow validation temperatures for the snow-free period of 2022.

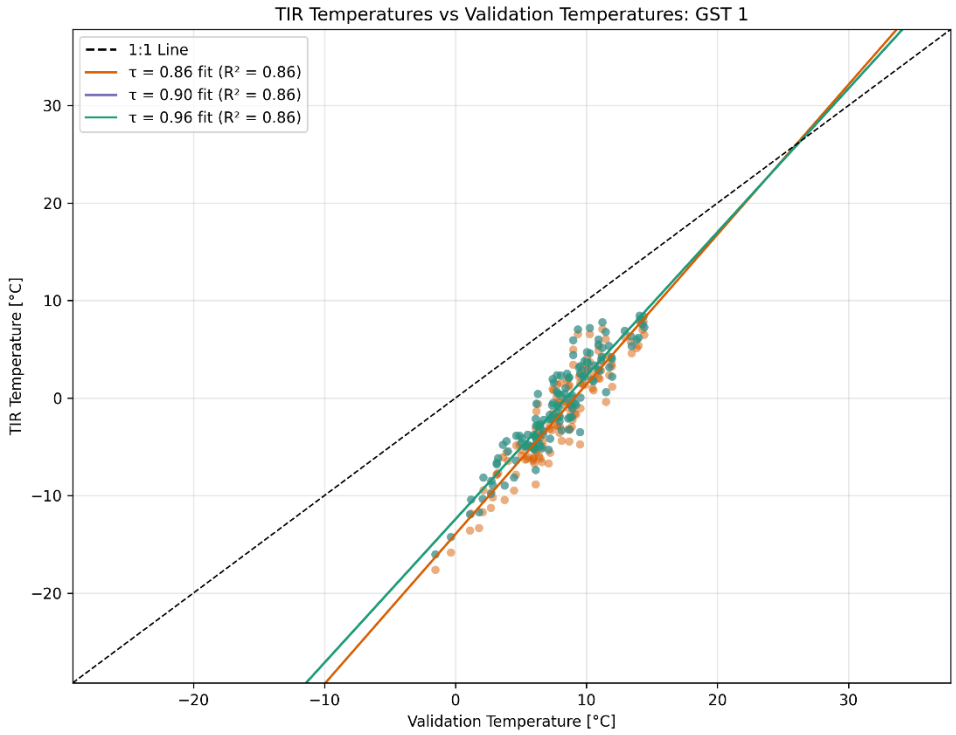

Figure B.39: Sensitivity of corrected TIR surface temperatures to window transmissivity (τ = 0.86, 0.90, 0.96), evaluated against GST 1 validation temperatures for the snow-free period of 2022.

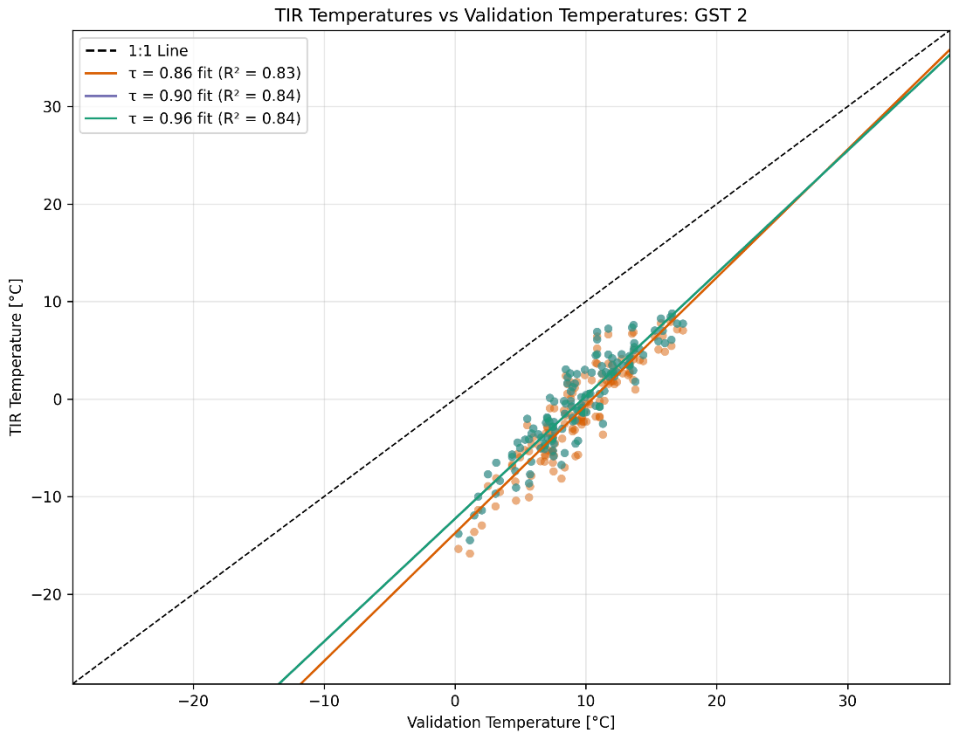

Figure B.40: Sensitivity of corrected TIR surface temperatures to window transmissivity (τ = 0.86, 0.90, 0.96), evaluated against GST 2 validation temperatures for the snow-free period of 2022.

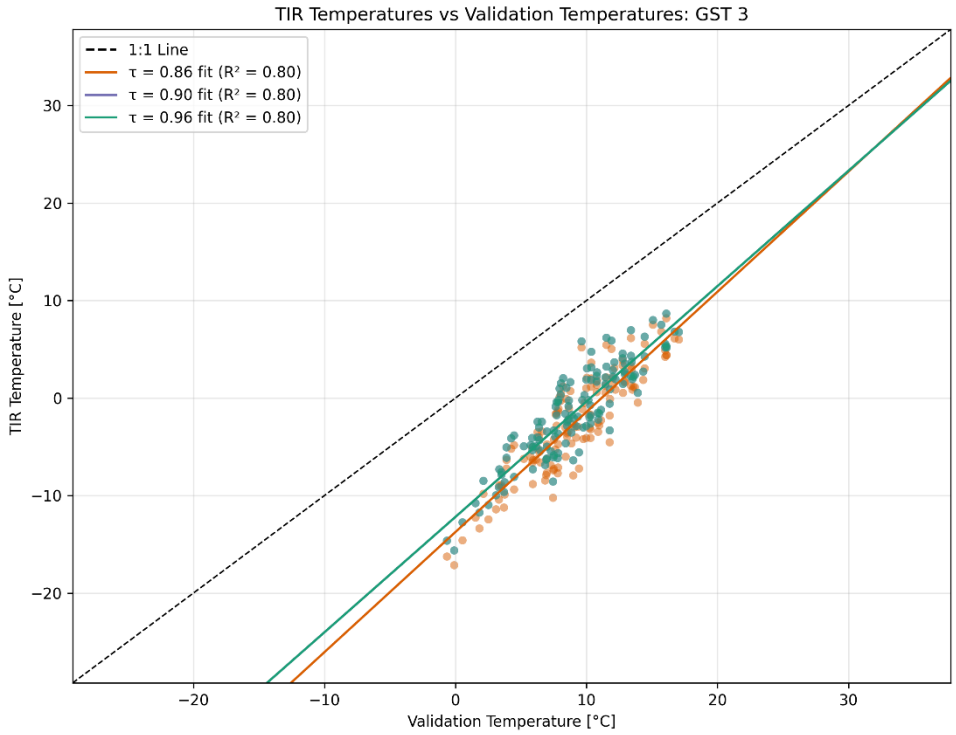

Figure B.41: Sensitivity of corrected TIR surface temperatures to window transmissivity (τ = 0.86, 0.90, 0.96), evaluated against GST 3 validation temperatures for the snow-free period of 2022.

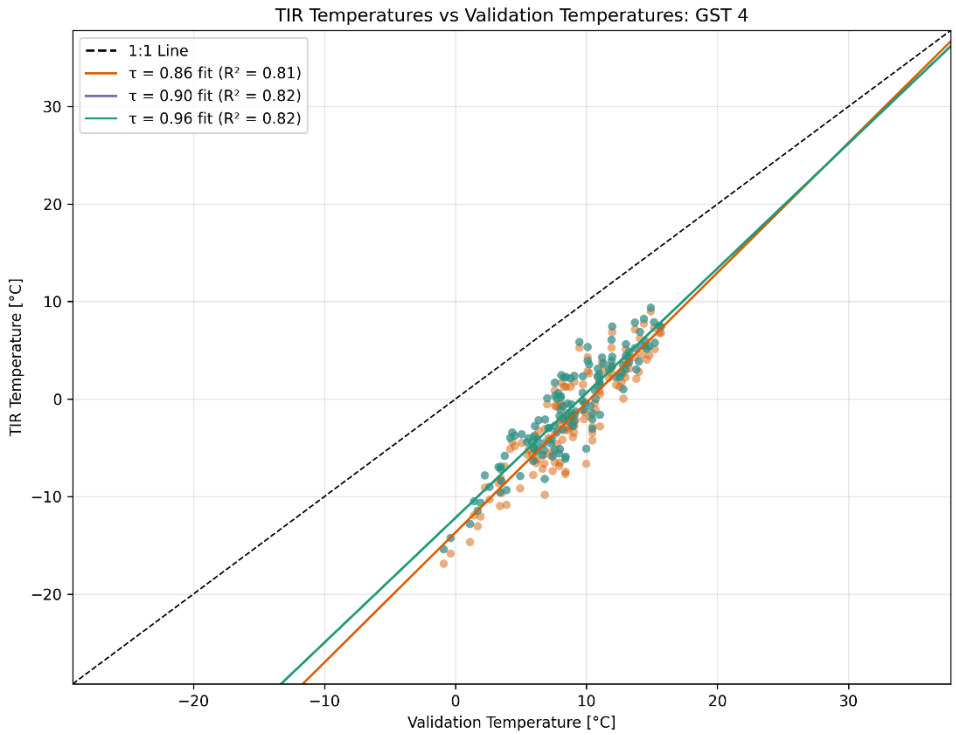

Figure B.42: Sensitivity of corrected TIR surface temperatures to window transmissivity (τ = 0.86, 0.90, 0.96), evaluated against GST 4 validation temperatures for the snow-free period of 2022.

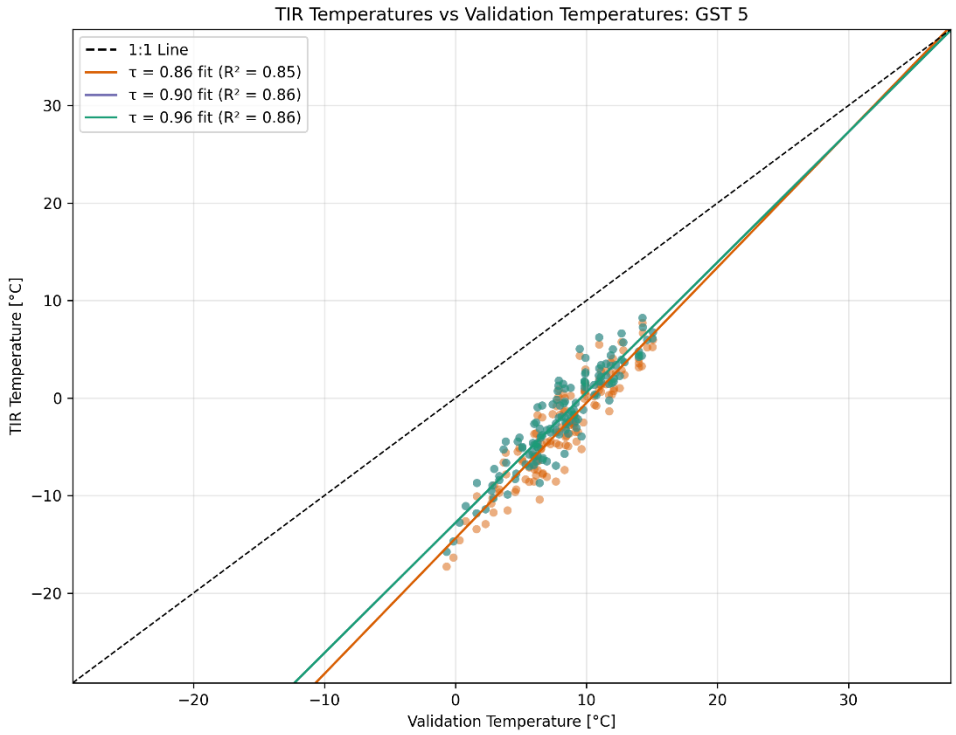

Figure B.43: Sensitivity of corrected TIR surface temperatures to window transmissivity (τ = 0.86, 0.90, 0.96), evaluated against GST 5 validation temperatures for the snow-free period of 2022.

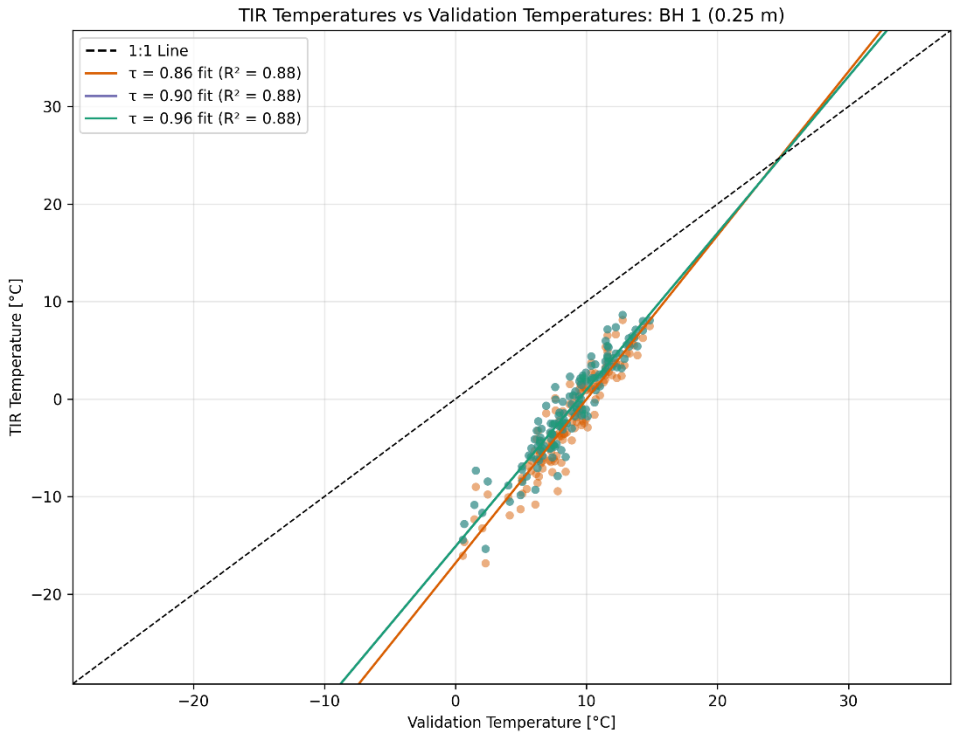

Figure B.44: Sensitivity of corrected TIR surface temperatures to window transmissivity (τ = 0.86, 0.90, 0.96), evaluated against borehole 1 validation temperatures for the snow-free period of 2022.

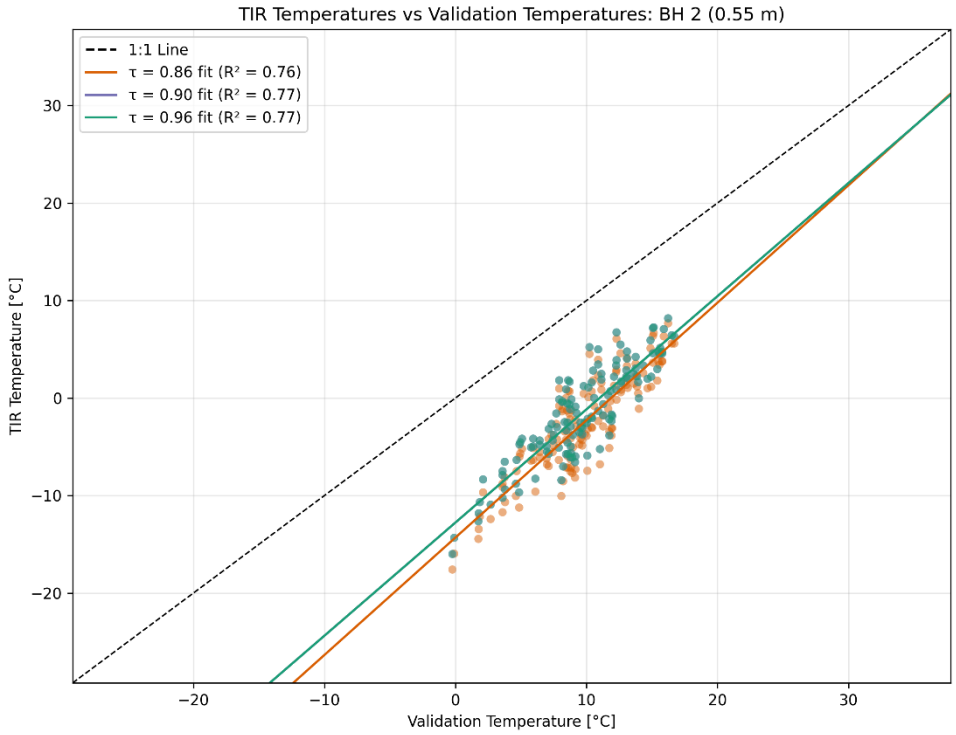

Figure B.45: Sensitivity of corrected TIR surface temperatures to window transmissivity (τ = 0.86, 0.90, 0.96), evaluated against borehole 2 validation temperatures for the snow-free period of 2022.

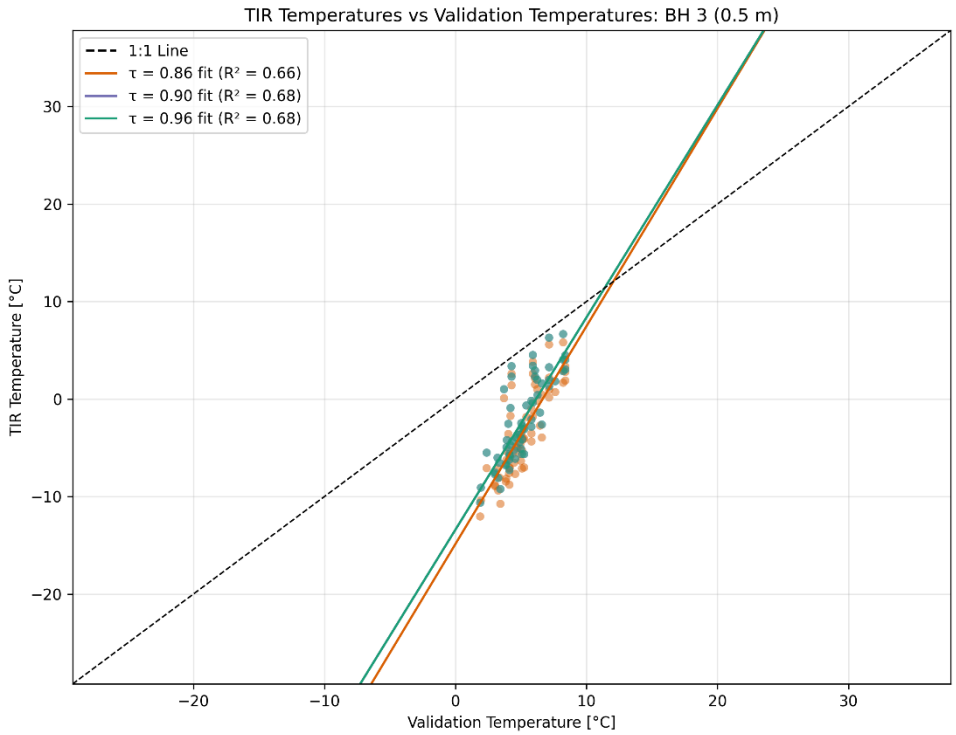

Figure B.46: Sensitivity of corrected TIR surface temperatures to window transmissivity (τ = 0.86, 0.90, 0.96), evaluated against borehole 3 validation temperatures for the snow-free period of 2022.

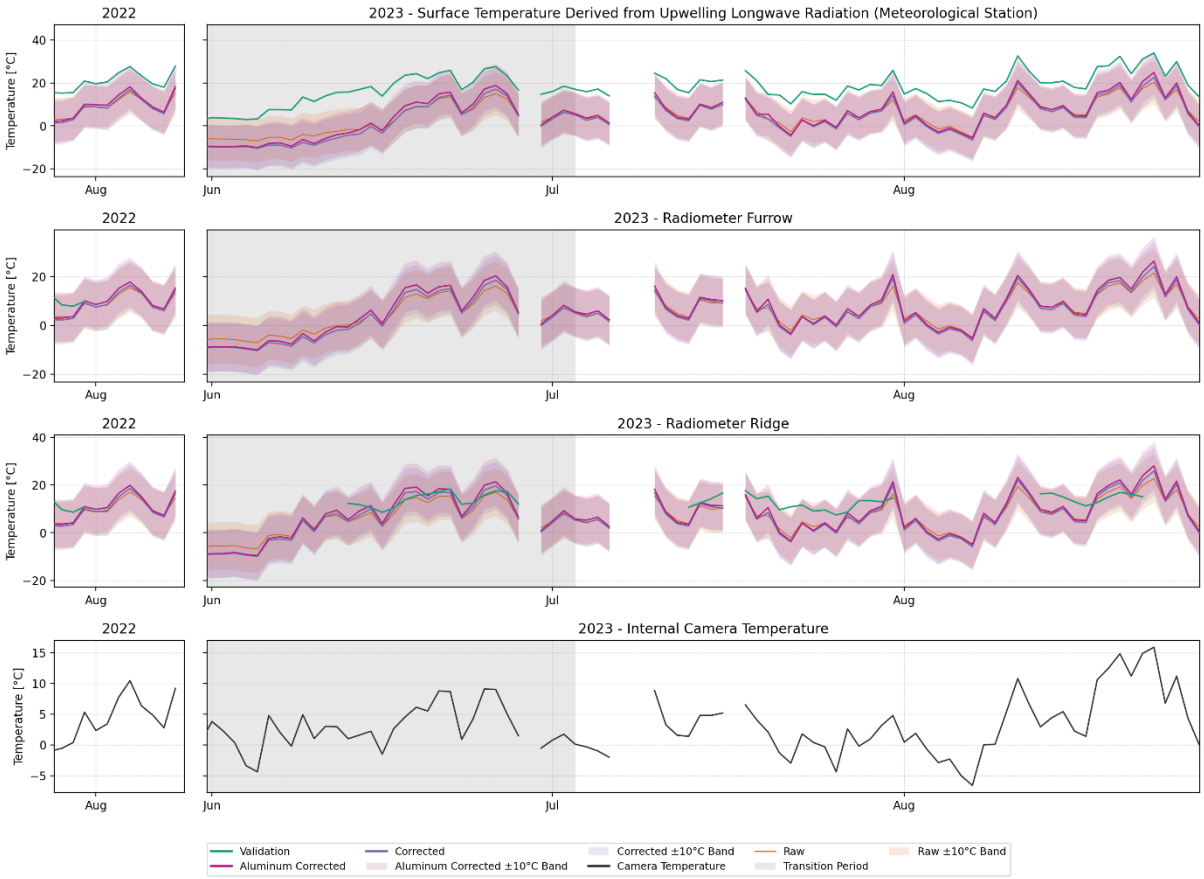

Figure B.47: Comparison of corrected, raw and aluminium-corrected TIR-derived pixel temperatures with surface temperatures derived from upwelling longwave radiation at the meteorological station, as well as with radiometer measurements at ridge and furrow locations for 2022. Grey shaded areas indicate transition periods between snow-covered and snow-free conditions. All time series represent daily mean values.

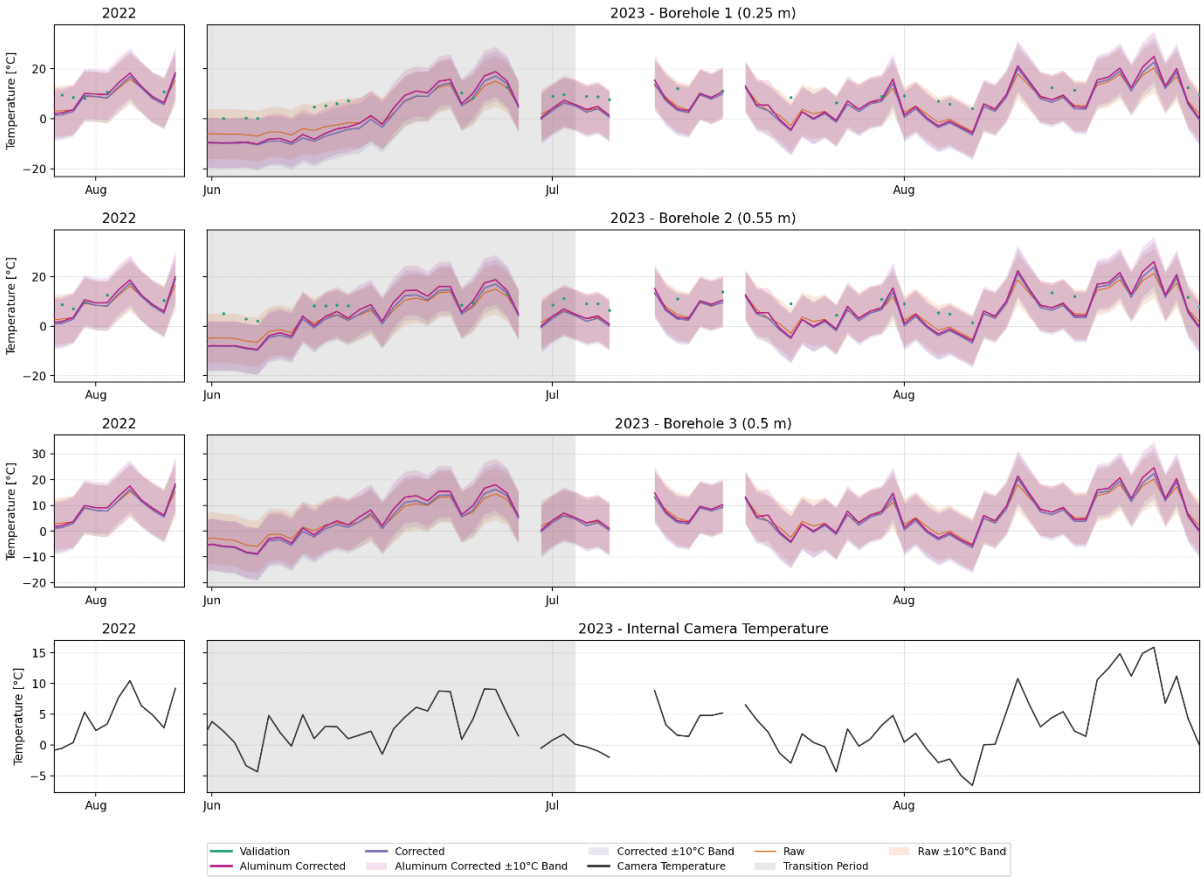

Figure B.48: Comparison of corrected, raw and aluminium-corrected TIR-derived pixel temperatures with borehole temperatures for 2023. Grey shaded areas indicate transition periods between snow-covered and snow-free conditions. All time series represent daily mean values.

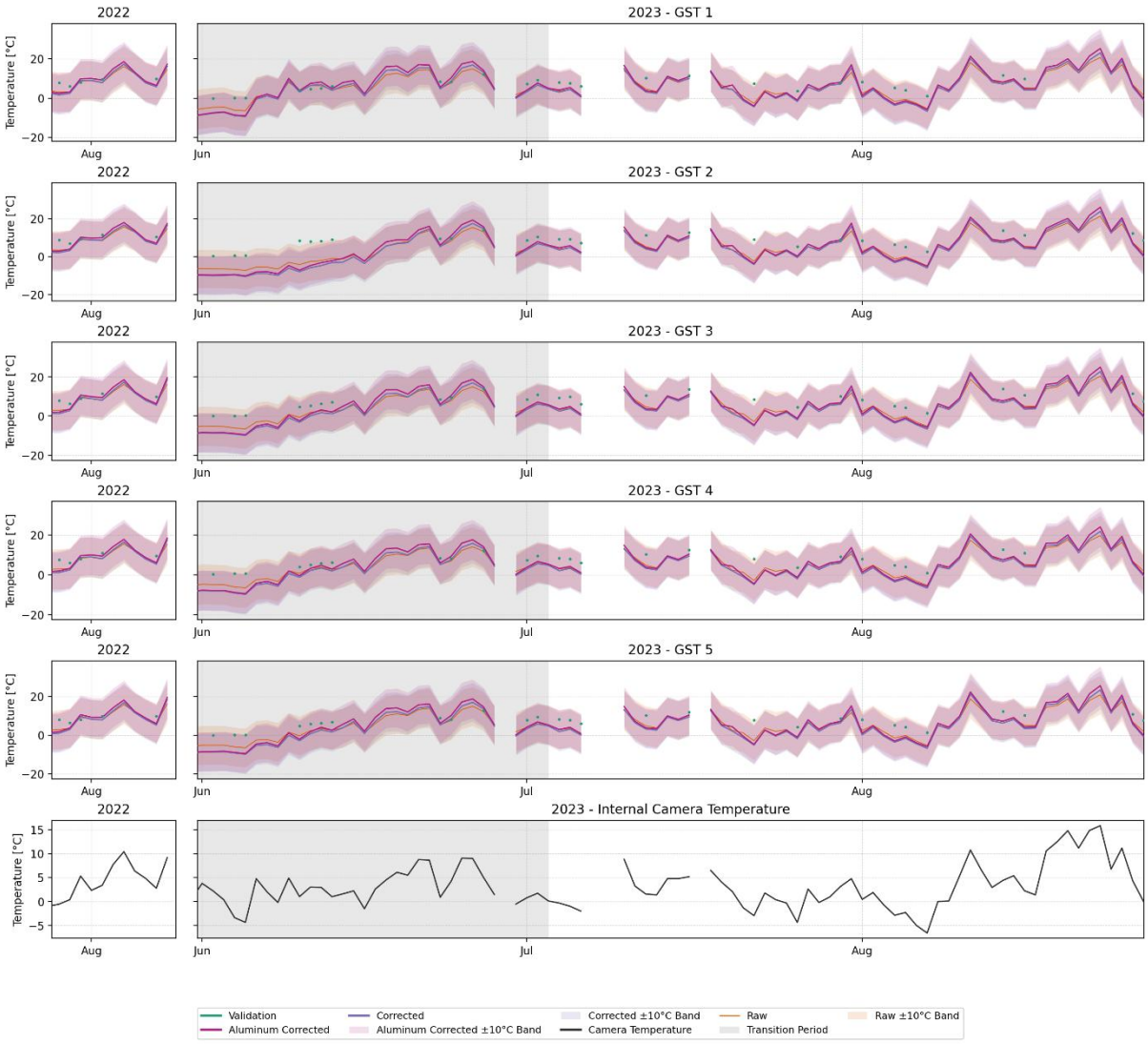

Figure B.49: Comparison of corrected, raw and aluminium-corrected TIR-derived pixel temperatures with GST logger measurements for 2023. Grey shaded areas indicate transition periods between snow-covered and snow-free conditions. All time series represent daily mean values.

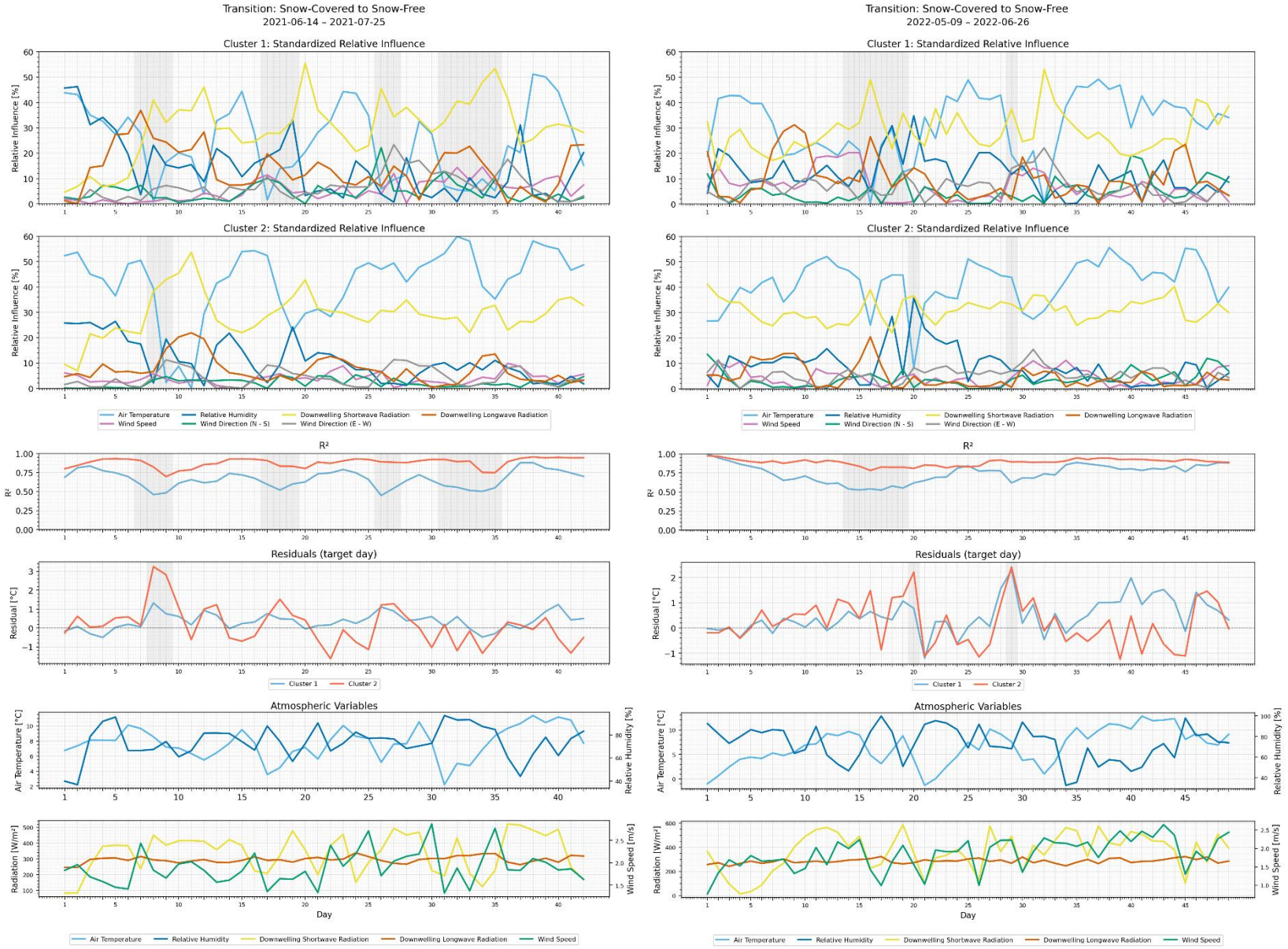

Figure C.1: Relative influence plots of seven predictor variables used in the multiple linear regression models of the diurnal curve clustering approach with corresponding R^2 and residual values and the temporal evolution of the predictor variables. Grey shaded areas indicate days which were flagged for too low R^2 or residual values. Left: Snow-Covered to Snow-Free transition 2021; right: Snow-Covered to Snow-Free transition 2022



Figure C.2: Relative influence plots of seven predictor variables used in the multiple linear regression models of the diurnal curve clustering approach with corresponding R^2 and residual values and the temporal evolution of the predictor variables. Grey shaded areas indicate days which were flagged for too low R^2 or residual values. Left: Snow-Covered to Snow-Free transition 2023; right: Snow-Free to Snow-Covered transition 2021

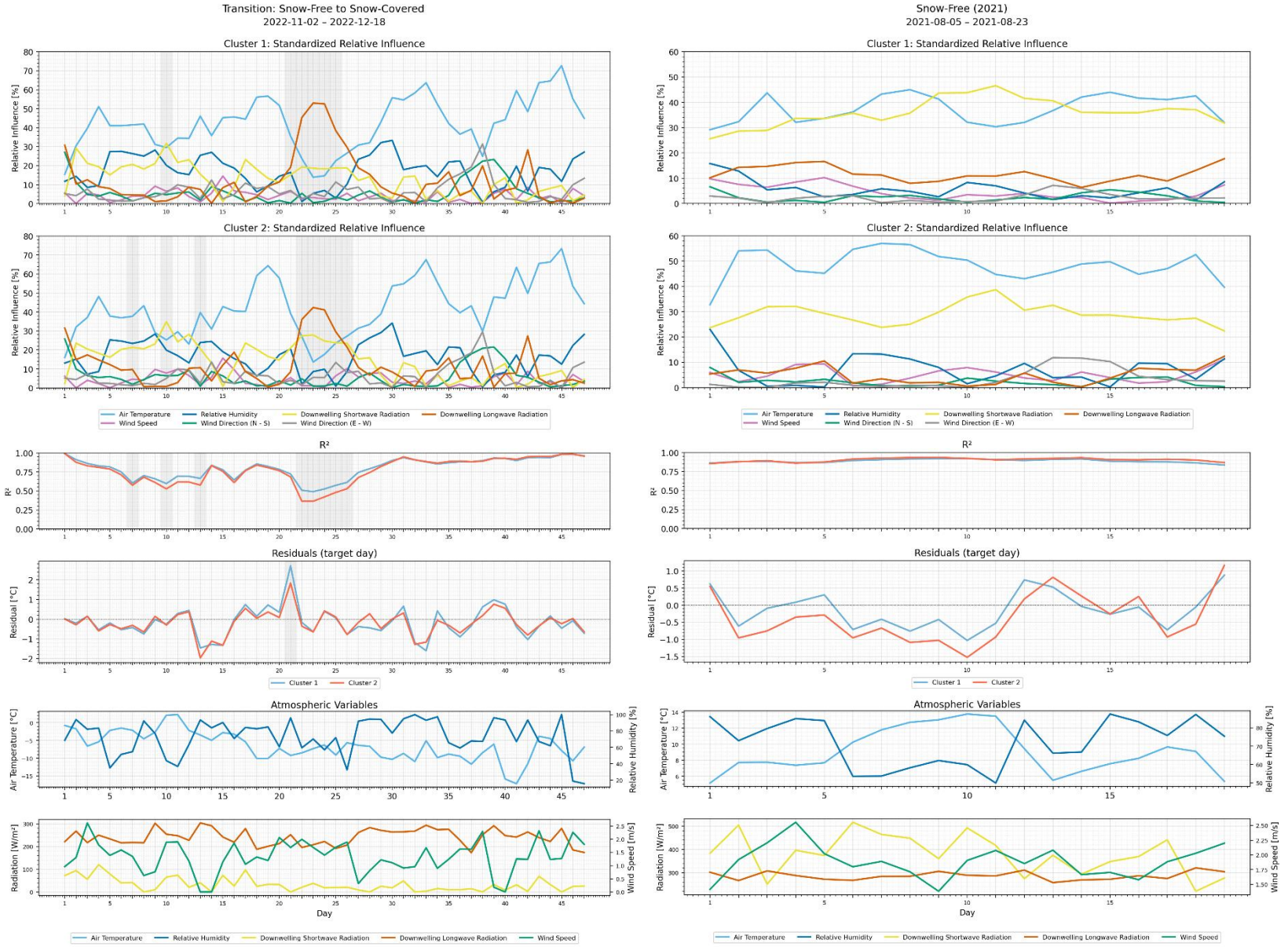

Figure C.3: Relative influence plots of seven predictor variables used in the multiple linear regression models of the diurnal curve clustering approach with corresponding R^2 and residual values and the temporal evolution of the predictor variables. Grey shaded areas indicate days which were flagged for too low R^2 or residual values. Left: Snow-Free to Snow-Covered transition 2022, right: Snow-Free period 2021

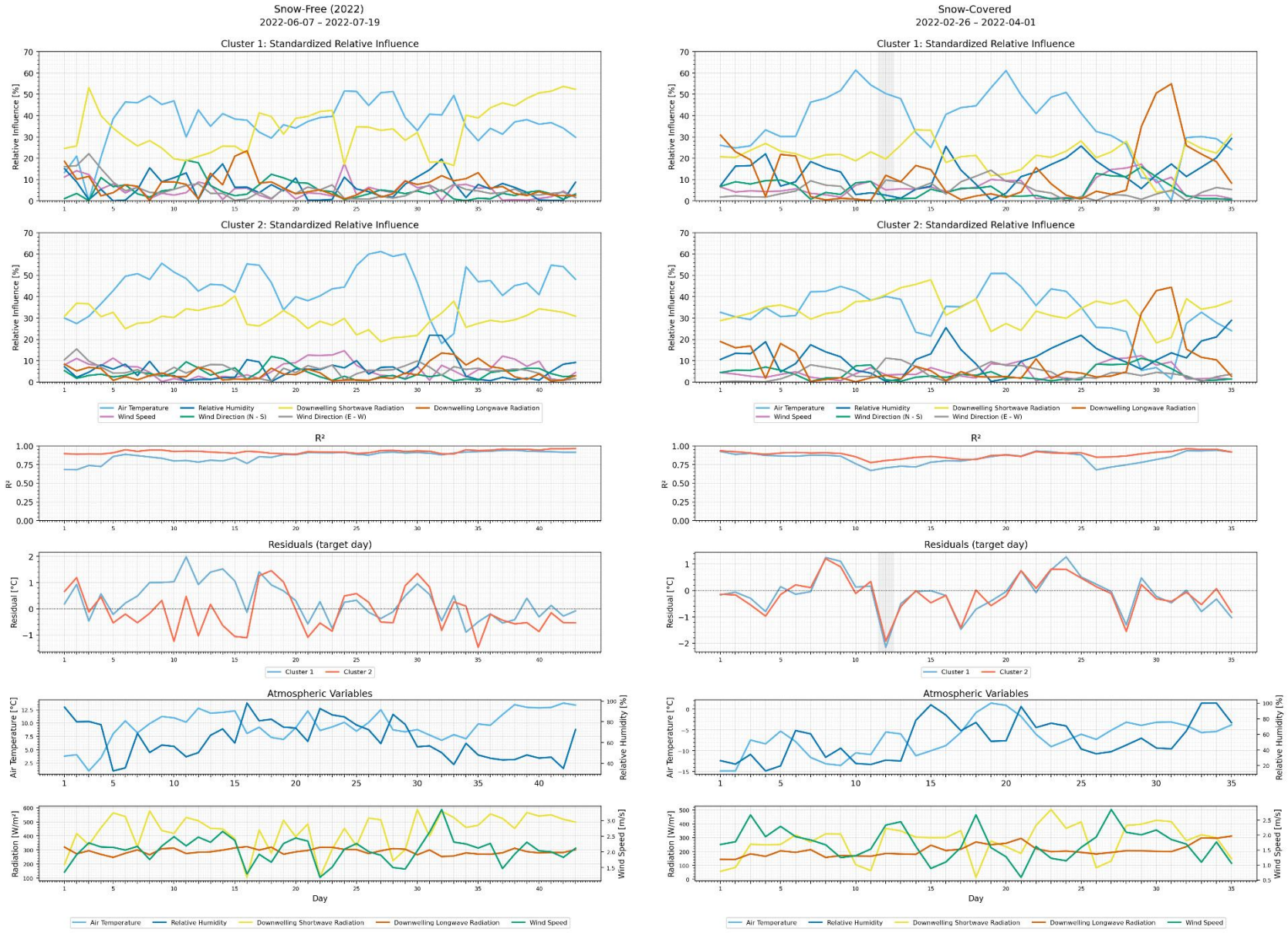

Figure C.4: Relative influence plots of seven predictor variables used in the multiple linear regression models of the diurnal curve clustering approach with corresponding R^2 and residual values and the temporal evolution of the predictor variables. Grey shaded areas indicate days which were flagged for too low R^2 or residual values. Left: Snow-Free period 2022; right: Snow-Covered period

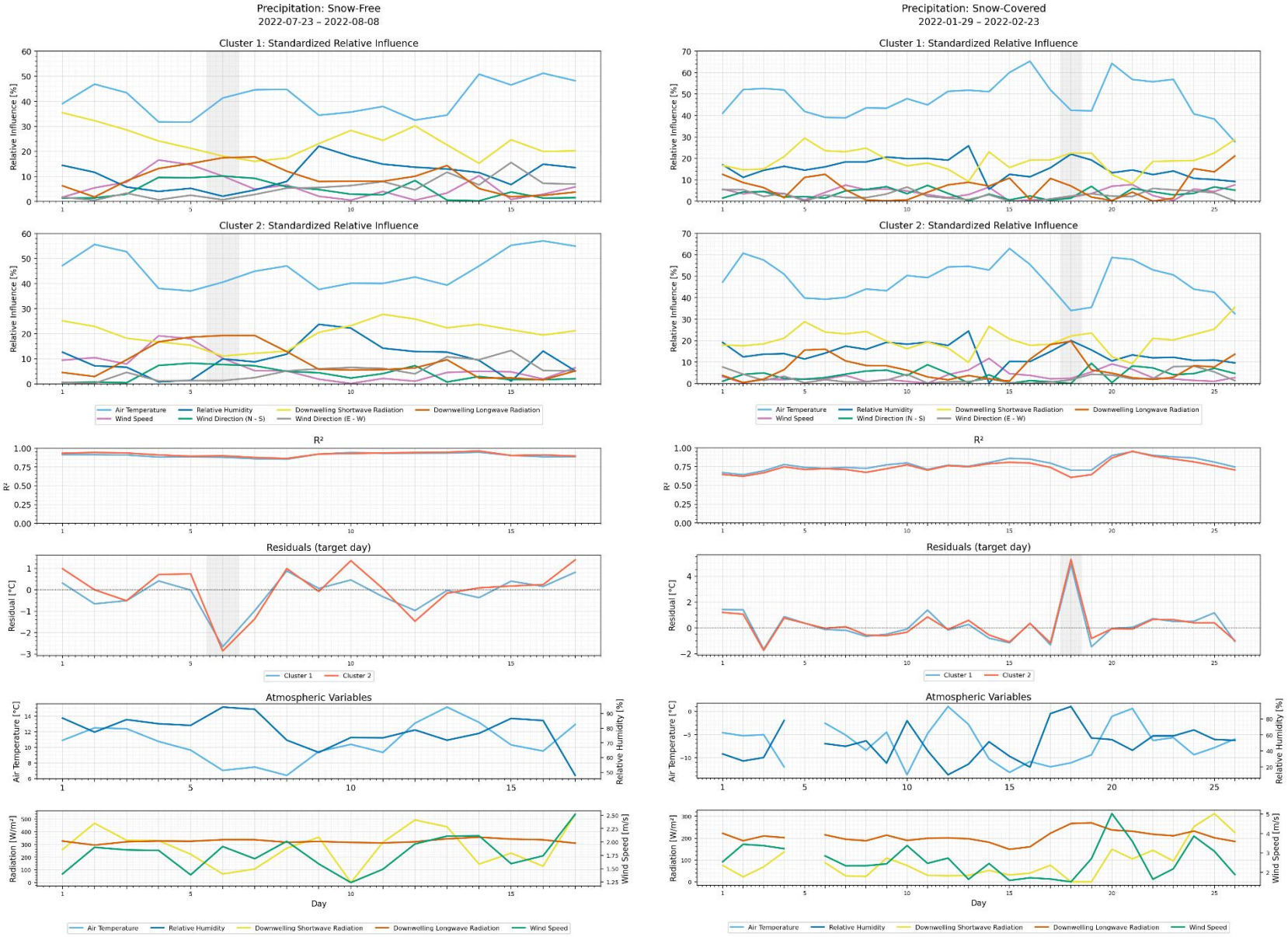

Figure C.5: Relative influence plots of seven predictor variables used in the multiple linear regression models of the diurnal curve clustering approach with corresponding R^2 and residual values and the temporal evolution of the predictor variables. Grey shaded areas indicate days which were flagged for too low R^2 or residual values. Left: Snow- Free Precipitation period; right: Snow-Covered Precipitation period

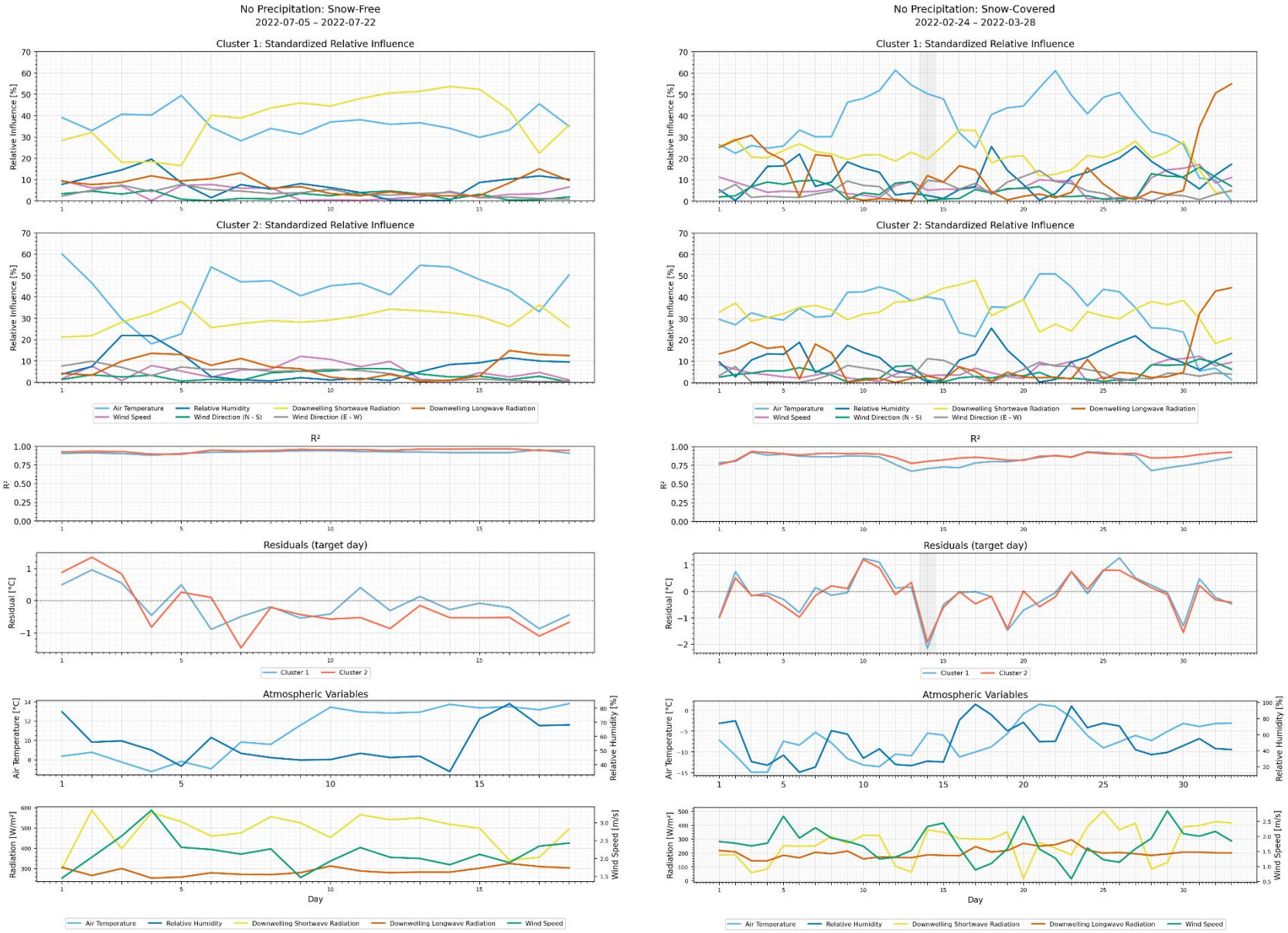

Figure C.6: Relative influence plots of seven predictor variables used in the multiple linear regression models of the diurnal curve clustering approach with corresponding R^2 and residual values and the temporal evolution of the predictor variables. Grey shaded areas indicate days which were flagged for too low R^2 or residual values. Left: Snow-Free No Precipitation period; right: Snow-Covered Precipitation period

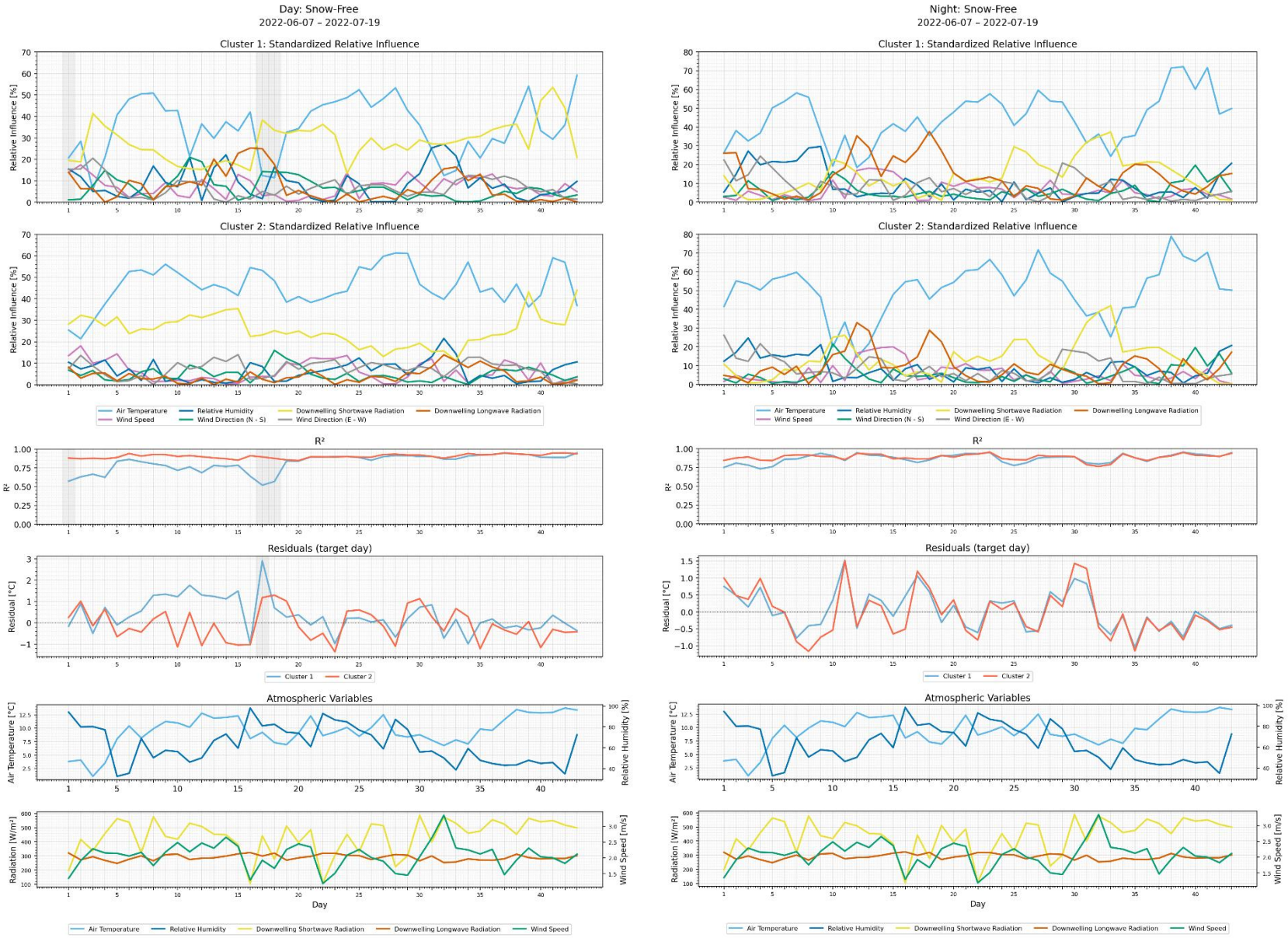

Figure C.7: Relative influence plots of seven predictor variables used in the multiple linear regression models of the diurnal curve clustering approach with corresponding R^2 and residual values and the temporal evolution of the predictor variables. Grey shaded areas indicate days which were flagged for too low R^2 or residual values. Left: Snow-Free Day period; right: Snow-Free Night period

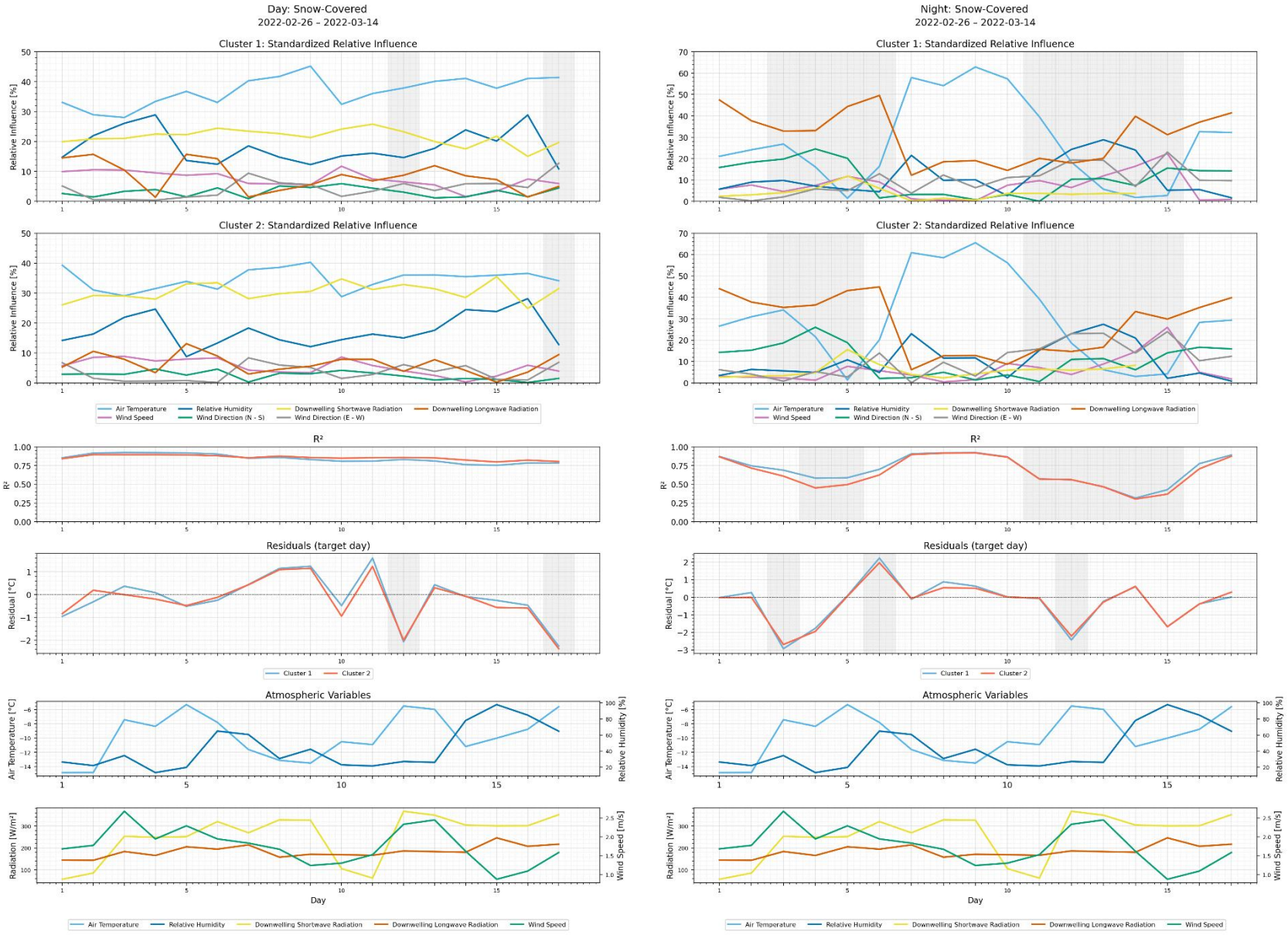

Figure C.8: Relative influence plots of seven predictor variables used in the multiple linear regression models of the diurnal curve clustering approach with corresponding R^2 and residual values and the temporal evolution of the predictor variables. Grey shaded areas indicate days which were flagged for too low R^2 or residual values. Left: Snow-Covered Day period; right: Snow-Covered Night period

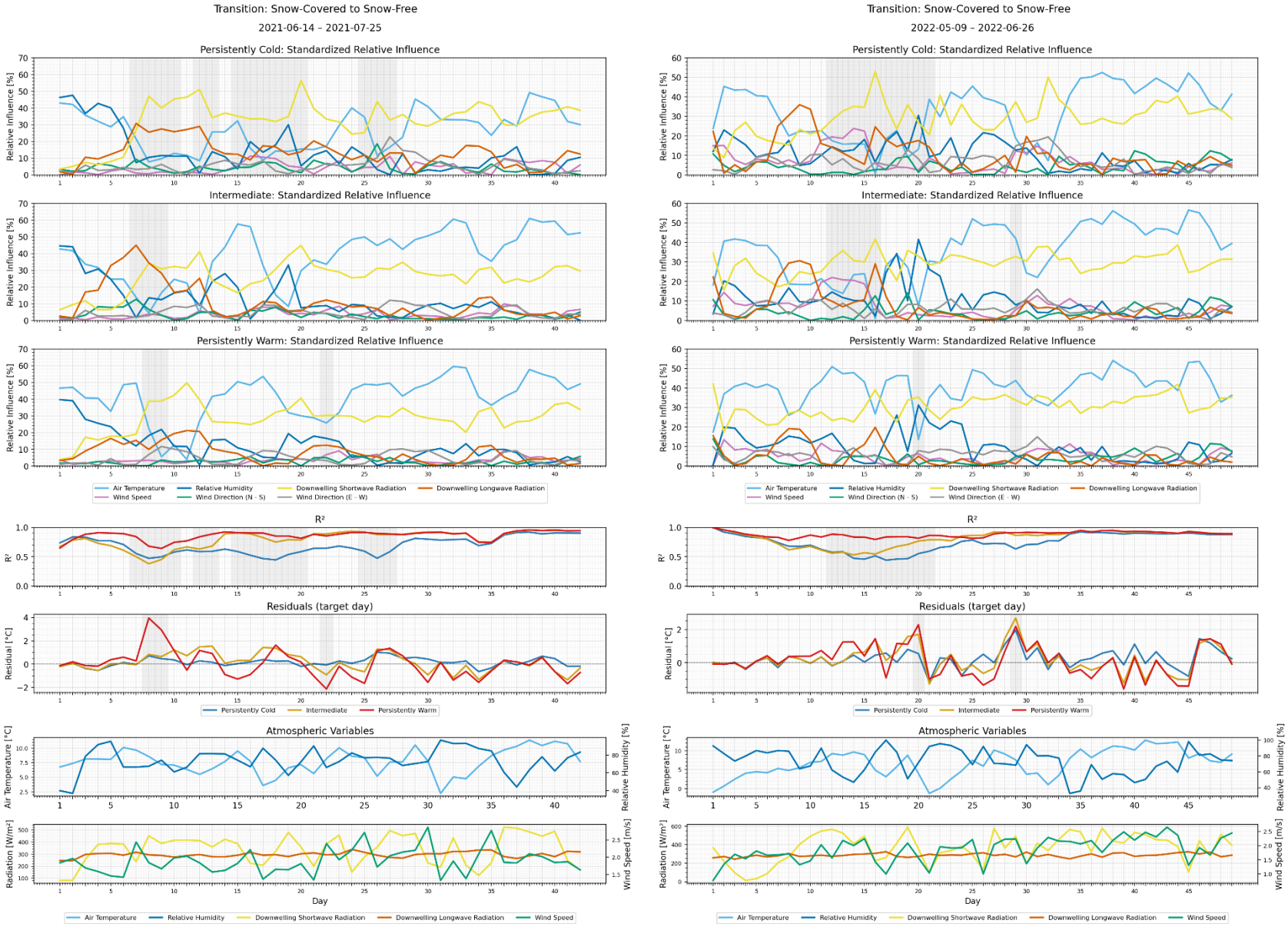

Figure C.9: Relative influence plots of seven predictor variables used in the multiple linear regression models of the anomaly persistence classification approach with corresponding R^2 and residual values and the temporal evolution of the predictor variables. Grey shaded areas indicate days which were flagged for too low R^2 or residual values. Left: Snow-Covered to Snow-Free transition 2021; right: Snow-Covered to Snow-Free transition 2022

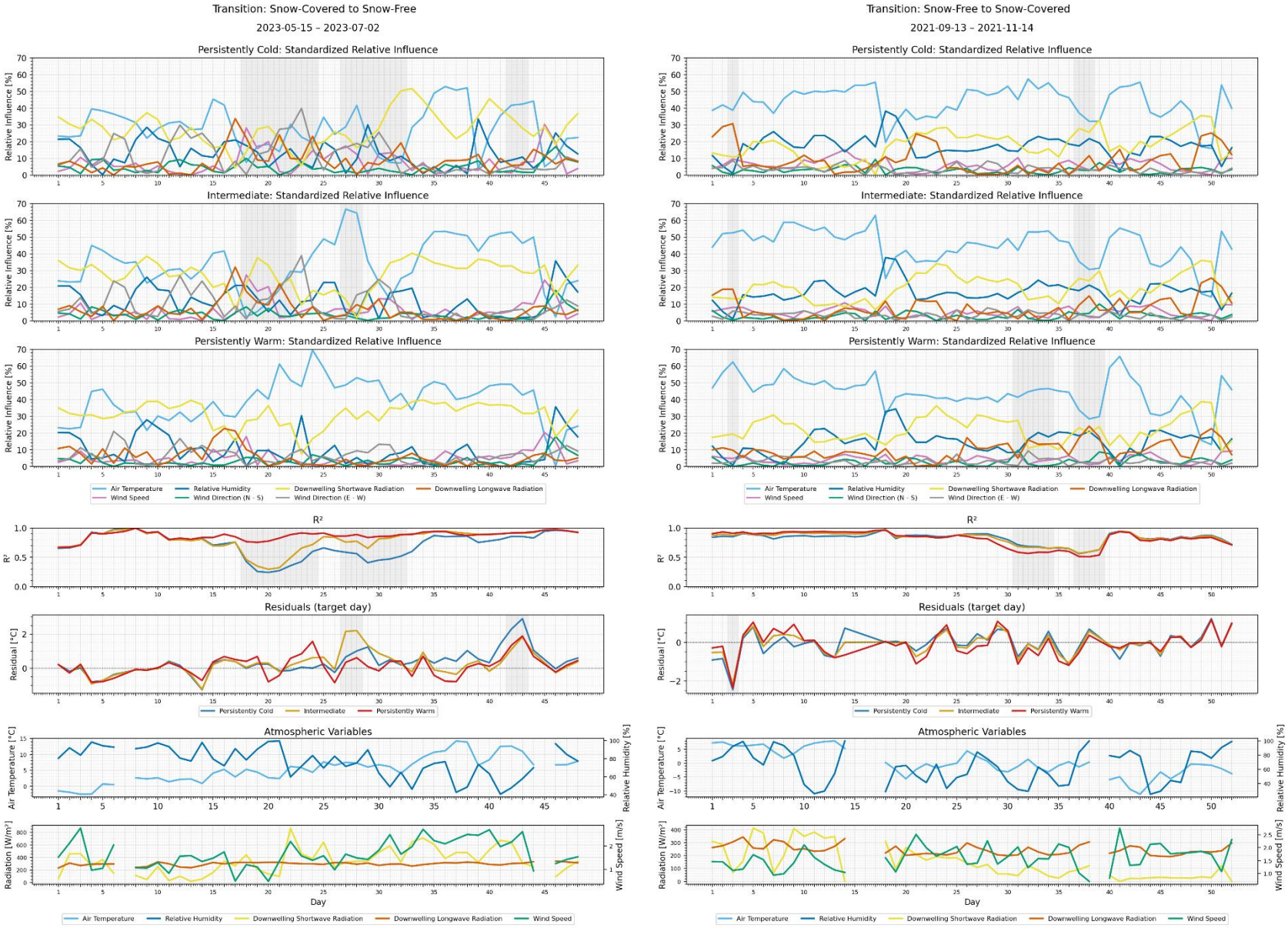

Figure C.10: Relative influence plots of seven predictor variables used in the multiple linear regression models of the anomaly persistence classification approach with corresponding R^2 and residual values and the temporal evolution of the predictor variables. Grey shaded areas indicate days which were flagged for too low R^2 or residual values. Left: Snow-Covered to Snow-Free transition 2023; right: Snow-Free to Snow-Covered transition 2021

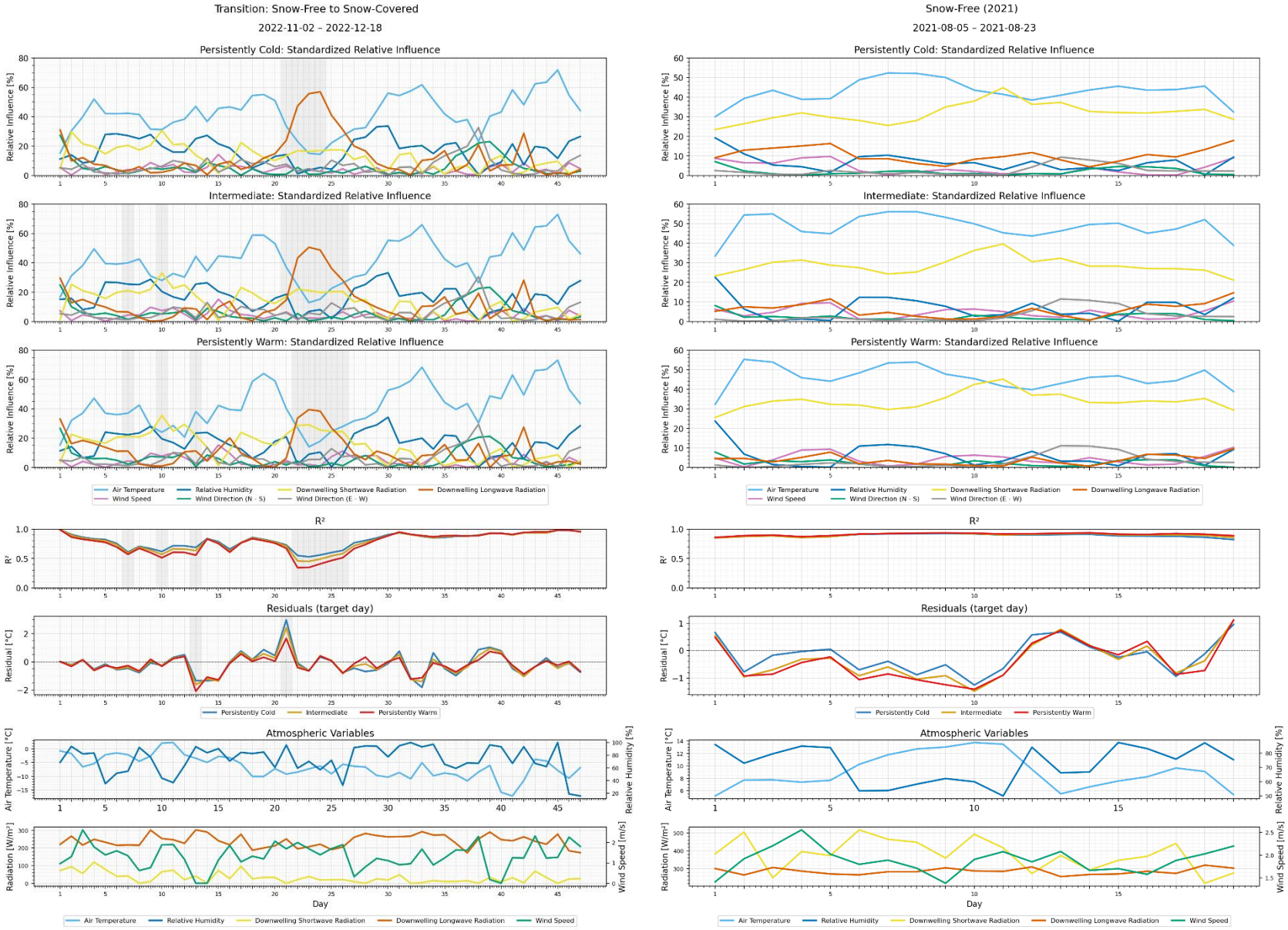

Figure C.11: Relative influence plots of seven predictor variables used in the multiple linear regression models of the anomaly persistence classification approach with corresponding R^2 and residual values and the temporal evolution of the predictor variables. Grey shaded areas indicate days which were flagged for too low R^2 or residual values. Left: Snow-Free to Snow-Covered transition 2022; right: Snow-Free period 2021

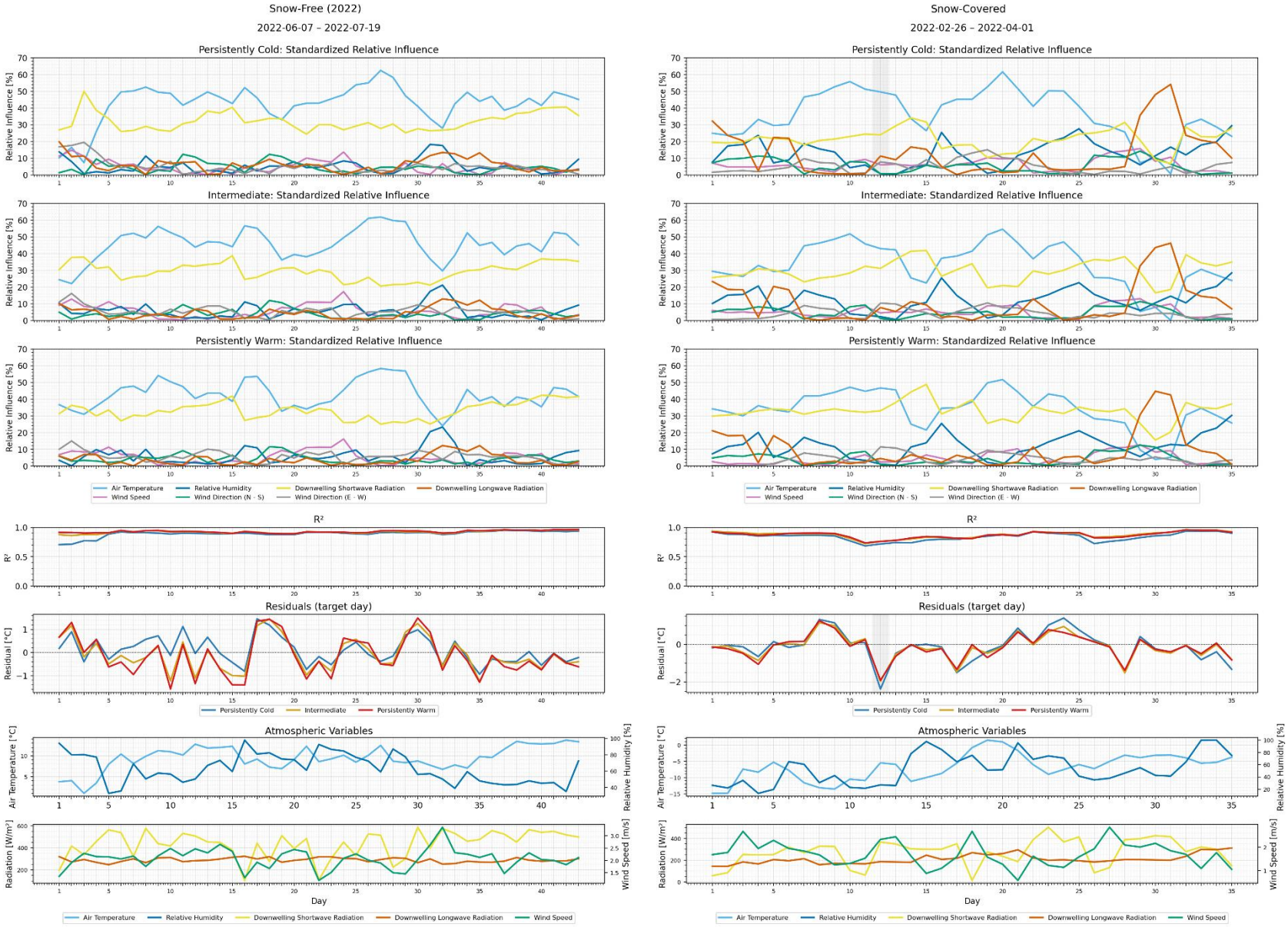

Figure C.12: Relative influence plots of seven predictor variables used in the multiple linear regression models of the anomaly persistence classification approach with corresponding R^2 and residual values and the temporal evolution of the predictor variables. Grey shaded areas indicate days which were flagged for too low R^2 or residual values. Left: Snow-Free period 2022; right: Snow-Covered period 2022

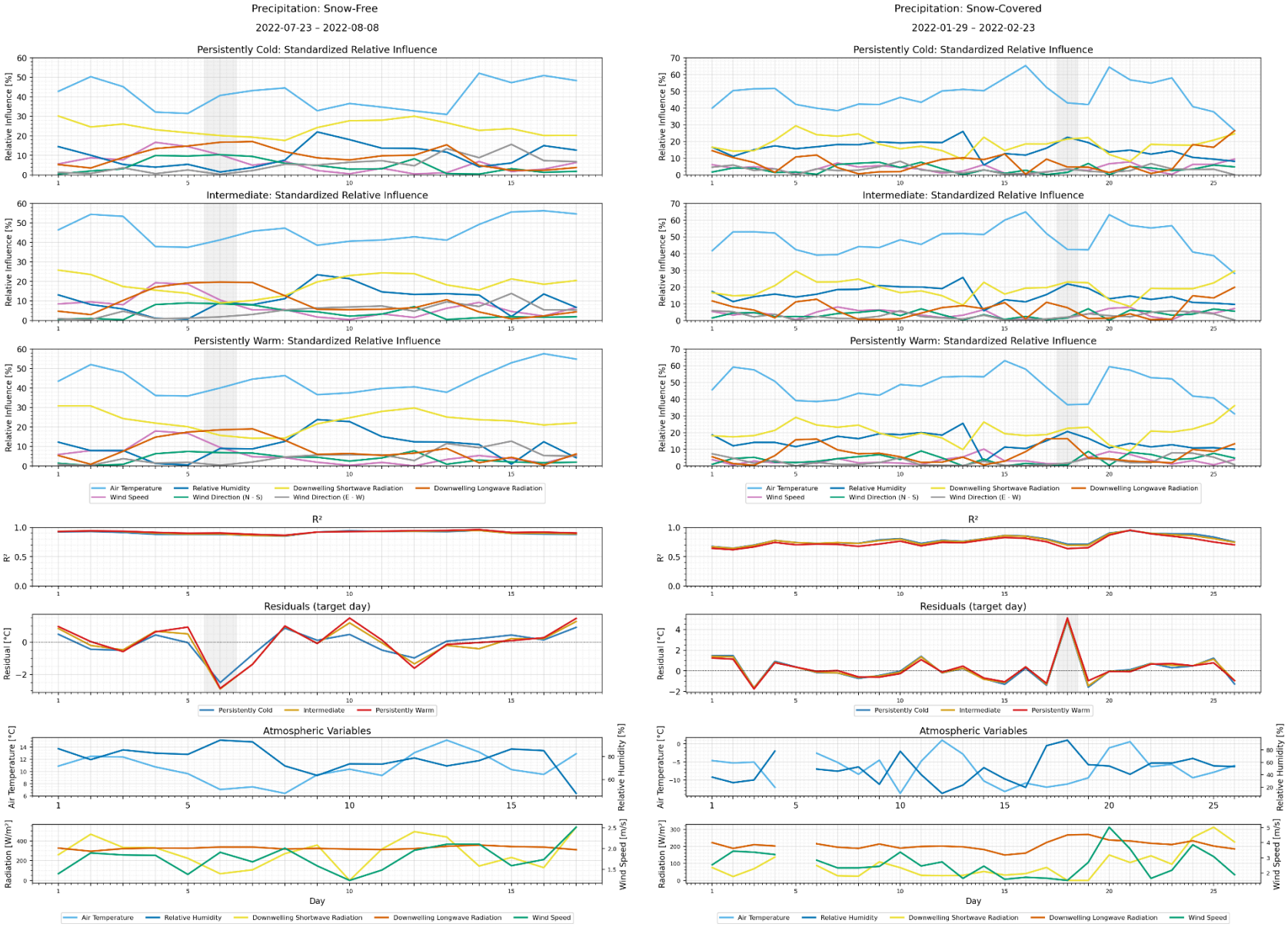

Figure C.13: Relative influence plots of seven predictor variables used in the multiple linear regression models of the anomaly persistence classification approach with corresponding R^2 and residual values and the temporal evolution of the predictor variables. Grey shaded areas indicate days which were flagged for too low R^2 or residual values. Left: Snow-Free Precipitation period, right: Snow-Covered Precipitation period

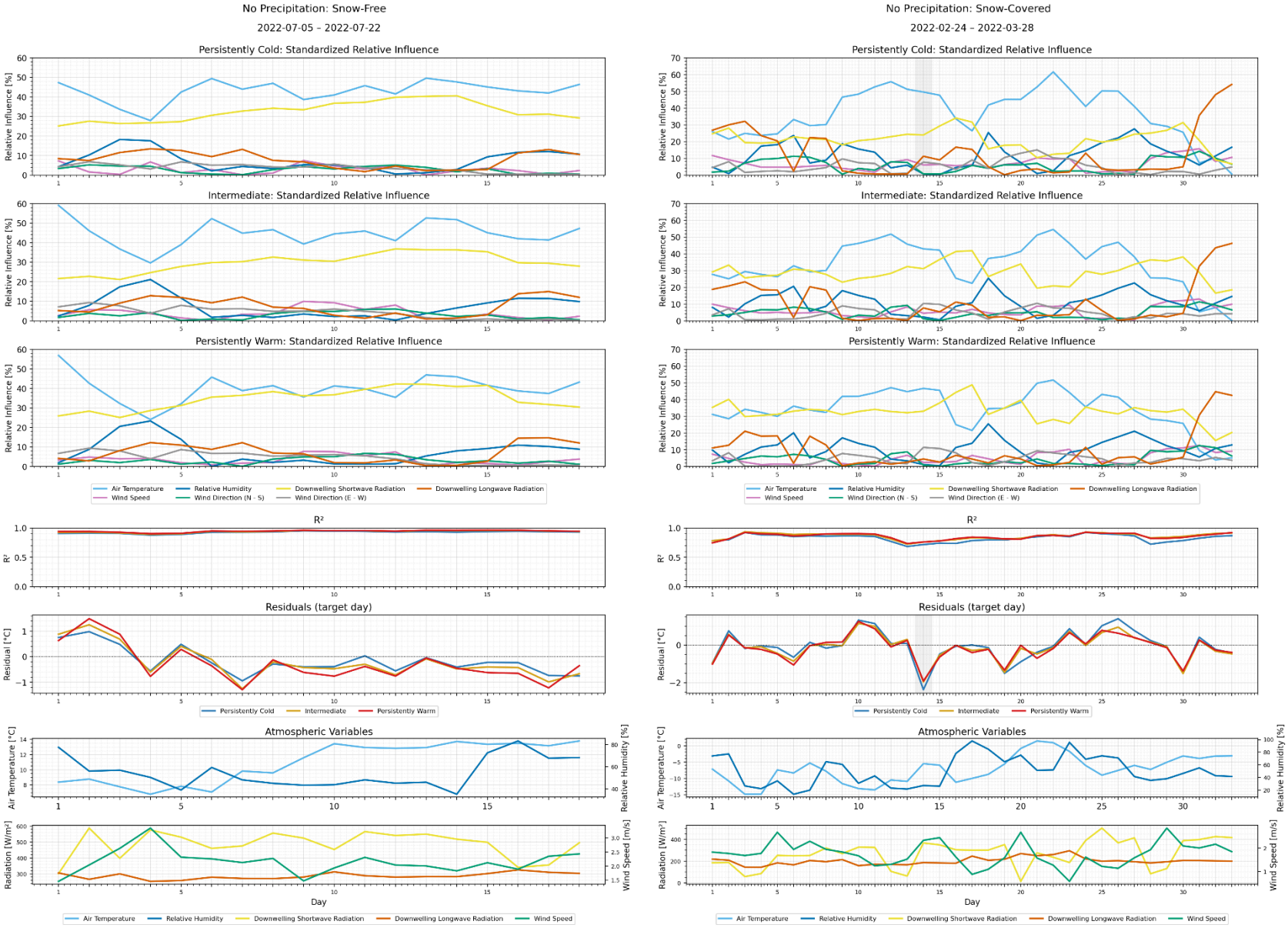

Figure C.14: Relative influence plots of seven predictor variables used in the multiple linear regression models of the anomaly persistence classification approach with corresponding R^2 and residual values and the temporal evolution of the predictor variables. Grey shaded areas indicate days which were flagged for too low R^2 or residual values. Left: Snow-Free No Precipitation period, right: Snow-Covered No Precipitation period

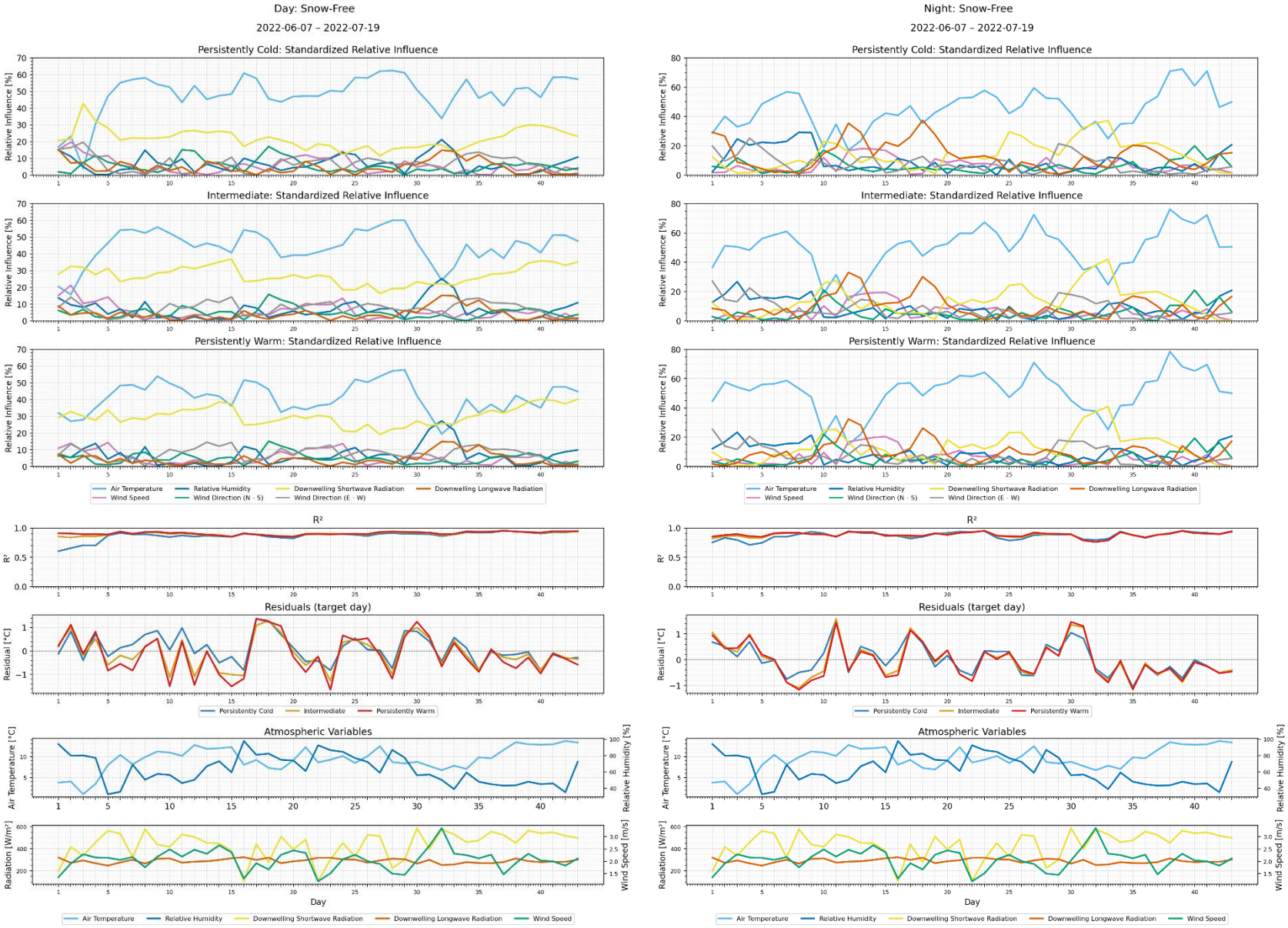

Figure C.15: Relative influence plots of seven predictor variables used in the multiple linear regression models of the anomaly persistence classification approach with corresponding R^2 and residual values and the temporal evolution of the predictor variables. Grey shaded areas indicate days which were flagged for too low R^2 or residual values. Left: Snow-Free Day period, right: Snow-Free Night period

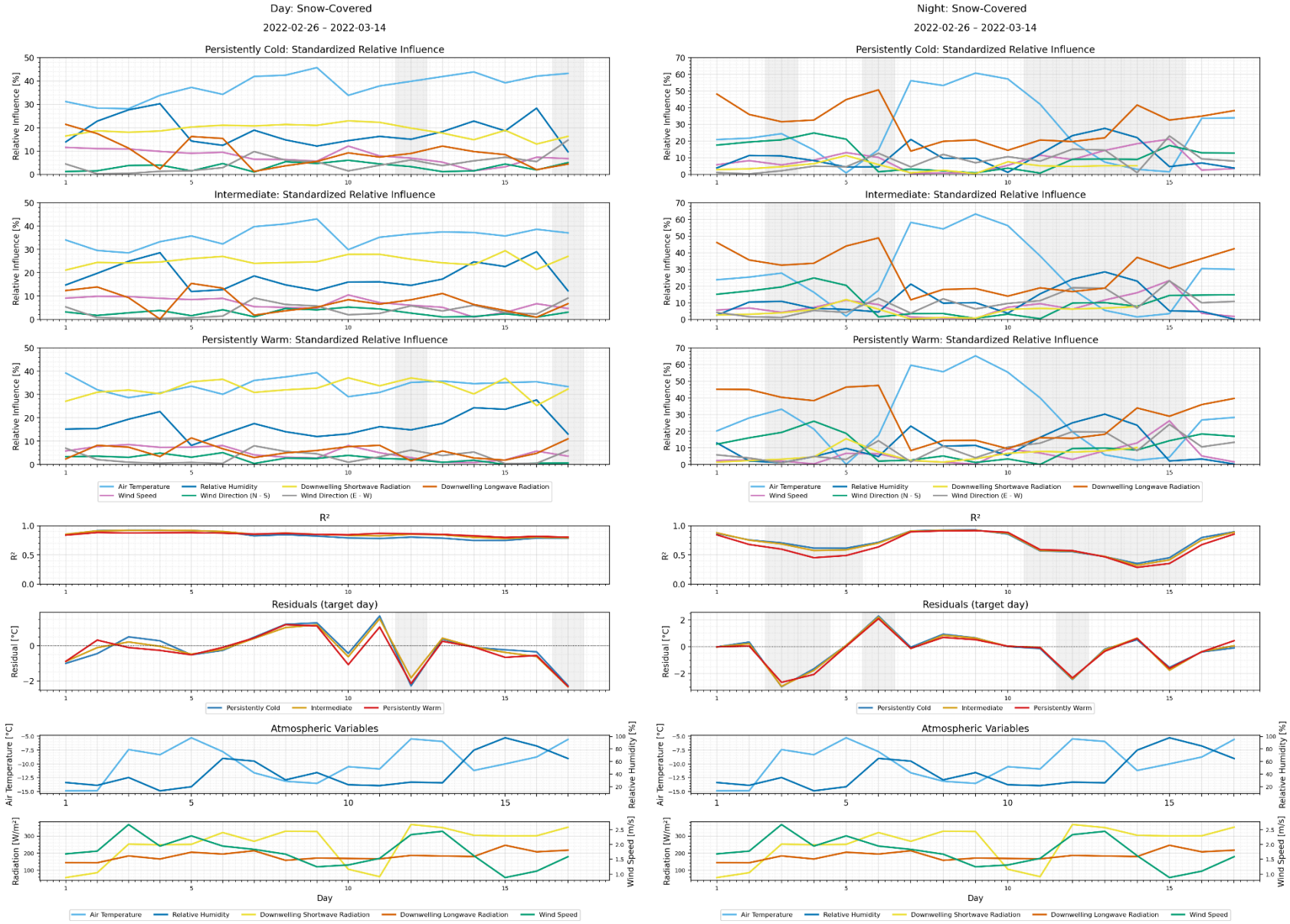

Figure C.16: Relative influence plots of seven predictor variables used in the multiple linear regression models of the anomaly persistence classification approach with corresponding R^2 and residual values and the temporal evolution of the predictor variables. Grey shaded areas indicate days which were flagged for too low R^2 or residual values. Left: Snow-Covered Day period, right: Snow-Covered Night period

Table C.1: Summary of multiple linear regression results based on groups from the diurnal curve clustering approach for transition periods. Values represent the number of observations (n), mean, standard deviation, minimum and maximum R^2 across all days within each subgroup and cluster. Driver importance is determined based on the cumulative rank of standardized regression coefficients across all days. Values in parentheses denote how often a variable was the dominant driver in this period (i.e. ranked first in influence). Cluster 1 represents the cooler temperature curve, while cluster 2 represents the warmer temperature curve.

TRANSITION PERIODS				
	Snow-Covered to **Snow-Free**		**Snow-Free** to **Snow-Covered**	
	Cluster 1	**Cluster 2**	**Cluster 1**	**Cluster 2**
N DAYS	140	140	102	102
R^2 MEAN	0.708	0.88	0.818	0.801
R^2 STD	0.139	0.066	0.118	0.152
R^2 MAX	1	0.992	1	1
R^2 MIN	0.306	0.603	0.49	0.364
FIRST DRIVER	Downwelling Shortwave Radiation (39%)	Air Temperature (76%)	Air Temperature (84%)	Air Temperature (87%)
SECOND DRIVER	Air Temperature (46%)	Downwelling Shortwave Radiation (23%)	Relative Humidity (2%)	Downwelling Shortwave Radiation (4%)
THIRD DRIVER	Relative Humidity (7%)	Relative Humidity (1%)	Downwelling Shortwave Radiation (7%)	Relative Humidity (1%)
FOURTH DRIVER	Downwelling Longwave Radiation (4%)	Downwelling Longwave Radiation (1%)	Downwelling Longwave Radiation (6%)	Downwelling Longwave Radiation (7%)
FIFTH DRIVER	Wind Direction (E–W) (1%)	Wind Direction (E–W) (0%)	Wind Speed (0%)	Wind Speed (0%)
SIXTH DRIVER	Wind Speed (2%)	Wind Speed (0%)	Wind Direction (E–W) (1%)	Wind Direction (E–W) (1%)
SEVENTH DRIVER	Wind Direction (N–S) (0%)	Wind Direction (N–S) (0%)	Wind Direction (N–S) (0%)	Wind Direction (N–S) (0%)

Table C.2: Summary of multiple linear regression results based on groups from the diurnal curve clustering approach for snow-free and snow-covered periods. Values represent the number of observations (n), mean, standard deviation, minimum and maximum R^2 across all days within each subgroup and cluster. Driver importance is determined based on the cumulative rank of standardized regression coefficients across all days. Values in parentheses denote how often a variable was the dominant driver in this period (i.e. ranked first in influence Cluster 1 represents the cooler temperature curve, while cluster 2 represents the warmer temperature curve.

SNOW COVER VS. SNOW FREE				
	Snow-Free		**Snow-Covered**	
	Cluster 1	**Cluster 2**	**Cluster 1**	**Cluster 2**
N DAYS	62	62	35	35
R^2 MEAN	0.872	0.918	0.836	0.884
R^2 STD	0.059	0.025	0.08	0.045
R^2 MAX	0.941	0.965	0.942	0.962
R^2 MIN	0.68	0.855	0.67	0.776
FIRST DRIVER	Air Temperature (58%)	Air Temperature (92%)	Air Temperature (77%)	Downwelling Shortwave Radiation (46%)
SECOND DRIVER	Downwelling Shortwave Radiation (42%)	Downwelling Shortwave Radiation (8%)	Downwelling Shortwave Radiation (11%)	Air Temperature (46%)
THIRD DRIVER	Downwelling Longwave Radiation (0%)	Relative Humidity (0%)	Relative Humidity (0%)	Relative Humidity (0%)
FOURTH DRIVER	Relative Humidity (0%)	Wind Speed (0%)	Downwelling Longwave Radiation (11%)	Downwelling Longwave Radiation (9%)
FIFTH DRIVER	Wind Speed (0%)	Wind Direction (E–W) (0%)	Wind Speed (0%)	Wind Speed (0%)
SIXTH DRIVER	Wind Direction (N–S) (0%)	Downwelling Longwave Radiation (0%)	Wind Direction (N–S) (0%)	Wind Direction (N–S) (0%)
SEVENTH DRIVER	Wind Direction (E–W) (0%)	Wind Direction (N–S) (0%)	Wind Direction (E–W) (0%)	Wind Direction (E–W) (0%)

Table C.3: Summary of multiple linear regression results based on groups from the diurnal curve clustering approach for precipitation periods. Values represent the number of observations (n), mean, standard deviation, minimum and maximum R^2 across all days within each subgroup and cluster. Driver importance is determined based on the cumulative rank of standardized regression coefficients across all days. Values in parentheses denote how often a variable was the dominant driver in this period (i.e. ranked first in influence). Cluster 1 represents the cooler temperature curve, while cluster 2 represents the warmer temperature curve.

PRECIPITATION PERIOD VS. DRY PERIOD				
	Snow-Free Precipitation		**Snow-Covered Precipitation**	
	Cluster 1	**Cluster 2**	**Cluster 1**	**Cluster 2**
N DAYS	17	17	26	26
R^2 MEAN	0.904	0.917	0.78	0.746
R^2 STD	0.028	0.027	0.079	0.084
R^2 MAX	0.946	0.962	0.949	0.954
R^2 MIN	0.853	0.863	0.641	0.605
FIRST DRIVER	Air Temperature (100%)	Air Temperature (100%)	Air Temperature (96%)	Air Temperature (96%)
SECOND DRIVER	Downwelling Shortwave Radiation (0%)	Downwelling Shortwave Radiation (0%)	Downwelling Shortwave Radiation (4%)	Downwelling Shortwave Radiation (4%)
THIRD DRIVER	Relative Humidity (0%)	Relative Humidity (0%)	Relative Humidity (0%)	Relative Humidity (0%)
FOURTH DRIVER	Downwelling Longwave Radiation (0%)	Downwelling Longwave Radiation (0%)	Downwelling Longwave Radiation (0%)	Downwelling Longwave Radiation (0%)
FIFTH DRIVER	Wind Speed (0%)	Wind Speed (0%)	Wind Speed (0%)	Wind Direction (N–S) (0%)
SIXTH DRIVER	Wind Direction (E–W) (0%)	Wind Direction (E–W) (0%)	Wind Direction (N–S) (0%)	Wind Speed (0%)
SEVENTH DRIVER	Wind Direction (N–S) (0%)	Wind Direction (N–S) (0%)	Wind Direction (E–W) (0%)	Wind Direction (E–W) (0%)

Table C.4: Summary of multiple linear regression results based on groups from the diurnal curve clustering approach for day / night comparison during snow-free periods. Values represent the number of observations (n), mean, standard deviation, minimum and maximum R^2 across all days within each subgroup and cluster. Driver importance is determined based on the cumulative rank of standardized regression coefficients across all days. Values in parentheses denote how often a variable was the dominant driver in this period (i.e. ranked first in influence). Cluster 1 represents the cooler temperature curve, while cluster 2 represents the warmer temperature curve.

DAY VS. NIGHT (SNOW-FREE)				
	Snow-Free Day		**Snow-Free Night**	
	Cluster 1	**Cluster 2**	**Cluster 1**	**Cluster 2**
N DAYS	43	43	43	43
R^2 MEAN	0.82	0.904	0.87	0.886
R^2 STD	0.115	0.027	0.06	0.042
R^2 MAX	0.948	0.949	0.953	0.953
R^2 MIN	0.519	0.847	0.731	0.763
FIRST DRIVER	Air Temperature (67%)	Air Temperature (88%)	Air Temperature (86%)	Air Temperature (88%)
SECOND DRIVER	Downwelling Shortwave Radiation (30%)	Downwelling Shortwave Radiation (12%)	Downwelling Shortwave Radiation (7%)	Downwelling Shortwave Radiation (7%)
THIRD DRIVER	Relative Humidity (2%)	Wind Direction (E–W) (0%)	Downwelling Longwave Radiation (7%)	Downwelling Longwave Radiation (5%)
FOURTH DRIVER	Wind Speed (0%)	Relative Humidity (0%)	Relative Humidity (0%)	Relative Humidity (0%)
FIFTH DRIVER	Wind Direction (E–W) (0%)	Wind Speed (0%)	Wind Direction (E–W) (0%)	Wind Direction (E–W) (0%)
SIXTH DRIVER	Wind Direction (N–S) (0%)	Wind Direction (N–S) (0%)	Wind Speed (0%)	Wind Speed (0%)
SEVENTH DRIVER	Downwelling Longwave Radiation (0%)	Downwelling Longwave Radiation (0%)	Wind Direction (N–S) (0%)	Wind Direction (N–S) (0%)

Table C.5: Summary of multiple linear regression results based on groups from the diurnal curve clustering approach for day / night comparison during snow-free periods. Values represent the number of observations (n), mean, standard deviation, minimum and maximum R^2 across all days within each subgroup and cluster. Driver importance is determined based on the cumulative rank of standardized regression coefficients across all days. Values in parentheses denote how often a variable was the dominant driver in this period (i.e. ranked first in influence). Cluster 1 represents the cooler temperature curve, while cluster 2 represents the warmer temperature curve.

DAY VS. NIGHT (SNOW-COVERED)				
	Snow-Covered Day		**Snow-Covered Night**	
	Cluster 1	**Cluster 2**	**Cluster 1**	**Cluster 2**
N DAYS	17	17	17	17
R^2 MEAN	0.842	0.856	0.694	0.659
R^2 STD	0.058	0.031	0.191	0.204
R^2 MAX	0.924	0.896	0.923	0.919
R^2 MIN	0.753	0.798	0.315	0.302
FIRST DRIVER	Air Temperature (100%)	Air Temperature (88%)	Downwelling Longwave Radiation (59%)	Downwelling Longwave Radiation (59%)
SECOND DRIVER	Downwelling Shortwave Radiation (0%)	Downwelling Shortwave Radiation (12%)	Air Temperature (29%)	Air Temperature (29%)
THIRD DRIVER	Relative Humidity (0%)	Relative Humidity (0%)	Relative Humidity (12%)	Wind Direction (E–W) (6%)
FOURTH DRIVER	Downwelling Longwave Radiation (0%)	Downwelling Longwave Radiation (0%)	Wind Direction (N–S) (0%)	Relative Humidity (6%)
FIFTH DRIVER	Wind Speed (0%)	Wind Speed (0%)	Wind Direction (E–W) (0%)	Downwelling Shortwave Radiation (0%)
SIXTH DRIVER	Wind Direction (E–W) (0%)	Wind Direction (E–W) (0%)	Downwelling Shortwave Radiation (0%)	Wind Direction (N–S) (0%)
SEVENTH DRIVER	Wind Direction (N–S) (0%)	Wind Direction (N–S) (0%)	Wind Speed (0%)	Wind Speed (0%)

Table C.6: Summary of multiple linear regression results based on groups from the anomaly persistence classification approach for transition periods. Values represent the number of observations (n), mean, standard deviation, minimum and maximum R^2 across all days within each subgroup and cluster. Driver importance is determined based on the cumulative rank of standardized regression coefficients across all days. Values in parentheses denote how often a variable was the dominant driver in this period (i.e. ranked first in influence).

TRANSITION PERIODS						
	Snow-Covered to Snow-Free			**Snow-Free to Snow-Covered**		
	Persistently Cold	**Indermediate**	**Persistently Warm**	**Persistently Cold**	**Intermediate**	**Persistently Warm**
N DAYS	139	139	139	99	99	99
R^2 MEAN	0.722	0.809	0.875	0.817	0.811	0.792
R^2 STD	0.172	0.15	0.068	0.11	0.126	0.157
R^2 MAX	0.999	1	0.997	0.992	0.994	0.989
R^2 MIN	0.243	0.295	0.642	0.529	0.452	0.344
FIRST DRIVER	Downwelling Shortwave Radiation (44%)	Air Temperature (63%)	Air Temperature (76%)	Air Temperature (88%)	Air Temperature (89%)	Air Temperature (90%)
SECOND DRIVER	Air Temperature (43%)	Downwelling Shortwave Radiation (24%)	Downwelling Shortwave Radiation (23%)	Relative Humidity (2%)	Relative Humidity (1%)	Downwelling Shortwave Radiation (4%)
THIRD DRIVER	Relative Humidity (6%)	Relative Humidity (4%)	Relative Humidity (1%)	Downwelling Shortwave Radiation (3%)	Downwelling Shortwave Radiation (3%)	Relative Humidity (1%)
FOURTH DRIVER	Downwelling Longwave Radiation (4%)	Wind Direction (E–W) (1%)	Wind Direction (E–W) (0%)	Downwelling Longwave Radiation (6%)	Downwelling Longwave Radiation (6%)	Downwelling Longwave Radiation (5%)
FIFTH DRIVER	Wind Direction (E–W) (1%)	Downwelling Longwave Radiation (6%)	Downwelling Longwave Radiation (0%)	Wind Speed (0%)	Wind Speed (0%)	Wind Speed (0%)
SIXTH DRIVER	Wind Speed (1%)	Wind Speed (1%)	Wind Speed (0%)	Wind Direction (E–W) (1%)	Wind Direction (E–W) (1%)	Wind Direction (E–W) (0%)
SEVENTH DRIVER	Wind Direction (N–S) (0%)	Wind Direction (N–S) (0%)	Wind Direction (N–S) (0%)	Wind Direction (N–S) (0%)	Wind Direction (N–S) (0%)	Wind Direction (N–S) (0%)

Table C.7: Summary of multiple linear regression results based on groups from the anomaly persistence classification approach for snow-free and snow-covered periods. Values represent the number of observations (n), mean, standard deviation, minimum and maximum R^2 across all days within each subgroup and cluster. Driver importance is determined based on the cumulative rank of standardized regression coefficients across all days. Values in parentheses denote how often a variable was the dominant driver in this period (i.e. ranked first in influence).

SNOW COVER VS. NO SNOW COVER						
	Snow-Free			**Snow-Covered**		
	Persistently Cold	**Indermediate**	**Persistently Warm**	**Persistently Cold**	**Intermediate**	**Persistently Warm**
N DAYS	62	62	62	35	35	35
R^2 MEAN	0.893	0.915	0.924	0.84	0.874	0.872
R^2 STD	0.047	0.027	0.023	0.068	0.056	0.054
R^2 MAX	0.953	0.959	0.965	0.94	0.96	0.959
R^2 MIN	0.707	0.851	0.859	0.685	0.724	0.735
FIRST DRIVER	Air Temperature (90%)	Air Temperature (95%)	Air Temperature (87%)	Air Temperature (77%)	Downwelling Shortwave Radiation (31%)	Downwelling Shortwave Radiation (43%)
SECOND DRIVER	Downwelling Shortwave Radiation (10%)	Downwelling Shortwave Radiation (5%)	Downwelling Shortwave Radiation (13%)	Downwelling Shortwave Radiation (9%)	Air Temperature (60%)	Air Temperature (49%)
THIRD DRIVER	Downwelling Longwave Radiation (0%)	Relative Humidity (0%)	Wind Speed (0%)	Relative Humidity (3%)	Relative Humidity (0%)	Relative Humidity (0%)
FOURTH DRIVER	Relative Humidity (0%)	Wind Speed (0%)	Relative Humidity (0%)	Downwelling Longwave Radiation (11%)	Downwelling Longwave Radiation (9%)	Downwelling Longwave Radiation (9%)
FIFTH DRIVER	Wind Direction (E–W) (0%)	Wind Direction (E–W) (0%)	Wind Direction (E–W) (0%)	Wind Speed (0%)	Wind Speed (0%)	Wind Speed (0%)
SIXTH DRIVER	Wind Speed (0%)	Downwelling Longwave Radiation (0%)	Wind Direction (N–S) (0%)	Wind Direction (N–S) (0%)	Wind Direction (E–W) (0%)	Wind Direction (E–W) (0%)
SEVENTH DRIVER	Wind Direction (N–S) (0%)	Wind Direction (N–S) (0%)	Downwelling Longwave Radiation (0%)	Wind Direction (E–W) (0%)	Wind Direction (N–S) (0%)	Wind Direction (N–S) (0%)

Table C.8: Summary of multiple linear regression results based on groups from the anomaly persistence classification approach for precipitation periods. Values represent the number of observations (n), mean, standard deviation, minimum and maximum R^2 across all days within each subgroup and cluster. Driver importance is determined based on the cumulative rank of standardized regression coefficients across all days. Values in parentheses denote how often a variable was the dominant driver in this period (i.e. ranked first in influence).

PRECIPITATION PERIOD VS. DRY PERIOD						
	Snow-Free Precipitation			**Snow-Covered Precipitation**		
	Persistently Cold	**Indermediate**	**Persistently Warm**	**Persistently Cold**	**Intermediate**	**Persistently Warm**
N DAYS	17	17	17	26	26	26
R^2 MEAN	0.906	0.913	0.921	0.788	0.779	0.748
R^2 STD	0.03	0.028	0.024	0.078	0.078	0.084
R^2 MAX	0.949	0.949	0.963	0.945	0.95	0.953
R^2 MIN	0.852	0.859	0.867	0.645	0.641	0.619
FIRST DRIVER	Air Temperature (100%)	Air Temperature (100%)	Air Temperature (100%)	Air Temperature (100%)	Air Temperature (96%)	Air Temperature (96%)
SECOND DRIVER	Downwelling Shortwave Radiation (0%)	Downwelling Shortwave Radiation (0%)	Downwelling Shortwave Radiation (0%)	Downwelling Shortwave Radiation (0%)	Downwelling Shortwave Radiation (4%)	Downwelling Shortwave Radiation (4%)
THIRD DRIVER	Downwelling Longwave Radiation (0%)	Relative Humidity (0%)	Relative Humidity (0%)	Relative Humidity (0%)	Relative Humidity (0%)	Relative Humidity (0%)
FOURTH DRIVER	Relative Humidity (0%)	Downwelling Longwave Radiation (0%)	Downwelling Longwave Radiation (0%)	Downwelling Longwave Radiation (0%)	Downwelling Longwave Radiation (0%)	Downwelling Longwave Radiation (0%)
FIFTH DRIVER	Wind Speed (0%)	Wind Speed (0%)	Wind Speed (0%)	Wind Speed (0%)	Wind Speed (0%)	Wind Direction (N–S) (0%)
SIXTH DRIVER	Wind Direction (E–W) (0%)	Wind Direction (E–W) (0%)	Wind Direction (E–W) (0%)	Wind Direction (N–S) (0%)	Wind Direction (N–S) (0%)	Wind Speed (0%)
SEVENTH DRIVER	Wind Direction (N–S) (0%)	Wind Direction (N–S) (0%)	Wind Direction (N–S) (0%)	Wind Direction (E–W) (0%)	Wind Direction (E–W) (0%)	Wind Direction (E–W) (0%)

Table C.9: Summary of multiple linear regression results based on groups from the anomaly persistence classification approach for day / night comparison during snow-free periods. Values represent the number of observations (n), mean, standard deviation, minimum and maximum R^2 across all days within each subgroup and cluster. Driver importance is determined based on the cumulative rank of standardized regression coefficients across all days. Values in parentheses denote how often a variable was the dominant driver in this period (i.e. ranked first in influence).

DAY VS. NIGHT (SNOW-FREE)						
	Snow-Free Day			**Snow-Free Night**		
	Persistently Cold	**Indermediate**	**Persistently Warm**	**Persistently Cold**	**Intermediate**	**Persistently Warm**
N DAYS	43	43	43	43	43	43
R^2 MEAN	0.871	0.903	0.911	0.871	0.883	0.888
R^2 STD	0.073	0.03	0.026	0.06	0.044	0.042
R^2 MAX	0.952	0.955	0.955	0.953	0.953	0.954
R^2 MIN	0.604	0.838	0.852	0.713	0.761	0.762
FIRST DRIVER	Air Temperature (93%)	Air Temperature (91%)	Air Temperature (88%)	Air Temperature (84%)	Air Temperature (88%)	Air Temperature (91%)
SECOND DRIVER	Downwelling Shortwave Radiation (7%)	Downwelling Shortwave Radiation (7%)	Downwelling Shortwave Radiation (9%)	Downwelling Shortwave Radiation (7%)	Downwelling Shortwave Radiation (7%)	Downwelling Shortwave Radiation (5%)
THIRD DRIVER	Wind Direction (E–W) (0%)	Wind Direction (E–W) (0%)	Wind Direction (E–W) (0%)	Downwelling Longwave Radiation (9%)	Downwelling Longwave Radiation (5%)	Downwelling Longwave Radiation (5%)
FOURTH DRIVER	Relative Humidity (0%)	Relative Humidity (2%)	Relative Humidity (2%)	Relative Humidity (0%)	Relative Humidity (0%)	Relative Humidity (0%)
FIFTH DRIVER	Wind Speed (0%)	Wind Speed (0%)	Wind Direction (N–S) (0%)	Wind Direction (E–W) (0%)	Wind Direction (E–W) (0%)	Wind Direction (E–W) (0%)
SIXTH DRIVER	Wind Direction (N–S) (0%)	Wind Direction (N–S) (0%)	Wind Speed (0%)	Wind Speed (0%)	Wind Speed (0%)	Wind Speed (0%)
SEVENTH DRIVER	Downwelling Longwave Radiation (0%)	Downwelling Longwave Radiation (0%)	Downwelling Longwave Radiation (0%)	Wind Direction (N–S) (0%)	Wind Direction (N–S) (0%)	Wind Direction (N–S) (0%)

Table C.10: Summary of multiple linear regression results based on groups from the anomaly persistence classification approach for day / night comparison during snow-covered periods. Values represent the number of observations (n), mean, standard deviation, minimum and maximum R^2 across all days within each subgroup and cluster. Driver importance is determined based on the cumulative rank of standardized regression coefficients across all days. Values in parentheses denote how often a variable was the dominant driver in this period (i.e. ranked first in influence).

DAY VS. NIGHT (SNOW-COVERED)						
	Snow-Covered Day			**Snow-Covered Night**		
	Persistently Cold	**Indermediate**	**Persistently Warm**	**Persistently Cold**	**Intermediate**	**Persistently Warm**
N DAYS	17	17	17	17	17	17
R^2 MEAN	0.833	0.856	0.853	0.706	0.694	0.654
R^2 STD	0.062	0.046	0.027	0.184	0.19	0.204
R^2 MAX	0.924	0.919	0.884	0.928	0.922	0.916
R^2 MIN	0.748	0.78	0.8	0.352	0.322	0.286
FIRST DRIVER	Air Temperature (100%)	Air Temperature (100%)	Air Temperature (59%)	Downwelling Long-wave Radiation (59%)	Downwelling Long-wave Radiation (59%)	Downwelling Long-wave Radiation (59%)
SECOND DRIVER	Downwelling Short-wave Radiation (0%)	Downwelling Short-wave Radiation (0%)	Downwelling Short-wave Radiation (41%)	Air Temperature (29%)	Air Temperature (29%)	Air Temperature (29%)
THIRD DRIVER	Relative Humidity (0%)	Relative Humidity (0%)	Relative Humidity (0%)	Relative Humidity (12%)	Relative Humidity (12%)	Relative Humidity (12%)
FOURTH DRIVER	Downwelling Long-wave Radiation (0%)	Downwelling Long-wave Radiation (0%)	Downwelling Long-wave Radiation (0%)	Wind Direction (N–S) (0%)	Wind Direction (E–W) (0%)	Wind Direction (E–W) (0%)
FIFTH DRIVER	Wind Speed (0%)	Wind Speed (0%)	Wind Speed (0%)	Wind Direction (E–W) (0%)	Wind Direction (N–S) (0%)	Downwelling Short-wave Radiation (0%)
SIXTH DRIVER	Wind Direction (E–W) (0%)	Wind Direction (E–W) (0%)	Wind Direction (E–W) (0%)	Downwelling Short-wave Radiation (0%)	Downwelling Short-wave Radiation (0%)	Wind Direction (N–S) (0%)
SEVENTH DRIVER	Wind Direction (N–S) (0%)	Wind Direction (N–S) (0%)	Wind Direction (N–S) (0%)	Wind Speed (0%)	Wind Speed (0%)	Wind Speed (0%)

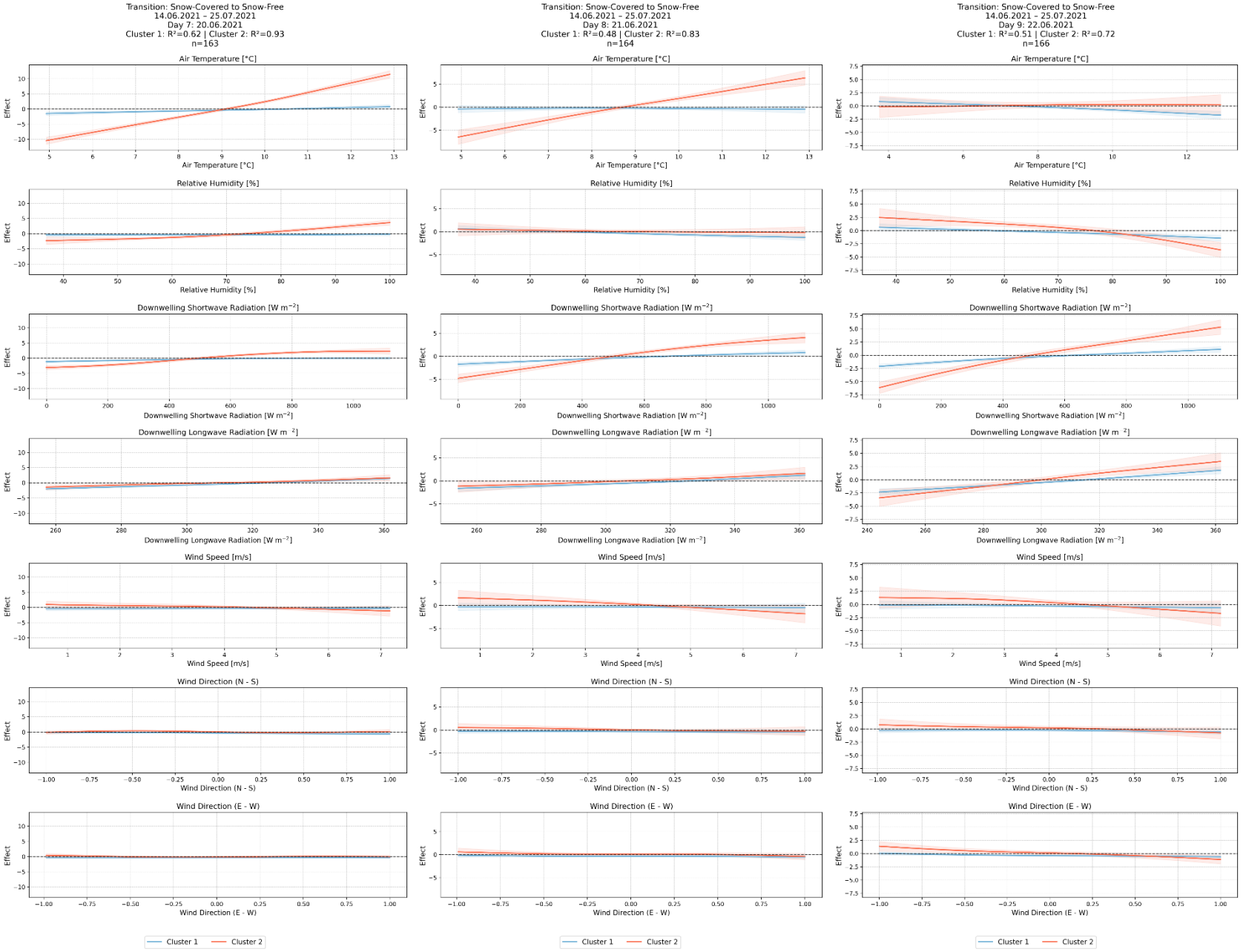

Figure C.17: GAM results of the diurnal curve clustering approach of days 7, 8 and 9 of the 2021 snow-covered to snow-free transition period.

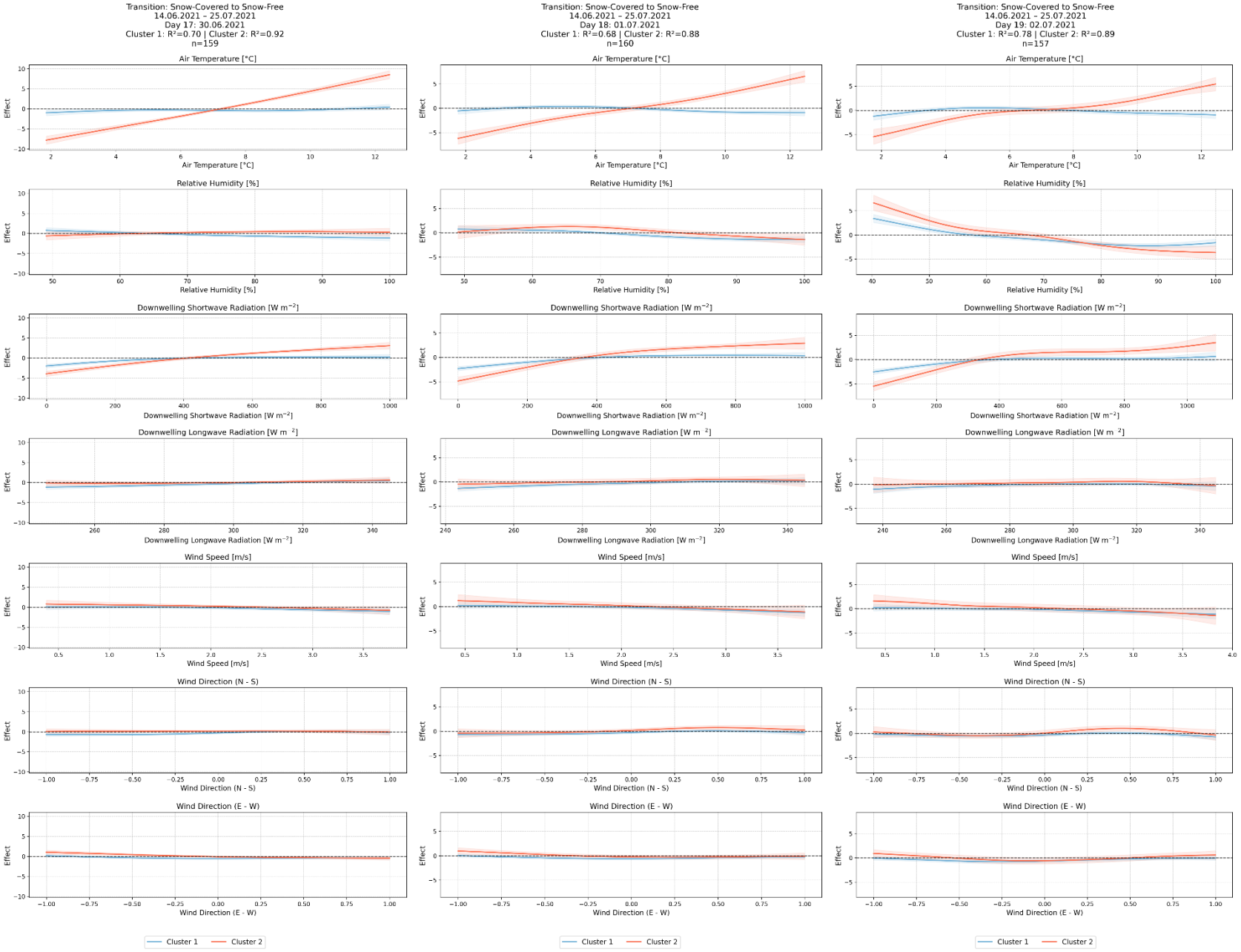

Figure C.18: GAM results of the diurnal curve clustering approach of days 17, 18 and 19 of the 2021 snow-covered to snow-free transition period.

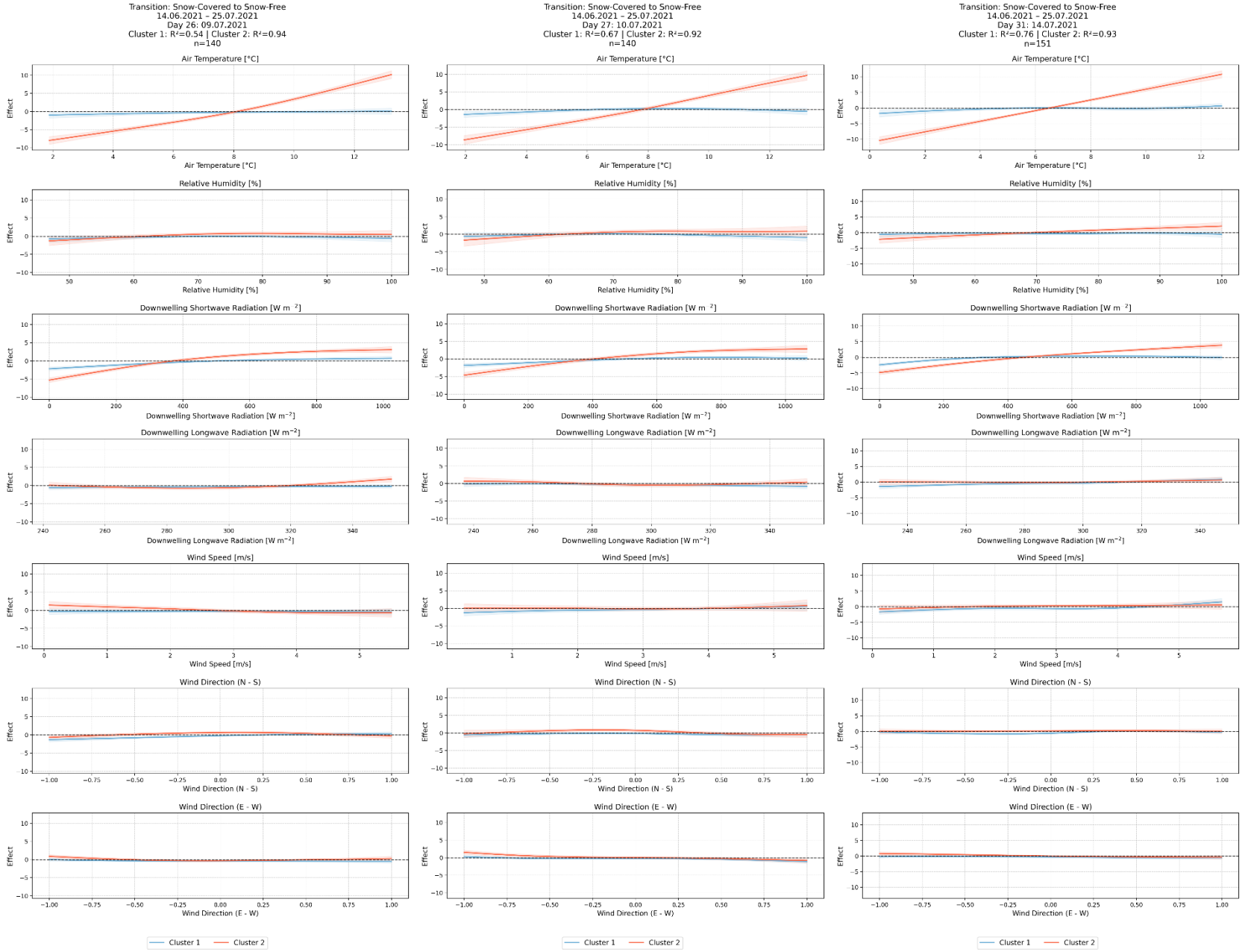

Figure C.19: GAM results of the diurnal curve clustering approach of days 26, 27 and 31 of the 2021 snow-covered to snow-free transition period.

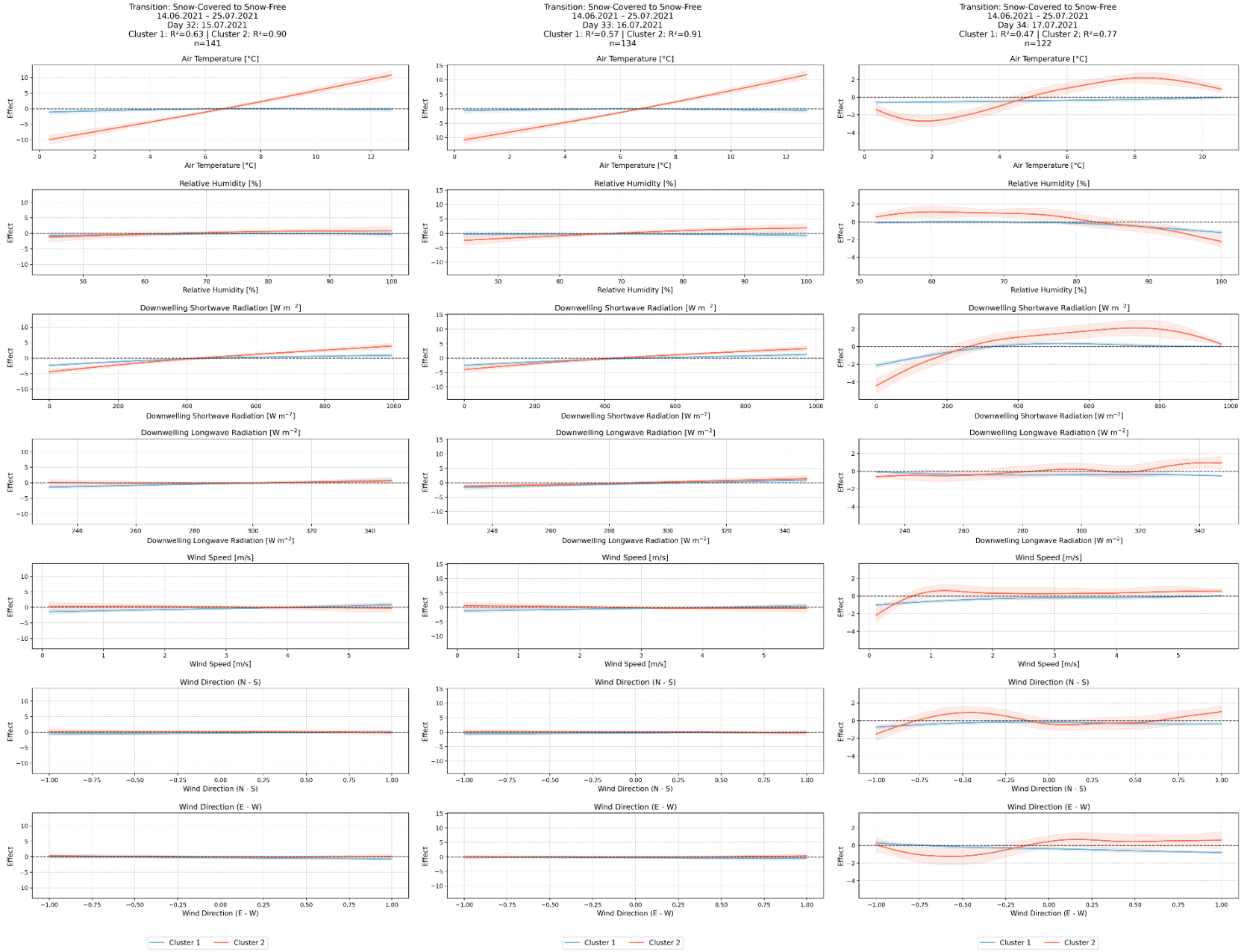

Figure C.20: GAM results of the diurnal curve clustering approach of days 32, 33 and 34 of the 2021 snow-covered to snow-free transition period.

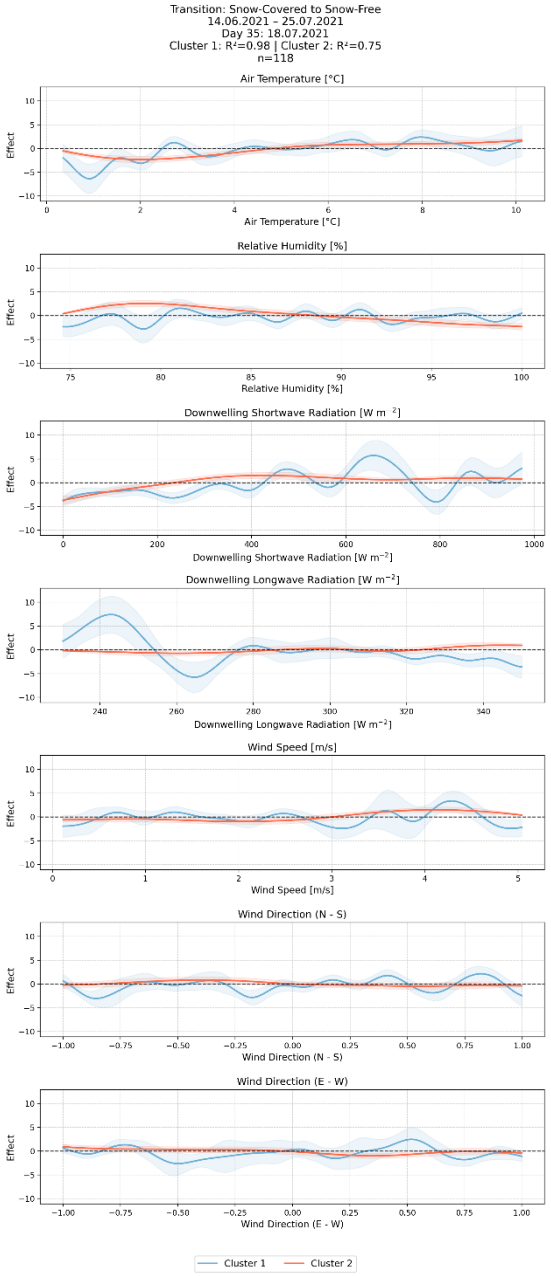

Figure C.21: GAM results of the diurnal curve clustering approach of day 35 of the 2021 snow-covered to snow-free transition period.

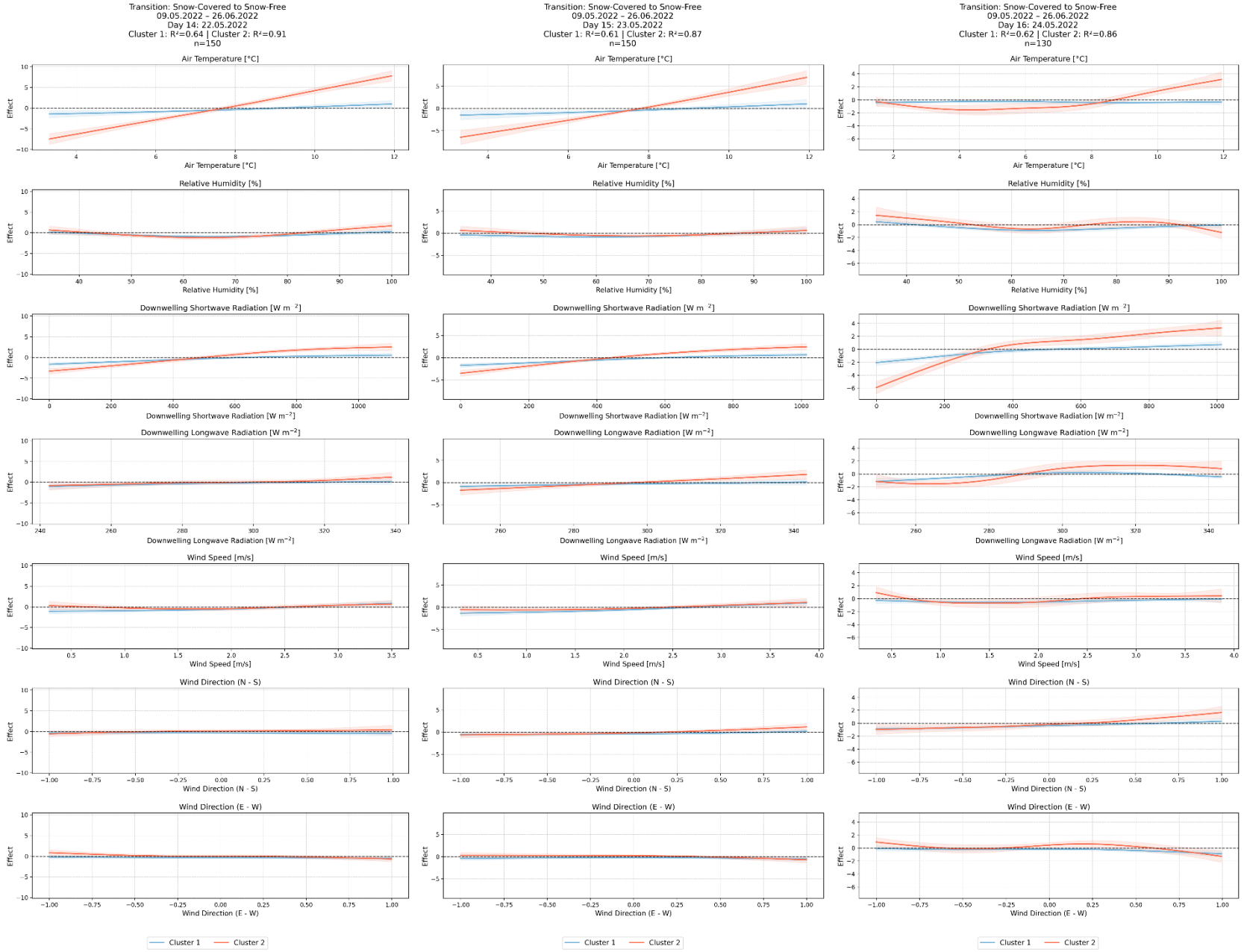

Figure C.22: GAM results of the diurnal curve clustering approach of days 14, 15 and 16 of the 2022 snow-covered to snow-free transition period.

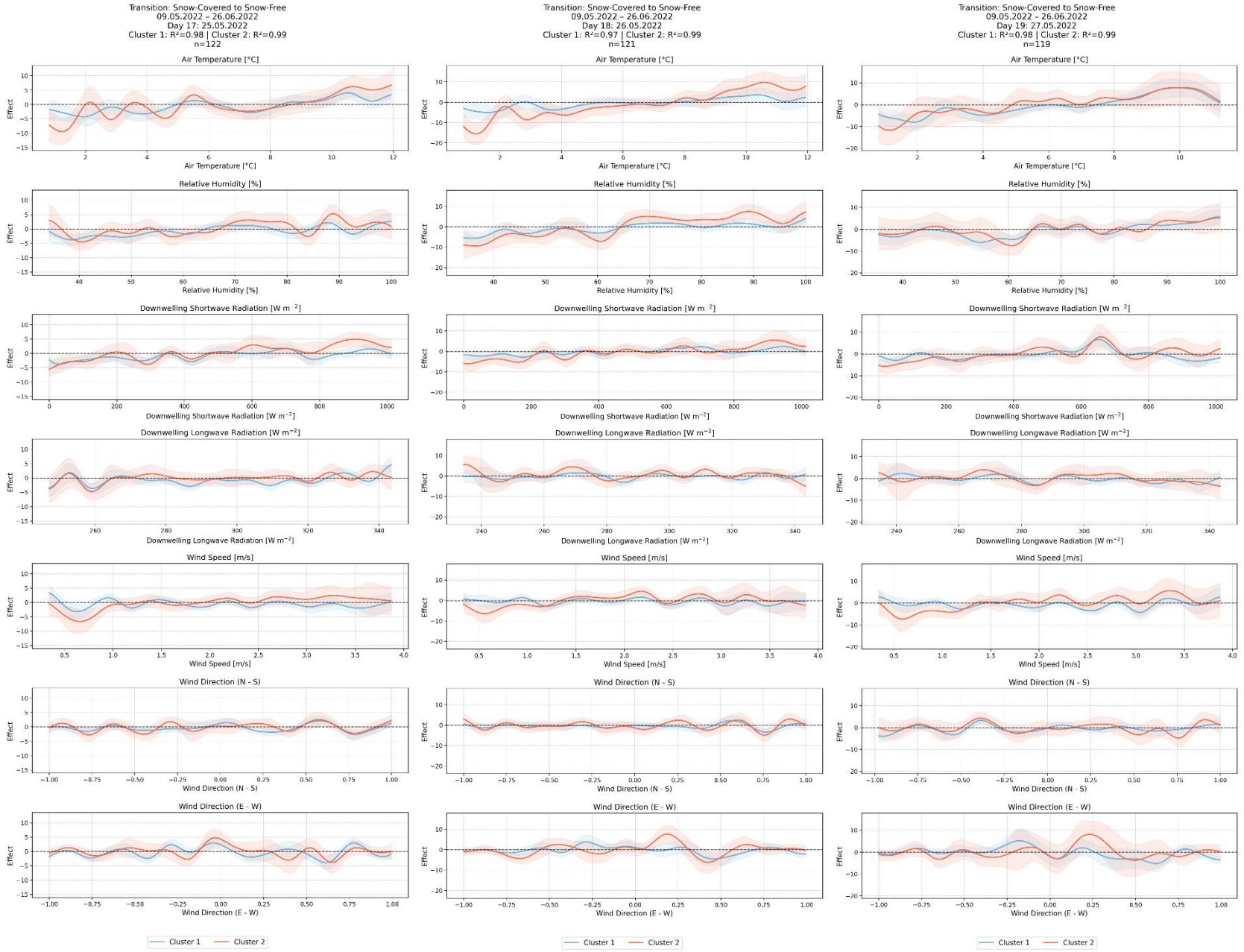

Figure C.23: GAM results of the diurnal curve clustering approach of days 17, 18 and 19 of the 2022 snow-covered to snow-free transition period.

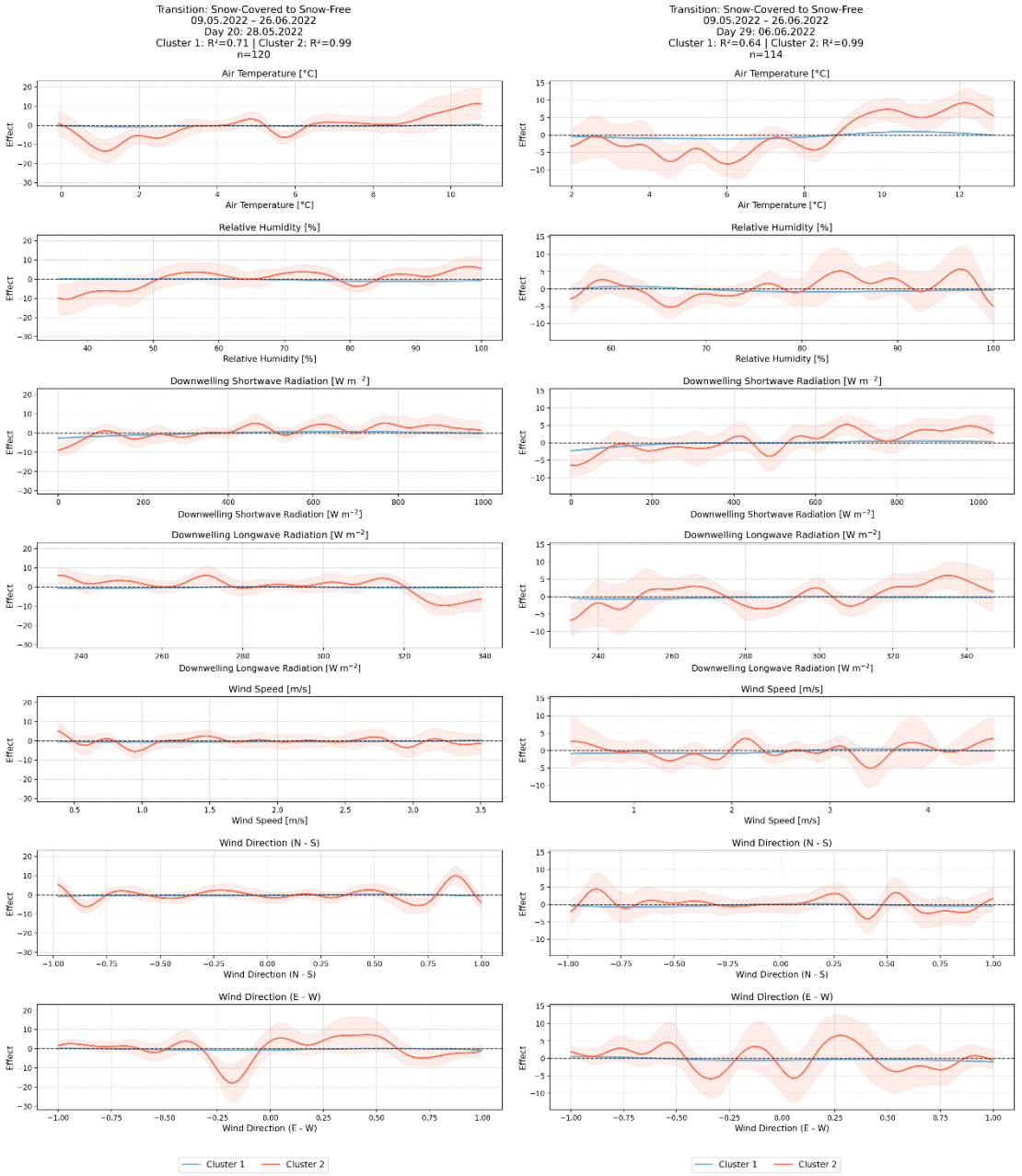

Figure C.24: GAM results of the diurnal curve clustering approach of days 20 and 29 of the 2022 snow-covered to snow-free transition period.

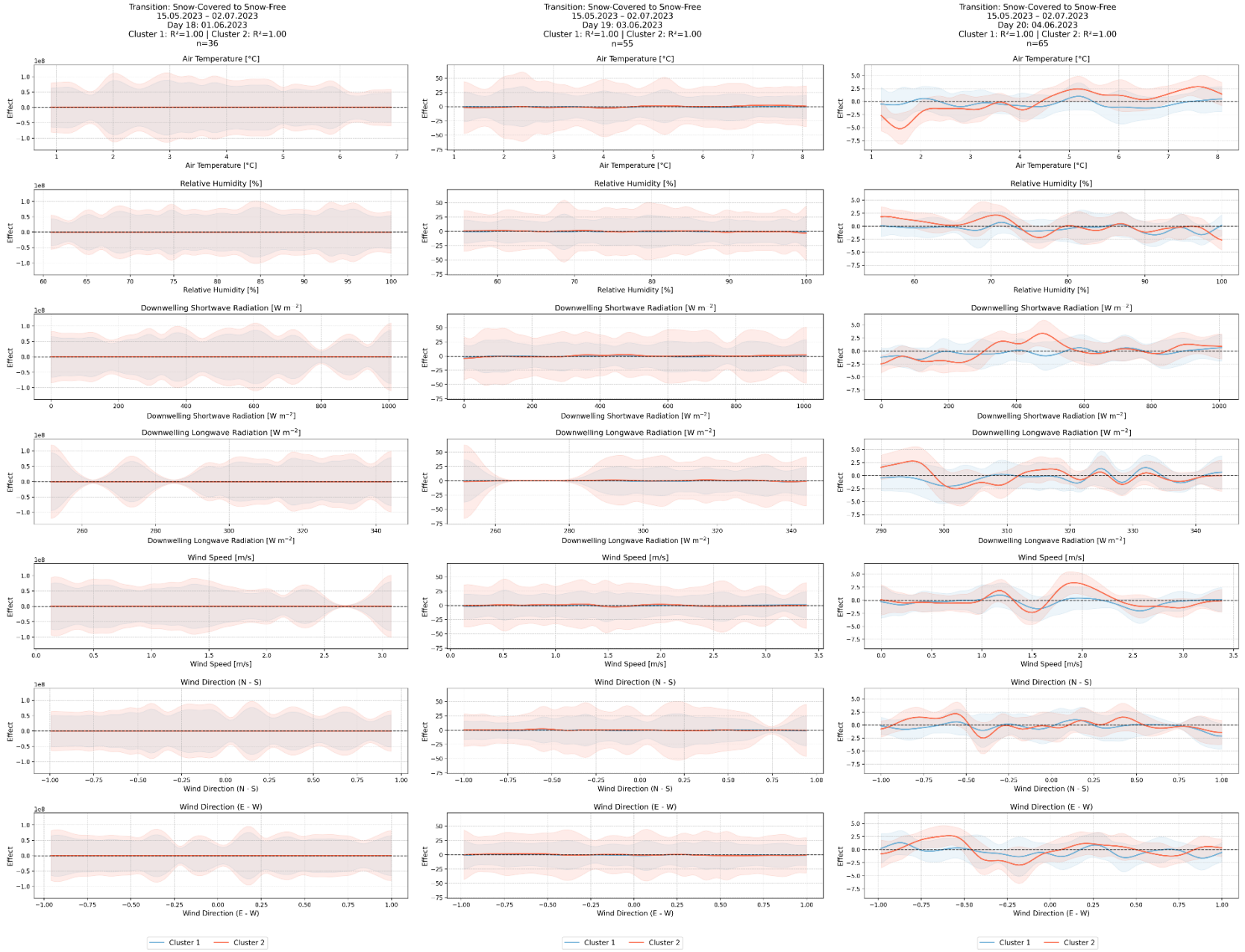

Figure C.25: GAM results of the diurnal curve clustering approach of days 18, 19 and 20 of the 2023 snow-covered to snow-free transition period.

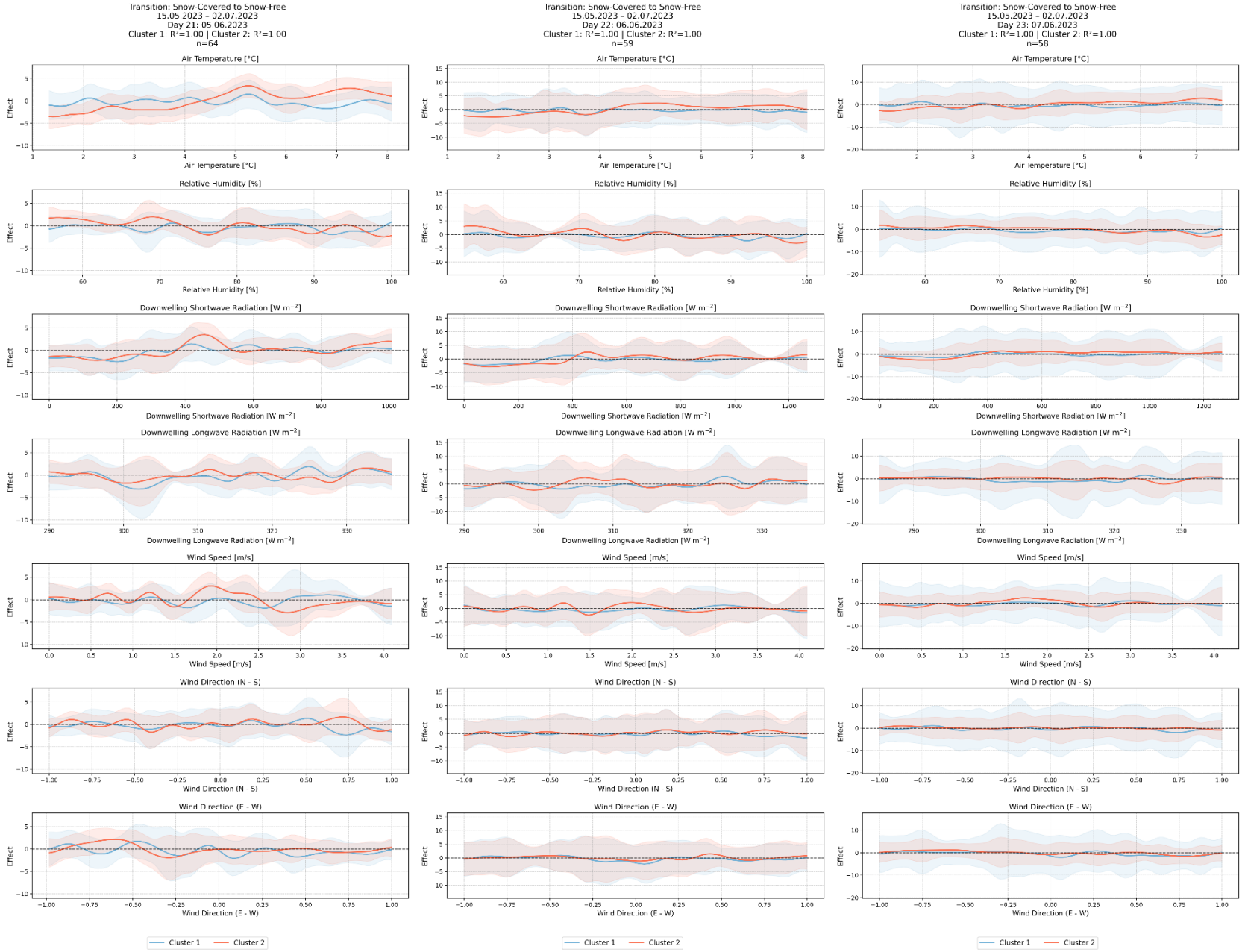

Figure C.26: GAM results of the diurnal curve clustering approach of days 21, 22 and 23 of the 2023 snow-covered to snow-free transition period.

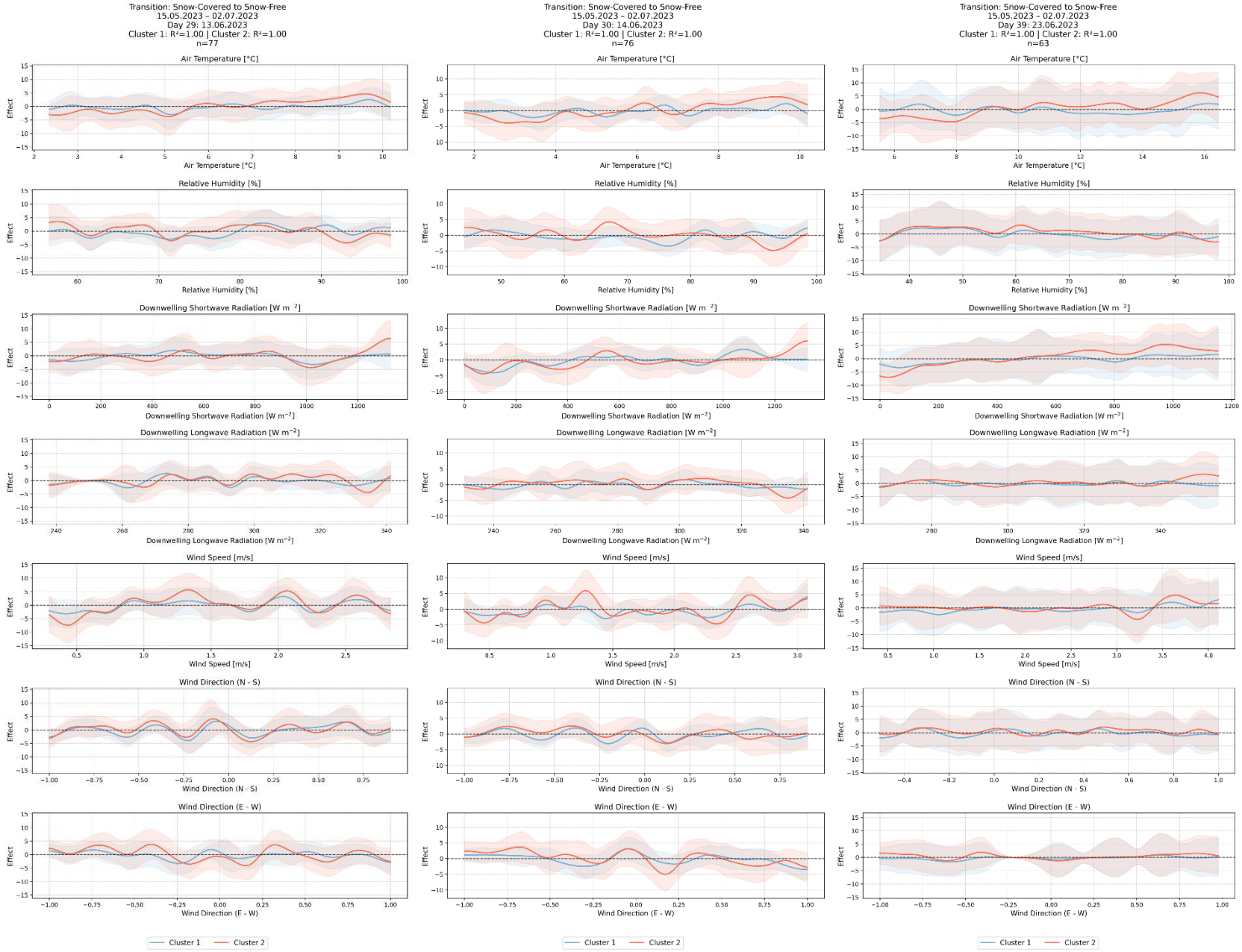

Figure C.27: GAM results of the diurnal curve clustering approach of days 29, 30 and 39 of the 2023 snow-covered to snow-free transition period.

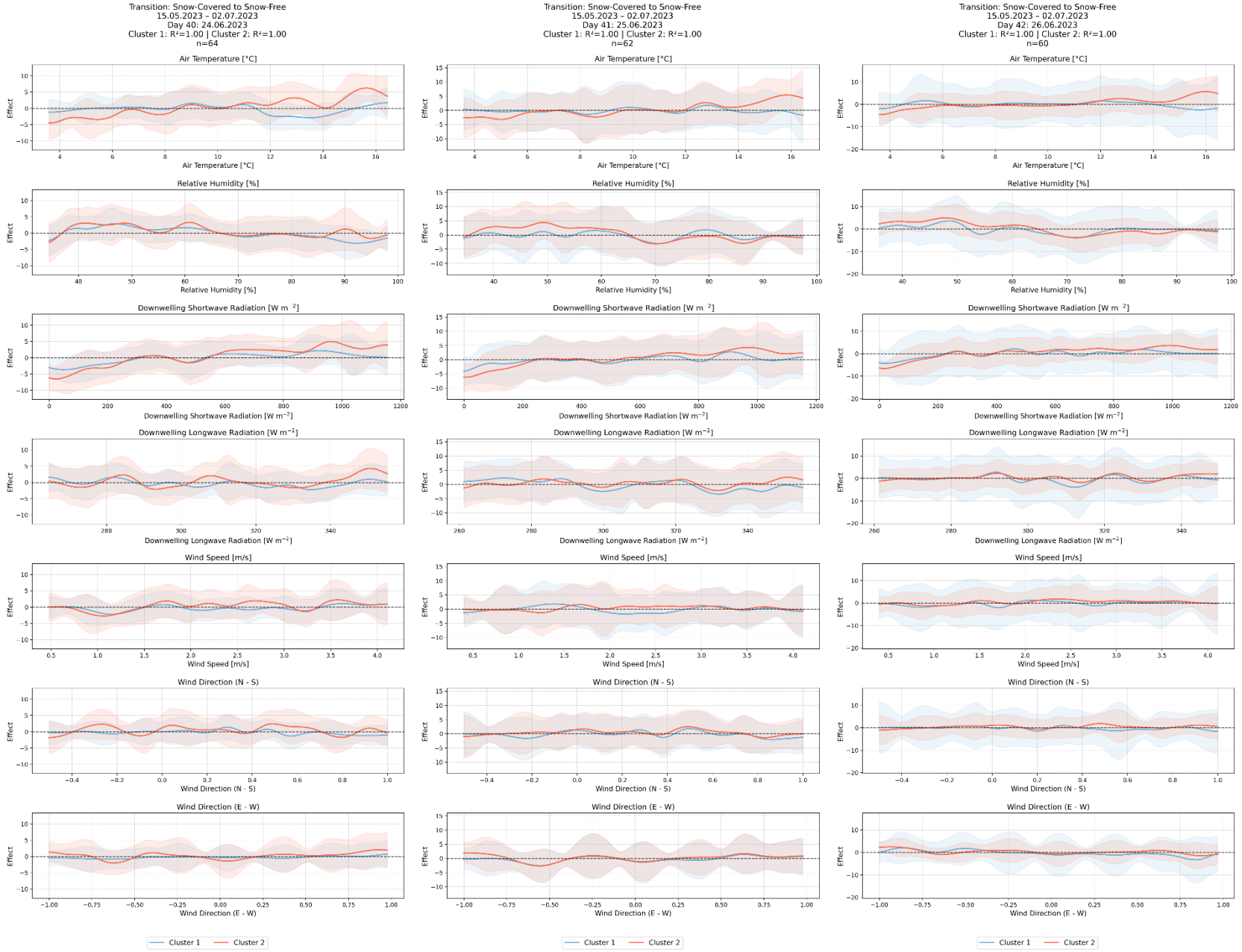

Figure C.28: GAM results of the diurnal curve clustering approach of days 40, 41 and 42 of the 2023 snow-covered to snow-free transition period.

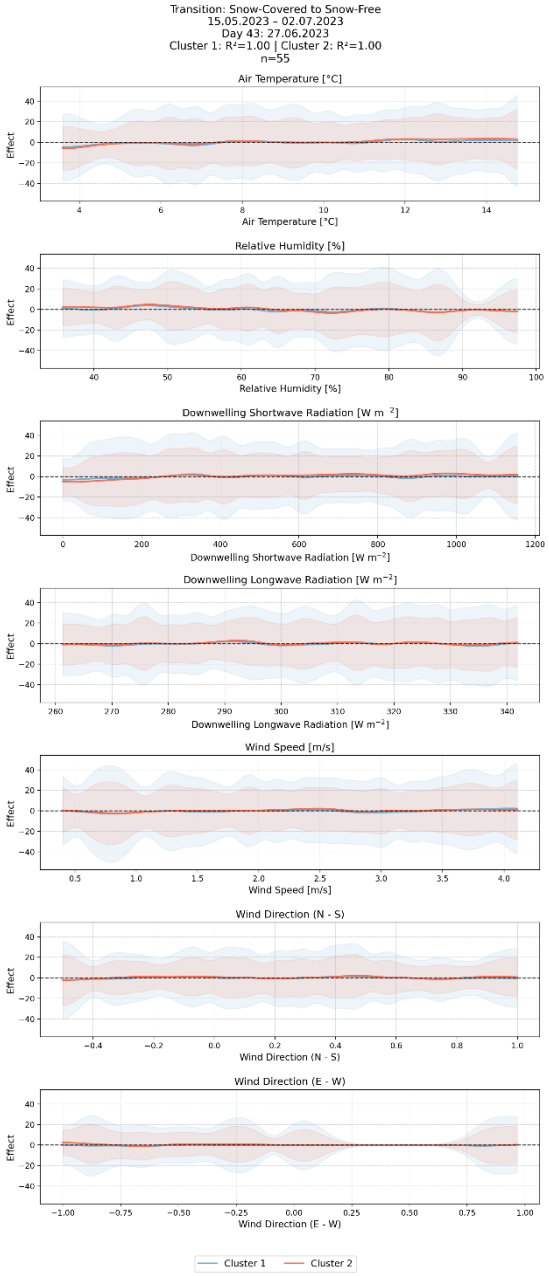

Figure C.29: GAM results of the diurnal curve clustering approach of day 43 of the 2023 snow-free to snow-covered transition period.

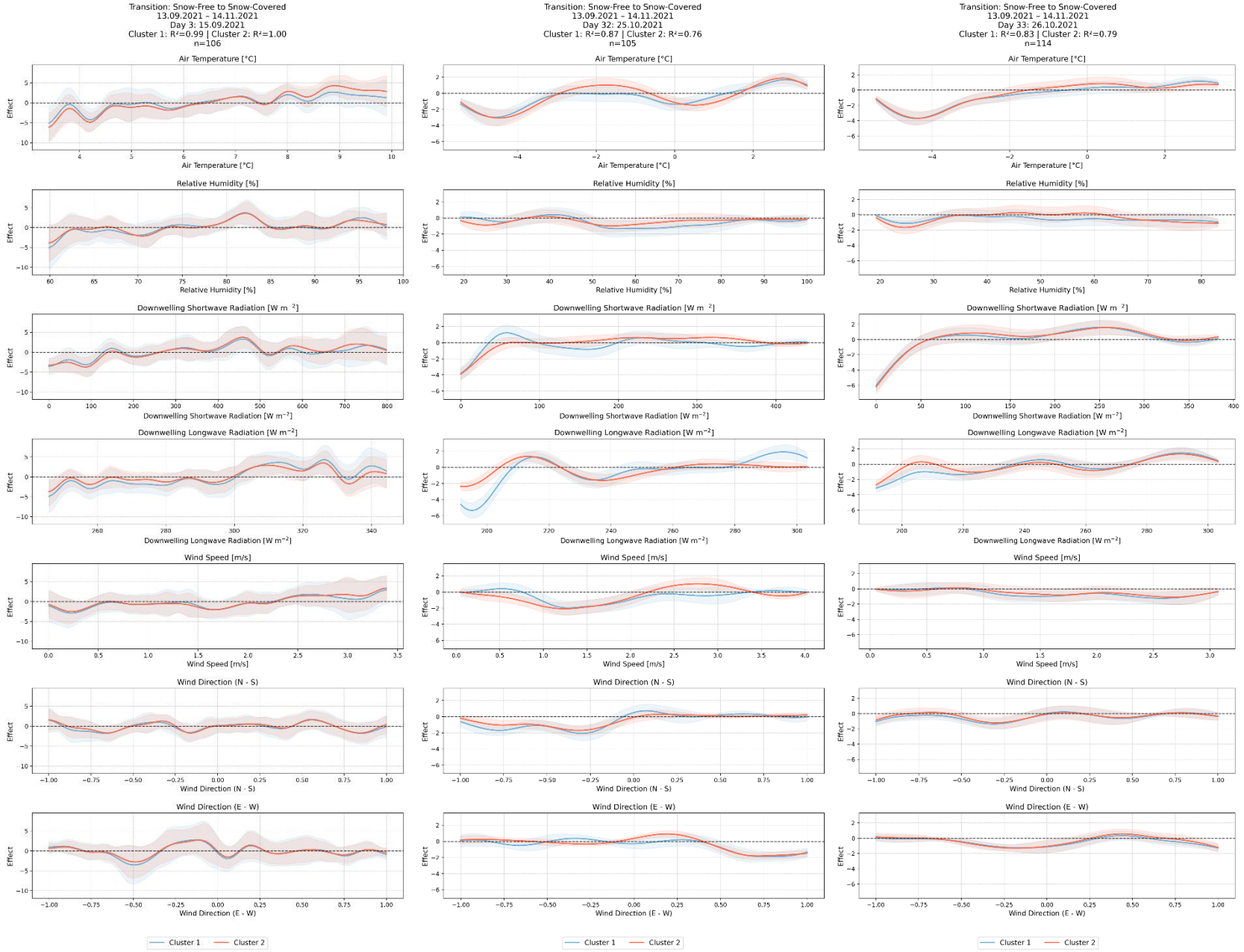

Figure C.30: GAM results of the diurnal curve clustering approach of days 3, 32 and 33 of the 2021 snow-free to snow-covered transition period.

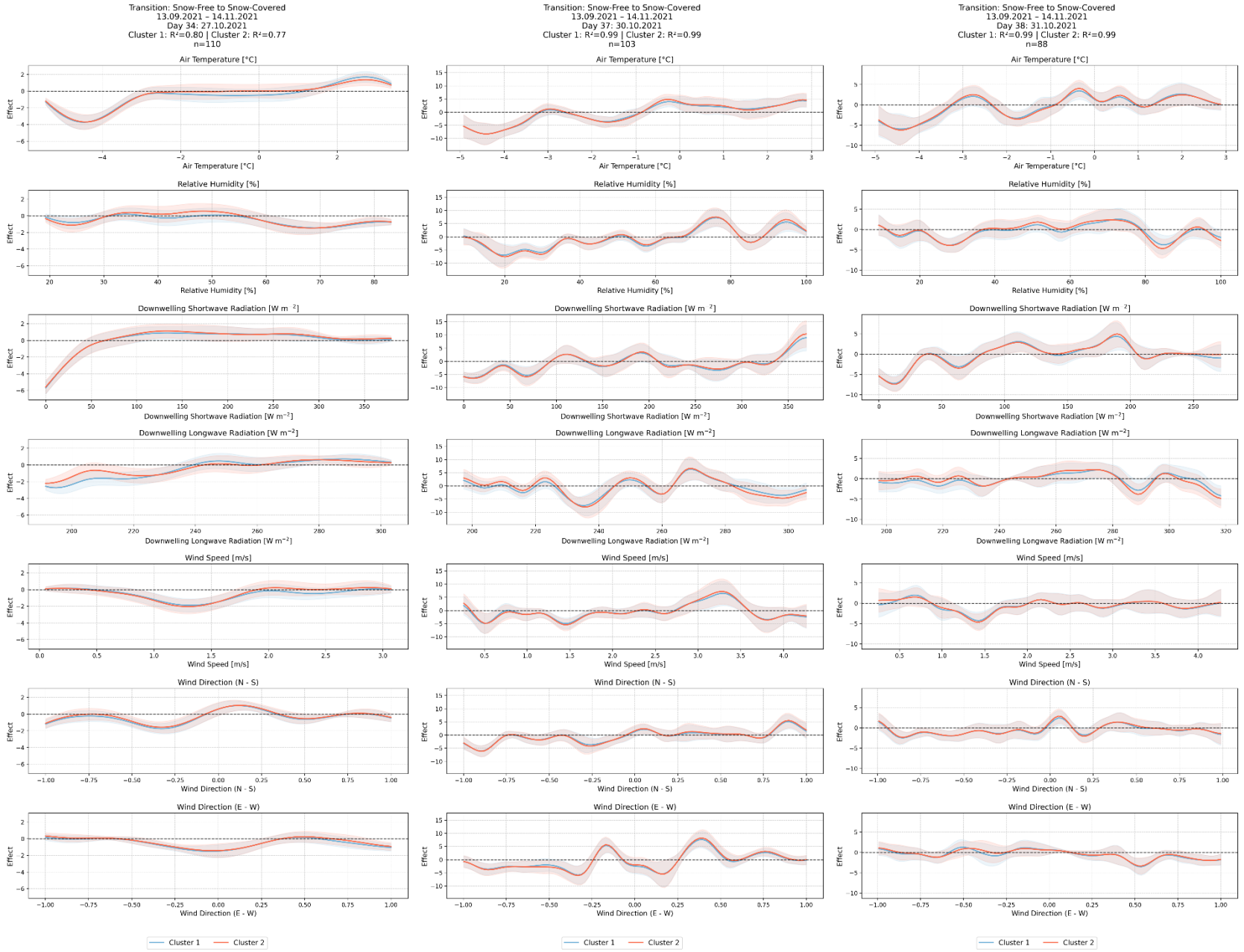

Figure C.31: GAM results of the diurnal curve clustering approach of days 34, 37 and 38 of the 2021 snow-free to snow-covered transition period.

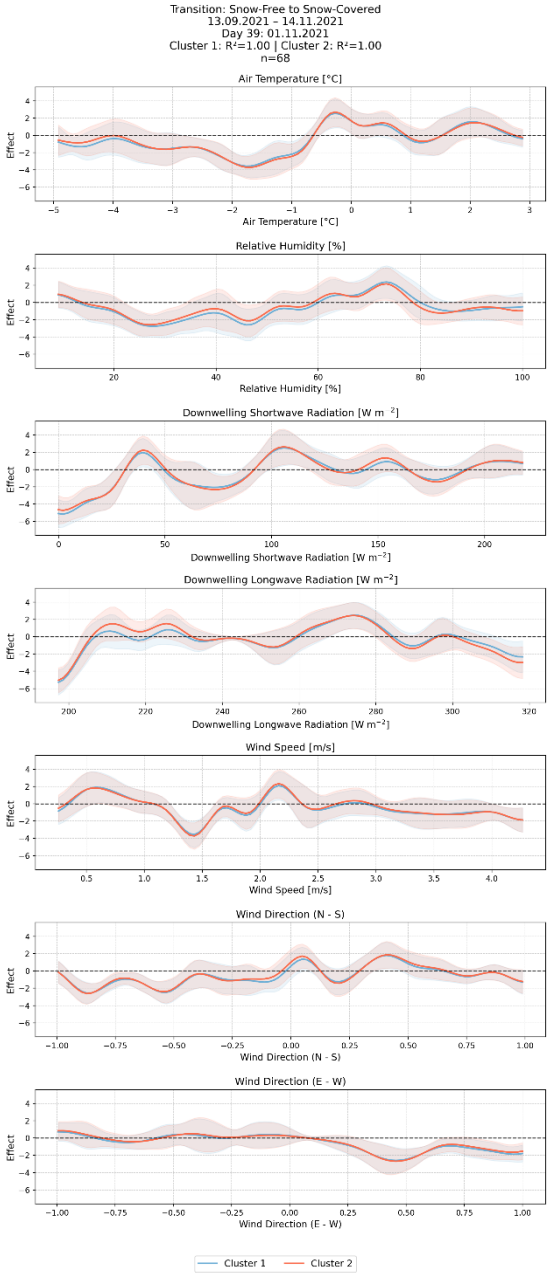

Figure C.32: GAM results of the diurnal curve clustering approach of day 39 of the 2021 snow-free to snow-covered transition period.

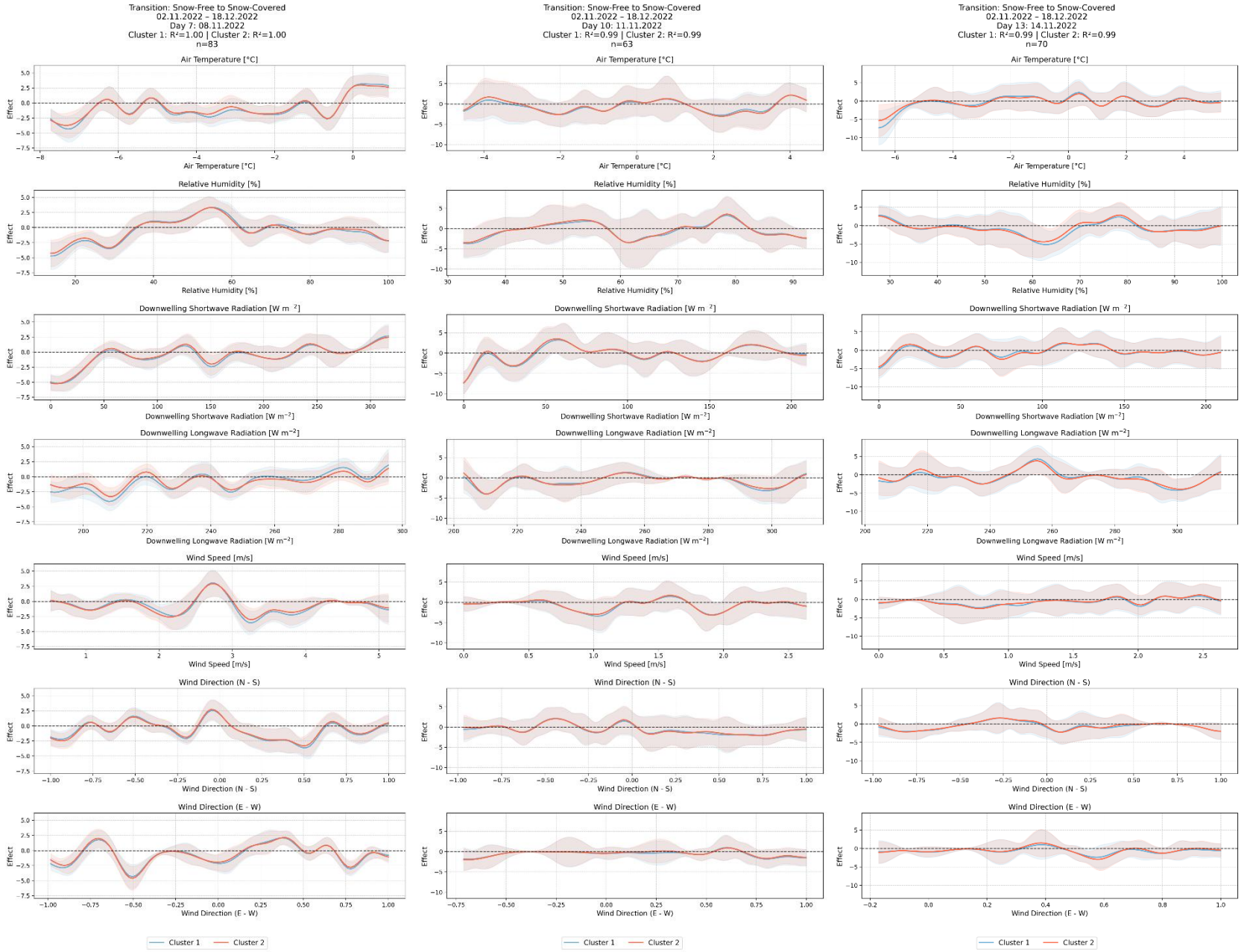

Figure C.33: GAM results of the diurnal curve clustering approach of days 7, 10 and 13 of the 2022 snow-free to snow-covered transition period.

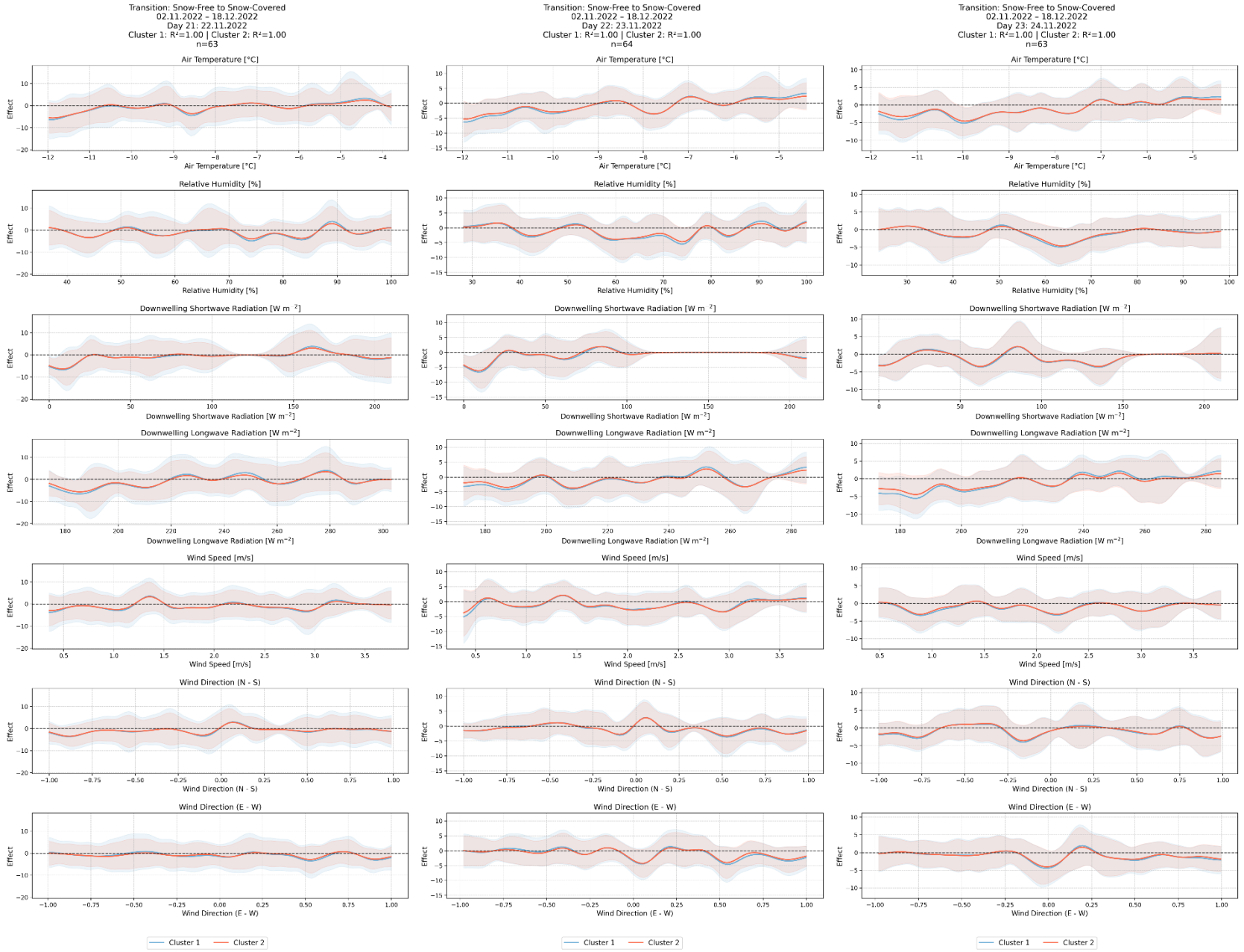

Figure C.34: GAM results of the diurnal curve clustering approach of days 21, 22 and 23 of the 2021 snow-free to snow-covered transition period.

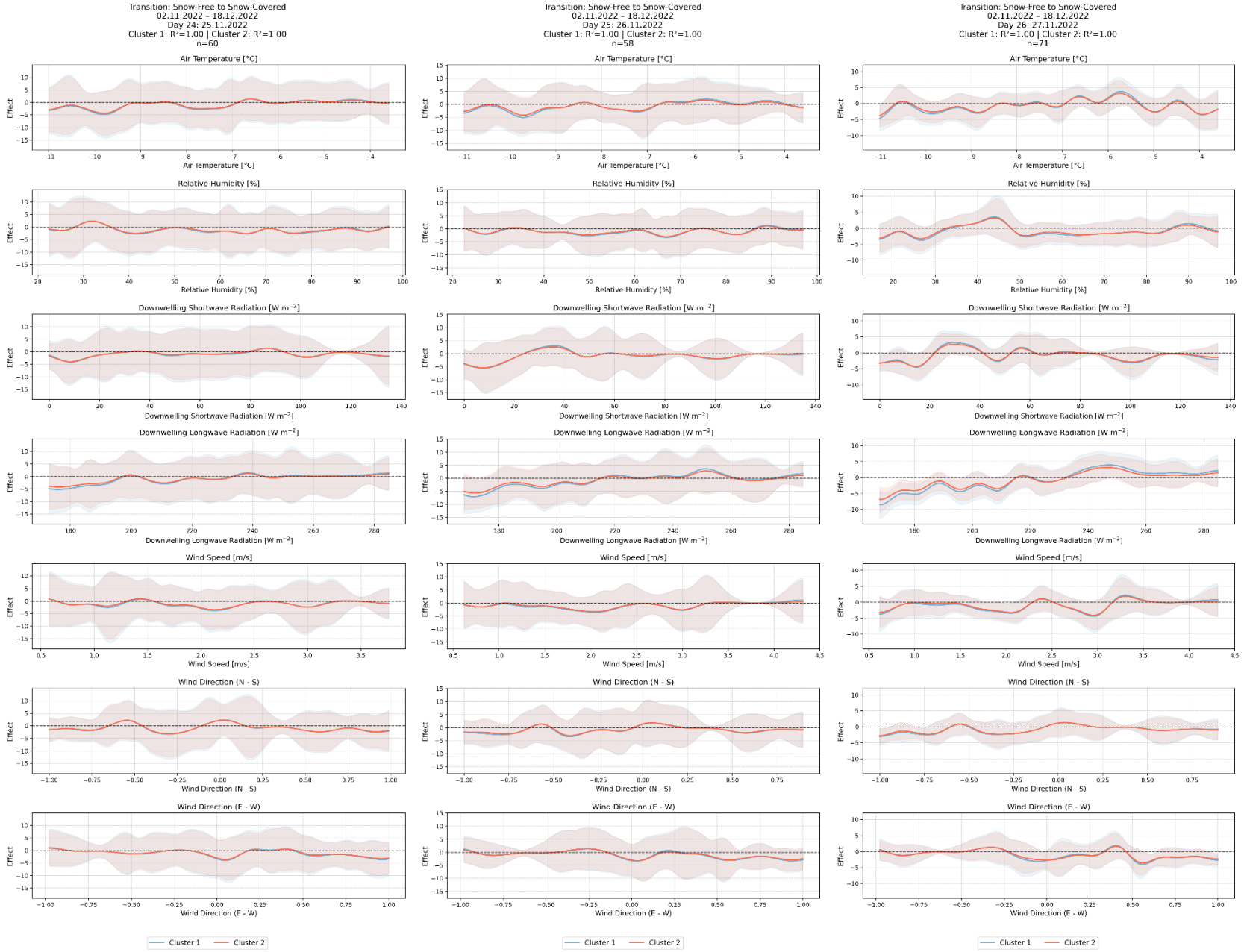

Figure C.35: GAM results of the diurnal curve clustering approach of days 24, 25 and 26 of the 2021 snow-free to snow-covered transition period.

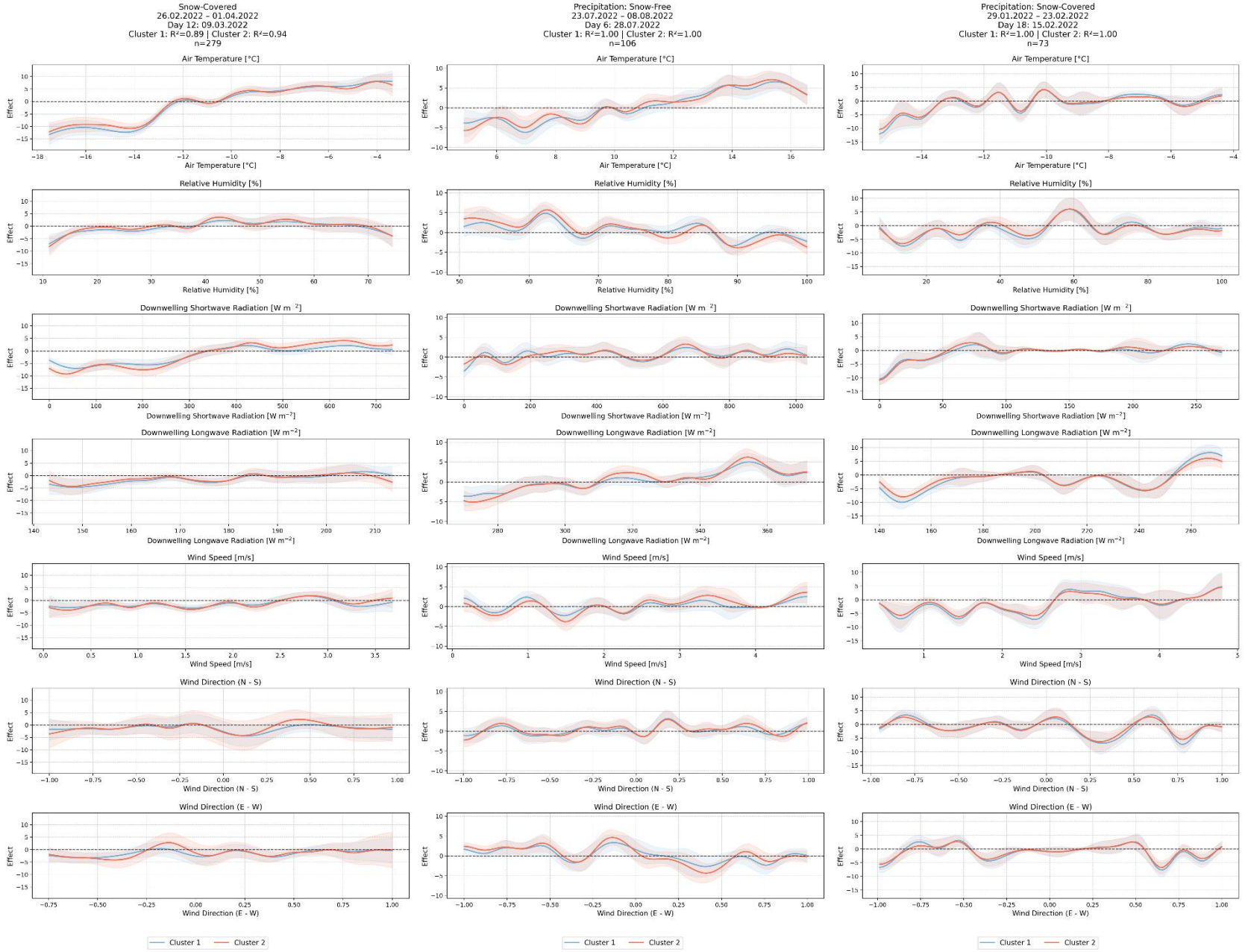

Figure C.36: GAM results of the diurnal curve clustering approach of day 12 of the snow-covered period (left), day 6 of the snow-free precipitation period (middle) and day 18 of the snow-free precipitation period (right). Day 12 of the snow-covered period is day 14 of the snow-covered no precipitation period simultaneously.

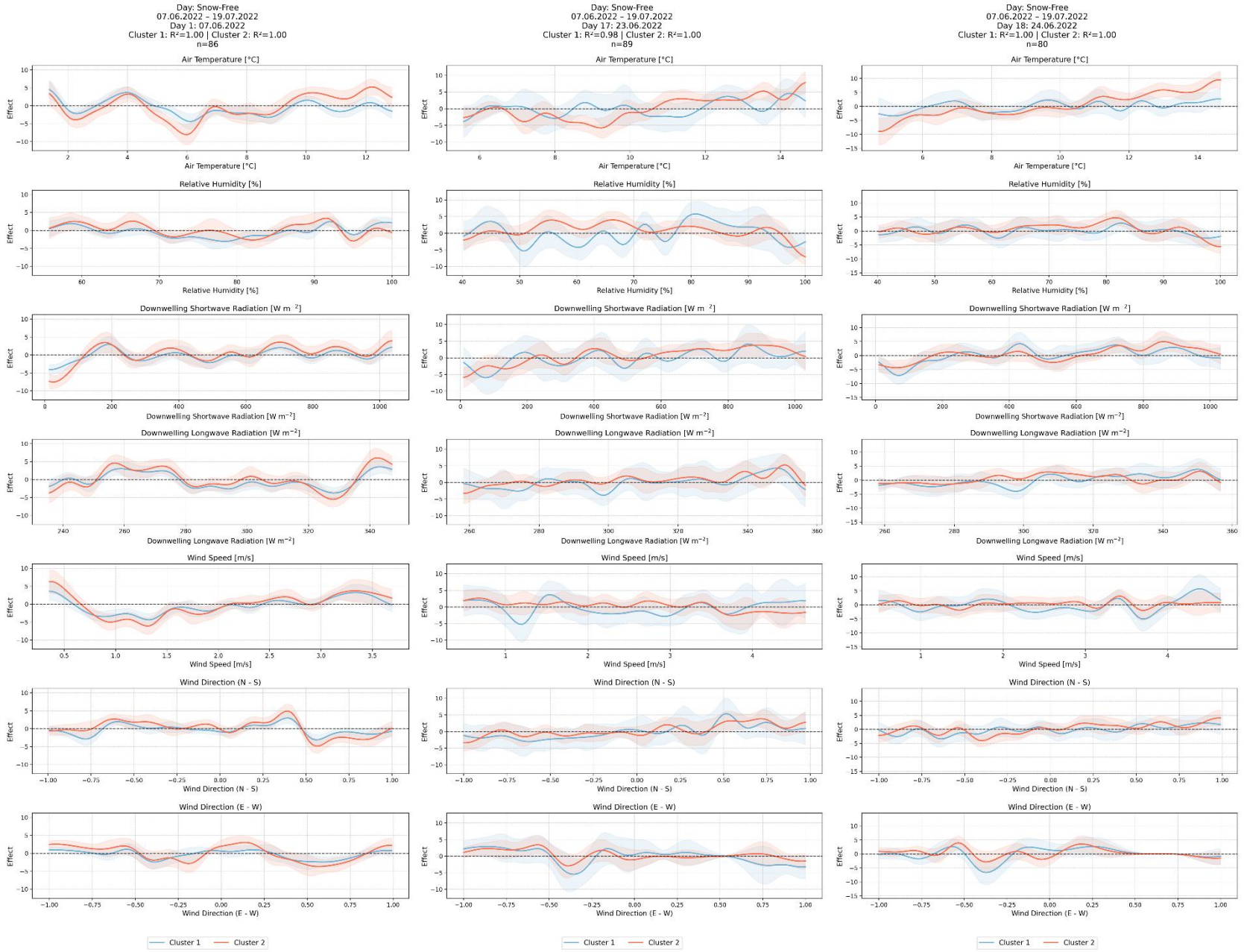

Figure C.37: GAM results of the diurnal curve clustering approach of days 1, 17 and 18 of the snow-free day period.

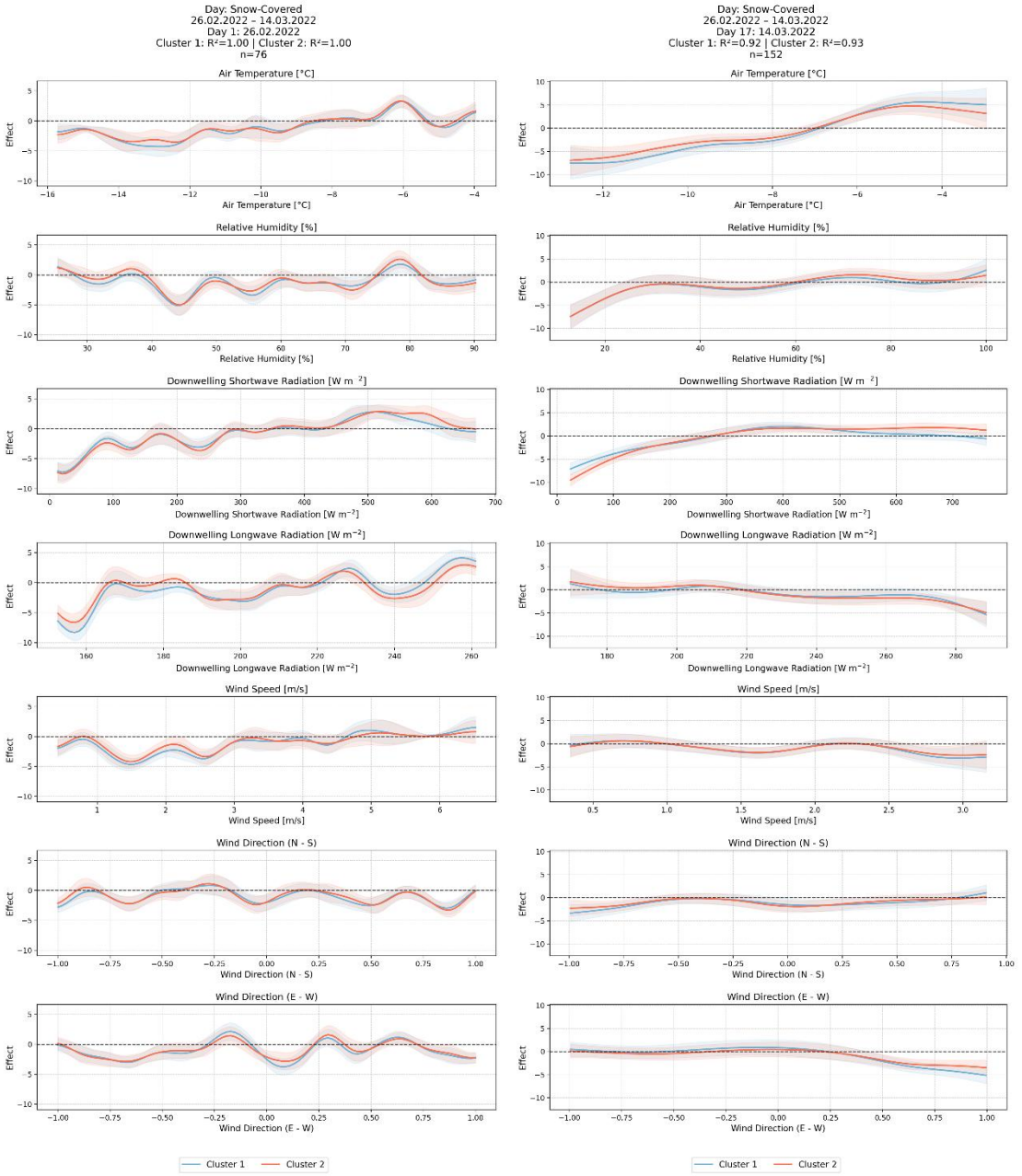

Figure C.38: GAM results of the diurnal curve clustering approach of days 1 and 17 of the snow-covered day period.

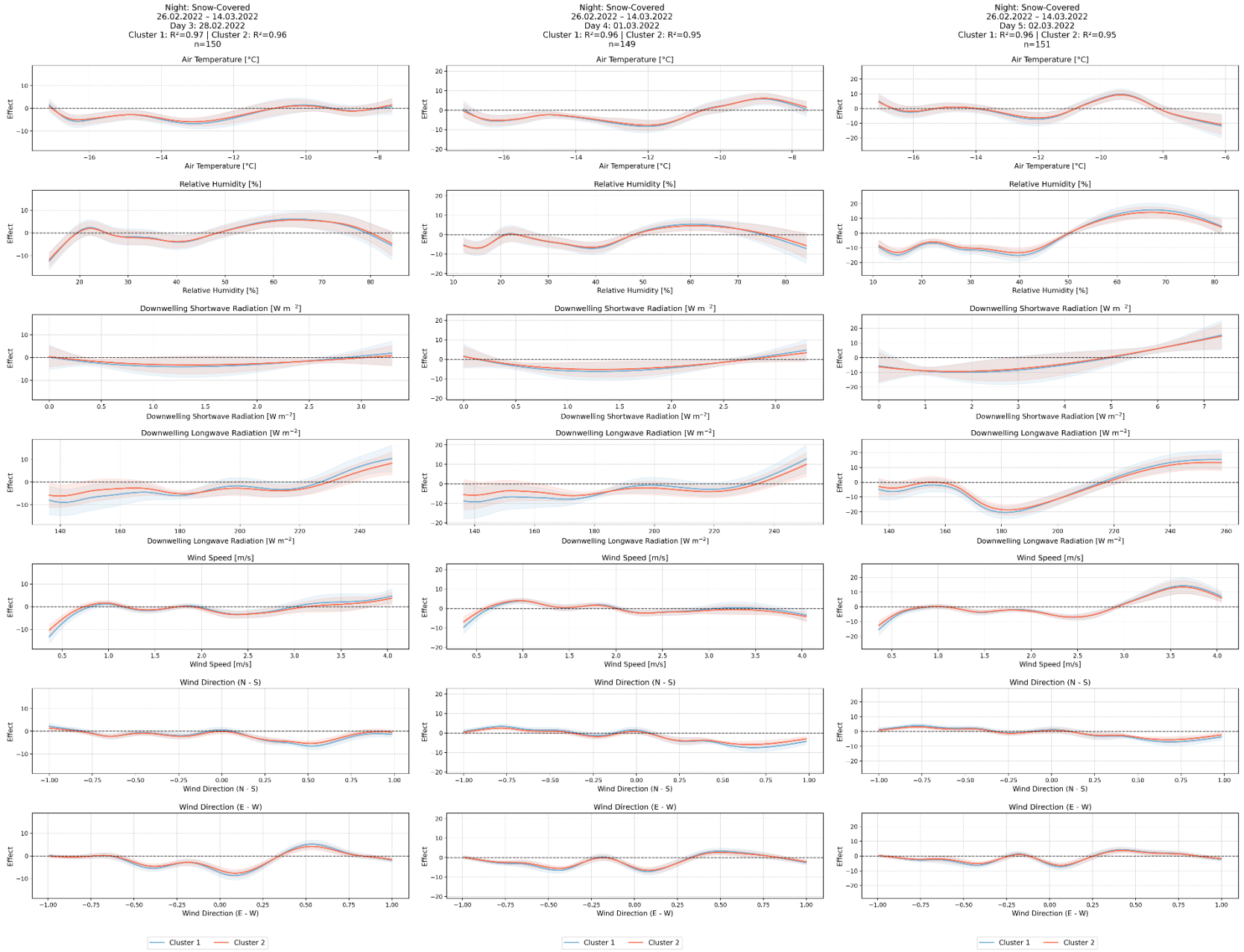

Figure C.39: GAM results of the diurnal curve clustering approach of days 3, 4 and 5 of the snow-covered night period.

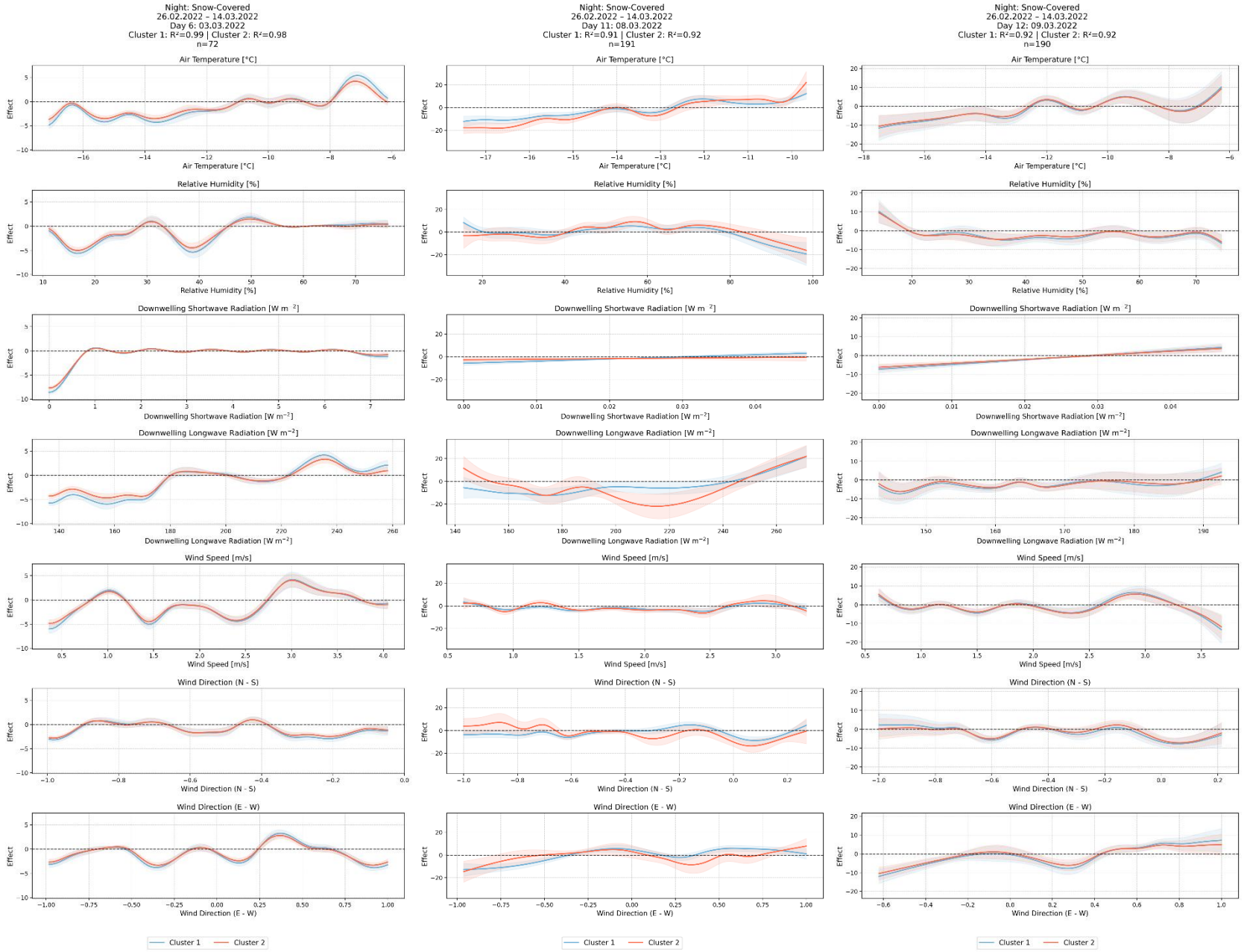

Figure C.40: GAM results of the diurnal curve clustering approach of days 6, 11 and 12 of the snow-covered night period.

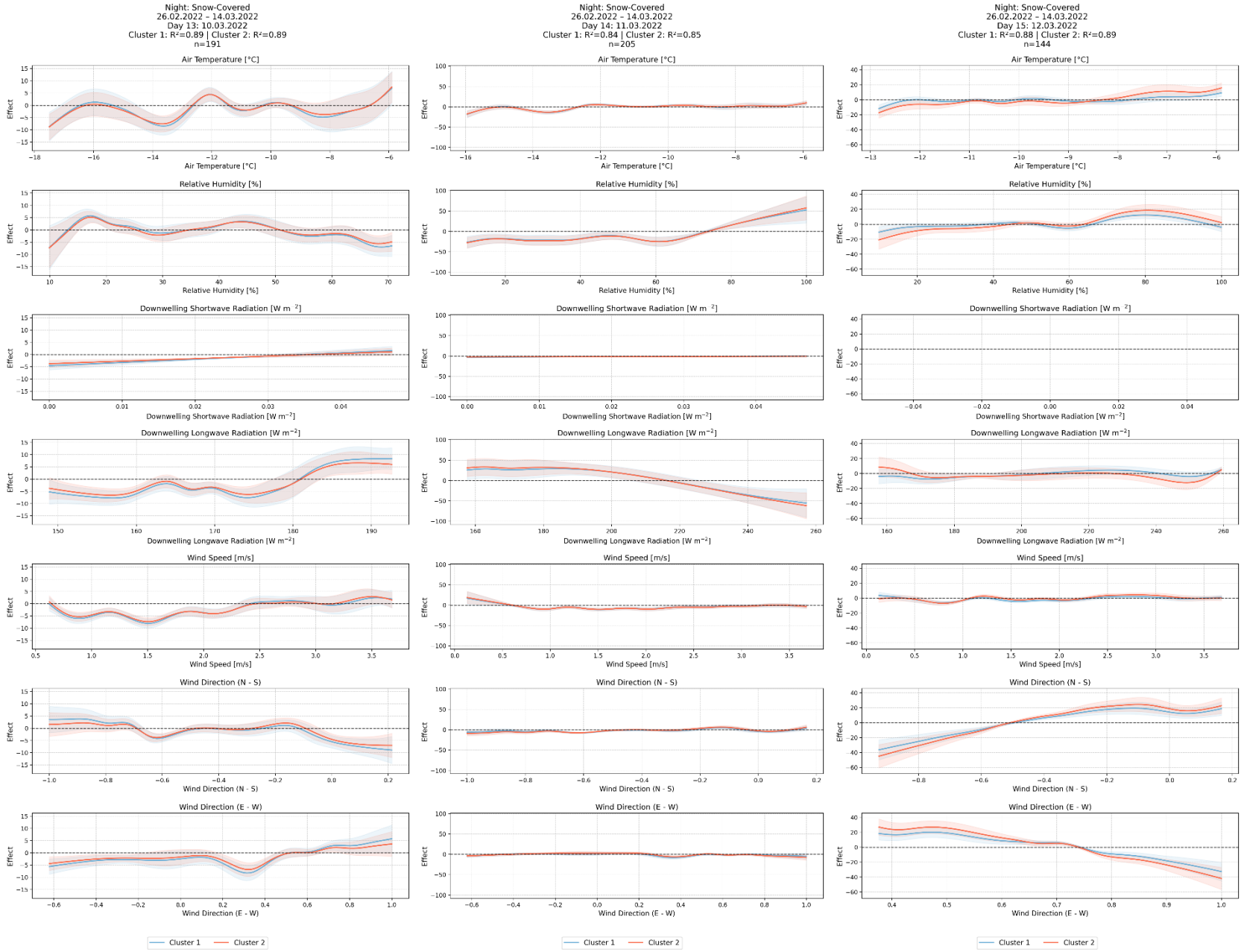

Figure C.41: GAM results of the diurnal curve clustering approach of days 13, 14 and 15 of the snow-covered night period.

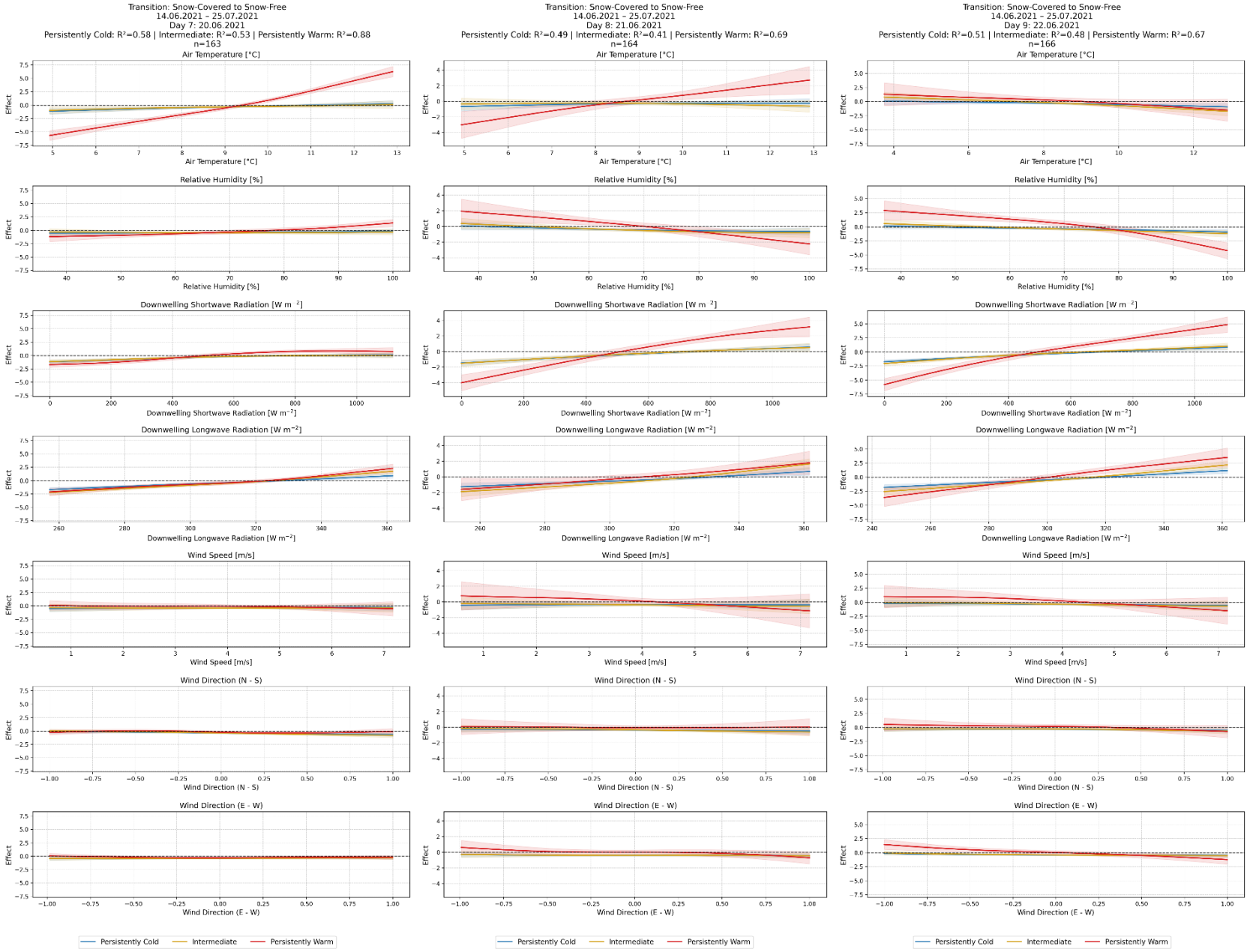

Figure C.42: GAM results of the anomaly persistence classification approach of days 7, 8 and 9 of the 2021 snow-covered to snow-free transition period.

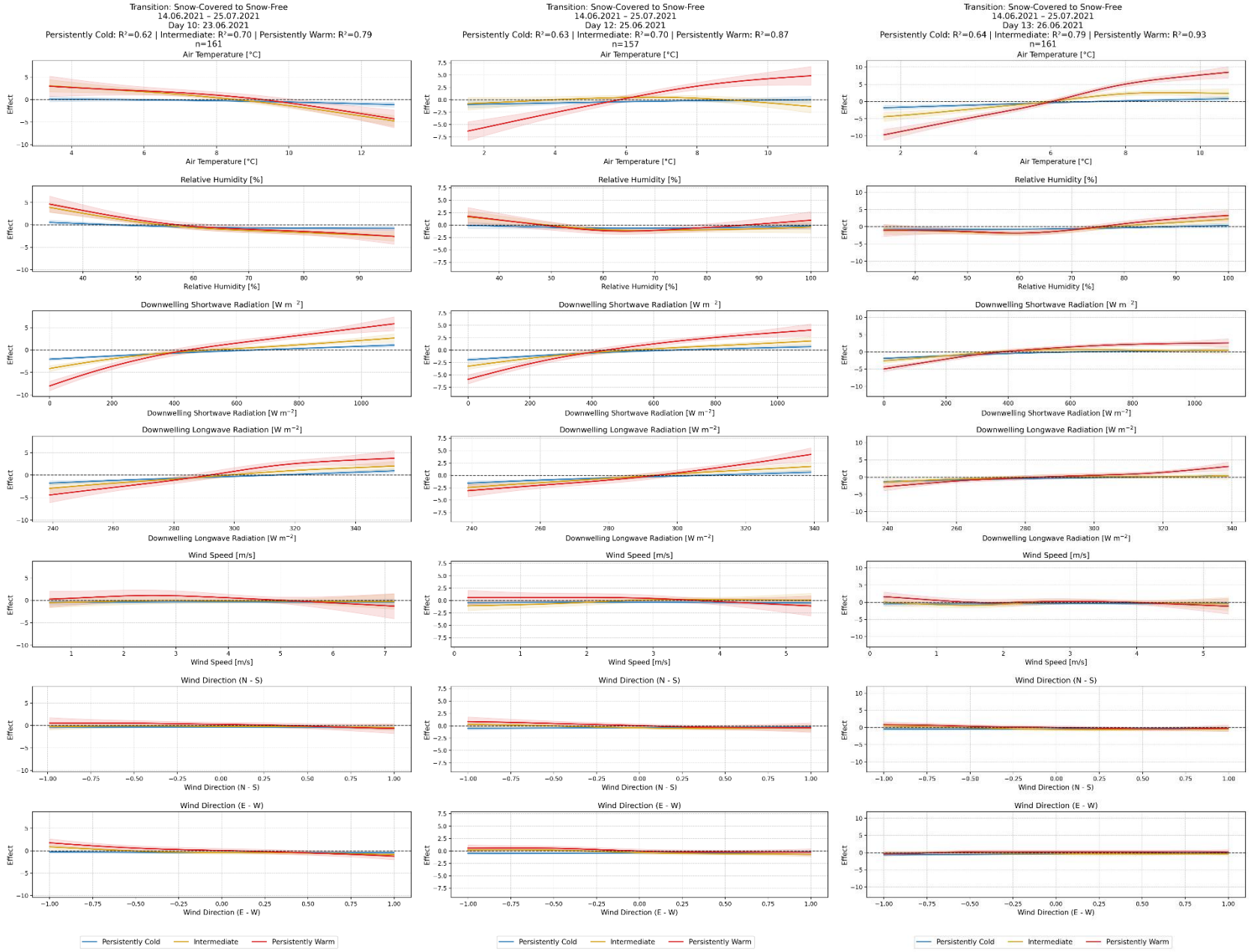

Figure C.43: GAM results of the anomaly persistence classification approach of days 10, 12 and 13 of the 2021 snow-covered to snow-free transition period.

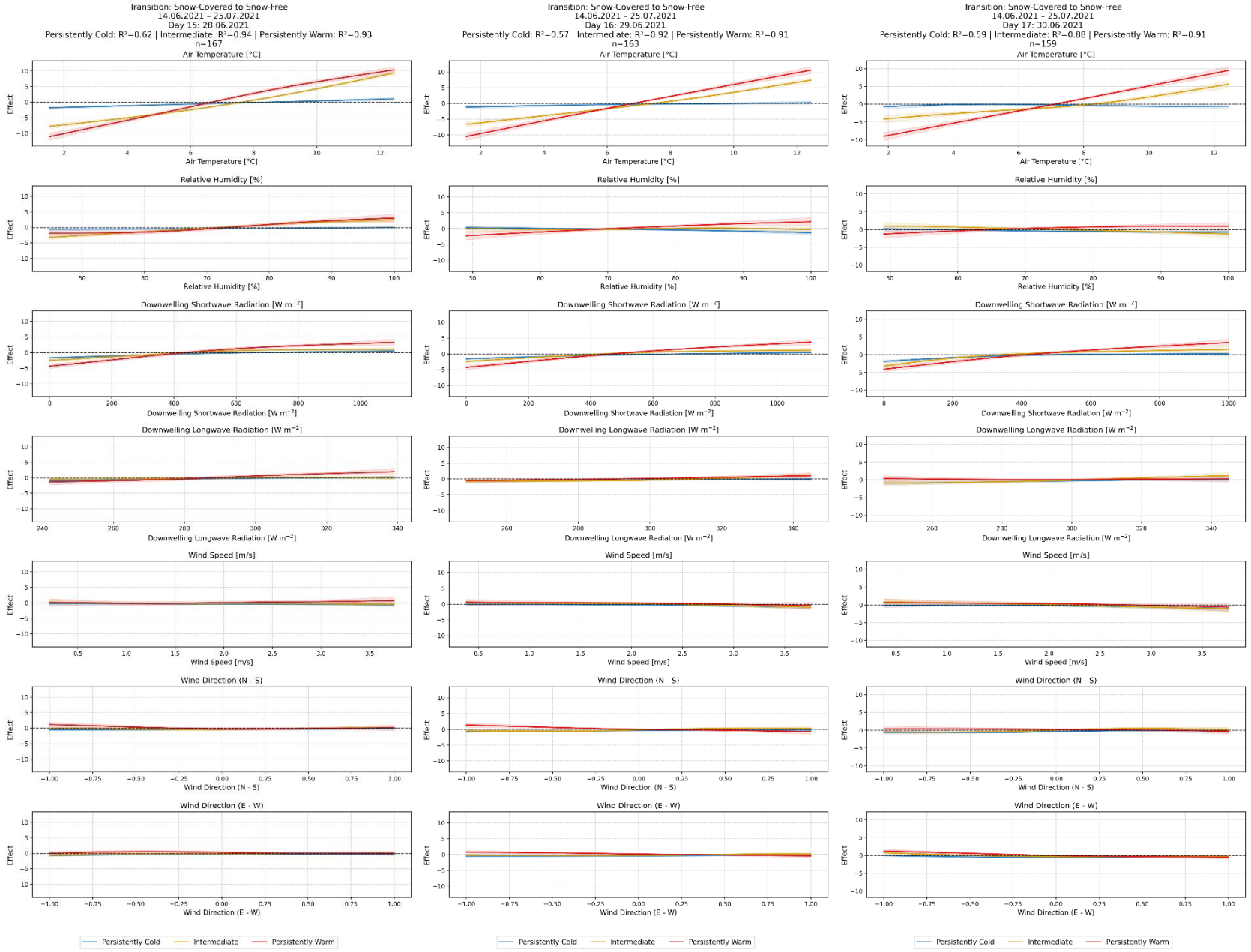

Figure C.44: GAM results of the anomaly persistence classification approach of days 15, 16 and 17 of the 2021 snow-covered to snow-free transition period.

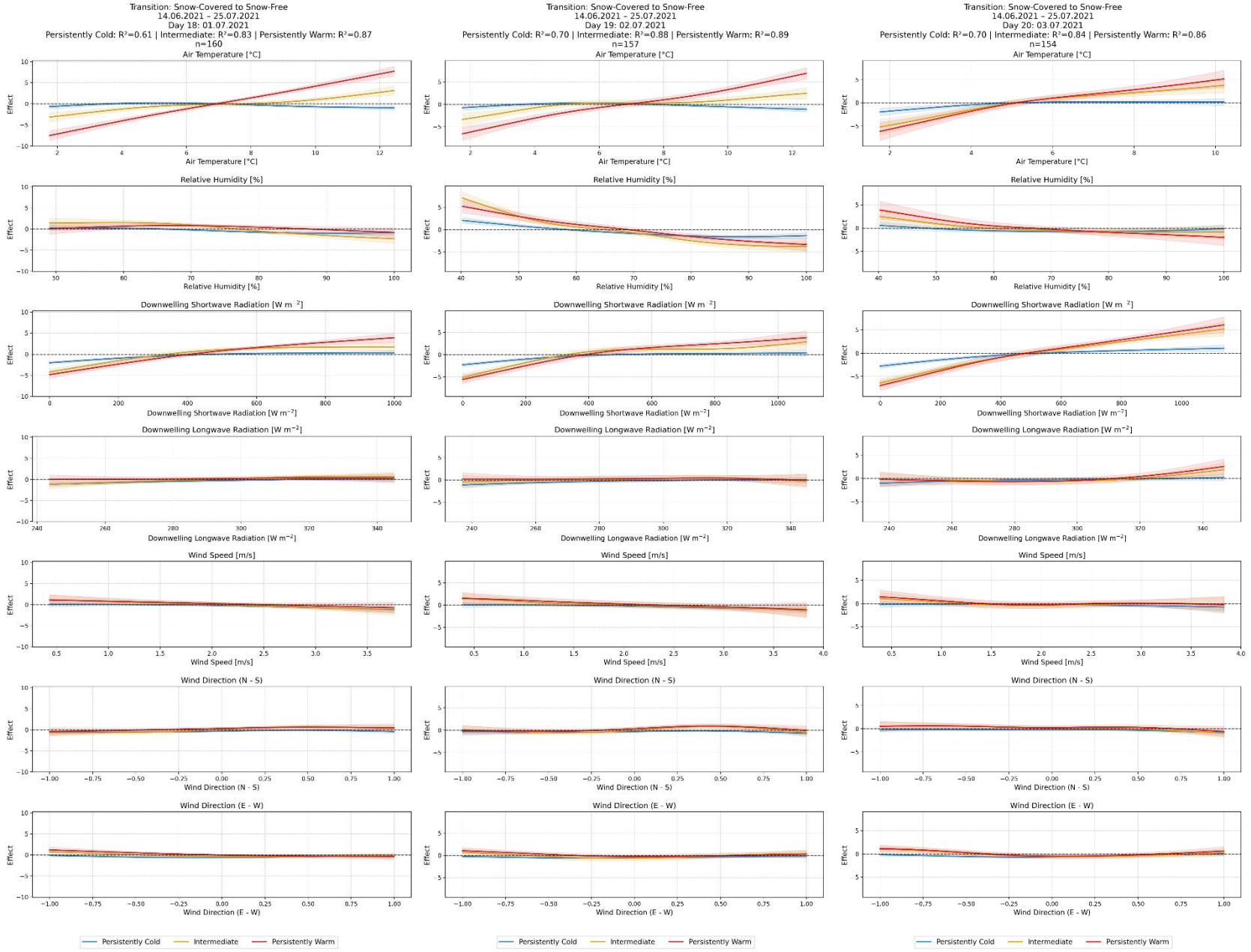

Figure C.45: GAM results of the anomaly persistence classification approach of days 18, 19 and 20 of the 2021 snow-covered to snow-free transition period.

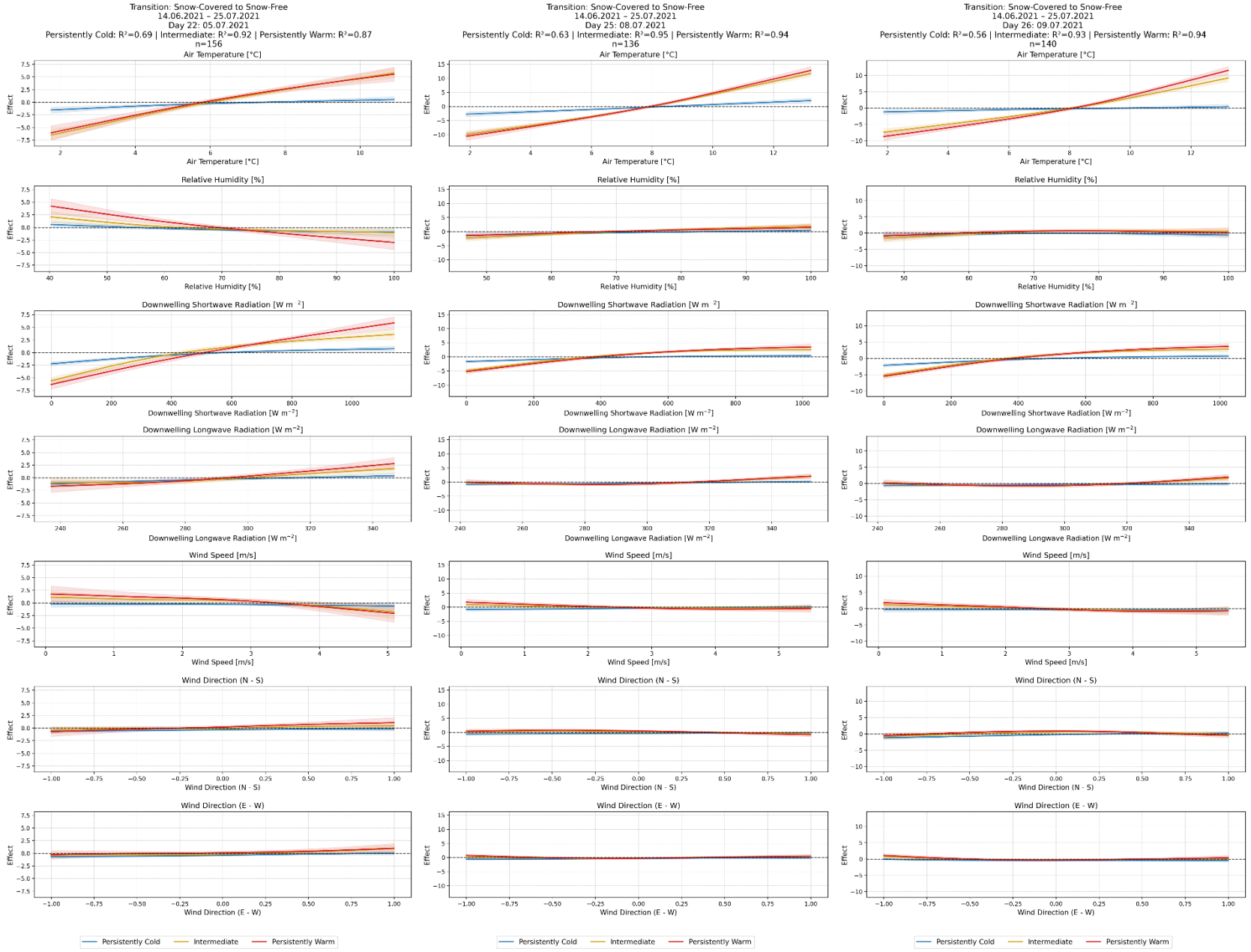

Figure C.46: GAM results of the anomaly persistence classification approach of days 22, 25 and 26 of the 2021 snow-covered to snow-free transition period.

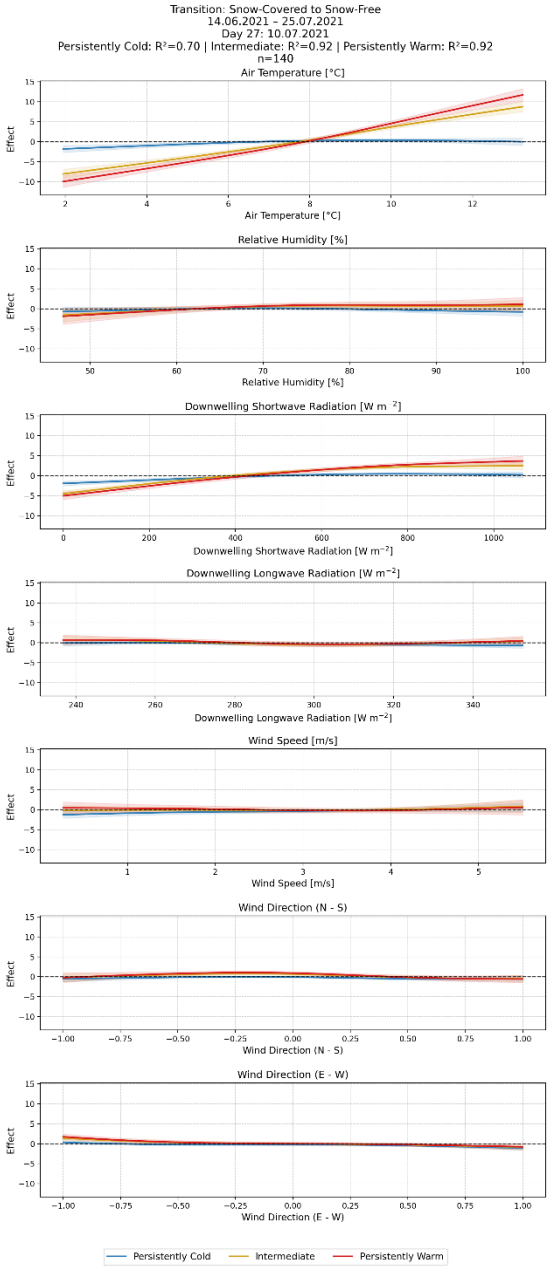

Figure C.47: GAM results of the anomaly persistence classification approach of day 27 of the 2021 snow-covered to snow-free transition period.

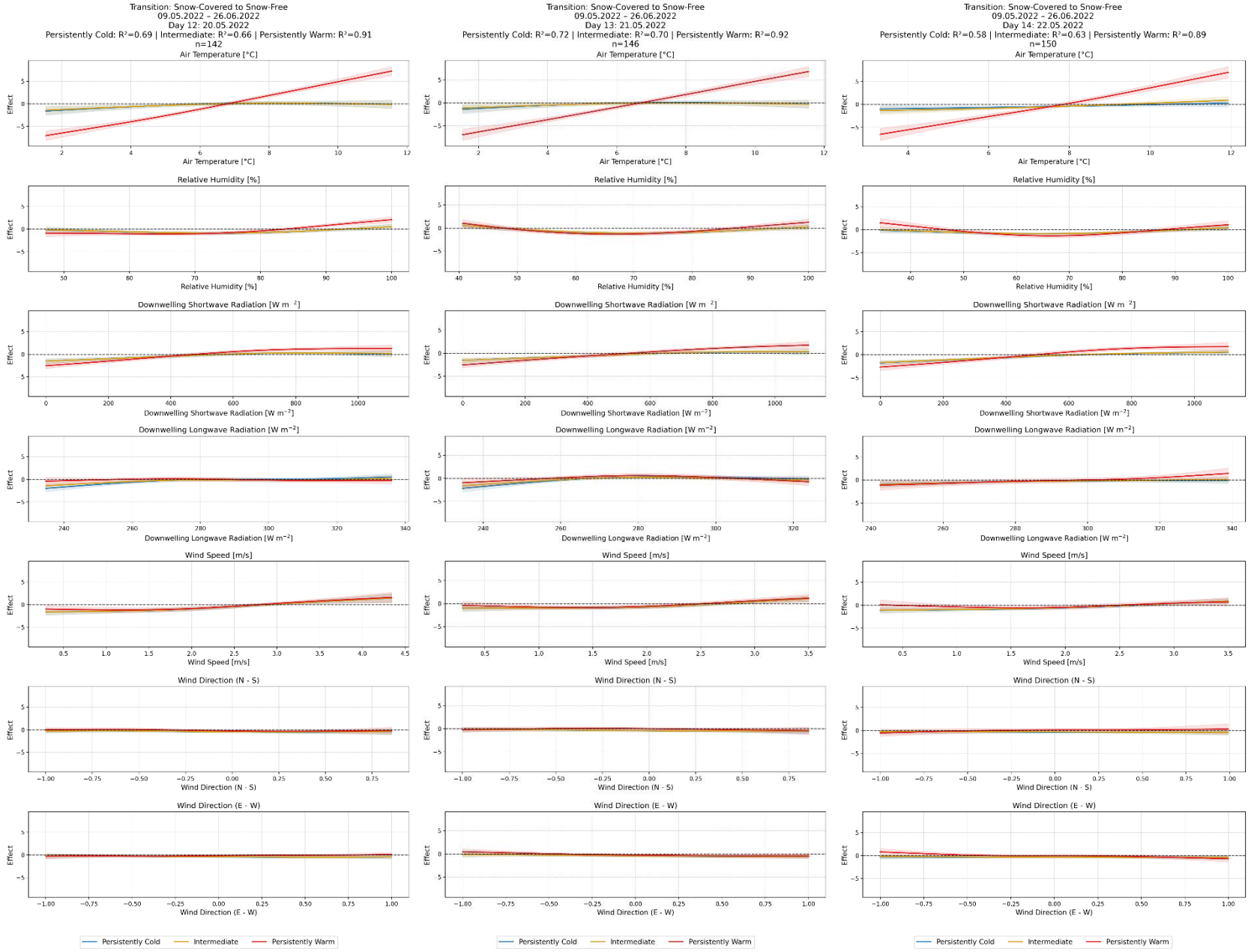

Figure C.48: GAM results of the anomaly persistence classification approach of days 12, 13 and 14 of the 2022 snow-covered to snow-free transition period.

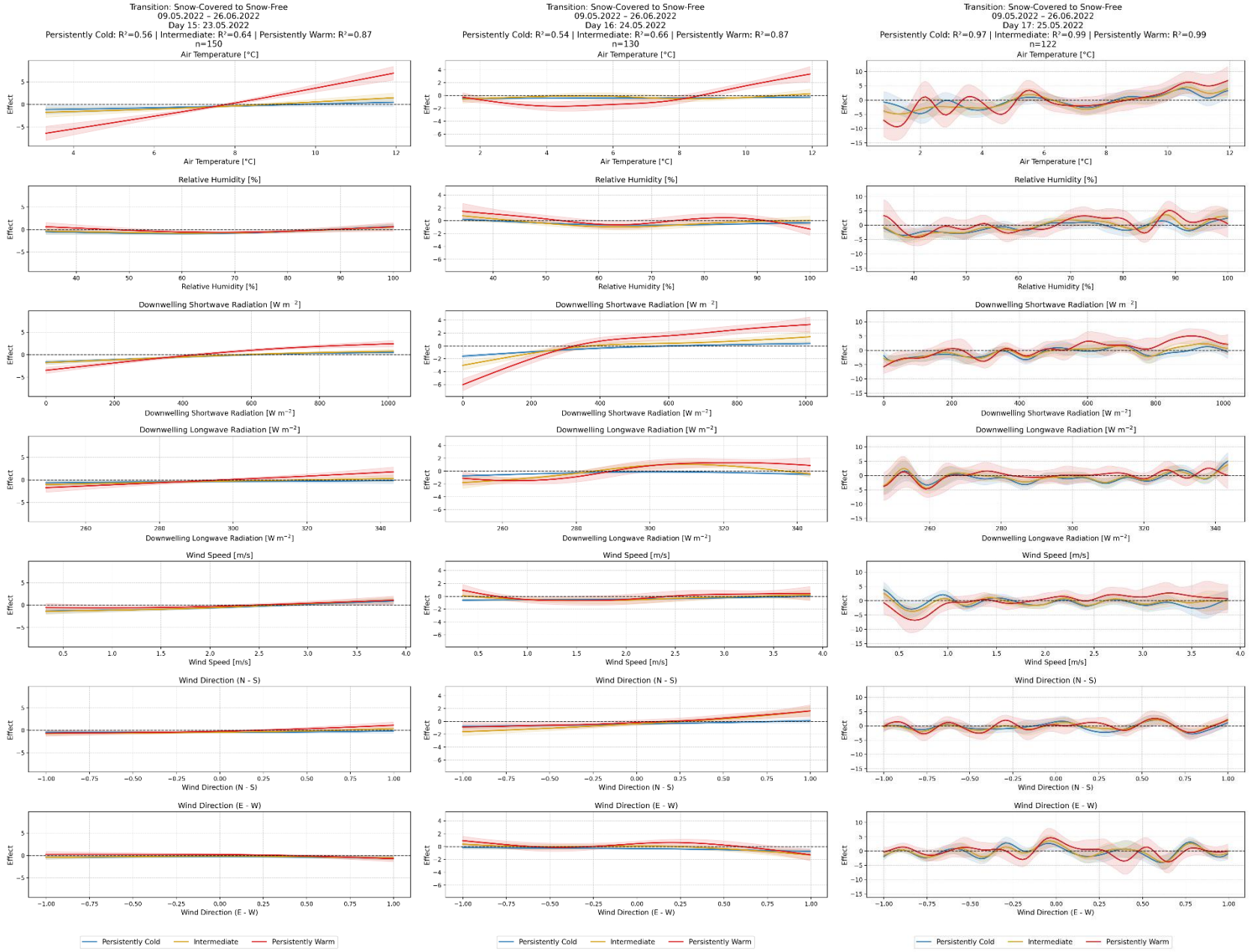

Figure C.49: GAM results of the anomaly persistence classification approach of days 15, 16 and 17 of the 2022 snow-covered to snow-free transition period.

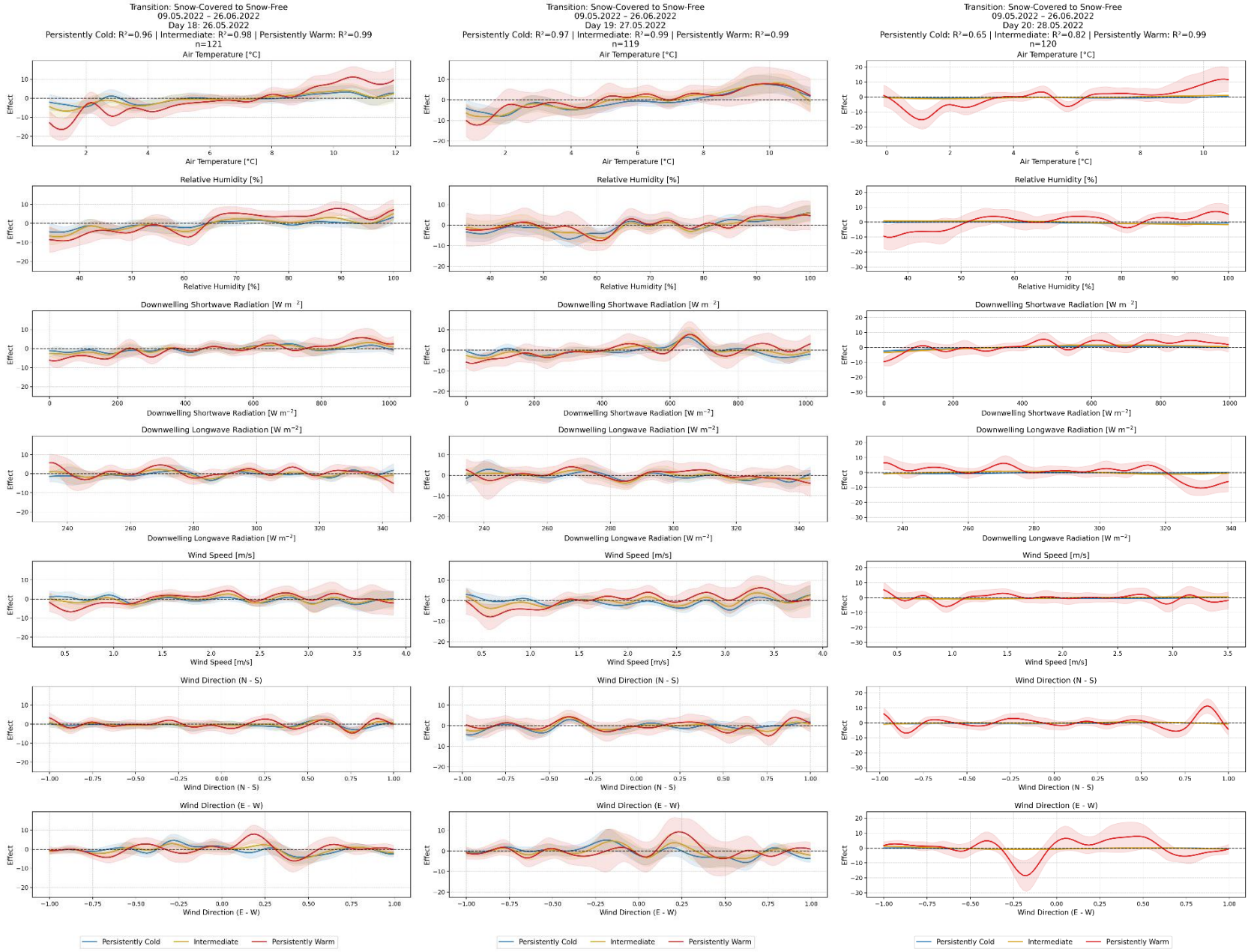

Figure C.50: GAM results of the anomaly persistence classification approach of days 18, 19 and 20 of the 2022 snow-covered to snow-free transition period.

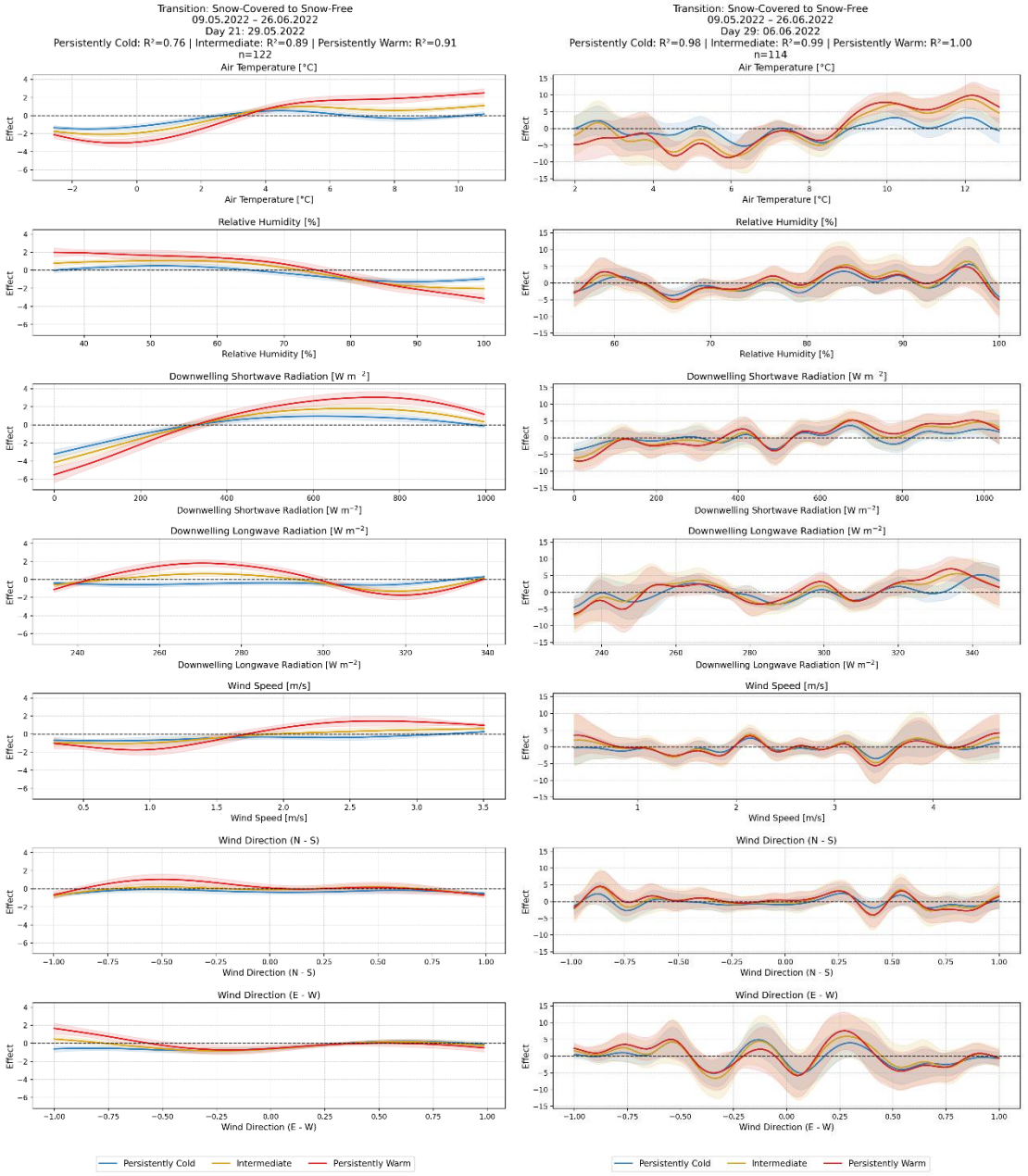

Figure C.51: GAM results of the anomaly persistence classification approach of days 21 and 29 of the 2022 snow-covered to snow-free transition period.

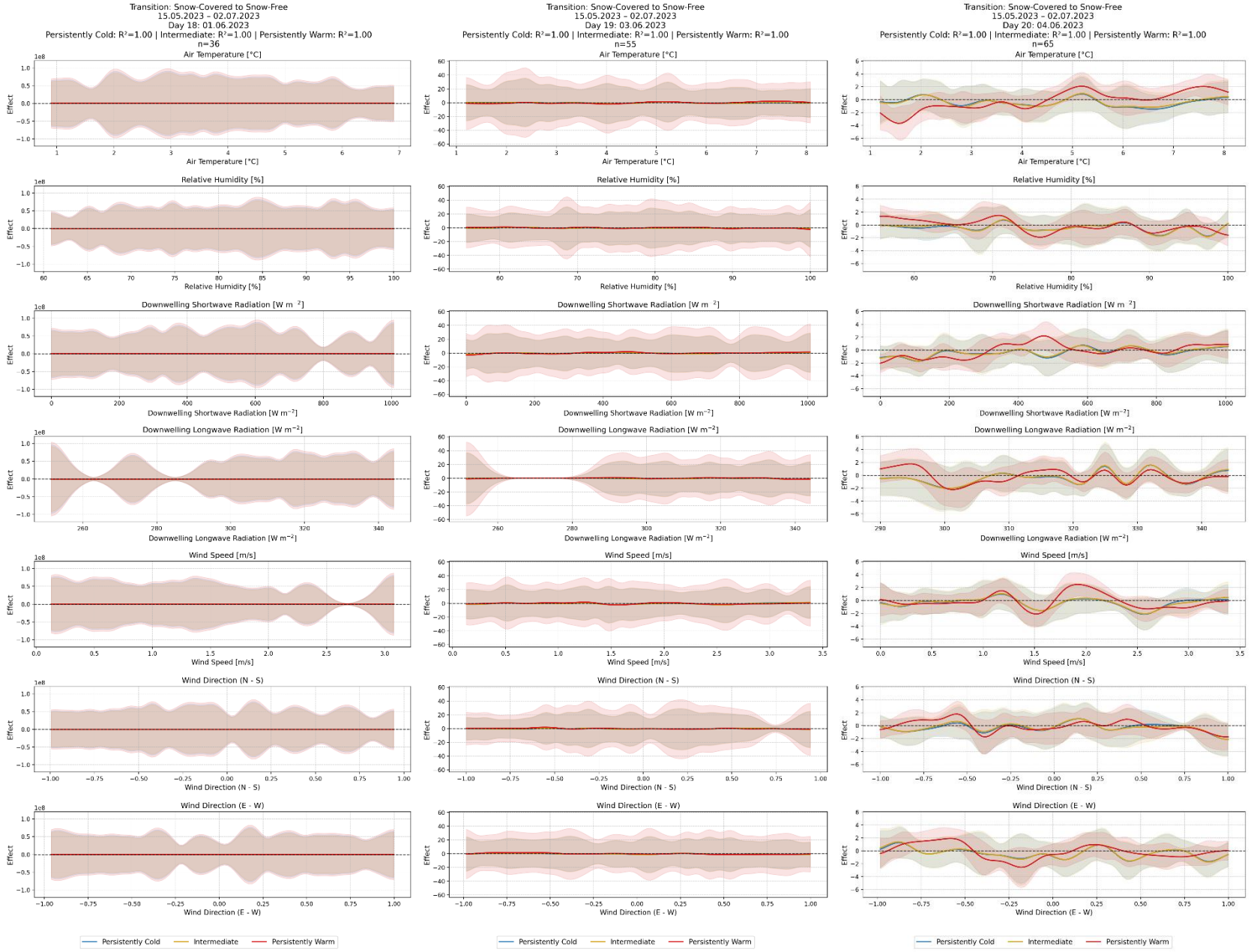

Figure C.52: GAM results of the anomaly persistence classification approach of days 18, 19 and 20 of the 2023 snow-covered to snow-free transition period.

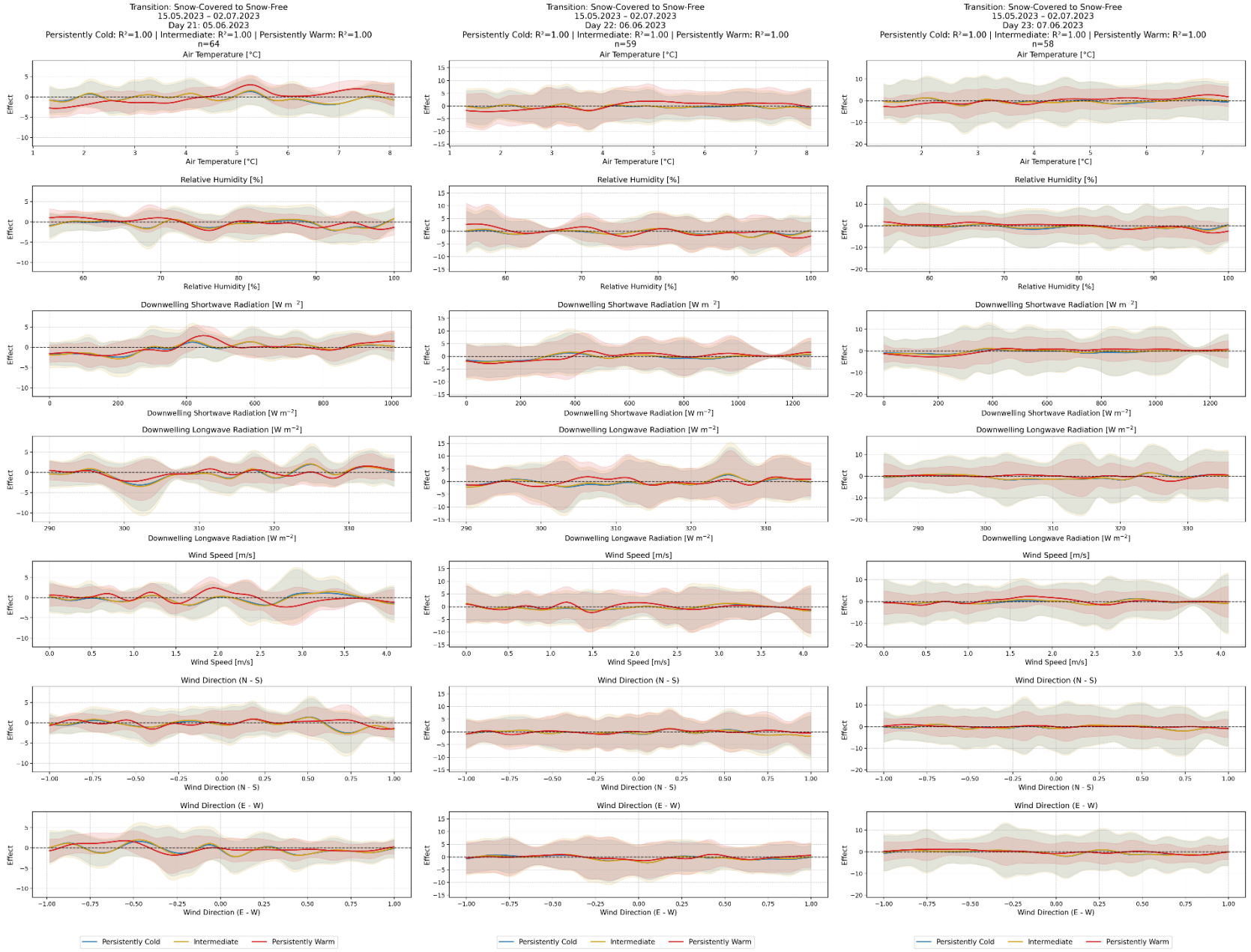

Figure C.53: GAM results of the anomaly persistence classification approach of days 21, 22 and 23 of the 2023 snow-covered to snow-free transition period.

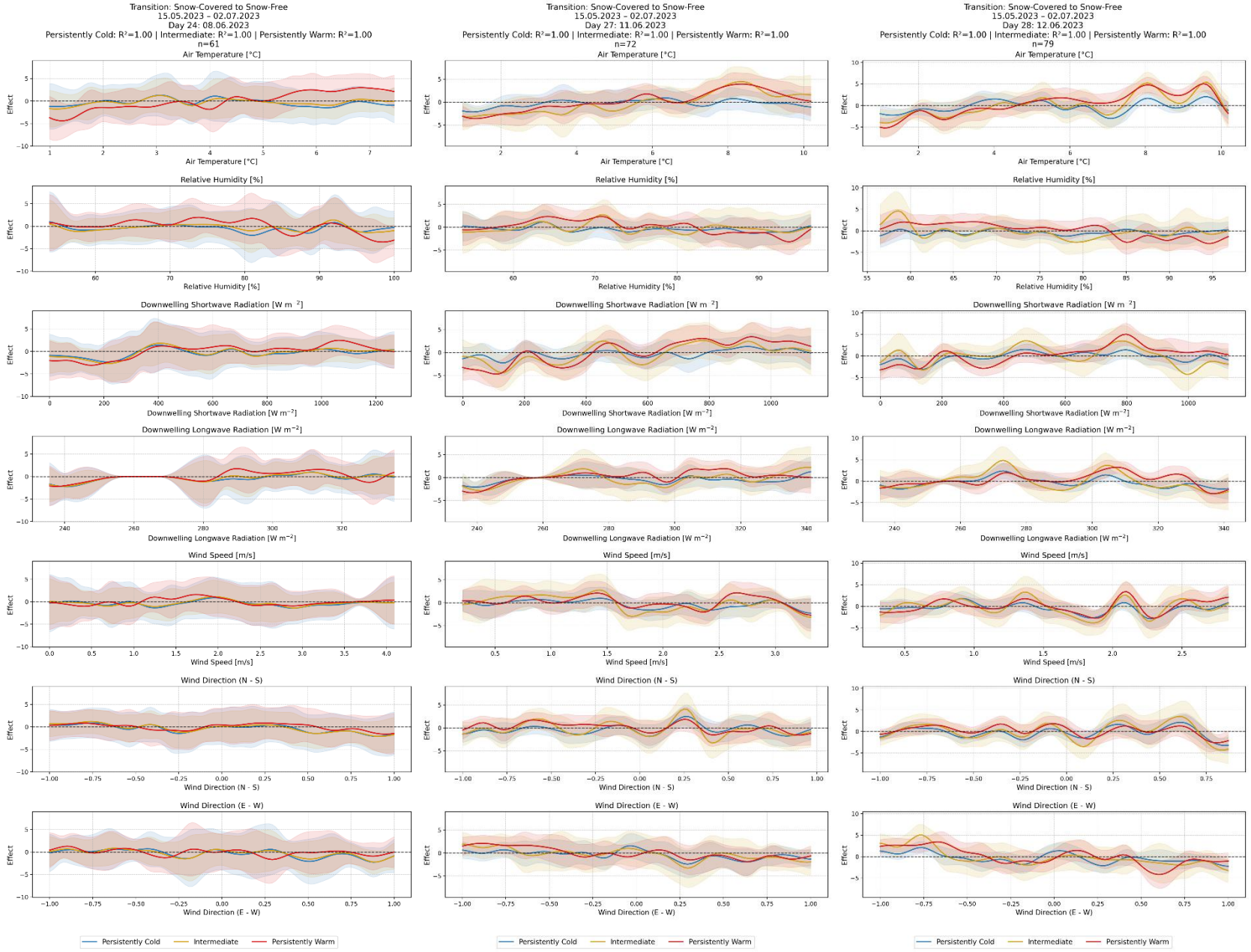

Figure C.54: GAM results of the anomaly persistence classification approach of days 24, 27 and 28 of the 2023 snow-covered to snow-free transition period.

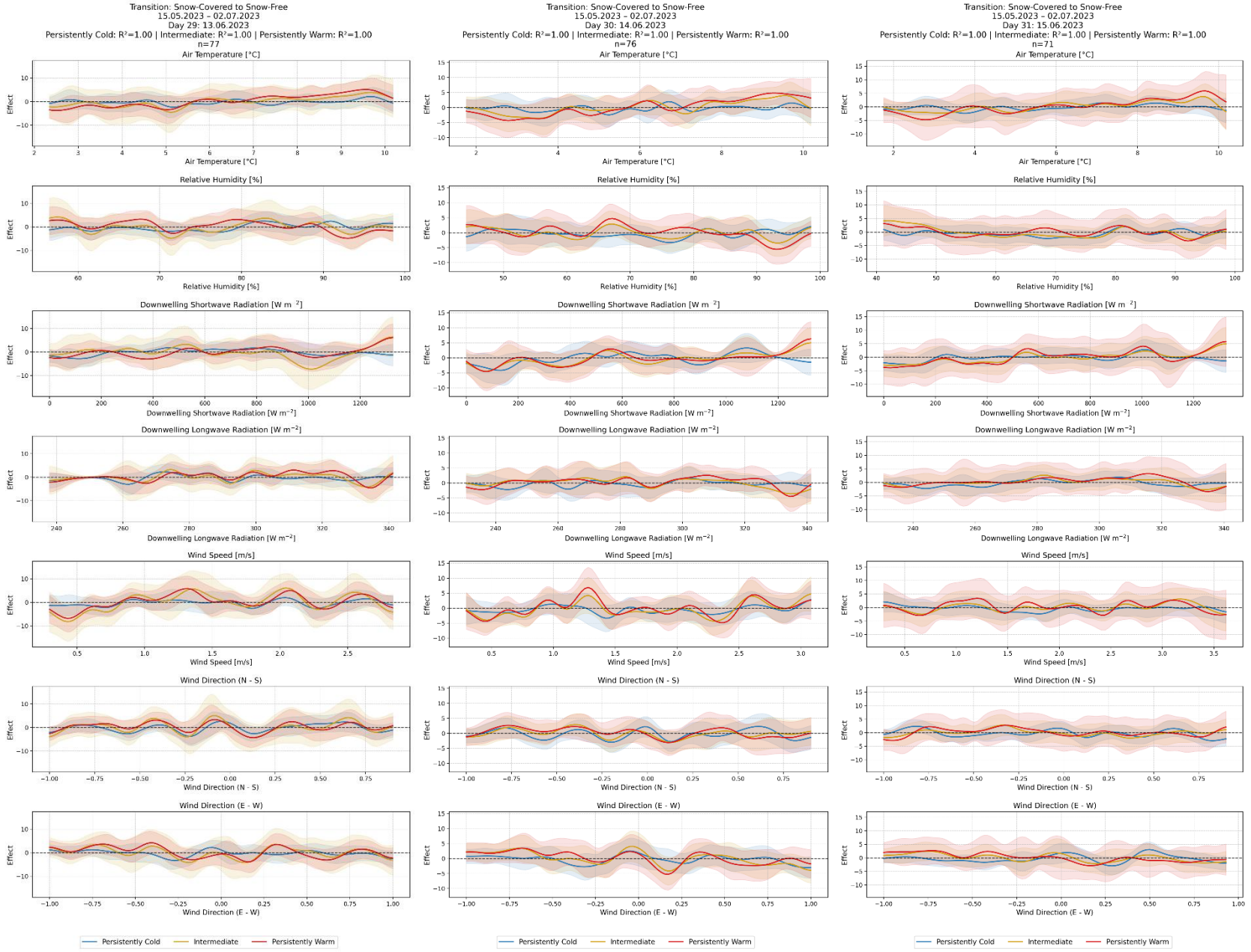

Figure C.55: GAM results of the anomaly persistence classification approach of days 29, 30 and 31 of the 2023 snow-covered to snow-free transition period.

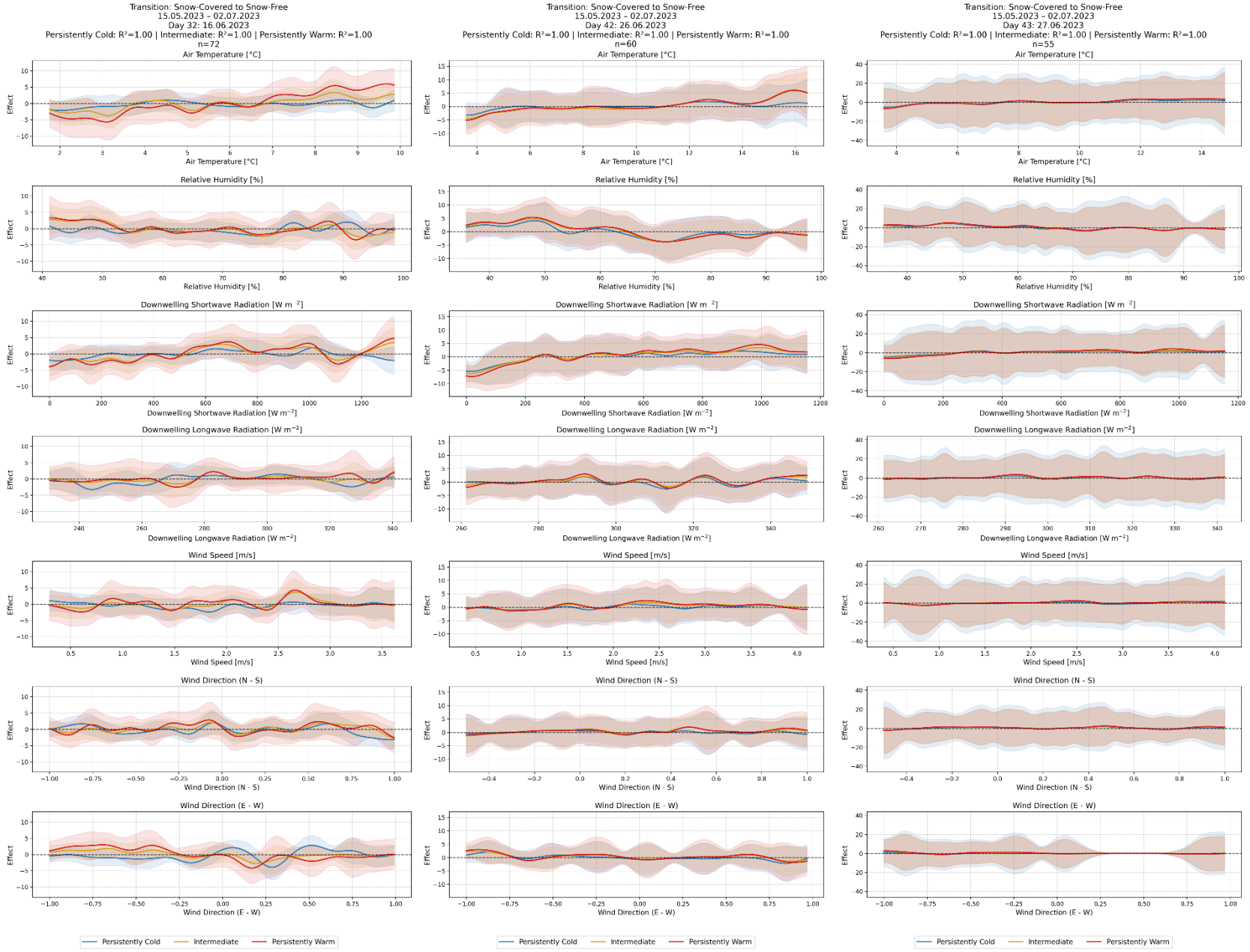

Figure C.56: GAM results of the anomaly persistence classification approach of days 32, 42 and 43 of the 2023 snow-covered to snow-free transition period.

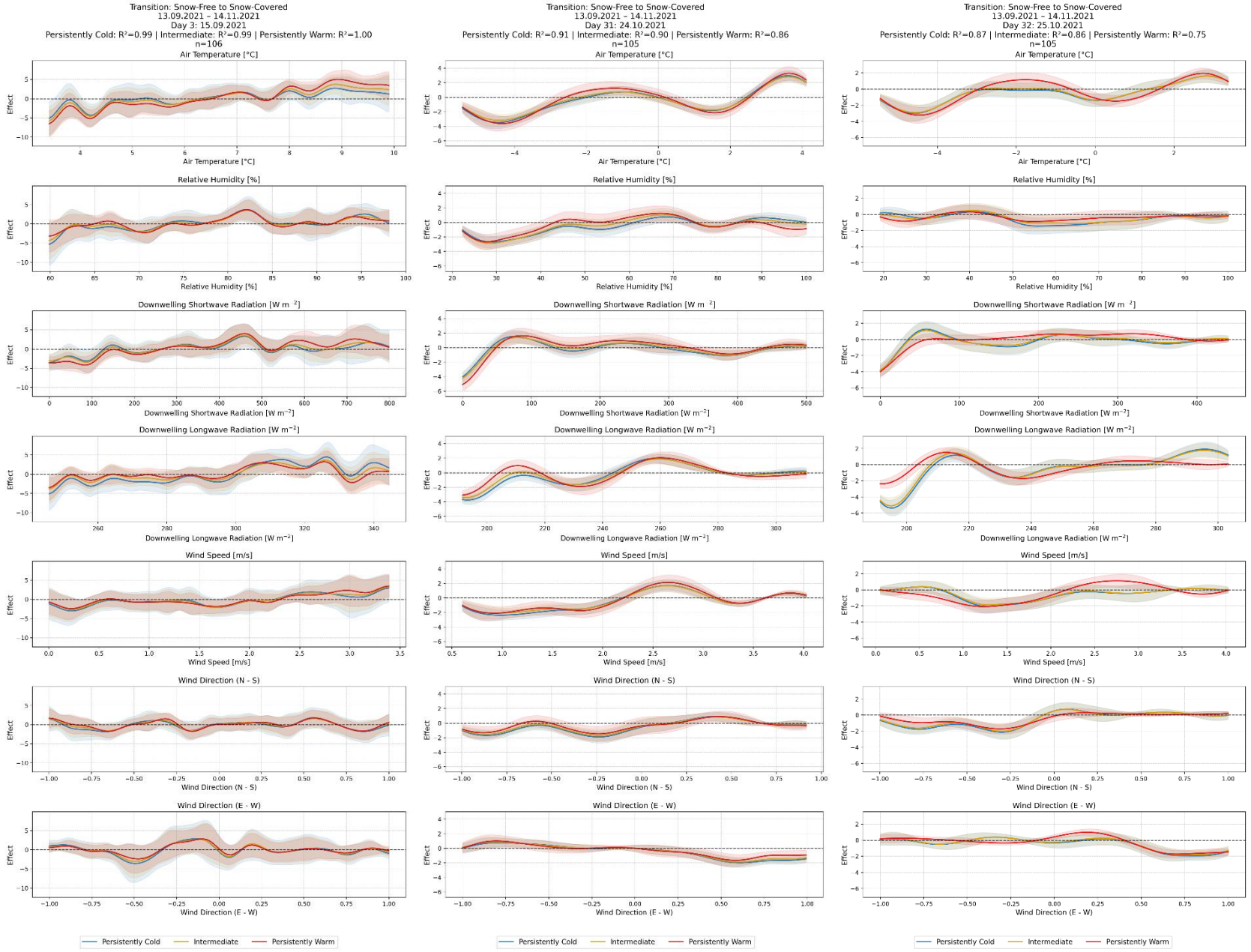

Figure C.57: GAM results of the anomaly persistence classification approach of days 3, 31 and 32 of the 2021 snow-free to snow-covered transition period.

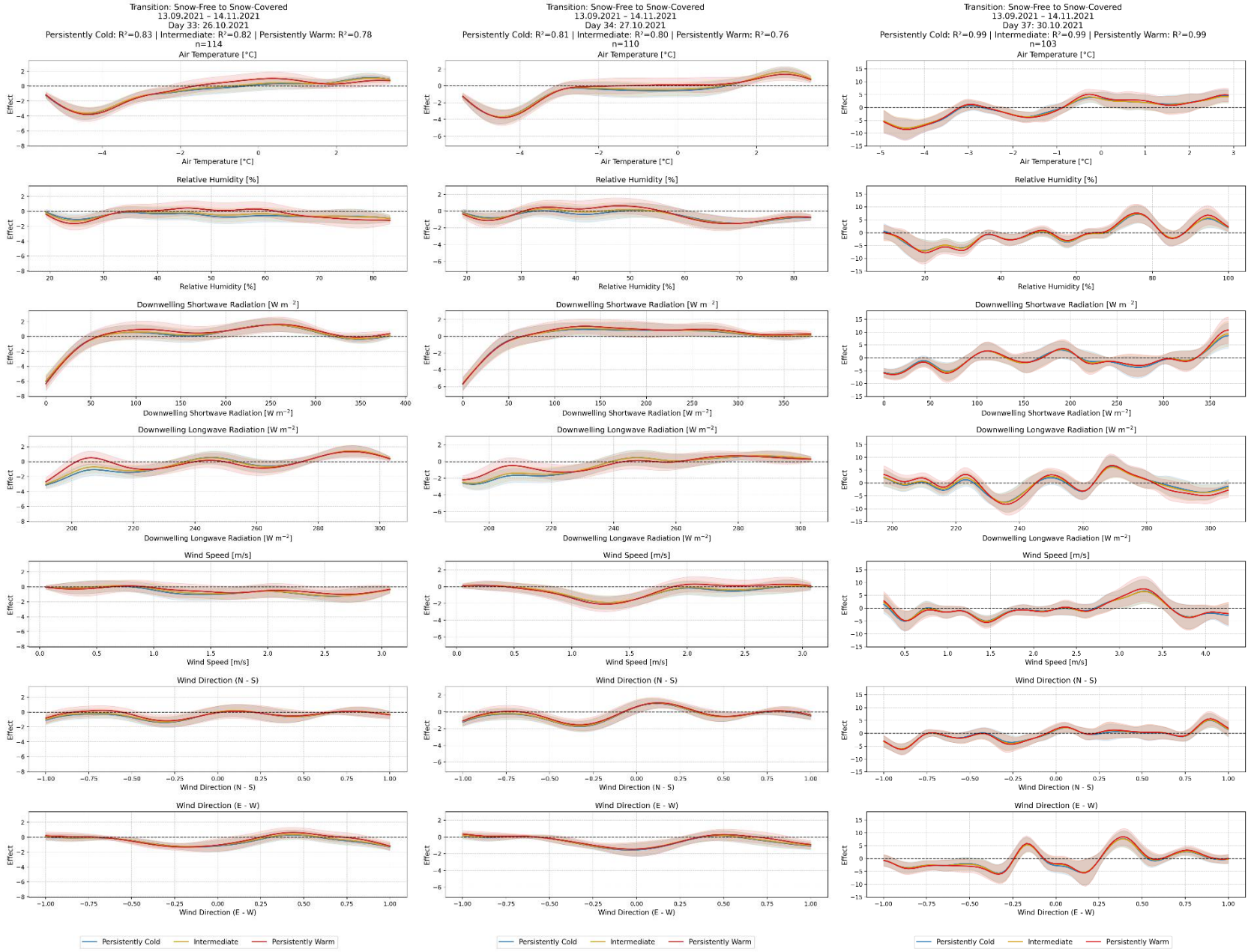

Figure C.58: GAM results of the anomaly persistence classification approach of days 33, 34 and 37 of the 2021 snow-free to snow-covered transition period.

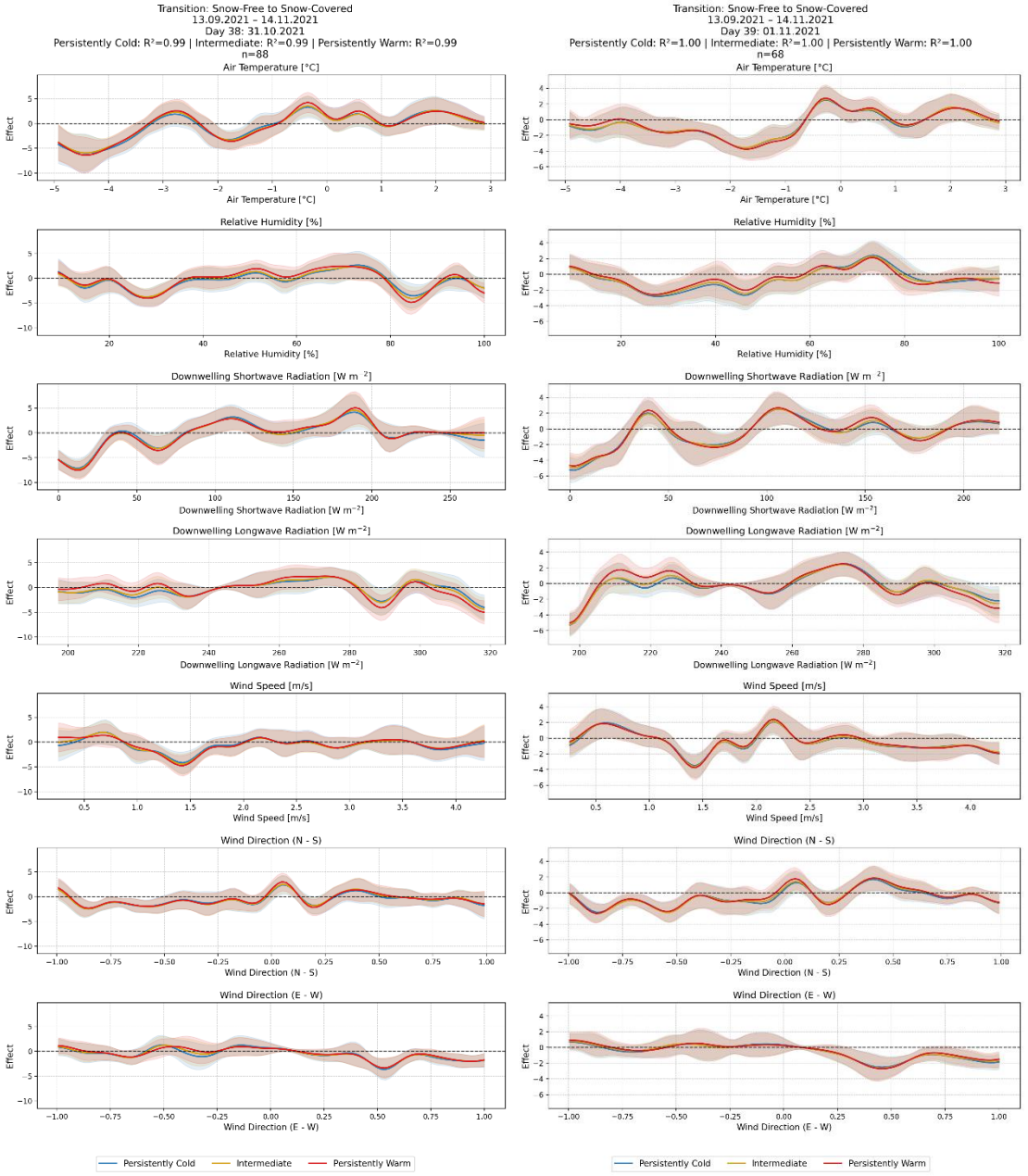

Figure C.59: GAM results of the anomaly persistence classification approach of days 38 and 39 of the 2021 snow-free to snow-covered transition period.

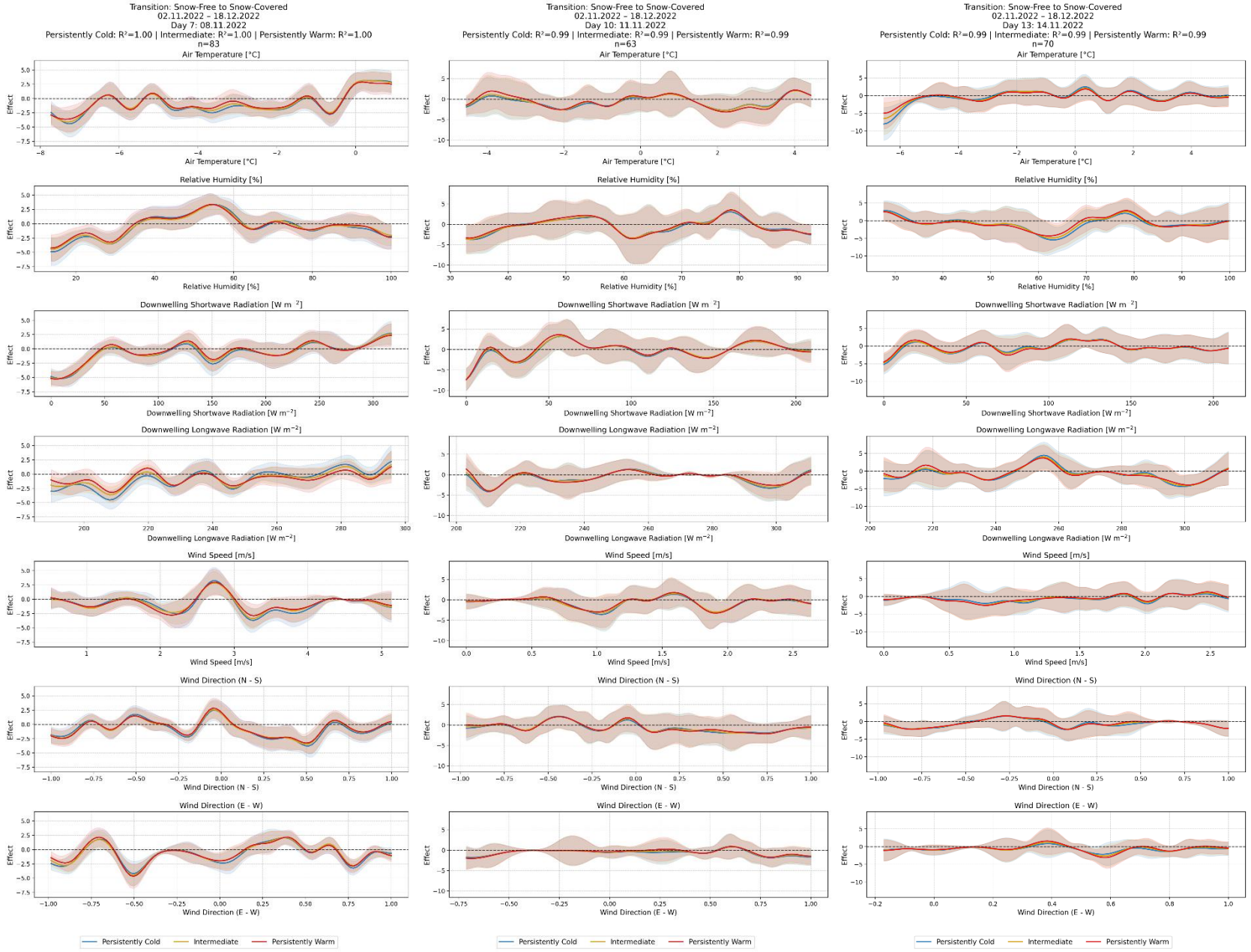

Figure C.60: GAM results of the anomaly persistence classification approach of days 7, 10 and 13 of the 2022 snow-free to snow-covered transition period.

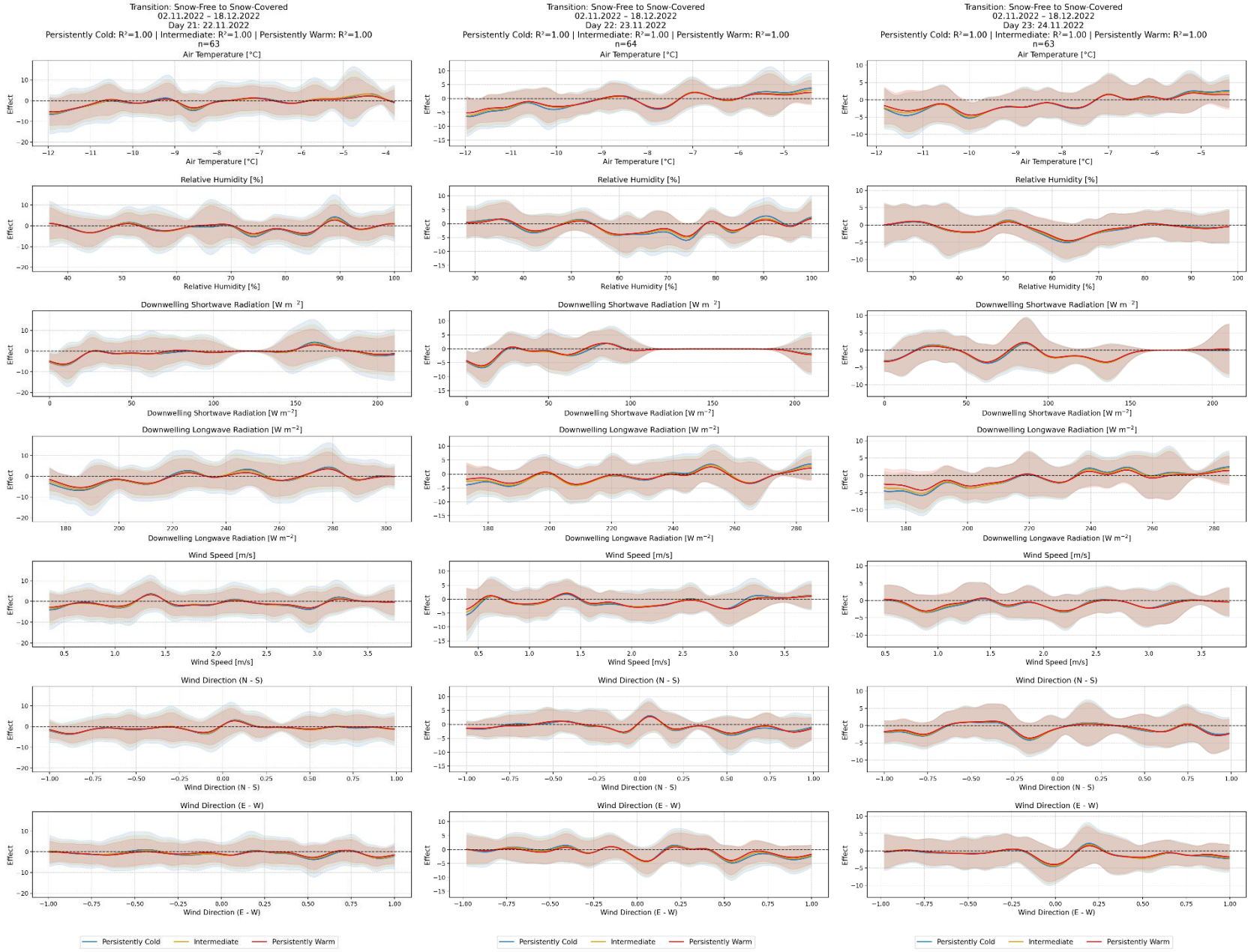

Figure C.61: GAM results of the anomaly persistence classification approach of days 21, 22 and 23 of the 2022 snow-free to snow-covered transition period.

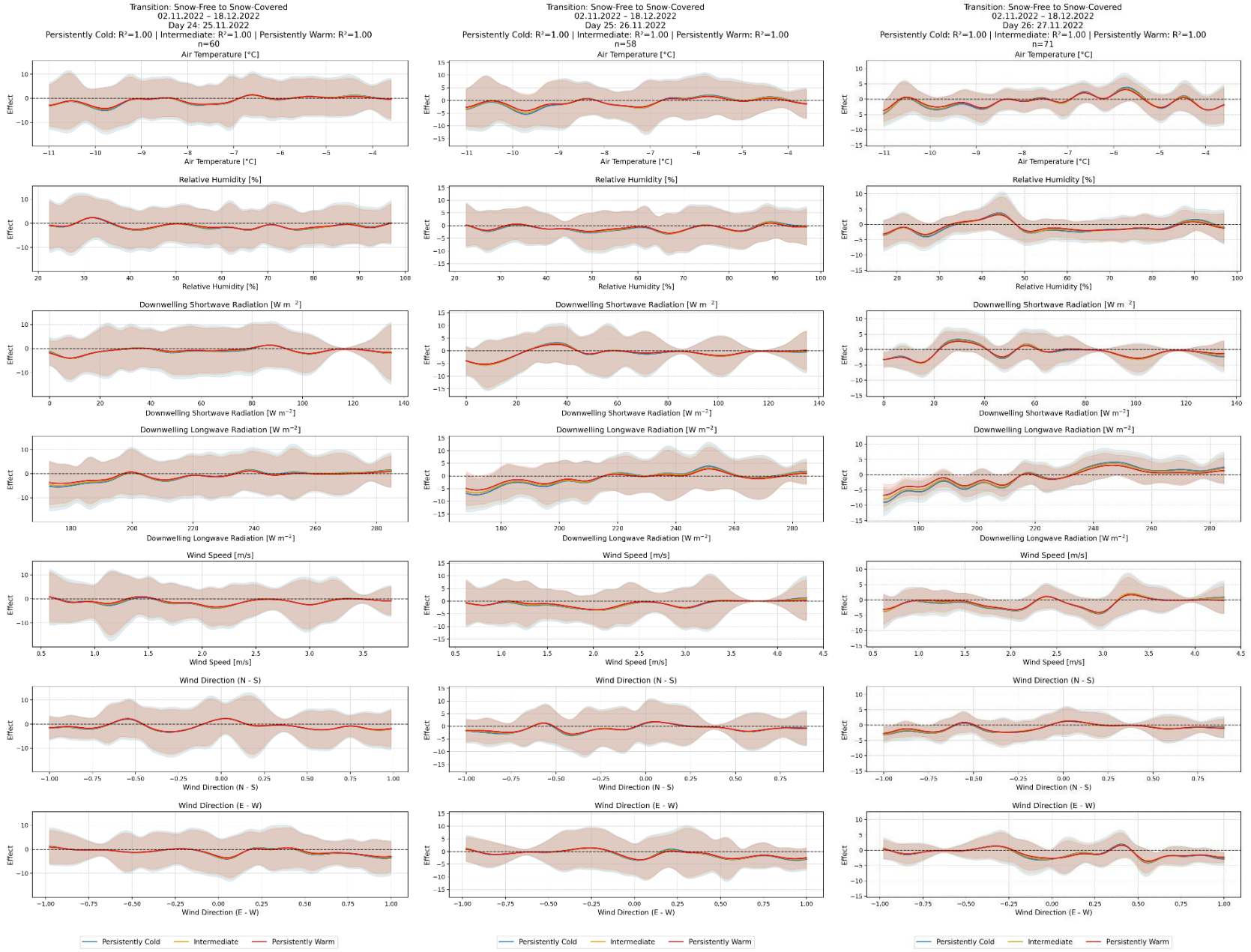

Figure C.62: GAM results of the anomaly persistence classification approach of days 24, 25 and 26 of the 2022 snow-free to snow-covered transition period.

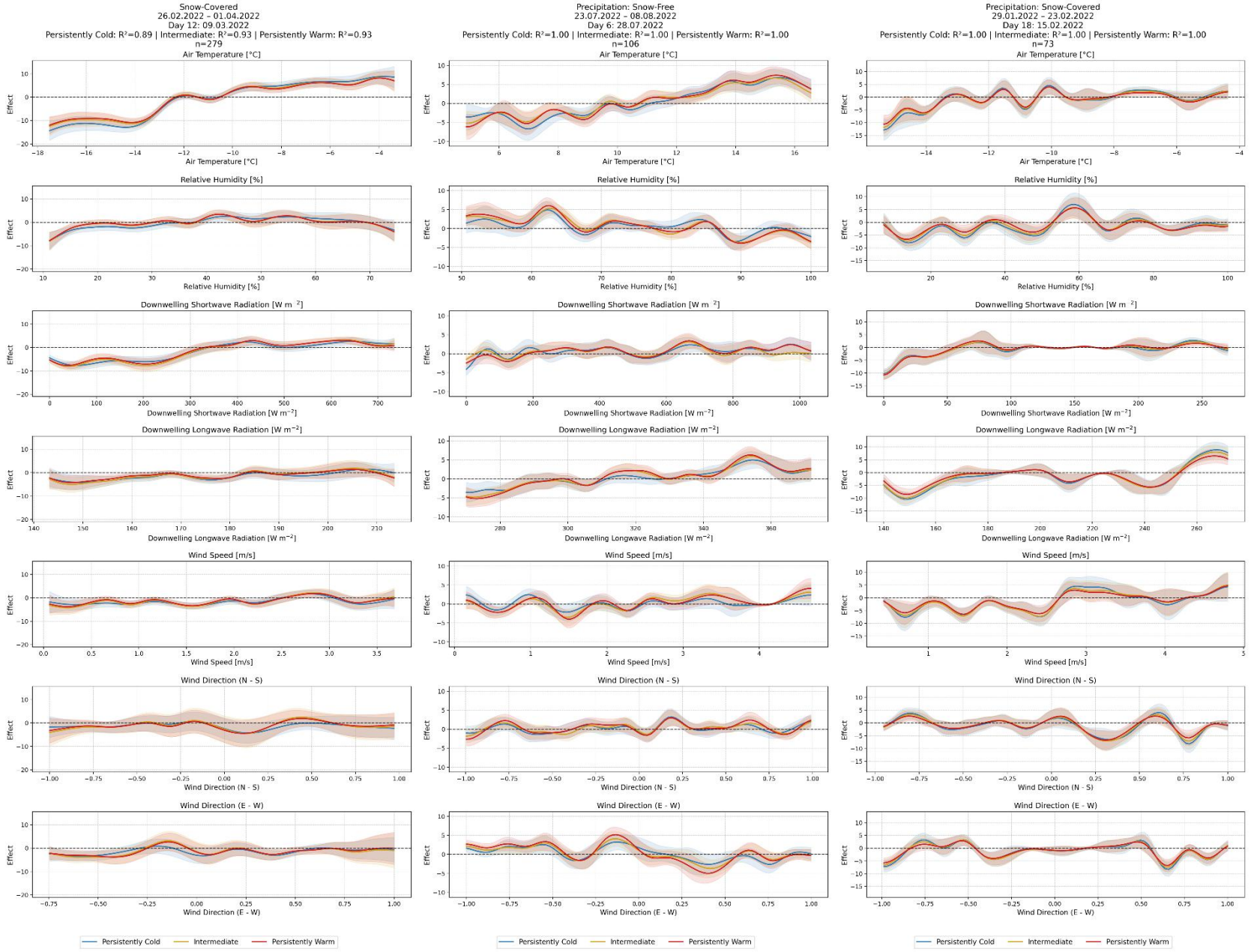

Figure C.63: GAM results of the anomaly persistence classification approach of day 12 of the snow-covered period (left), day 6 of the snow-free precipitation period (middle) and day 18 of the snow-covered precipitation period (right). Day 12 of the snow-covered period is day 14 of the snow-covered no precipitation period simultaneously.

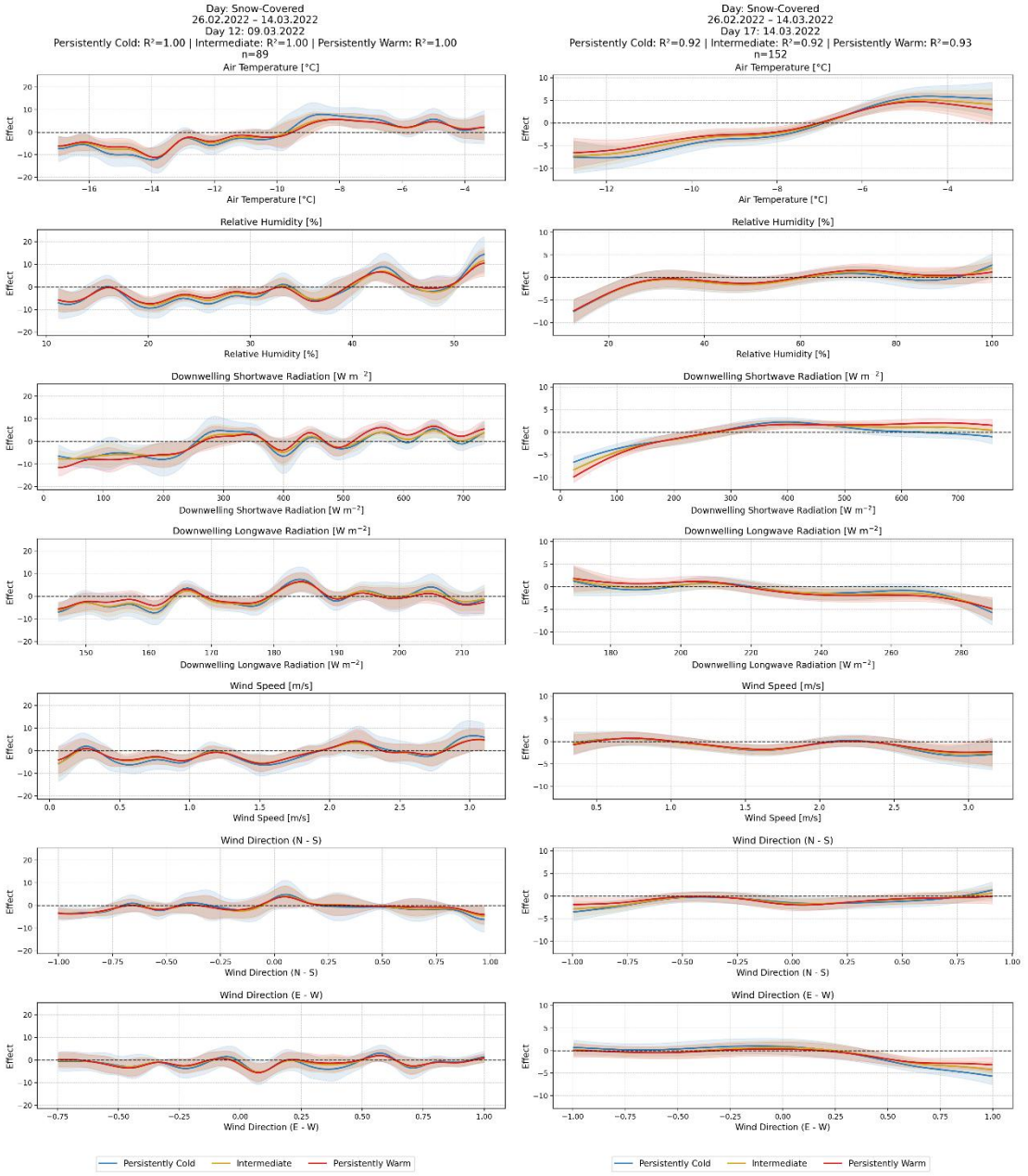

Figure C.64: GAM results of the anomaly persistence classification approach of days 12 and 17 of the snow-covered day period.

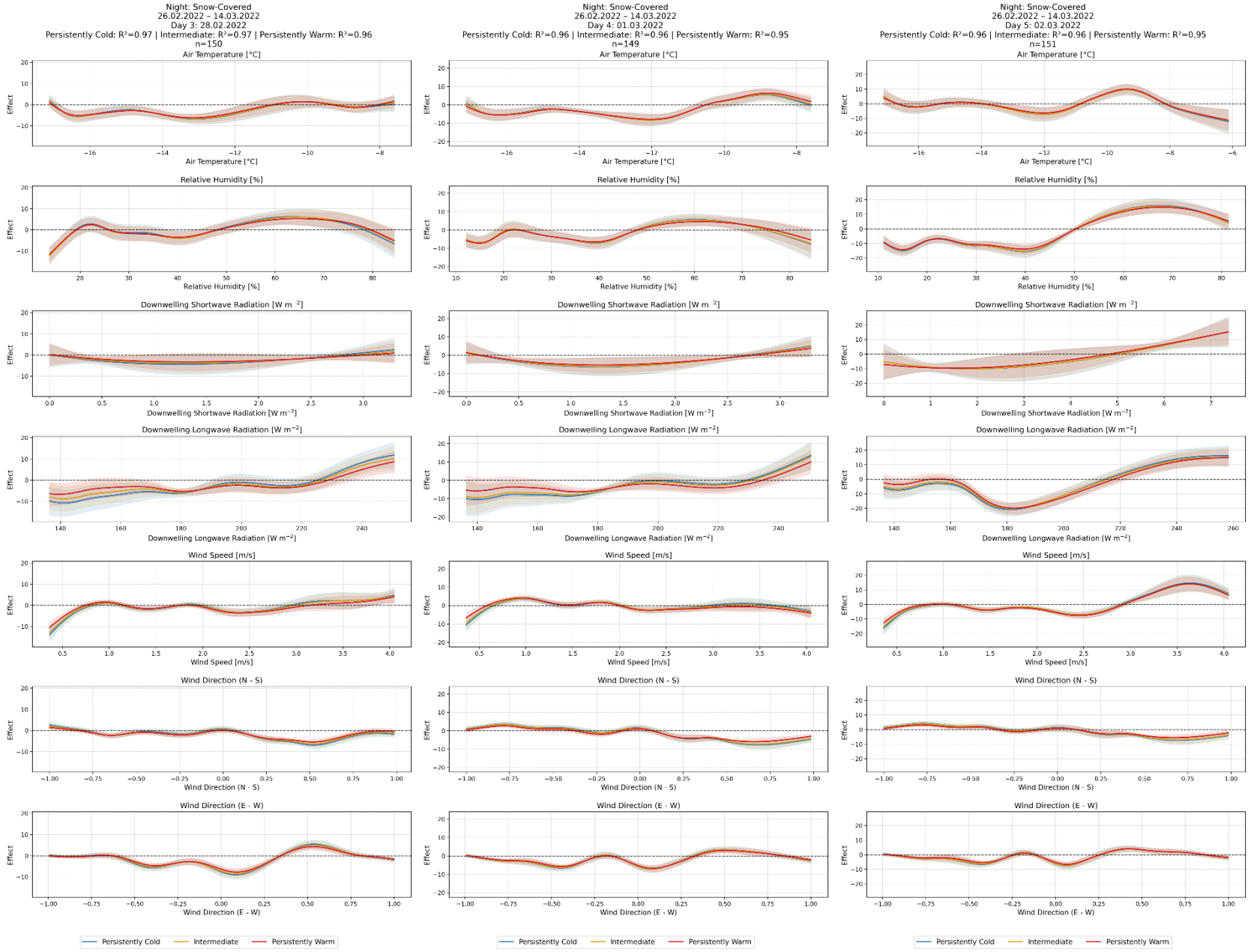

Figure C.65: GAM results of the anomaly persistence classification approach of days 3, 4 and 5 of the snow-covered night period.

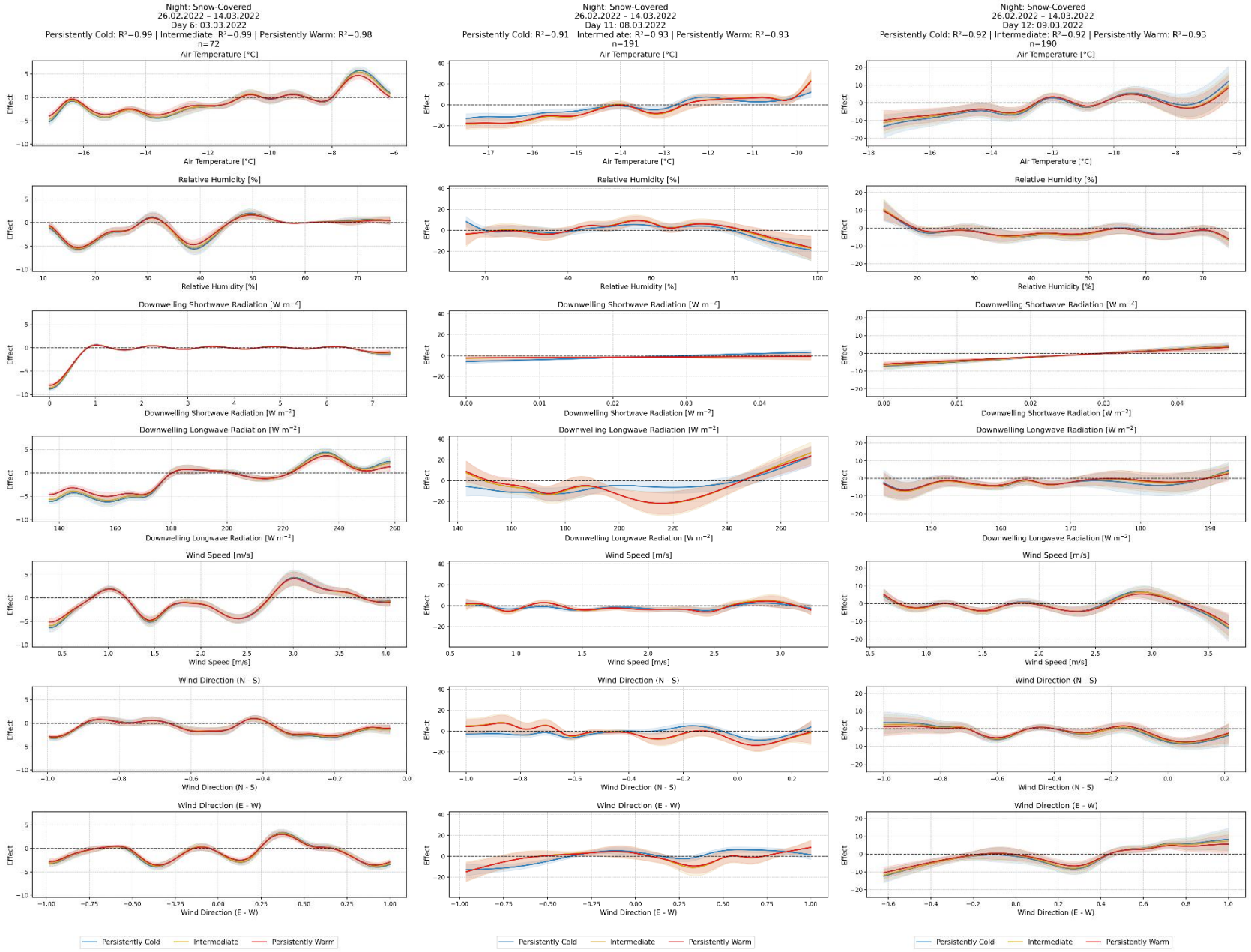

Figure C.66: GAM results of the anomaly persistence classification approach of days 6, 11 and 12 of the snow-covered night period.

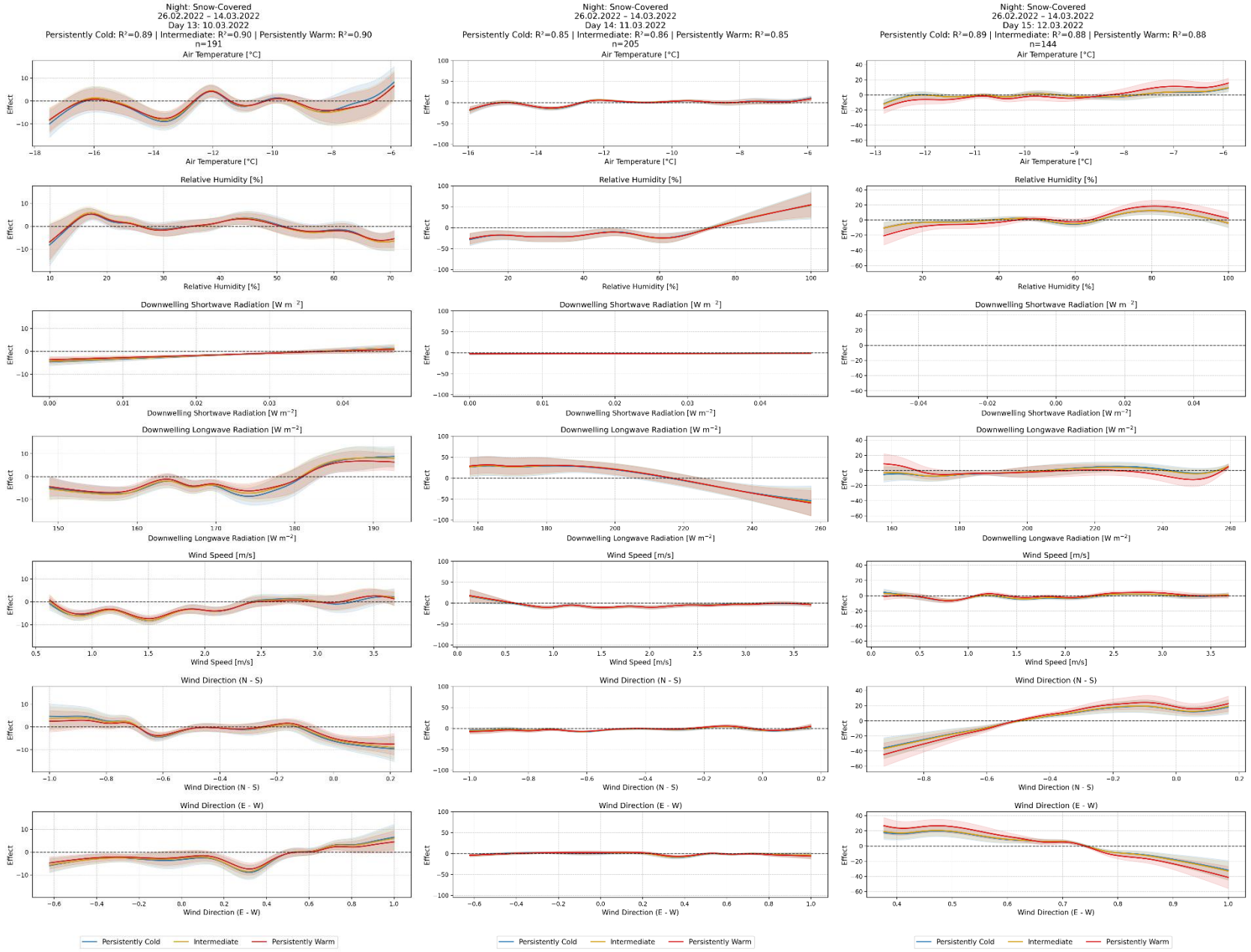

Figure C.67: GAM results of the anomaly persistence classification approach of days 13, 14 and 15 of the snow-covered night period.

Disclosure Statement for the use of AI

In the process of working on this thesis, AI was used for the following purposes:

1. Consensus AI to identify and find additional, peer-reviewed scientific sources relevant to the topics covered in the thesis which I couldn't find with my usual literature research methods. *"Which meteorological variables control surface temperature on coarse-blocky permafrost terrain?"*

2. Chat GPT5.1 – 5.3 and Claude Opus 4.7 to improve grammar and language in written texts. *"Check this text for grammatical errors and restructure it to improve the readability of it and the user's understanding. Don't change or add any facts that aren't explicitly mentioned in the original text. [text]"*

3. Chat GPT5.1 – 5.3 and Claude Code for assisting in writing python scripts to carry out the analysis. It was especially used to speed up plotting purposes like generating the broad structure of plotting code that I than modified to use the correct variables, colour schemes and labels. It was also used to help me find errors in the scripts and resolve them.
   "Generate the structure of a python script for a barplot showing how many times each k (2-7) achieved the best silhouette score across all clustering windows. Load all silhouette_summary_*.csv files in the clusters root folder, find the best k for each window, count how often each k wins and plot those counts in the barplot."
   "I got following error [error] while working on this script [script]. Help me locate the source of the error using debugging statements or provide ideas on how to fix this error if you can spot it without debugging statements."

I hereby declare that I have completed this thesis independently and without the use of any unauthorized aids (including generative AI tools, which are considered aids). I understand that I bear full responsibility for the selection, adoption, and all results of any AI-generated output that I have used. Furthermore, I certify that all use of generative AI in this thesis has been fully and accurately disclosed.

With my signature I confirm that the information provided above is true and accurate.

Date, Place

Signature

08.07.26, Effretikon

Personal Declaration

I hereby declare that the submitted thesis is the result of my own, independent work. All external sources are explicitly acknowledged in the thesis.

Date, Place	Signature
08.07.26, Effretikon	